A microanalytical study of Pb and Cu uptake coupled to siderite dissolution

Lisa C. Füllenbach

A thesis submitted in fulfilment of the degree of

Doctor of Philosophy

Department of Earth Sciences

University College London

London, 30. March 2022

Principal supervision:	S. H. Little[1], PhD (2021–2022)
	Prof. E. H. Oelkers[2] (2017–2020)
Subsidiary supervision:	Prof. I. Wood[1]

[1]University College London, Department of Earth Sciences

Kathleen Lonsdale Building, Gower Street, WC1E 6BT, London, United Kingdom

[2]GET, CNRS UMR 5563, 14 Avenue Edouard Belin, 3400 Toulouse, France

Declaration

I, Lisa C. Füllenbach, confirm that the work presented in this thesis is my own. Where information has been derived from other sources, I confirm that this has been indicated in the thesis.

Abstract

Heavy metal contamination of aqueous environments is a worldwide problem and remediation is particularly challenged by natural redox fluctuations, causing acidity and increased metal solubility. Siderite ($FeCO_3$) is a promising candidate material for heavy metal sequestration, as its carbonate component may regulate acidity, while the redox active Fe(II) component may act as reductant or as sorbent upon oxidative precipitation as Fe(III) (oxyhydr)oxides. To tap the full potential of siderite and its auspicious properties, this thesis investigates the efficacy of metal uptake coupled to siderite dissolution from oxic and anoxic acidic aqueous solutions. Lead (Pb) and copper (Cu) are chosen as case studies for weakly (Pb) and strongly (Cu) redox active metals. In laboratory experiments, metal uptake and pH development are monitored during siderite dissolution in Pb- and Cu-bearing oxic and anoxic acidic waters. Special focus is laid on characterising the solid reaction products using high-resolution analyses to determine the metal speciation and type of bonding decisive for metal retention. Siderite surface-controlled adsorption and dissolution–precipitation reactions buffer the reactive solution pH, while the properties of the dissolved metals determine the reaction pathways. Under oxic conditions, metals predominantly adsorb onto secondary Fe(III) (oxyhydr)oxide precipitates, while under anoxic conditions, metals are captured by sparingly soluble cerussite ($PbCO_3$) and native copper precipitation. Key to these processes is the continuous dissolution of siderite, which is promoted by non-epitaxial growth and phase transformations of the precipitates on the reacting siderite surface.

This study corroborates the great potential of siderite dissolution to remediate metal polluted water-saturated dynamic redox environments by counteracting acidity and capturing metals in secondary minerals. The thorough documentation of the reaction products and mechanisms advances our understanding of siderite–metal (redox) interactions to predict sustainable metal contaminant immobilisation and metal cycling in other modern and ancient Fe(II) and carbonate-rich natural aqueous environments.

Impact Statement

Environmental heavy metal pollution is a worldwide problem, harming wildlife and affecting the health of local workers and communities. Local, regional, national, and international industries, policy makers, and environmental agencies rely on geochemical model predictions to assess and mitigate potential risks and damage induced by the metal contamination of the affected environments. The quality of drainage waters from mining or industrial sites, for example, need to meet stringent (inter)national standards to prevent environmental and human health hazards. To limit potential impacts of the often acidic and highly metal-enriched drainage waters, the geochemistry of the site and of the drainage waters needs to be well understood to allow sustainable and cost-effective treatment strategies to be implemented accordingly. Metal immobilisation through the interaction with the natural mineral siderite is a promising method to limit potential metal mobility and bioavailability. Natural changes of the geochemical conditions of the metal-contaminated sites challenge the durability of many treatment strategies, and the effect on siderite as a reagent is not well understood.

The work presented in this thesis addresses this challenge by providing detailed evidence for the effective metal uptake by reacting siderite with dissolved metal-bearing aqueous solutions under two naturally most relevant geochemical conditions. The interaction of the two common metal contaminants lead (Pb) and copper (Cu) with siderite under the two study conditions are thereby presented as case studies for different uptake pathways that chemically similar metals may follow. The findings of this study advance our understanding of how the geochemical conditions and the chemical properties of the metal contaminants affect the uptake mechanisms by siderite. The analytical techniques used to identify how the metals are bound additionally advance the scientific approach to verify the efficacy of potential novel metal remediation materials at unprecedented resolution.

The comprehensive data presented in this thesis allows to accurately assess the metal uptake mechanisms and binding forms, which are crucial parameters to be considered in geochemical model predictions and decisive for the suitability of a method to be applied at a specific contaminated site. As siderite and the mineral reaction products are common constituents in natural and engineered environments, the results can be translated to other geochemical settings. The application of Enhanced Rock Weathering strategies on croplands to capture airborne carbon dioxide and mitigate climate change, for example, follows comparable chemical reaction pathways. One potential pitfall of Enhanced rock Weathering is the possible

release of metals into the soils. The documented metal uptake mechanisms in this study may help to evaluate this potential risk of metal contamination. On a more fundamental approach, the specific behaviour of siderite under the studied conditions provides insights into the geochemical cycling of elements relevant during the evolution of the early Earth's oxygenated atmosphere. The knowledge gained from this study hence aids industries, policy makers, and researchers to better estimate potential environmental risks and make informed decisions on mitigation strategies to tackle global challenges.

Acknowledgements

The work presented in this thesis was funded by the European Union's Horizon 2020 Marie Skłodowska-Curie Actions Innovative Training Network program (MSCA-ITN, grant no. 675219). Additional support provided by the German Helmholtz Recruiting Initiative (award number I-044-16-01), the Diamond Light Source I14 (proposal MG21719-1), and the ANKA-KIT SUL-X (proposal A2017-028-012253) are kindly acknowledged.

Special thanks to:

E. H. Oelkers, S. H. Little, I. Wood, D. J. Wilson, C. L. Peacock, L. G. Benning, J. P. H. Perez, S. L. Stipp, D. J. Tobler, C. Desplats, A. N. Thomas, J. Göttlicher, R. Steiniger, J. E. Parker, J. Stockmann, J. Radnik, J. Davy, G. Tarbuck, H. M. Freeman, S. Mayanna, G. Saldi, A. Schreiber, J. J. P. A. Mulders, A. G. Grima, G. Magnarini, A. Harrison, M. Murphy, C. S. Füllenbach, H. W., I., J. A., and A. T. Brombacher.

Preface

This thesis addresses many different aspects of mineral–water–metal interactions. To provide the most essential terminology, basic concepts and analytical methods used and referred to in this work, a thorough introduction is included over the first three chapters.

Chapter 1 provides a brief overview on the issue of heavy metal remediation of aqueous environments. It follows a more in-depth introduction to the most important geochemical concepts underlying mineral–water–metal (redox)interactions. These concepts essentially describe the stability of chemical species and minerals in aqueous solutions and thus determine whether or not a dissolved metal can be effectively and sustainably sequestered.

Besides the geochemical fundamentals, microanalytical techniques play a key role in understanding mineral–water–metal interactions. **Chapter 2** introduces the most important electron microscopic, and X-ray spectroscopic techniques used in this study. These powerful tools provide the essential evidence for the theoretical considerations resulting from aqueous solution analyses and geochemical modelling, such as identifying the morphology and (local) structure of the reaction products, metal distribution, speciation, and type of bonding.

Chapter 3 details a review of our current knowledge of metal–mineral interactions in aqueous systems. As siderite combines the properties of divalent metal carbonates and iron oxides upon oxidation, this chapter particularly focuses on metal sorption to iron oxides, the interaction of metals with carbonate minerals, and on siderite used to remove metal(loid)s from aqueous solutions. Building on the basis of knowledge from chapters 1 to 3, this chapter concludes with outlining the objectives of this thesis.

In **chapter 4** and **5** follows the original research. The acquired conceptual and technical knowledge on carbonate and iron oxide mineral interaction with dissolved metals in aqueous systems is applied to experimentally investigate the efficacy and mechanisms of metal uptake upon siderite dissolution in acidic oxic and anoxic aqueous solutions, using extensive microanalysis to evaluate the metal retention by the reaction products.

Chapter 4 reports on the interaction of the only weakly redox-active metal lead (Pb) with dissolving siderite under oxic and anoxic conditions. The partitioning of Pb between iron (Fe) and carbonate reaction products is of particular interest, as Pb forms sparingly soluble carbonate minerals but is also known to form strong surface complexes with ferric iron (oxyhydr)oxides. The findings of this study are published in *ACS Earth and Space Chemistry* in 2020.

Chapter 5 explores the interaction of the redox-active metal copper (Cu) with dissolving siderite under oxic and anoxic conditions. The high redox sensitivity of both Fe and Cu is of particular interest, as these metals may form strong redox couples under both redox conditions. Whether such redox processes outcompete any interactions between Cu and carbonate, and whether stable solid, Cu-containing reaction products are formed that sustainably retain Cu is investigated in this chapter.

Chapter 6 draws conclusions from the insights gained in chapter 4 and 5, reflecting on whether siderite dissolution is an effective method to remove potentially toxic dissolved metals from aqueous environments, putting the findings into a broader context. It further discusses future implications of the findings on related redox-affected mineral dissolution–precipitation processes in natural environments in which metal release and immobilisation are of importance, such as during Enhanced Weathering strategies or in early Earth environments around the early evolution of our oxygenated atmosphere.

Ultimately, an elaborate **Appendix** includes additional information on experimental design, control experiments, methodology and data processing, as well as supporting information to chapters 4 and 5 including geochemical modelling and supplementary chemical, microscopic, and spectroscopic analytical results.

Contents

List of Figures

1 Introduction

2 Microanalytical tools to study mineral–water interaction

3 Metal–mineral interaction in aqueous solutions

4 Pb uptake coupled to siderite dissolution

5 Cu uptake coupled to siderite dissolution

Appendix

List of Tables

3 Metal–mineral interaction in aqueous solutions

4 Pb uptake coupled to siderite dissolution

5 Cu uptake coupled to siderite dissolution

Appendix

List of Symbols and Acronyms

Symbols

a	Activity
A	Chemical affinity
aq	Aqueous
C_{aq}	Concentration or activity of a solute
CN	Coordination number
E	Redox potential
E^0	Standard electrode potential
E_a	Activation energy
Eh	Redox potential of an aqueous solution
F	Faraday's constant (96485 C mol^{-1})
G	Gibbs free energy
hkl	Crystallographic Miller indices
I	Ionic strength
IAP	Ion activity product
K	Kelvin
$k_{+,-}$	Proportionality or rate constant
K_d	Distribution coefficient
K_{eq}	Equilibrium constant
K_F	Freundlich isotherm (equilibrium constant)
K_L	Langmuir isotherm (equilibrium constant)
K_{sp}	Solubility product
L	Ligand
m	Molality
Me	Metal ion

p*e*	Electron potential
pH	Proton potential
pH_{50}	Sorption edge
pH_{IEP}	Isoelectric point
pH_{PPC}	Pristine point of zero charge
pH_{PZC}	Point of zero charge
pH_{PZNPC}	Point of zero net proton charge
Q	Reaction quotient
q	Mole fraction
R	Gas constant (1.9872 cal mol^{-1} K^{-1}; 8.134 J mol^{-1} K^{-1})
r_-	Rate of backward reaction
r_+	Rate of forward reaction
S_{total}	Total amount of available surface sites
SA	Surface area
SI	Saturation index
T	Temperature
Γ	Sorption density
V	Volume
Z	Ion charge / atomic number
γ	Activity coefficient
μ	Chemical potential
σ_H	Proton surface charge
σ_o	Coordinative surface charge
ν	Valence
ψ	Electric potential
Ω	Saturation state

Acronyms

AE	Auger electron
AFM	Atomic force microscopy
AMD	Acid mine drainage
ARD	Acid rock drainage
BET	Brunauer–Emmett–Teller method to determine surface area
BIF	Banded iron formation
BSE	Backscattered electron
CCM	Constant capacitance model
(CD)MUSIC	(Charge Distribution) Multisite Complexation
DDLM	Diffuse double layer model
EDAX	Energy dispersive area X-ray spectroscopy
EDL	Electric double layer
EDS / EDX	Energy dispersive X-ray spectroscopy
EXAFS	Extended X-ray absorption fine structure
(FE)SEM	(Field emission) scanning electron microscopy
FFT / FT	Fast Fourier transform / Fourier transform
FIB	Focused ion beam
GIF	Granular iron formation
GOE	Great oxidation event
HAADF	High-angle angular dark field
(HR)TEM	(High resolution) transmission electron microscopy
ICP-OES	Inductively coupled plasma optical emission spectroscopy
IF	Iron formation
LCF	Linear combination fitting
LLNL	Lawrence Livermore National Laboratory (database)
LMWCA	Low molecular weight carboxylic acids

RSD	Relative standard deviation
SCM	Surface complexation model
SE	Secondary electron
SFA	Segmented flow analysis
TLM	Triple layer model
XAFS	X-ray absorption fine structure (spectroscopy)
XANES	X-ray absorption near edge structure
XPS	X-ray photoelectron spectroscopy
XRD	X-ray (powder) diffraction
XRF	X-ray fluorescence spectroscopy

1 Introduction

Heavy metal contamination is a worldwide issue. Methods to remediate metal polluted aqueous environments must consider both the geochemistry of the contaminants and of the contaminated site. The potential application, development, and evaluation of the efficacy of a method to remediate metal contaminated sites hence requires a thorough understanding of general water–rock, and more specifically, water–mineral–metal interactions. The underlying environmental geochemical concepts that are fundamental to these interactions and thus for metal sequestration are introduced in this chapter.

1.1. Heavy metal removal from aqueous environments

Heavy metal contamination, naturally or through human use of land, is a worldwide problem. Natural chemical rock weathering and alteration processes can leach trace amounts of metals out of the rock, upon which metals may become enriched in riverine or lake sediments, soils and groundwaters (Islam et al., 2000; Couture et al., 2010; Xie et al., 2011; Hseu et al., 2017; Shaheen et al., 2017). One prominent example is the geogenic arsenic pollution reaching toxic levels in groundwaters of the Bengal Basin (Acharyya et al., 2000; Islam et al., 2000; McArthur et al., 2004; Weinman et al., 2008; Reza et al., 2010; Chakraborty et al., 2015). Anthropogenic activities can likewise locally increase heavy metal concentrations to highly toxic levels, putting the health of humans, animals, and plants exposed to contaminated waters, soils, and food sources at high risk (Payne et al., 1998; Han et al., 2002; Cheng, 2003; Järup, 2003; Bloundi et al., 2009; Brinkel et al., 2009; Pourrut et al., 2011; Pareja-Carrera et al., 2014; Yunus et al., 2016). Most common anthropogenic sources of metal pollution include areas affected by mining (Marron, 1989; Gäbler & Schneider, 2000; Merten et al., 2004; Lim et al., 2008; Lecce & Pavlowsky, 2014; Antoniadis et al., 2017), industrial discharge (Cheng, 2003; Li et al., 2009; Sun et al., 2013; Xu, X. et al., 2014), waste disposal and landfills (Kasassi et al., 2008; Sun et al., 2013; Adamcová et al., 2017), atmospheric emissions (Steinnes et al., 1997; Sun et al., 2013; Xu, X. et al., 2014), petrol and fuel combustion (Vouk & Piver, 1983; Cheng, 2003; Dragović & Mihailović, 2009; Sun et al., 2013), agricultural use of fertilisers, fungicides, and pesticides (Kimura & Miller, 1964; Saha et al., 1970; Gimeno-García et al., 1996; Atafar et al., 2010; Defarge et al., 2018), and livestock farming (Nicholson et al., 1999; Cang et al., 2004; Wang et al., 2014). Contaminated sites commonly contain a variety of heavy metal(loid)s such as As, Cd, Co, Cr, Cu, Hg, Ni, Pb, Se, Zn, and radionuclides like Th and U at various concentrations (e.g., Wuana & Okieimen, 2011; Khalid et al., 2017). Particularly in areas affected by mining and industrial activities, metal concentrations may reach up to several thousand mg of metal per kg of sediment, soil (Gäbler & Schneider, 2000; Chen et al., 2012; Pan & Li, 2016), or wastewater (Wong et al., 2003).

Various strategies have been developed to sequester toxic metals in soils and from aqueous environments. Among the most rapid and effective techniques are *in situ* chemical immobilisation efforts, such as the use of soil amendments, injection of reactive particles or substances, or installation of permeable reactive barriers that inhibit further dispersal of the pollutants (e.g., Blowes et al., 1997; Baker et al., 1998; Obiri-Nyarko et al., 2014; Kumpiene et

al., 2008; Reischer et al., 2022). The effectiveness and sustainability of chemical treatments to immobilise metals from soils and aqueous environments are primarily dependent on

(1) the geological/pedological setting, which governs the geochemical environmental conditions and thus the speciation and solubility of metals and particulate matter,

(2) the chemical reactivity of the metal-binding material, which determines the metal uptake mechanisms and therewith the type of metal bonding.

Geological setting and environmental conditions. The geochemical environmental conditions of a contaminated site determine the stability of solids and the chemical form (species) of the metal contaminants. Key variables are the closely interlinked redox and pH conditions, which directly affect the chemical form of metals and mineral solubility in water-saturated soils, sediments, or aquatic systems (Lindsay, 1983; Calmano et al., 1993; Chuan et al., 1996; Karimian et al., 2018). These variables can be affected by seasonal (e.g., heavy rainfall, flooding) and/or periodic (e.g., tidal currents) fluctuations of water saturation, and change with depth of the water column, sedimentary, or soil profile. Deeper subsurface sedimentary layers are more likely reduced (anoxic), and metals are more likely securely bound in stable solid compounds (e.g., sulphide minerals). The exposure of reduced sediments to the atmosphere or oxygenated water changes the redox conditions and thus the binding forms of metals in the sediments (Calmano et al., 1993). The oxidative dissolution of reduced minerals and secondary mineral formation causes acidity, which increases metal solubility and can lead to high levels of elemental leaching from natural and synthetic materials (e.g., rocks, tailings, construction materials, or slags; Stumm & Lee, 1961; Nordstrom, 1982; Jamieson, 2011; Nordstrom, 2011a,b; Plumlee & Morman, 2011; Dold, 2016). A prominent example for such processes is the formation of acid mine or, more generally, rock drainage (AMD or ARD; Figure 1.1), caused by oxidative dissolution of sulphide-rich rocks, particularly of ferrous iron sulphides (pyrite, pyrrhotite; Garrels & Thompson, 1960; Singer & Stumm, 1970; Nordstrom, 1982; Dold, 2016). The redox activity of microbes and organic ligands also affects the redox conditions in soils and sediments, as they mediate and catalyse redox reactions leading to oxidative or reductive decomposition of minerals (e.g., Stumm & Sulzberger, 1992; Nordstrom, 2011a; Dong & Lu, 2012; Lu & Wang, 2012).

Metal uptake mechanisms and type of bonding. Metals are most mobile and easily available for uptake by living organisms in the form of dissolved metal ions. Common methods to chemically constrain metal ion transport, dispersion, and availability include

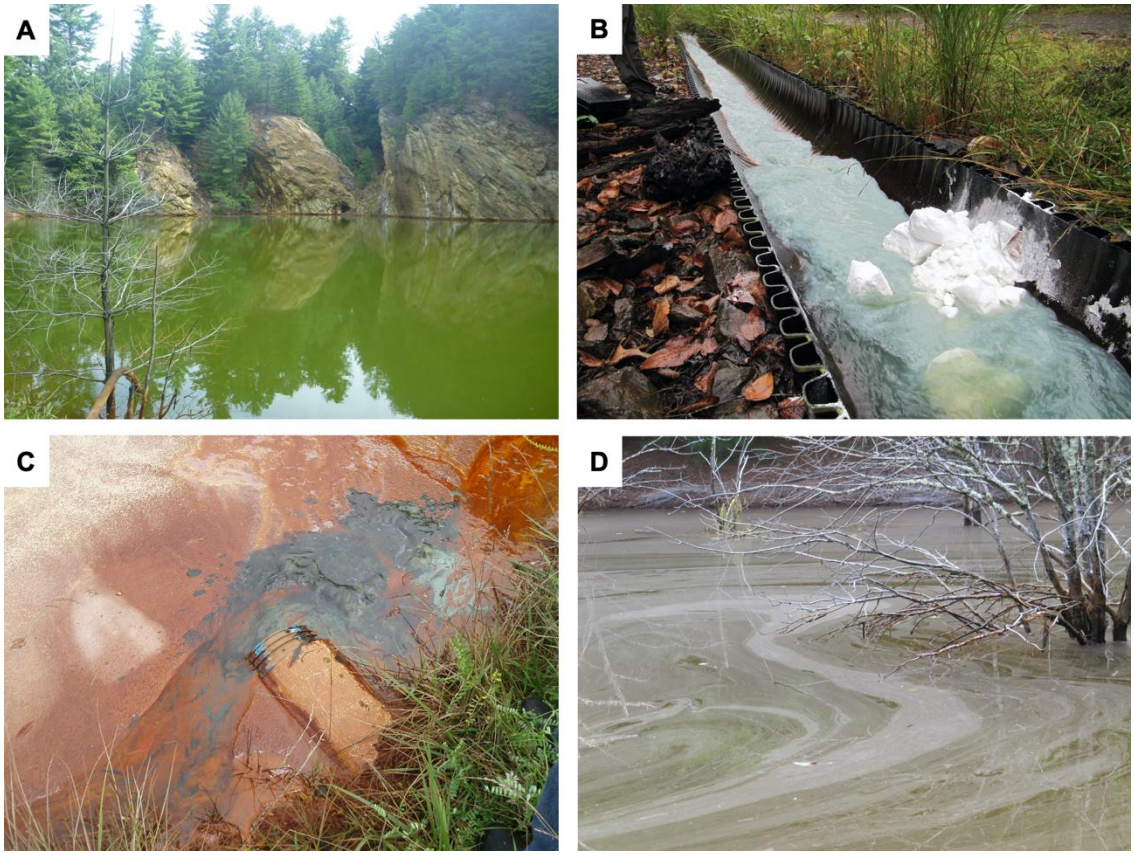

Figure 1.1. Acid mine waters at the Iron Ridge Mine, Virginia, USA. (A) Pit lake, pH ≤ 3, (B) soda neutralisation treatment of the pit lake outlet leading to limestone treatment ponds, (C) stirred iron mineral precipitation sludge in the first treatment pond (note the black and green colours indicating anoxic conditions just below the surface), (D) untreated surface waters on the property. *Photos: L. C. Füllenbach.*

(1) **adsorption** of metals to (nano)particulate materials with large reactive surfaces such as clays (e.g., Celis et al., 2000; Veli & Alyüz, 2007; Uddin, 2017), iron (oxyhydr)oxides (e.g., Eary & Rai, 1988; Crawford et al., 1993; Fuller et al., 1993; Raven et al., 1998; Arthur et al., 1999; Dixit & Hering, 2003; Fischer et al., 2007; Marshall et al., 2014) and other metal oxides (e.g., Al, Mn, Fe; Gadde & Laitinen, 1974; Bargar et al., 1996; Feng et al., 2007; Hua et al., 2012),

(2) (co)**precipitation** of metals in less soluble phases resulting from dissolution–precipitation reactions of, for example, calcium carbonate minerals (e.g., Stipp et al., 1992; Godelitsas et al., 2003; Prieto et al., 2003; Köhler et al., 2007; Renard et al., 2019),

(3) **sorption and/or (co)precipitation coupled to metal reduction** by Fe(II)-bearing minerals such as Fe-clays (nontronite; e.g., Jaisi et al., 2009; Joe-Wong et al., 2017), green rust (e.g., O'Loughlin et al., 2003a,b; Bearcock et al., 2011; Thomas et al., 2018), and siderite (e.g., Tang & Martin, 2011; Scheinost et al., 2016; Bibi et al., 2018).

These methods represent different types of uptake mechanisms, resulting in different types of metal bonding and thus vary in their metal retention efficacy, particularly in environments prone to redox and pH fluctuations. Metal adsorption to sparingly soluble sorbents, for example, is reversible upon changes in pH (e.g., Schultz et al., 1987; Parks, 1990; Dale et al., 2015), while sorbed and structurally incorporated metals may be released upon reductive dissolution and/or interaction with strong reductants such as Fe(II) as conditions become more reducing (Zinder et al., 1986; Davranche & Bollinger, 2000; Pedersen et al., 2006; Frierdich & Calmano, 2012a,b). The (co)precipitation of metals in sparingly soluble and redox insensitive solids is the most stable form of metal uptake as the metals are strongly bound within the crystal lattice. Such partitioning or structural incorporation into a separate solid phase, however, cannot always be achieved, particularly not for all metals in the same contaminant assemblage, as the various metals have different chemical properties and are differently affected by the environmental conditions (e.g., redox, pH, pCO_2). Thus metal solubilities strongly vary with their redox activities, specific sorption affinities and partitioning behaviour, for example, between organic matter, (hydr)oxide or carbonate species (e.g., Carroll et al., 1998; O'Day et al., 1998; Fischer et al., 2007; Macías et al., 2012; Khalid et al., 2017; Rinklebe & Shaheen, 2017; Shaheen & Rinklebe, 2017; Gankhurel et al., 2020).

Ideally, all metal contaminants of a polluted water-saturated environment would be sequestered equally securely and sustainably via a cost-efficient method without introducing additional harmful substances to the environment. The aspired immobilisation reagent would further prevent metal release during redox cycling in the aqueous system.

In this thesis, I investigate the metal immobilisation efficacy of the ferrous iron carbonate siderite ($Fe^{II}CO_3$) under oxic and anoxic conditions. Siderite is a promising candidate material as it combines the properties of acidity regulating carbonate minerals, with the redox activity of Fe(II) that may act as reductant and as sorbent upon oxidative precipitation as Fe(III) (oxyhydr)oxides.

To experimentally assess the full potential of these properties, I used siderite as a reagent rather than a mere sorbent. Therefore, I added fine-grained siderite to initially acidic, metal-bearing oxic and anoxic aqueous solutions to induce siderite dissolution and thus the release of carbonate to regulate the acidity and Fe(II) to (redox) interact with the dissolved metals. For this purpose, I deliberately chose two very common metal contaminants with distinctly different chemical properties: Lead (Pb) as representative for only weakly redox-sensitive metals that instead tend to partition into carbonates, and copper (Cu) as representative for redox-active

metals that redox-interact with Fe(II). Both metals are known to adsorb to iron (oxyhydr)oxides under oxic conditions, however, the interaction of dissolved Pb and Cu with siderite under either redox condition is poorly understood. A particular focus of this study is hence laid on the characterisation of the solid reaction products to assess the metal speciation and type of bonding after the reaction with dissolving siderite. These characteristics determine the metal capturing efficacy of siderite dissolution and allow for an in-depth understanding of the responsible uptake mechanisms to help predictions of metal fate and transport in similar environments.

All metal–mineral interactions in aqueous environments are based on aqueous geochemistry thermodynamics and reaction kinetics. Therefore, a broad introduction to the most important thermodynamic and kinetic principles is provided in the following.

1.2. Geochemical processes in aqueous systems

When considering the immobilisation or liberation of metal contaminants in soils, water-saturated sediments, and particulate-rich aqueous environments where water and gases can freely circulate, chemical processes at solid–liquid boundaries are of particular importance. The aqueous environmental conditions determine the chemical form, i.e., the redox state and type of chemical bonding of an element. The chemical form is decisive as potentially toxic metals may be securely captured and unavailable when bound in solid mineral structures, whereas metals in the form of dissolved ions are highly mobile and readily available for uptake by, and thus most harmful to organisms (O'Day, 1999; Plumlee & Morman, 2011). Key processes constraining the fate and transport of metal contaminants and thus local enrichment to toxic levels in aqueous environments are based on **thermodynamic and kinetic concepts**, including (1) solubility and dissolution/precipitation kinetics, (2) processes at the mineral–water interface, and (3) redox reactions.

In all chemical reactions, the reactants tend towards the energetically most stable state of the system – the thermodynamic equilibrium. The concept of thermodynamic equilibrium is thus fundamental to geochemical processes that determine and predict the mobilisation or immobilisation of metal contaminants in aqueous systems. Hence, some important principles of thermodynamics and related reaction kinetics are introduced.

1.2.1. Basic principles of aqueous solution thermodynamics

When considering reactions in aqueous environments, defining the chemical form of the components in the system is crucial. The chemical form – or speciation – of a chemical element or molecule is defined by its redox state (e.g., Fe^{2+}, Fe^{3+}, Cu^{+}, Cu^{2+}, As^{3+}, As^{5+}) and its binding form (e.g., $Cu(H_2O)_6^{2+}$, $H_2AsO_4^{-}$, HPO_4^{2-}, HCO_3^{-}, CO_3^{2-}). The speciation of an element essentially influences its chemical behaviour – its mobility, reactivity, and partitioning between the solid and aqueous phase in an aqueous system. As such, the speciation of an element is particularly important with regards to environmental contaminants as it defines their bioavailability and toxicity, but also their persistence (e.g., Carroll et al., 1998; Barceloux, 1999; Gankhurel et al., 2020).

The speciation of a chemical element or molecule is determined by its immediate environment and the governing thermodynamic conditions. Key to understanding and describing geochemical processes that affect the fate of chemical species and solid compounds in aqueous systems is the concept of the **thermodynamic equilibrium**. Natural systems generally occur in a metastable state and (chemical) reactions tend towards the energetically most favourable, stable state of the system: the equilibrium state. That is, a dissolved metal ion, for instance, will partition into a solid phase if this is the thermodynamically more stable form of this metal under the given physicochemical conditions. Essential to this concept is the equilibrium constant *K*, which is based on the law of mass action and may be used in various forms and contexts. For a chemical reaction of the form

$$a\mathrm{Me}^{m+} + b\mathrm{L}^{n-} = \mathrm{MeL} \qquad \text{(eq. 1.1)}$$

where *a* and *b* are the number of mols of the metal ion Me and ligand L with charges *m* and *n*, respectively, the most basic form of the **equilibrium constant K_{eq}** is written as the ratio of the activities of the reaction products and reactants:

$$K_{\mathrm{eq}} = \frac{[\mathrm{MeL}]}{[\mathrm{Me}^{m+}]^{\mathrm{a}} \cdot [\mathrm{L}^{n-}]^{\mathrm{b}}} \qquad \text{(eq. 1.2).}$$

The **activity a_i** of a reaction component *i*, given in brackets in equation 1.2, is defined as

$$a_i = \frac{\gamma_i m_i}{\gamma^o_i m^o_i} \qquad \text{(eq. 1.3)}$$

where m_i is the actual molality of the component (concentration in mol kg^{-1} of solvent; often noted as M) and m_i^o is its molality at a chosen standard state (indicated by ^{o}). The dimensionless

activity coefficient γ_i in equation 1.3 corrects the activity of the species for its nonideal behaviour in a real aqueous solution in relation to its ideal behaviour in an ideal solution at infinite dilution. The standard state for solutes is usually defined as $m_i^o = 1$ molal with $\gamma_i^o = 1$ (unit activity), which causes the activity to be dimensionless and equation 1.3 to become reduced to $a_i = \gamma_i m_i$. For ideal (pure) solids and liquids, such as stoichiometric minerals and pure H_2O(l), the standard state is generally defined as $a_i = 1$ (Anderson, 2005). Activity coefficients are empirically estimated (tabulated) factors that are a function of temperature, ionic radius, and the ionic strength of the aqueous solution (Appelo & Postma, 2005; Scheffer & Schachtschabel, 2010). The activity of an aqueous species is thus dependent on the total concentration (molality) of the species, the degree of nonideal behaviour (γ), and the **ionic strength *I***, which is a measure of electrical charge of all dissolved species in the aqueous solution. In very dilute solutions such as pore waters or soil fluids with a low ionic strength ($I \leq 0.1$ M), the activity coefficient of a dissolved ion is $\gamma_i \approx 1$, therefore the activity a_i of this species approximates its molality m_i (Scheffer & Schachtschabel, 2010).

The equilibrium constant only represents the equilibrium state of a reaction. As a measure of the **chemical potential μ**, the concept of activity provides a link to the reaction direction, i.e., whether the reaction tends towards reactants or products. The relationship between the activity a_i and the difference in the chemical potential μ_i of a reaction component in one state relative to its chemical potential μ_i^o in a chosen reference state can be expressed as

$$\mu_i - \mu_i^o = RT \ln a_i \qquad \text{(eq. 1.4)}$$

where R is the gas constant (1.9872 cal mol^{-1} K^{-1}) and T is temperature (in K; Anderson, 2005). The effect of compositional change during a reaction is thence reflected in the change in *chemical potential of the reaction* μ_r, which is described by the general relationship of

$$\Delta\mu_r = \Delta\mu_r^o + RT \ln Q \qquad \text{(eq. 1.5)}$$

where ***Q*** is the **reaction quotient** of the activity products (also known as the *ion activity product*s, **IAP**) of all reaction products and reactants. The reaction quotient or IAP of the components (e.g., metal ions) in an aqueous system helps to assess whether the components remain dissolved or whether solid phases may become stable and vice versa. If the pressure and temperature conditions are defined, μ_i is described as the Gibbs energy G per mole of the component. The change in **Gibbs (free) energy ΔG** thereby describes the maximum change in heat and (chemical) work required of a system to proceed from a metastable state towards its

equilibrium state. At equilibrium, the chemical potentials of all reaction products and reactants become equal and thus $\Delta\mu_r = 0$ and $\Delta G_r = 0$. For equilibrium reactions, the difference in Gibbs energies of products and reactants is given in relation to the difference in Gibbs energies of the components in their pure (tabulated) standard state, $\Delta\mu_r^o$ or ΔG_r^o. Because the activity product of the reaction components becomes the constant K_{eq} at equilibrium (as in equation 1.2), equation 1.5 can be rewritten as

$$\Delta G_r^o = -RT \ln K_{eq} \qquad \text{(eq. 1.6)}$$

(Anderson, 2005). This relationship between the difference in Gibbs energies and the ion activity products of the reaction is fundamental to determine the saturation state and solubility of solid phases. These concepts are often the basis of geochemical model calculations to predict, for example, whether a metal contaminant may be immobilised by forming a solid phase or whether potential metal sorbents will remain or become stable under the given conditions.

In nonequilibrium reactions, the reaction components are not necessarily present in their reference (standard) state and the activities of the reaction components may change in course of the reaction. For such reactions, the concept of **saturation state** allows the prediction of the direction in which the reaction may proceed. More specifically, the saturation state indicates whether a (solid) phase may become stable or unstable in an aqueous solution at a given pressure and temperature. In this case, the difference in Gibbs energies between the reaction products and reactants as they actually occur in the system, ΔG_r, is then given as a function of the ratio between the actual or *observed* (Q) and the *theoretical* equilibrium (K_{eq}) ion activity products of the species in solution:

$$\Delta G_r = RT \ln \frac{Q}{K_{eq}} \qquad \text{(eq.1.7).}$$

In the case of $Q = K_{eq}$, i.e., if the quotient of the observed activity products equals that of the expected concentrations at equilibrium, $\ln(1) = 0$, and thus $\Delta G_r = 0$ and the system is at equilibrium. If $Q < K_{eq}$, then $\Delta G_r < 0$ and the reaction will be pushed towards the right. If $Q > K_{eq}$, then $\Delta G_r > 0$ and the reaction will be driven towards the left (Langmuir, 1997; Anderson, 2005). To assess if a mineral will be stable, i.e., precipitate or dissolve as a result of the reaction in question, the ratio of observed (Q) and expected equilibrium activities (K_{eq}), also denoted as Ω in some literature, is used as a measure of distance from equilibrium (Langmuir, 1997; O'Day, 1999; Appelo & Postma, 2005). The logarithm of this ratio (Ω) is called the **saturation index (SI)** and is given as

$$SI = \log_{10}\left(\frac{Q}{K_{eq}}\right) \quad \text{(eq. 1.8).}$$

Defining the saturation state of a mineral in an aqueous system is a useful tool to indicate in which direction a reaction would proceed – either towards the formation of aqueous species or the solid compound. At equilibrium, $Q = K_{eq}$ and therefore $SI = \log_{10}(1) = 0$, which means that a system is **saturated** with respect to the mineral in question; this mineral is stable at this point. If the $Q < K_{eq}$, and thus the $SI < 0$, the system is **undersaturated** with respect to the mineral of interest and the mineral tends to dissolve. If the $Q > K_{eq}$, hence $SI > 0$, the system is **supersaturated** with respect to the mineral and the mineral tends to precipitate from the aqueous solution (Langmuir, 1997; Anderson, 2005). This simple method to determine the preferential partitioning of dissolved species is widely applied to predict mineral stabilities with geochemical computer codes such as PHREEQC (Parkhurst & Appelo, 2013), which are based on empirical thermodynamic data for numerous aqueous species and minerals.

1.2.2. Solubility and dissolution/precipitation kinetics

Whether metals are released into the environment during chemical weathering processes or redox cycling in soils, aquifers, wetlands, or any other natural or industrial system in which minerals are in direct contact with water, metal liberation and capture result from solid–water interactions. One very important aspect is the dissolution and/or precipitation of solids in the aqueous system. For example, if a metal-containing solid or mineral is exposed to water at far from equilibrium conditions, it may become unstable and start to dissolve, releasing its metal components into the aqueous system – which may ultimately lead to local metal enrichment to potentially toxic levels. And vice versa, if the conditions of the aqueous system are favourable for a metal-bearing solid phase to become stable, it may precipitate, capturing the dissolved metal and making it less bioavailable (*see* section 1.2.1.). Whether either or which will occur depends on the activity of ions in the aqueous solution (IAP) and the solubility of the solid phases.

The **solubility** of a mineral is a measure of its thermodynamic stability and is defined as the maximum molality of its constituent ions or compounds in solution (Appelo & Postma, 2005; Scheffer & Schachtschabel, 2010). The solubility is generally viewed in terms of the saturation state of the aqueous solution with respect to a mineral and thus marks a threshold concentration of dissolved ions in the aqueous solution: above this maximum molality, the solution is

supersaturated and the mineral precipitates, while below it, the solution is undersaturated and the mineral dissolves. The aqueous solution is saturated and in equilibrium with the mineral if the concentration of the constituent ions in solution is equal to the solubility (Anderson, 2005). Hence the solubilities of both target products and reactants play an important role in metal-immobilisation strategies.

The most favourable form of sequestering a dissolved metal from an aqueous solution is to bind it in a thermodynamically stable solid. That is, for example, to provoke the precipitation of a mineral containing the metal, and vice versa, to prevent the metal-bearing mineral from dissolving and thus releasing the metal back into solution. To determine whether a mineral will dissolve or precipitate under a given geochemical condition, its solubility can be determined by the relationship between the Gibbs free energy and the ion activity product of the reaction as in equation 1.6. Notably, in contrast to the saturation state, the solubility of a solid is again a theoretical value based on standard state considerations of ΔG_r^{o} and equilibrium concentrations as expected from K_{eq}. That is, in a dissolution reaction of a very simple example (ionic) mineral MeL(s) given as

$$\mathrm{MeL(s)} \Leftrightarrow \mathrm{Me}^{m+} + \mathrm{L}^{n-} \qquad \text{(eq. 1.9)},$$

where Me^{m+} and L^{n-} denote the dissociated ionic metal and ligand components, the mineral is assumed to be in its (pure) standard state, thus its activity equals 1. Therefore, the activity product at equilibrium for equation 1.9, given as

$$K_{eq} = \frac{[\mathrm{Me}^{m+}]\cdot[\mathrm{L}^{n-}]}{[\mathrm{MeL}]} \qquad \text{(eq. 1.10)},$$

reduces to the **solubility product K_{sp}** of the activities of the dissolved ions

$$K_{sp} = [\mathrm{Me}^{m+}] \cdot [\mathrm{L}^{n-}] \qquad \text{(eq. 1.11)}.$$

Notably, this equilibrium constant K_{sp} only applies to reactions with a (pure) solid phase on one side and its ionic constituents on the other (Anderson, 2005). The solubility of a mineral strongly depends on the chemical composition of the aqueous solution; more specifically on the pH and the activity of other ionic species present in the reactive fluid. From its relation to the thermodynamic principle of Gibbs energy, it also varies as a function of pressure and temperature, whereby the thermodynamic constant K increases with temperature for endothermic reactions and decreases with temperature for exothermic reactions (Appelo & Postma, 2005). Metal complexation in an aqueous solution may have the effect of increasing

the solubility of minerals that contain the metal ion as major component: due to the lower energy of the aqueous complex compared to the non-complexed metal, the metal may preferentially form the complex, thereby increasing the stability of this metal in solution. Therefore, the mineral is forced to dissolve as to retain saturation, while the metal remains mobile as aqueous complex (Langmuir, 1997; Appelo & Postma, 2005). For example, high concentrations of dissolved carbonate species in water lead to the dissolution of carbonate minerals by the preferential consumption of CO_2 by the formation of aqueous carbonate complexes (Plummer et al., 1978; Plummer & Busenberg, 1982; Bruno et al., 1992; Pokrovsky & Schott, 2002).

Another important factor is time. The rate at which a chemical reaction will proceed until it attains chemical equilibrium may take seconds, hours, years of even hundreds of millions of years. Notably, short equilibration times may be favourable when considering the need for acute treatments of heavily polluted wastewater leakage, however, longer equilibration times may be preferential when metals are required to be immobilised over prolonged periods of time as in permanent AMD treatment systems. Reaction kinetics therefore are required to quantitatively describe deviations from equilibrium, while the link to thermodynamic equilibrium chemistry indicates the direction in which a reaction should proceed.

In an aqueous solution, **dissolution/precipitation rates** of minerals are governed by reactive transport of chemical species to and from the reacting mineral surface by diffusion (transport reactions) coupled with the sorption and detachment reactions at the active mineral surface sites (surface reactions; Lasaga, 1984). The slower of the two processes controls the kinetics of the overall dissolution or growth (precipitation) reaction. If transport (diffusion) of aqueous reactants is slow relative to reactions occurring at the mineral surface, the reaction is *transport* or *diffusion controlled*, whereas if the surface reactions are slower than the transport processes, the reaction is *surface controlled* (Lasaga, 1984; Schott et al., 2009). The dissolution rates of highly soluble salts and hydrous minerals, for example, tend to be transport controlled, whereas those of less to moderately soluble minerals such as most rock-forming silicates, oxides, phosphates, and carbonates are controlled by surface hydrolysis reactions (Stumm & Wollast, 1990; Langmuir, 1997; Schott et al., 2009). Precipitation and growth kinetics are more complex and the influence of both transport and surface processes tend to be more variable (Lasaga, 1990 *and references therein*; Stumm & Wollast, 1990).

Most of these reactions are reversible, which means they can proceed in both directions. That is, considering for example the reaction given in equation 1.9, the reaction can proceed towards the decomposition of the mineral into its components Me^{m+} and L^{n-} at a rate r_+ with a

rate constant k_+ (forward reaction) or towards the precipitation of the mineral MeL at a rate r_- with a rate constant k_- (reversed reaction; Langmuir, 1997). The rate r of a reaction describes the change in the concentrations of the reactants and products (in parentheses) at the mineral surface over time t (commonly given in mol m^{-2} s^{-1}), thus the rates may be given as

$$r_+ = -\frac{d(\mathrm{MeL})}{dt} = k_+ (\mathrm{MeL}) \qquad \text{(eq. 1.12)}$$

for the forward reaction, and

$$r_- = \frac{d(\mathrm{Me}^{m+})(\mathrm{L}^{n-})}{dt} = k_- \left(\mathrm{Me}^{m+}\right)(\mathrm{L}^{n-}) \qquad \text{(eq. 1.13)}$$

for the reversed reaction. At equilibrium, the overall reaction rate r must be zero, hence the difference between the concentration-dependent partial rates of the reaction can be used to calculate the overall rate of the reaction as $r = 0 = r_+ - r_-$. It follows that if the rates of the forward and backward reactions are equal, the **kinetic equilibrium constant K^*_{eq}** of the overall reaction can be written as

$$K^*_{\mathrm{eq}} = \frac{k_+}{k_-} = \frac{(\mathrm{Me}^{m+})(\mathrm{L}^{n-})}{(\mathrm{MeL(s)})} \qquad \text{(eq. 1.14).}$$

The solution pH may have a strong effect on the rate of a reaction. In some cases, the rate constant k can be proportionally correlated to the activity of protons in solution

$$k \propto [H^+]^n \qquad \text{(eq. 1.15)}$$

where n is a value based on various surface site reactions (Lasaga, 1984). Reaction rates are furthermore highly dependent on temperature, which is generally described by the Arrhenius equation

$$k = Ae^{-E_a/RT} \qquad \text{(eq. 1.16).}$$

It includes the temperature independent Arrhenius factor A and the activation energy E_a for the overall reaction that generally lies within the range of 40-80 kJ mol^{-1} (Lasaga, 1984; Langmuir, 1997). Taking the natural logarithm and differentiating allows rewriting of the Arrhenius relation to

$$\frac{d\ln K}{d\mathrm{T}} = \frac{E_\mathrm{a}}{RT^2} \qquad \text{(eq. 1.17).}$$

The surface area of the reacting mineral in a fluid also effects the dissolution rate. To include this dependence in the rate equation, a mineral dissolution rate can be expressed by

$$\frac{d(\mathrm{Me}^{m+})}{dt} = \frac{SA_{\mathrm{MeL}}}{V} k_{\mathrm{Me}^{m+},\,\mathrm{MeL}} \qquad \text{(eq. 1.18).}$$

where SA_{MeL} is the surface area of the dissolving mineral MeL, and V the volume of the aqueous solution the mineral is in contact with, while $k_{\mathrm{Me}^{m+},\mathrm{MeL}}$ is the rate constant of metal ion Me^{m+} release from the dissolving mineral MeL (Lasaga, 1984).

The effects of surface reactions, protons, temperature, and surface area (which can be translated into particle size) on mineral dissolution rates need to be considered to estimate reaction times, for example, when mineral reactants are used for metal immobilisation purposes.

Dissolution and precipitation reactions at the mineral surface are driven by the reactive transport of aqueous reactants to and from the surface. The kinetics of such reactions are based on the theoretical construct of the transition state, which can be viewed as a link between the thermodynamic equilibrium concepts and reaction kinetics. **Transition state theory** describes the presence of an energy barrier at the maximum energy that needs to be overcome for an elementary reaction to proceed. At this energy maximum, the *transition state*, the reaction rates are assumed to be equal, and the reactants (A+B) are in chemical equilibrium with an *activated complex* (AB*), from the decay of which the reaction products are formed:

$$\mathrm{A} + \mathrm{B} \rightleftharpoons \mathrm{AB}^* \rightarrow \mathrm{AB} \qquad \text{(eq. 1.19).}$$

The transition from AB* to AB is spontaneous, thus the formation of the activated complex is the rate limiting step (Lasaga, 1981; Langmuir, 1997; Schott et al., 2009). In the transition state theory, the activated complex functions as a true chemical species that is in equilibrium with the initial reactants (Lasaga, 1981), and takes part in the reaction with a stoichiometry equal to complexes on the reacting mineral surface (it is not an actual thermodynamic species; Lasaga, 1990). As reaction rates are a function of the mineral surface area and are particularly dependent on the reactions occurring at the mineral surface, mineral surface properties play an essential role in all mineral–water reactions (e.g., Hochella & White, 1990; Stumm & Wollast, 1990; Schott et al., 2009). These processes particularly involving most rock-forming minerals such as silicates, oxides, and carbonates, are key to whether metals are securely captured or released as will be discussed in the following.

1.2.3. Processes at the mineral–water interface

The mineral surface defines the boundary between the solid and the liquid phase. As such, processes occurring at this interface are governed by the topography, the atomic structure, and chemical properties of the mineral surface. The mineral surface properties further influence the reactivity of a mineral in terms of, for example, its affinity to bind or interact with dissolved species such as metals, protons, hydroxyls, organic or inorganic ligands in the aqueous solution.

1.2.3.1. Mineral surface properties

Reaction rates are a function of surface area, that is, rates increase with increasing surface roughness and smaller grain size. Mineral surfaces comprise of a complex topography, thus accurate surface areas are commonly determined using the Brunauer–Emmett–Teller (BET) method (Brunauer et al., 1938; Pikett, 1945), measuring the adsorption density of gases, namely krypton or nitrogen. The size and shape (habit) of the mineral or particle also influence its reactivity, i.e., the higher the surface area, the more potential surface sites are available for solute interaction. Nanoparticles have particularly large surface areas and are therefore extremely reactive (e.g., Waychunas & Zhang, 2008), which is why nanoparticles are often of great interest when considering dissolved metal immobilisation via interaction with solids.

The habit of a crystal is governed by the slowest growing crystal faces. Each crystal face (*hkl*) has individual bonding properties and thus different surface free energies. Consequently, sorption properties differ for the various crystal faces, affecting the rates of dissolution and precipitation/growth reactions (Figure 1.2; Lasaga, 1990). Mineral surfaces are heterogeneous, comprising various amounts of vacancies, defects, and ions attached to the surface. For simplicity, theoretical **topographic surface sites** are classified as faces (F), steps (S) and kinks (K) (Figure 1.3). Sites with the highest unit area of exposure, K followed by S, are energetically the most reactive, i.e., most favourable for sorption and desorption and therefore precipitation and dissolution reactions, hence exhibit the fastest reaction rates (Lasaga, 1990). The probabilities of dissolved ions or molecules to attach to, diffuse into or detach from the different surface topographies determine mineral growth and dissolution at the atomic level (Monte Carlo simulations; Lasaga, 1990). Smooth growth surfaces are a result of slow euhedral growth at low supersaturation, whereas rough surfaces may indicate fast growth at high supersaturation. Notably, surface relaxation through dissolution/precipitation reactions may cause the structure of the 2–5 topmost atomic layers to deviate from the bulk structure (Hochella, 1990; Lasaga, 1990).

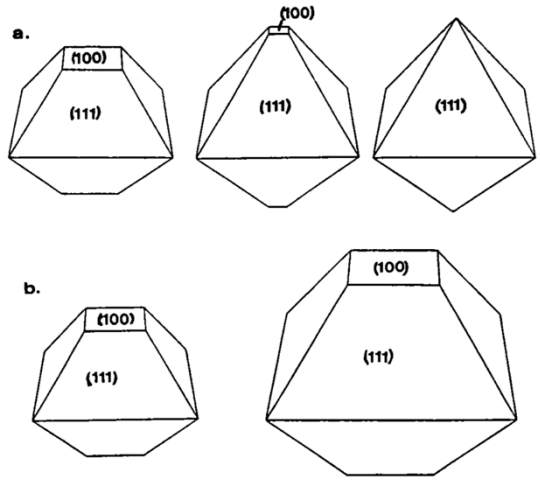

Figure 1.2. Examples of different habit evolution during growth of a cubic crystal. (a) The (111) face becomes predominant if the growth rate of the (100) face exceeds that of the (111) face, but less so if both growth rates are approximately similar (b). *From Lasaga (1990).*

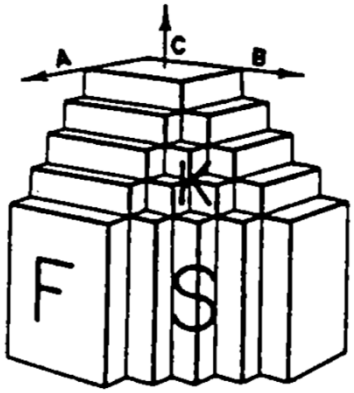

Figure 1.3. Schematic of the three most likely topographic surfaces that evolve during crystal growth: Faces (F), steps (S) and kinks (K). Other surface sites, e.g., defects or vacancies, are not shown here for simplicity. *From Lasaga (1990).*

At the mineral surface, the periodic arrangement of the crystal lattice is terminated. Thus, surface atoms have coordinatively unsatisfied, unbalanced bonds which are specific to the respective mineral structure and thus can be very different for each type of crystal face and mineral. Additionally, vacancy sites and structural defects at this topmost atomic layer also comprise such unsaturated bonds. Coordinatively exposed ions have an excess of charge, which may protonate or hydroxylate if exposed to air or an aqueous solution (e.g., Langmuir, 1918; Hochella, 1990; Parks, 1990). The resulting surface hydroxyl groups (or structural OH) are referred to as **surface functional groups**, which readily chemically react with the components present in their surrounding environment, e.g., gases and solutes (Hochella, 1990; Davis & Kent, 1990). Generally, mineral surface structures exhibit various types of surface functional groups, the form and reactivity of which are dependent on the coordination of the surface oxygens and cations. The type of surface group coordination and hence the surface charge distribution is therefore mineral specific. However, the surface-bound hydroxyls of most oxides and aluminosilicates are of amphoteric character, i.e., they react with both acids and bases due to their double pair of electrons and a dissociable proton (Brown, 1990; Davis & Kent, 1990; Cornell & Schwertmann, 2003). On iron oxides, for example, hydroxyl groups can be singly, doubly, and triply coordinated with underlying Fe atoms, resulting in negatively, neutral, and positively charged surface groups responsible for their amphoteric character in aqueous solutions (Figure 1.4; Cornell & Schwertmann, 2003). These surface characteristics are

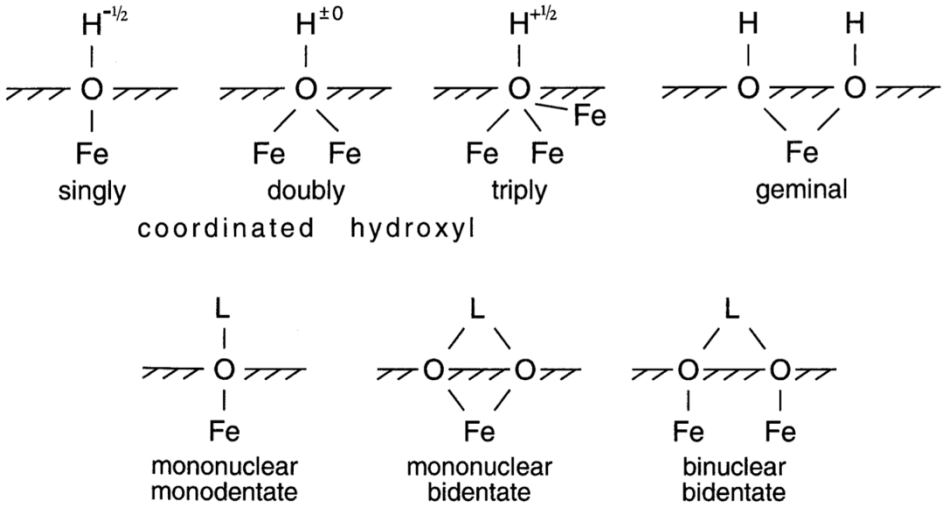

Figure 1.4. Surface coordination of hydroxyl groups (top) and ligands (or adions; bottom) on iron oxides. *From Cornell & Schwertmann (2003)*.

important, for example, when syntonising the types of solid reactants to the types of metal contaminant species aimed to be removed from an aqueous environment. This will become clearer as the link is drawn to surface charge and sorption in the following paragraphs.

In an aqueous solution, unbalanced charges as well as the amphoteric hydroxyl surface functional groups that can protonate or deprotonate contribute to the overall **surface charge** of a mineral, which is dependent on the initial solution pH_i. If the aqueous solution is pure, i.e., it only contains H^+ and OH^-, the pH at which neither protons nor hydroxyl ions are adsorbed to nor released from a mineral surface, hence when the charges at the surface are balanced to neutral, is known as the *pristine point of zero charge* or the *isoelectric point* (pH_{PPZC} or pH_{IEP}; Davis & Kent, 1990; Parks, 1990). In more natural systems, the surface charge develops as a result of protonation, hydroxylation, and the adsorption of other dissolved species to the mineral surface; the pH of neutral surface charge is thence called the *point of zero charge* (pH_{PZC}; Davis & Kent, 1990; Parks, 1990). The pH_{PZC} is dependent on the coordinative surface charge (σ_o), which results from coordination reactions (adsorption) of ions with the surface functional groups, and the proton surface charge (σ_H), which specifies the charge resulting from proton/hydroxylation of the pristine surface. By definition, the pH_{PZC} is the pH value at which σ_H equals zero. To distinguish the case when the pH_{PZC} occurs at a pH at which $\sigma_H = 0$ but $\sigma_o \neq 0$, this pH value is termed the *point of zero net proton charge* (pH_{PZNPC}; Figure 1.5; Davis & Kent, 1990).

Generally, at $pH_i < pH_{PZC}$, the sorption density of protons is higher than that of hydroxyl ions, and vice versa, at $pH_i > pH_{PZC}$, hydroxyl sorption density exceeds that of protons (Parks, 1990). Consequently, for many simple metal oxides and silicates, sorption of cations to the protonated surface is weak and anion sorption strong at low pH, while the opposite is the case and cations preferably sorb to the hydroxylated surface than anions at high pH. As other solutes such as dissolved metals may interact with the surface functional groups by the replacement of a proton, their sorption also contributes to the development of surface charge and therefore may shift the pH_{PZC} of the sorbent (e.g., Stumm et al., 1976; Davis & Kent, 1990; Van Cappellen et al., 1993). The sorption behaviour is also sorbate specific. The pH at which 50% of the total amount of solute species is adsorbed is known as the *sorption edge* or pH_{50}. The position of the pH_{50} depends on both the concentrations and types of sorbate and sorbent surface species (Figure 1.6; Parks, 1990; Appelo & Postma, 2005).

The origin of surface charge for oxides and silicates is mostly the adsorption of protons or hydroxyl ions, which is also referred to as the "ionisation of the surface functional groups"

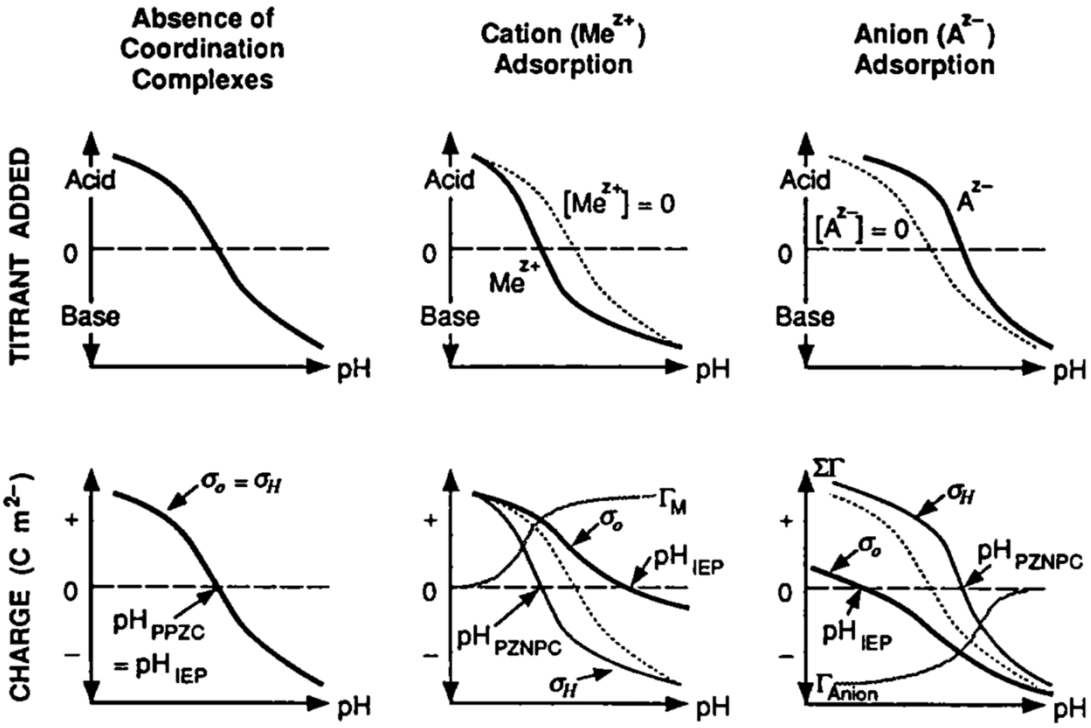

Figure 1.5. Schematic illustrating the effect of cation and anion adsorption on the coordinative surface charge (σ_o) on oxide surfaces in aqueous solution. Top row graphs show the effect of chemisorption on acid-base titration curves used to determine the pH_{PZC}. Bottom row graphs show the effect of chemisorption on σ_o and σ_H, which further determine the pH_{IEP} and pH_{PZNPC} (Γ represents the sorption densities of the potential-determining cations (M) and anions (A)). *Davis & Kent (1990)*.

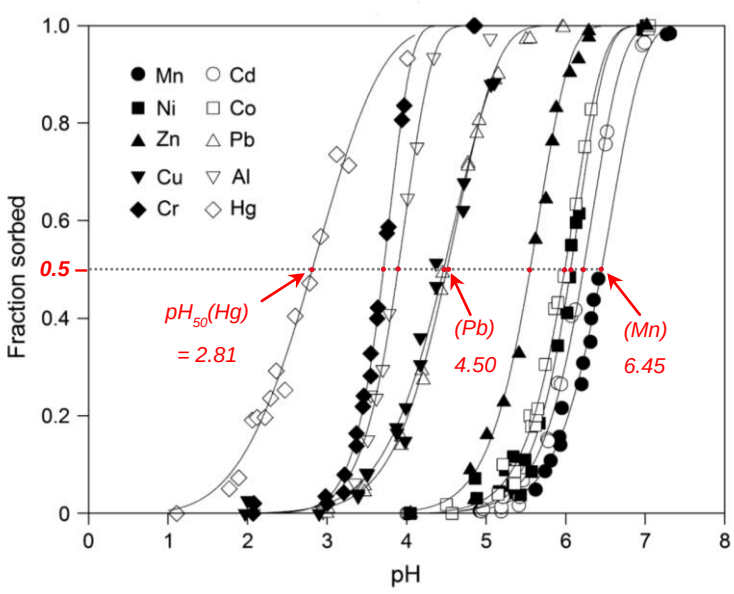

Figure 1.6. Adsorption curves of ten metals on goethite. The dotted line indicates the point at which 50% of the metal is adsorbed (pH_{50}), with some example values given in red for Hg, Pb, and Mn. *Taken from and modified after Fischer et al. (2007)*.

(Parks, 1990). Surface charge may also originate from permanent structural charge as in many aluminosilicates such as clays, micas, and zeolites, for example, in which isomorphous ion exchange and lattice defects result in an excess of exposed O^{2-} and OH^{-} ions, causing a mostly negative net surface charge. For ionic minerals such as carbonates, however, the constituent metal cations and the anionic carbonate ligand determine the surface charge, which is much more variable (Charlet et al., 1990; Parks, 1990). Similarly, different types of surface hydroxyl groups in hydrous oxides such as ferric oxyhydroxides have different reactivities due to different O-coordination in the structure (*see* Figure 1.4; Barrón & Torrent, 1996), resulting in variable, amphoteric surface charge that is strongly pH dependent (Davis & Kent, 1990; Langmuir, 1997).

1.2.3.2. Sorption and surface complexation

The term "sorption" has so far been used in a broader sense of the general attachment of ions to a solid or mineral surface. There are, however, several different types of sorption:

(1) **adsorption**, including *surface complexation* of an ion (the *adion*), which can be reversible and generally also involves *desorption* of surface ions,

(2) **absorption**, i.e., the *incorporation* of an adion into the crystal structure upon diffusion, which is less readily reversible,

(3) **precipitation**, i.e., the formation of a distinct new phase on the reactive mineral surface, which usually requires a precursor adsorption complex, and

(4) **coprecipitation**, i.e., the formation of a mixed phase or solid solution, often resulting from dissolution–precipitation reactions, adsorption, and growth of the secondary phase (Parks, 1990).

Sorption processes are surface reactions and as such strongly dependent on the mineral surface characteristics, but also on the pH and ionic strength of the reactive fluid as well as on the concentration and speciation of sorbate and sorbent (e.g., Benjamin & Leckie, 1981; Farley et al., 1985). In aqueous solutions, ions are solvated, i.e., they accumulate a hydration shell of dipole-ion bound water molecules in their first coordination sphere. Dissolved ions may also form *aquocomplexes*, where the central ion is surrounded by other ligands; these are often anionic ligands binding within the first coordination sphere. The reactivity of aquocomplexes is dependent on their speciation and therefore on the aqueous solution pH (Langmuir, 1997; Koretsky, 2000; Scheffer & Schachtschabel, 2010).

To form chemical bonds with ligands or reactive surface groups, hydrated aqueous ions need to hydrolyse, i.e., to liberate protons from their first coordination sphere. Large ions of low charge, such as Na^+ and K^+, tend to not hydrolyse, and thus only commit to weak bonding, namely *non-specific* or *physical adsorption* through electrostatic (coulombic) attraction to oppositely charged ions and surfaces. Anions are thereby attracted by protonated, positively charged surfaces at $pH < pH_{PZC}$, while hydroxylated, negatively charged surfaces attract cations at $pH > pH_{PZC}$ (Parks, 1990). As the hydration shell around such adions is retained, these complexes are called *outer–sphere* complexes or ion pairs (Figure 1.7). This type of sorption is dependent not only on the solution pH, but also on the ionic strength (e.g., Parks, 1990; Scheffer & Schachtschabel, 2010). The reactivity of the adsorbed species thereby remains similar to their aqueous hydrated form, as differences in complex structure and electron density distribution are negligible (Koretsky, 2000).

In contrast, multivalent (metal) ions, particularly Al^{3+}, Cu^{2+}, Fe^{3+}, Hg^{2+}, Pb^{2+} and U^{4+}, which also form strong aquocomplexes, hydrolyse more readily and form much stronger *specific* or *chemical adsorption* complexes with one or more oxygens or hydroxyl groups at the mineral surface. Since the hydration sphere of these adions is partially replaced by strong, covalent bonds sharing electron pairs between surface ions, these complexes, as well as aquocomplexes, are regarded as *inner–sphere* complexes. This type of coordinative surface complexation is

therefore particularly dependent on the mineral surface properties including the type and reactivity of the surface functional groups (Figure 1.7; e.g., Parks, 1990; Langmuir, 1997; Scheffer & Schachtschabel, 2010).

Chemical adsorption is a continuum of several processes: First, a sorbate is transported via diffusion through the aqueous solution towards the surface of the sorbent, where it is then exchanged for a proton of the surface functional groups within the hydrated surface layer to eventually form an adsorption complex (e.g., Stumm et al., 1976). These primary complexes may modify towards binding geometries of lower free energies, for example, reducing unsaturated bonds by diffusing to surface sites of higher binding energies, e.g., kink sites. In layered minerals such as clays, in porous media and (nano)particle aggregates, micropore diffusion may also occur (Scheffer & Schachtschabel, 2010). Adsorption is considered the

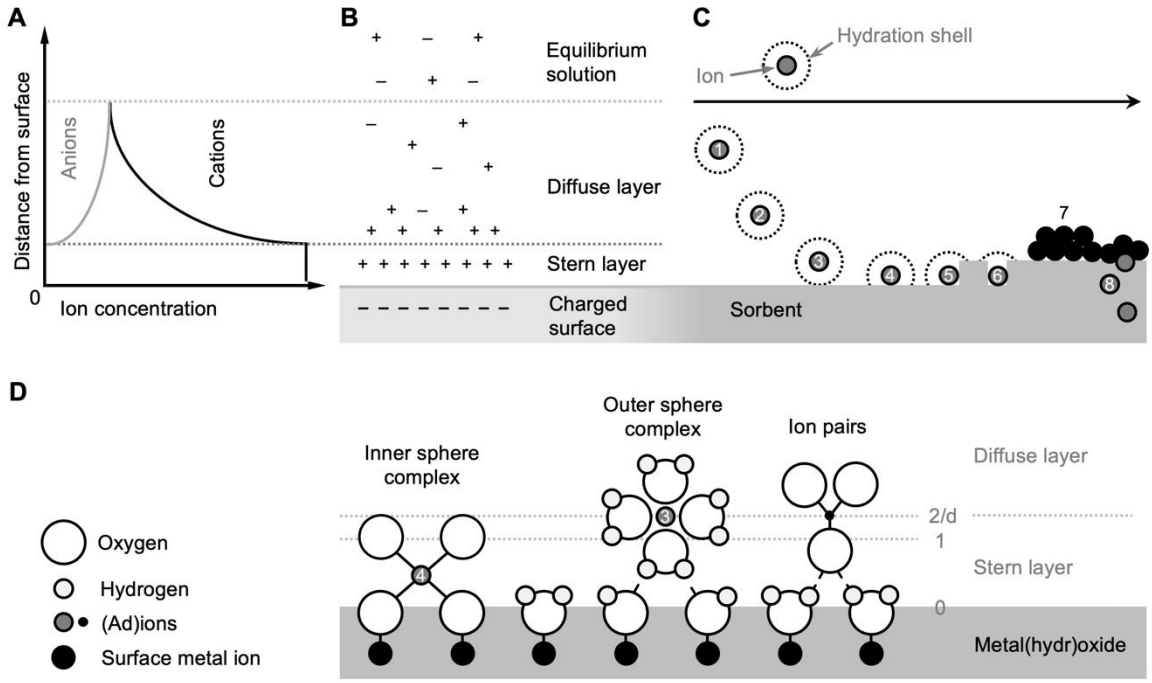

Figure 1.7. Schematic representation of the (A) ion concentration and (B) ion distribution in the electrical double layer of a metal (hydr)oxide sorbent–solution interface. The binding strength of the possible sorption mechanisms between adions and sorbent surface shown in (C) increases in the order from 1 to 8: (1) and (2) dissolved hydrated ions in the diffuse layer, (3) outer-sphere complex, (4) inner-sphere complex, (5) inner-sphere complex at a step or kink site, (6) inner-sphere complex at a vacancy site, (7) surface precipitates of the ion, (8) coprecipitation or incorporation. (D) More detailed graphic of (3) and (4), positioned at the minimum approachable distance of (hydrated) ions. Inner-sphere complexes penetrate the Stern layer as they exchange surface ligands, whereas outer-sphere complexes stay at distance through weak attraction within the 1-plane of the Stern layer. The d-plane corresponds to the beginning of the diffuse layer of counterions. *Modified after Hiemstra & Van Riemsdijk (1996), and Scheffer & Schachtschabel (2010).*

essential precursor step for surface precipitation reactions (Benjamin & Leckie, 1981; Farley et al., 1985), as well as for surface-controlled dissolution (Furrer & Stumm, 1986; Zinder et al., 1986; Schott et al., 2009).

When applying this theoretical knowledge to real pollution issues of aqueous environments, model predictions can be very useful. **Modelling of sorption processes** helps to quantitatively predict the reactive transport of aqueous species. All sorption models are based on the concept of thermodynamic equilibrium and thus include mass law equations to describe the chemical interaction between a sorbate and the surface of a sorbent. The formulation of sorption is generally constrained by defining adsorption at specific surface sites as the only mechanism described in a *single* chemical reaction from which thermodynamic equilibrium constants are derived to fit experimentally obtained data. There are two types of sorption equilibria: (1) entirely *empirical* models describe the sorption affinity (partitioning) of a solute to a solid surface at strictly constant pH, ionic strength, pressure, and temperature conditions, whereas (2) *conceptual* surface complexation models describe the coordinative surface reactions between aqueous species with mineral surface groups (e.g., Davis & Kent, 1990; Scheffer & Schachtschabel, 2010).

(1) In *empirical* adsorption models, adsorption is described in terms of partitioning relationships expressed as distribution coefficients (K_d) that relate the activity of a solute, C_{aq}, to the adsorption density Γ, i.e., the amount of solute sorbed to a mineral surface as a function of surface site density:

$$K_d = \Gamma / C_{aq} \qquad \text{(eq. 1.20)}$$

(Davis & Kent, 1990). Most of these models are based on the *Langmuir sorption isotherm*, which was originally developed to describe the sorption of gas molecules onto oxide, silicate, and metal surfaces (Langmuir, 1918). To simplify the complexity of adsorption, Langmuir formulated his model by assuming: (1) single occupation of only one type of adion at one kind of surface site, (2) only "true adsorption" through strong chemical bonds continues until all sites are occupied (sorption maximum), (3) the thickness of the sorption layer is constrained to a single (mono)layer of sorbed species (Langmuir, 1918). The isotherm is based on the equilibrium constant K_L of the ion adsorption reaction at an ideal surface site, assuming unit activity (i.e., a_{Caq} and $\gamma_{Caq} = 1$). Rewriting the equation for K_L and solving for the mole fraction of surface sites occupied by adsorbed species (q; mol kg^{-1}) yields the generalised form of the Langmuir isotherm for a solute:

$$q = \frac{S_{total} K_L C_{aq}}{1 + K_L C_{aq}} \quad \text{(eq. 1.21)},$$

where C_{aq} is the solute concentration (mol L^{-1}), and S_{total} is the total amount of available surface sites (mol kg^{-1}), which represents an empirical sorption maximum to correct for the finite number of sorption sites on a surface (may also be given as adsorption capacity in mg sorbate per g sorbent; Jeppu & Clement, 2012). Notably, K_L turns into a *sorption coefficient* that is no longer dimensionless (L kg^{-1}) and which describes the affinity of a sorbate to a sorbent surface (*modified from* Langmuir, 1918; Koretsky, 2000; Scheffer & Schachtschabel, 2010). At very low solute concentrations, C_{aq} and q are linearly correlated, while at high solute concentrations q tends towards the sorption maximum defined as $q = S_{total}$, i.e., the theoretical saturation of surface sites (Figure 1.8A; Scheffer & Schachtschabel, 2010).

Another model developed around the same time is the *Freundlich isotherm*, of which a generalised form can be written as

$$q = K_F C_{aq}^{n} \quad \text{(eq. 1.22)}.$$

Again, q refers to the adsorbate and C_{aq} to the solute concentration. Similar to K_L, the Freundlich coefficient K_F is derived from the equilibrium constant of the adsorption reaction and describes the sorption affinity of the sorbate towards the sorbent surface. The exponential parameter n is a constant that describes the curvature of the isotherm: If $n > 1$, sorption affinity of the sorbate increases with increasing sorbate concentration, and if $n < 1$, sorption affinity of the sorbate decreases with increasing sorbate concentration; if $n = 1$, K_F corresponds to a constant distribution coefficient and the sorption isotherm is linear (Figure 1.8B). This isotherm is only applicable at concentrations far below a sorption maximum and cannot be extrapolated. It also does not take any characteristics of the sorbent surface into account, thus principally assumes an infinite number of available, undefined surface sites. This generalisation, however, makes the Freundlich isotherm applicable to very heterogeneous systems such as soils (Koretsky, 2000; Scheffer & Schachtschabel, 2010).

Such partitioning models, however, are limited to specific and constant experimental conditions; they do not account for aqueous speciation and provide no information on the sorption mechanism, as they take neither reaction kinetics, nor the adsorption geometries nor surface characteristics of the sorbent into account. Small changes in experimental conditions, such as in pH or surface morphology of the sorbent, may modify the calculated sorption coefficient significantly. As natural systems are very heterogeneous, such isotherms must be

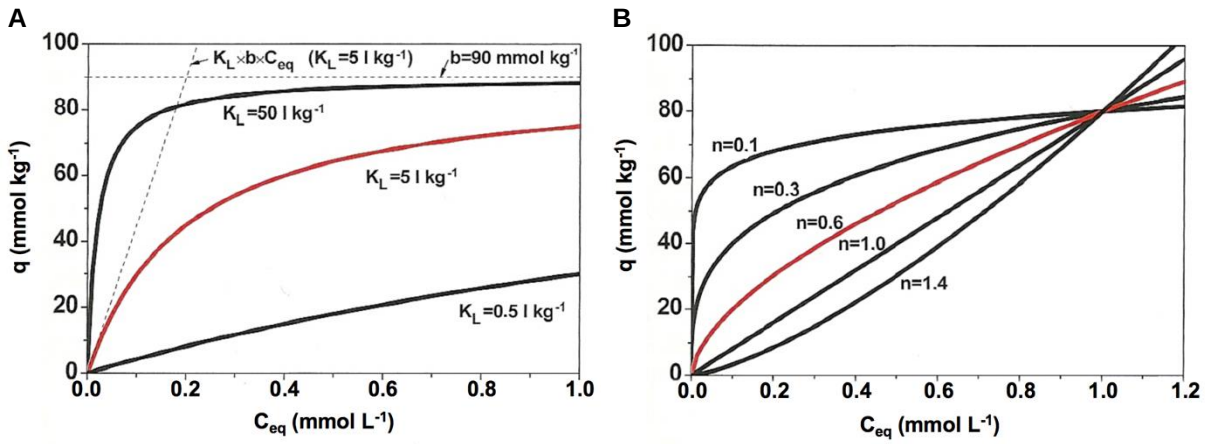

Figure 1.8. Examples for sorption isotherms according to the Langmuir (A) and Freundlich (B) models, shown as the adsorbate concentration q as a function of the equilibrium concentration of the solute C_{eq}. Note that here S_{total} is given as parameter b. Shown are three Langmuir isotherms at a given sorption maximum of 90 mmol kg^{-1} but different affinities (K_L), and five Freundlich isotherms with K_F = 80. Examples are highlighted in red. *Taken from and modified after Scheffer & Schachtschabel (2010).*

treated with great caution (Langmuir, 1997; Koretsky, 2000; Appelo & Postma, 2005; Scheffer & Schachtschabel, 2010). Despite these limitations, there have been numerous efforts of modifying, combining, and optimising these models, improving their applicability to various to single-component systems (e.g., Sahai & Sverjensky, 1997a,b; Jeppu & Clement, 2012).

(2) In addition to the empirical approach of isotherms, *conceptual* electrochemical models have been developed focussing on molecular surface speciation and mechanisms, which consider pH, sorbate speciation and surface site properties (e.g., Stumm et al., 1976; Stumm et al., 1980; Benjamin & Leckie, 1981; Farley et al., 1985; Hiemstra et al., 1989a,b; Hiemstra & Van Riemsdijk, 1996). These models are based on the concept of the reactive surface functional groups, which interact with aqueous species in chemical reactions (Sposito, 1990). In all models, the charged sorbent surface attracts ions of opposite charge (counterions), which "neutralise" and separate the charged surface from the charge-balanced aqueous solution. This is known as the *electrical double layer* (EDL) theory, which is adapted from electrochemistry and is used to describe the electrical charge distribution at and in the vicinity of the mineral surface. The resulting difference in the electrostatic potential within the sorbent–water interface rapidly decreases with increasing distance from the charged surface. This EDL has been described in various models, assuming a predominance of counterions and a deficiency of co-ions (same charge as the surface) near the surface (Figure 1.7A–B, Figure 1.9; Davis & Kent, 1990; Langmuir, 1997).

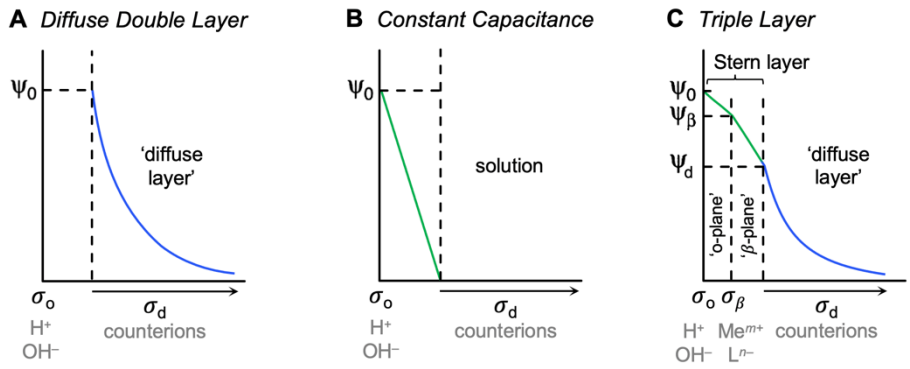

Figure 1.9. Idealised illustration of the electrical potential (**ψ**) as it decays with distance from the surface in different surface complexation models. The diffuse double layer model (A) assumes specific sorption and $\psi_0 = \psi_d$ at the surface plane. The surface charge-potential relationship of the diffuse layer is based on the Gouy-Chapman theory (indicated in blue) according to which the resulting surface charge σ_o is counterbalanced by the charge of dissociated counterions, σ_d, and the electrical potential decays exponentially away from the charged surface. The constant capacitance model (B) assumes a linear charge-potential relationship similar to that within the Stern Layer (indicated in green). The triple layer model (C) is based on the Stern-Grahame theory and accounts for the maximum distances of different types of ions from the surface: specifically sorbed adions within the surface (o-)plane, and non-specifically sorbed adions within the β-plane (respective charge defined as σ_β) before counterions balance the charge in the diffuse layer. *Modified after Davis & Kent (1990).*

The early theory of the separation of charges in the EDL proposed by **Gouy** and **Chapman** in the 1910's is based only on electrostatic interactions between ions and a charged planar surface, forming a diffuse swarm of counterions that neutralises the surface charge. The calculated electrical potential is a function of the concentration of sorbed cations, which is assumed to decline exponentially away from the charged surface according to the Boltzmann distribution function (Davis & Kent, 1990; Sposito, 1990), while the concentration of anions increases contrariwise (Figure 1.7A, Figure 1.9A). The pH_{PZC} is hence the point where the net of sorbed charges and surface potential equals zero and marks the transition from the diffuse layer to the equilibrium solution (Langmuir, 1997). This theory, however, was insufficient in terms of electrical capacity, which exceeded experimental observations. In the 1920's and 1940's, **Stern** and **Grahame** further developed the EDL model by distinguishing between an inner layer of chemically sorbed ions and a diffuse outer layer of fully hydrated, only electrostatically attracted ions. The electrical potential is assumed to decay linearly from the surface through the charged layers, while an exponential decay is assumed through the diffuse layer according to the Gouy-Chapman charge–potential relationship (Figure 1.9C; Davis & Kent, 1990).

Later theories, known as **surface complexation models (SCM)**, progressively account for the sorbent surface characteristics by defining the chemical surface species as amphoteric surface functional groups that are used to formulate mass law equations for their reaction with dissolved ions to form (coordinative) *surface complexes*. These later models mainly differ in their definition of the mineral–water interface, thereby considering the effect of physical limitations on ion size and distance to the charged surface and the concept of specific sorption (chemisorption) on the electrical capacity (e.g., Stumm et al., 1970; Stumm et al., 1976; Stumm et al., 1980; Davis & Kent, 1990). The *diffuse double layer* model (DDLM) assumes that all adions are specifically sorbed within the surface plane, while the diffuse layer represents the closest approximation of counterions. The Gouy-Chapman theory is applied for the electrical charge–potential relationship in the diffuse layer, while the electrical potential in the sorption layer is assumed to be equal to the surface potential (Figure 1.9A). The DDLM takes variable ionic strength effects upon adsorption into account but does not yet consider differences in sorption bond strengths. The *constant capacitance model* (CCM) considers a linear relationship between the surface charge and potential resulting from specific sorption at the surface plane constrained by the ion exchange capacity of the (amphoteric) mineral surface, i.e., the density of surface functional groups. The CCM refined the applicability of the DDLM to describe specific sorption at high and constant ionic strength conditions (Stumm et al., 1970). The *triple layer model* (TLM) directly originates from Stern's theory, which accounts for strong specific sorption that determines the electrical potential near the surface, and a layer of weak non-specific sorption that separates the Stern sorption layer from the diffuse layer of closest approximation of dissociated charges (Figure 1.9C; Davis et al., 1978; Davis & Leckie, 1978; Hayes & Leckie, 1987). The TLM refines the relationship between the various charges and potentials to more realistic conditions which are of further importance in the interparticle relations, particularly of iron and aluminium oxide particle aggregation (Davis & Kent, 1990).

Despite describing specific surface coordination of sorption complexes (Davis & Leckie, 1978; Stumm et al., 1980), these models only consider adsorption to occur at the amphoteric >MeOH surface site (Goldberg, 1985). Modern SCM build upon the EDL concept but consider the *heterogeneity* of surface properties and thus the different intrinsic affinity constants that describe the chemical reaction between the adion and the various functional groups of various mineral classes to overcome this single-site oversimplification. Surface complexation in general defines the spatial arrangement of the sorption complex, i.e., the interatomic distance, orientation, and coordination with the surface functional groups. This refinement was facilitated by the advances in microanalytical techniques of mineral surfaces which provided evidence for

the concepts of chemisorption of metals on oxide minerals (e.g., Chisholm-Brause et al., 1989; 1990a,b; Bassett & Brown, 1990) and of surface roughness by characterising the atomistic structure of surfaces (Hochella, 1990).

Modern SCM particularly address the sorption of dissolved metal ions to naturally abundant oxide and carbonate mineral surfaces. All SCM are based on thermodynamic principles and are analogous to aqueous complexation concepts where the number of shared electron pairs (i.e., bonds, commonly referred to as "-*dentate*") as well as the number of core ions involved in the complex (referred to as "-*nuclear*") determine the stability of a complex. The respective reaction used in model calculations of for instance the sorption of an aqueous divalent metal ion on a mineral surface in an *outer–sphere complex* is given as

$$>MeOH + Me^{2+}_{(aq)} \rightleftharpoons >MeOH–Me^{2+}_{(aq)} \qquad \text{(eq. 1.23)},$$

whereas the reaction for an *inner–sphere complexation* is written as

$$>MeOH + Me^{2+}_{(aq)} \rightleftharpoons >MeOMe^{+} + H^{+} \quad (\textit{monodentate}) \text{ (eq. 1.24)}$$

$$>2MeOH + Me^{2+}_{(aq)} \rightleftharpoons >(MeO)_2Me^{0} + 2H^{+} \quad (\textit{bidentate}) \text{ (eq. 1.25)}$$

(e.g., Brown, 1990). From these reactions, one can infer changes in solution pH upon the sorption reaction, which might be used to distinguish between specific (inner-sphere) and non-specific (outer-sphere) processes. There are four principle assumptions which are fundamental to all SCM: (1) Mineral surfaces have a finite number of sorption sites per surface area (site density) with specific surface functional groups that react with solutes to form specific or non-specific complexes, (2) surface reactions are assumed to be stoichiometric and at local equilibrium that can be formulated by mass law equations, (3) surface reactions result in surface charge and change in electrical potential, (4) intrinsic thermodynamic constants calculated under consideration of the effect of surface species can be used to determine apparent binding constants (Davis & Kent, 1990; Langmuir, 1997; Koretsky, 2000; Scheffer & Schachtschabel, 2010). Differences among the models are in various formulations of the protonation reaction and the modelling of the EDL. Most modern models account for the heterogeneity of mineral surfaces (e.g., Rustad & Felmy, 2005). More specifically, a variety of different surface sites are considered to be involved in sorption complexation reactions with sorbates as first introduced by Hiemstra and colleagues for (hydr)oxide mineral surfaces (1989a). Bargar and colleagues (1996) emphasised the importance of specific sorption characteristics of different surface sites in their spectroscopic study on an α-Al_2O_3 single crystal. They demonstrated that Pb(II) adsorbs

in an outer-sphere complex on the (0001) surface but sorbs inner-spherically on the $(1\bar{1}02)$ surface. Thus, considering only one of these sorption mechanisms to formulate SCM reactions to describe the sorption mechanism of a metal may have implications for predictions of its behaviour in contaminated environments.

Probably the most sophisticated SCM to date is the Multisite Complexation (MUSIC) Model. It builds on the surface coordination models that recognise specific adsorption as ion or ligand exchange reactions with surface-bound protons or hydroxyls (e.g., Stumm et al., 1980), and initially focused on proton adsorption to various **metal (oxyhydr)oxides** (Hiemstra et al., 1989a). Accounting for the heterogeneity of surface group types, the MUSIC model distinguishes between singly, doubly, and triply coordinated metal ions with protons or hydroxyl groups (*see* Figure 1.4), each described by individual intrinsic affinity constants. The model uses Pauling's principle of local neutralisation of charge within an ionic crystal that is expressed as a formal bond valence υ,

$$\upsilon = \frac{Z}{\mathrm{CN}} \qquad \text{(eq. 1.26)},$$

where Z is the charge of the (metal) cation and CN is its coordination number. For ferric iron (oxyhydr)oxides, for example, where the trivalent Fe ion is octahedrally coordinated with hydroxyls, the formal bond valence per Fe–OH would be υ = ½, hence two Fe^{3+} ions are required for local charge neutralisation of one OH^- within the crystal structure. At the crystal surface, however, the oxygens have unsaturated bonds, which become neutralized by proton adsorption, forming >MeOH and/or $>MeOH_2$ surface groups. This concept of the bond valence allows the individual treatment of surface groups, which have charges ≤ 1, separately from the surface (Hiemstra et al., 1989a). The prediction of proton affinity is expressed as surface charge density curves as function of pH and was tested for protonation on various surface group types on the naturally most common metal (oxyhydr)oxides including gibbsite ($Al(OH)_3$), goethite (α-FeOOH), hematite (Fe_2O_3), rutile (TiO_2), and silica (SiO_2), accentuating the dissimilar protonation behaviour of different mineral faces (Hiemstra et al., 1989b). For singly (>Me), doubly ($>Me_2$) and triply ($>Me_3$) coordinated surface sites to the Me ions in the bulk structure of, for example, the trivalent metal (oxy)hydroxides gibbsite and goethite, protonation reactions are written as

$$>MeOH^{-1/2} + H_s^+ \rightleftharpoons >MeOH_2^{-1/2} \qquad \text{(eq. 1.27)}$$

$$>Me_2O^- + H_s^+ \rightleftharpoons >Me_2OH^0 \qquad \text{(eq. 1.28)}$$

$$>Me_2OH^0 + H_s^+ \rightleftharpoons >Me_2OH_2^+ \qquad \text{(eq. 1.29)}$$

$$>Me_3O^{-1/2} + H_s^+ \rightleftharpoons >Me_3OH^{+1/2} \qquad \text{(eq. 1.30),}$$

where H_s^+ represents a local near-surface proton (*from* Hiemstra et al., 1989a,b). These surface groups occur at different abundances on the different crystal faces and have different proton affinities. The affinity of the $>Me_2OH^0$ site is close to zero and thus considered nearly inert. The protonation capacity of the solid therefore arises from the different site contributions at the various crystal faces. In other words, the predominance of particular crystal faces for typical crystal morphologies, e.g., the acicular habit of goethite with predominantly (110) faces, governs the overall protonation affinity and therewith the pH_{PZC} of the mineral. For (oxyhydr)oxides, the proton affinity thus decreases with increasing pH and becomes zero around neutral to slightly alkaline conditions (Hiemstra et al., 1989b; Hiemstra et al., 1996). This pH dependence on charge distribution hence effects the stoichiometric adsorption of oxyanions such as phosphate, arsenate, and chromate (Rietra et al., 1999), and may generate a shift of the IEP upon various ion adsorption.

Hiemstra and Van Riemsdijk (1996) extended their model based on Pauling's concept of *charge distribution* (CD) to account for the structural dependency of charge distribution within the molecular structure of the surface groups and adsorption complexes. Since the bond valence is a function of the valence of the central metal ion and its coordination with oxygens, the sorption affinity of a surface group depends on the charges available from unsaturated oxygens. In contrast to Pauling's assumption of even distribution of charges and therefore equal distances between the central metal ion and the coordinating oxygens, Me–O distances in ionic mineral structures may vary due to the contribution of other coordinative ions. For metal (oxy)hydroxides such as goethite, for instance, the partial contribution of coordinative charge from –OH groups within the higher $Fe_3OH–OFe_3$ configuration of the surface structure leads to an asymmetric charge distribution and thus to different Fe–O bond distances. Generally, shorter Me–O distances imply higher bonding contributions of the metal to neutralise the oxygen charge (Figure 1.10; Hiemstra et al., 1996). Since the charge of an adsorbed ion is shared by the structural oxygen or hydroxyl ion, the bond valence is directly related to the distances between the structural and adsorbed metal ions via their –O/–OH coordination environments, which allows the prediction of possible metal sorption species (Hiemstra et al., 1996; Venema et al., 1996). The bond valence approach has since been used, for example, to describe the stoichiometric hydrolysis and sorption reactions of the various complexation

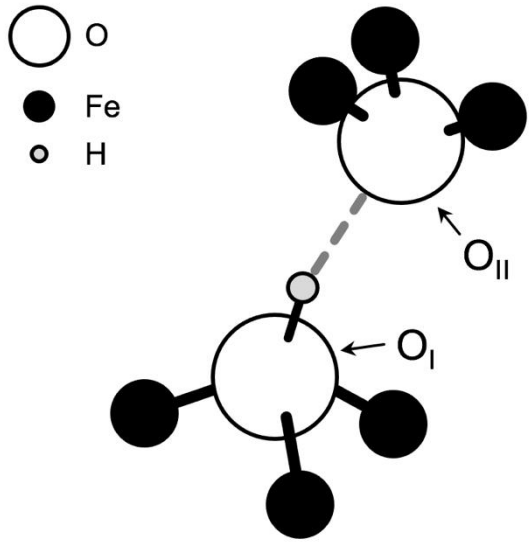

Figure 1.10. Schematic of a basic structural unit of goethite illustrating the two types of oxygens O_I and O_{II} that are both triply coordinated to Fe and connected to each other by a hydrogen bond (grey broken line). This bond distributes the hydrogen charge asymmetrically. Here, O_I is in a Fe_3OH configuration, in which it receives a larger charge contribution of H for neutralisation than O_{II} does, but a smaller charge contribution from the coordinating Fe atoms. As a result, the Fe–O distances in Fe_3OH configurations are larger (R = 2.09–2.10 Å) than in Fe_3O groups (O_{II}; R = 1.95–1.96 Å) with smaller H but higher Fe charge contributions. *After Hiemstra et al. (1996)*.

geometries of Pb(II) and Co(II) upon adsorption to aluminium and iron oxide surfaces (Bargar et al., 1996; Bargar et al., 1997a,b,c).

For **carbonates**, and specifically for the divalent metal carbonates of the form $MeCO_3$ (Me = Ca, Mn, Fe, etc.), the boundary between surface sorption and precipitation is more difficult to determine as these processes strongly depend on the saturation state of the aqueous solution with respect to the carbonate mineral (Morse, 1986). Additionally, the pH_{PZC} of the carbonate minerals is dependent on the pCO_2 in the aqueous solution (Charlet et al., 1990). As shown for metal oxides, the pH dependent formation of surface species upon protonation and deprotonation of the surface carbonate groups and metal centres also applies for carbonate surface groups. Protonation of the carbonate surface site $>CO_3^-$ leads to the hydration species $>CO_3H^0$ which is dominant under acidic conditions, whereas the hydrated divalent central metal ion site $>MeOH^0$ is prevalent at circumneutral conditions, and $>MeOH_2^+$ is dominant at neutral to alkaline pH (Charlet et al., 1990; Pokrovsky & Schott, 2002). Surface sorption reactions at the hydrated surface species can be written as

$$>CO_3H^0 + Me_{aq}^{m+} \rightleftharpoons >CO_3Me^{(m-1)+} + H^+ \qquad \text{(eq. 1.31)}$$

$$>MeOH^0 + L_{aq}^{n-} \rightleftharpoons >MeOL^{(n+1)-} + H^+ \qquad \text{(eq. 1.32),}$$

where m denotes the cationic and n the anionic charge of the aqueous species (*modified after* Van Cappellen et al., 1993). Surface speciation upon ion adsorption to these hydration sites is strongly pH dependent and results in the formation of protonated ($>MeOH_2^+$),

deprotonated ($>MeO^-$, $>CO_3^-$), metal sorption ($>CO_3Me^+$) or carbonatation ($>MeCO_3^-$, $>MeHCO_3^0$) species. Surface complexation models using these surface species indicate that the surface-controlled dissolution/precipitation reaction kinetics of divalent metal carbonates are controlled by the protonation of the $>CO_3H^0$ surface group at acidic pH conditions, and by the hydrolysis of the $>MeOH_2^+$ surface group at neutral to alkaline pH (Van Cappellen et al., 1993; Pokrovsky et al., 1999; Pokrovsky & Schott, 2002; Schott et al., 2009). Although metal ions may also sorb to the surface metal centres equivalent to metal oxide surface reactions

$$>MeOH^0 + Me_{aq}^{m+} \rightleftharpoons >MeOMe^{(m-1)+} + H^+ \qquad \text{(eq. 1.33)},$$

the adsorption of divalent metals was found to be strongly favoured to the carbonate surface sites according to equation 1.31 (Van Cappellen et al., 1993). Notably, the surface chemistry of divalent metal carbonates is much more complex compared to metal oxides and thus poses increased difficulties for such modelling approaches (Wolthers et al., 2008).

Generally, specific (chemical) sorption of protons or hydroxyls, metal cations or anionic ligands involves concurrent desorption of protons and/or surface ions and creates heterogeneities in the surface composition. This change in surface chemistry contributes to the development of surface charge and may mediate a shift of the pH_{PZC} of the sorbent (e.g., Stumm et al., 1980; Van Cappellen et al., 1993). It was found that in comparison to (oxyhydr)oxide minerals, build-up of surface charge on carbonate minerals is one order of magnitude higher, while ionic strength effects on surface charge are lower for carbonates than for (oxyhydr)oxides. Both characteristics imply a relatively higher capacitance of the EDL for carbonate surfaces in aqueous solutions (Charlet et al., 1990; Van Cappellen et al., 1993). As indicated by equations 1.31 and 1.33, specific sorption of metal cations to either oxide or carbonate hydration sites involves deprotonation and may promote dissociation of the surface complexes and thus enhance dissolution if desorption rates exceed adsorption rates (Lasaga, 1984; Furrer & Stumm, 1986; Schott et al., 2009). Protonation of the carbonate surface sites, for example, enhances the detachment rate of the weakened interatomic bonds of complexed lattice ions from the carbonate mineral surface and thus facilitates mineral dissolution (e.g., Charlet et al., 1990; Van Cappellen et al., 1993; Schott et al., 2009). For carbonates in particular, the presence of dissolved carbonate species in the aqueous solution may affect surface-controlled reactions. Increased pCO_2 for instance decreases the surface charge of Mn-carbonate and enhances calcite dissolution at near to circumneutral pH by carbonatation of the surface metal centres (Charlet et al., 1990; Van Cappellen et al., 1993). Complementarily, the formation

of multinuclear sorption species on mineral surfaces is the precursor reaction for surface precipitation (Benjamin & Leckie, 1981; Farley et al., 1985).

In specific metal sorption reactions according to equation 1.33, the central metal ion >Me acts as a Lewis acid and the deprotonated –OH group as a Lewis base. The amphoteric –OH can undergo exchange reactions with other ligands binding covalently to the central metal ion and, in some cases, may form ternary surface complexes, e.g., with organic acids or inorganic ligands such as Cl^- or dissolved carbonate species (Sulzberger et al., 1989; Wehrli et al., 1989; Stumm & Wollast, 1990; Schindler, 1990; Bargar et al., 1998; Ostergren et al., 1999; 2000a,b):

$$>\mathrm{MeOH} + \mathrm{L}_{\mathrm{aq}}^{n-} + \mathrm{Me}_{\mathrm{aq}}^{m+} \rightleftharpoons >\mathrm{MeLMe}^{(n+m)} + \mathrm{OH}^- \qquad \text{(eq. 1.34).}$$

The thermodynamic adsorption constants for surface complexation reactions are obtained based on the same equilibrium concept as for mineral–solution reactions using computer programs that include thermodynamic databases for numerous geochemically important aqueous species (e.g., PHREEQC; Appelo & Postma, 2005; Parkhurst & Appelo, 2013). Notably, adsorption occurs at relatively low metal sorbate concentrations, whereas increased metal concentrations may lead to saturation and precipitation of secondary or solid–solution phases at the sorbent surface (e.g., Farley et al., 1985; Morse, 1986).

1.2.4. Redox processes in aqueous environments

In the introduction to heavy metal contamination of aqueous environments (*see* section 1.1), the importance of the redox conditions of such environments was emphasised. This is because the chemical form or oxidation state of an element – its speciation and therewith its geochemical behaviour – changes according to the reducing or oxidising (short: redox) conditions of its immediate environment. Geochemical reactions involving redox-sensitive elements play a crucial role in environments that naturally undergo dynamic changes in their redox conditions. Redox dependency directly affects mineral solubilities and is thus closely interlinked with element cycling of, for example, carbon, sulphur, nitrogen, and iron, but also of potential toxicants such as arsenic, chromium, copper, and uranium (e.g., Stumm & Sulzberger, 1992; Appelo & Postma, 2005).

1.2.4.1. Redox reactions and conditions

Reduction reactions commonly consume protons as in the reductive dissolution of goethite

$$FeOOH(s) + 3H^+ + e^- \rightleftharpoons Fe^{2+} + 2H_2O \qquad \text{(eq. 1.35)},$$

which may increase the aqueous solution pH. Oxidation reactions, in turn, often lead to proton release as in the oxidative precipitation of goethite

$$Fe^{2+} + 2H_2O \rightleftharpoons FeOOH(s) + 3H^+ + e^- \qquad \text{(eq. 1.36)}$$

which may decrease the aqueous solution pH. In an overall reduction-oxidation reaction, the ion transferring an electron, the *electron donor*, oxidises and acts as *reductant* by reducing the *electron acceptor* ion, which in turn acts as the *oxidant*. In redox reactions, electrons are transferred directly between atoms, which can occur through the aqueous solution. The **redox potential *E*** thereby indicates if an element or molecule may be reduced or oxidised. The electron transfer during such reactions develops a voltage, which can be directly related to the standard state Gibbs free energy of the reaction

$$\Delta G_r^o = -nFE^o \qquad \text{(eq. 1.37)}$$

where F is the Faraday's constant (96485 C mol^{-1}) and n the number of transferred electrons (Anderson, 2005). The **standard electrode potential E^0** (in V (J C^{-1})) of an aqueous system depends on the activities of reducing and oxidising species in solution – the higher the activities of reducing species, the higher the reducing potential of the system and vice versa. The **redox potential *Eh* of an aqueous solution** is a value given relative to the standard state hydrogen reduction reaction ($H_2 \rightleftharpoons 2H^+ + e^-$), which is used as reference electrode ($E^0 = 0$ at 25 ºC and 1 atm). Considering the effect of the electron transfer in thermodynamic equilibrium concepts, the *Eh* of a redox reaction can be described by the Nernst-equation, which relates the standard potential E^0 to the activity ratio of the reduced and oxidized species. The E^0 of half-reactions indicates the tendency for reduction or oxidation, whereby electron donors have a more negative, electron acceptors a more positive value of E^0. The standard potential E^0 for any redox reaction can therefore be derived from thermodynamic data to calculate the redox potential of an aqueous system using the simplified **Nernst-equation** at 25 ºC

$$Eh = E^0 - \frac{RT}{nF} \ln Q \qquad \text{(eq. 1.38)}$$

where R is the gas constant (8.134 J mol^{-1} K^{-1}), T is the temperature in K, and Q is the reaction quotient (Anderson, 2005; Appelo & Postma, 2005). When considering single electron transfer reactions at 25 ºC (n = 1), the term $\frac{RT}{nF}\cdot$ 2.303 in equation 1.38 reduces to the Nernst slope value of 0.05916, whereby 2.303 is a constant to convert the natural to the base 10 logarithm. The Nernst slope is commonly used to calculate redox potentials of non-ideal (natural) systems (Anderson, 2005).

Based on the law of mass action and analogous to pH, the *Eh* can also be given as the electron potential p*e* of an aqueous solution, which is the log activity of electrons that are exchanged in the redox reaction (–log[e^-]). These two concepts can be converted via *Eh* = 0.05916 p*e* (V, at 25 ºC). Since most redox reactions involve the consumption or release of protons, the proton potential (pH) and electron potential (p*e*) of an aqueous solution are closely interlinked. This relationship is used to construct p*e*–(or *Eh*–)pH diagrams which indicate the stability fields of aqueous species in natural aqueous environments with respect to the stability field of water, which is only stable at conditions of 0 < p*e* + pH < 20.8. Above this value, water oxidises and decays into O_2 + H^+; at lower values, water reduces to H^+ and OH^-. For natural aqueous systems, sequential redox processes lead to a spatial zoning into **anoxic** (p*e* + pH < 9), **suboxic** (9 < p*e* + pH < 14), and **oxic** (p*e* + pH > 14) conditions (Figure 1.11; Postma & Jakobsen, 1996; Hunter et al., 1998; Scheffer & Schachtschabel, 2010).

As oxygen diffuses much more quickly through air than through aqueous solutions, water saturation of contaminated soils and sediments can have a significant effect on the redox potential – oxygen remaining in water-saturated systems may be respired more quickly than airborne oxygen can be supplied, leading to a decrease in the *Eh* and thus to increasingly reducing conditions. Well aerated systems thus have higher redox potentials (oxic environments) and tend to be much more acidic, whereas water-saturated systems exhibit lower redox potentials (sub- to anoxic environments) and tend to be neutral to alkaline (Scheffer & Schachtschabel, 2010). Examples for the latter are flooded soils, deep lake sediments and groundwaters, where the exchange with atmospheric oxygen is restricted and microbial degradation of organic substances leads to a depletion of oxygen and production of various reduced species (Hering & Stumm, 1990).

Note that the stability of redox species may not only depend on the *Eh*–pH condition, but also on the solubility of minerals containing these redox species as major components. In a reduced Fe–S–C environment for example the formation of siderite ($FeCO_3$) will be inhibited

until all free S^{2-} is consumed by the precipitation of less soluble pyrite (FeS_2), before sufficient Fe^{2+} concentrations remain to allow siderite stabilisation (Appelo & Postma, 2005).

1.2.4.2. Redox reactions at the iron oxide mineral–water interface

As one of the major components in soils and sediments, the reduction and oxidation behaviour of Fe plays an essential part in biogeochemical element cycles of nutrients as well as of metal pollutants. The most abundant forms of Fe in weathering, sedimentary, soil and aqueous environments are as dissolved Fe^{2+} (ferrous iron) species, and/or as Fe^{3+} (ferric iron) solids in the form of the (oxyhydr)oxides ferrihydrite, lepidocrocite, goethite, magnetite, and hematite (Postma, 1993; Cornell & Schwertmann, 2003). Under circumneutral oxic conditions, these **ferric iron (oxyhydr)oxides** are nearly insoluble and due to their amphoteric surfaces have been the subject of numerous studies as effective metal sorbents (*see* section 1.2.3.2). However, these minerals can become unstable upon reduction of their ferric component (Figure 1.12; Sulzberger et al., 1989; Stumm & Wollast, 1990; Pedersen et al., 2005).

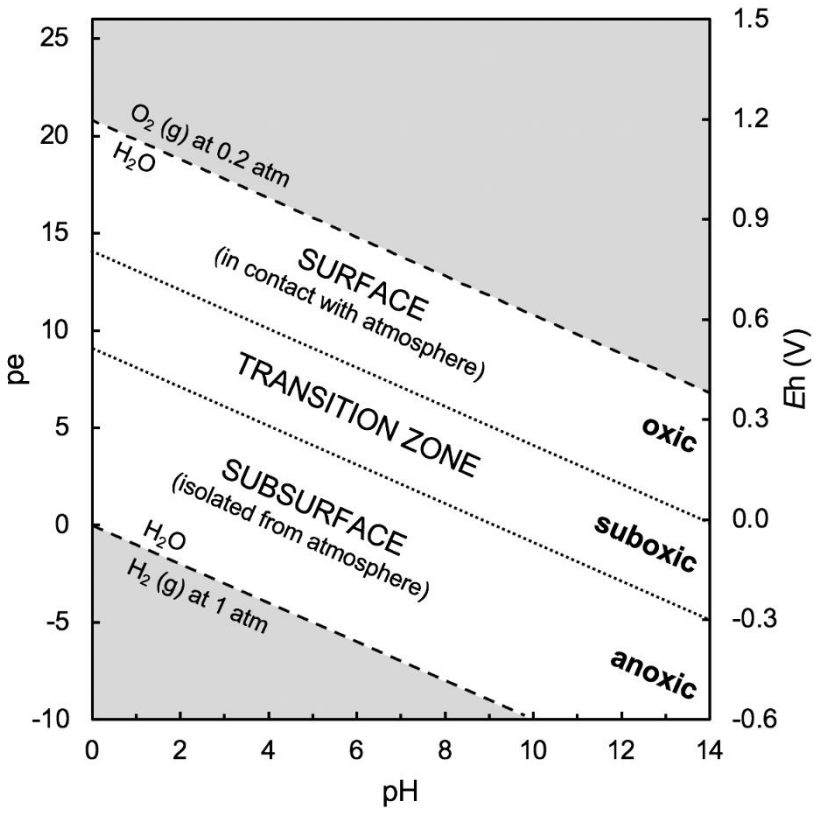

Figure 1.11. Stability diagram of water and the theoretically possible ranges of pe–pH conditions in natural aqueous environments. Soil fluids may occur over a wide range of pe–pH conditions, groundwaters are usually constraint between suboxic to anoxic conditions, whereas peat logs, paddy fields and the hypolimnion are anoxic environments. *Modified after Appelo & Postma (2005) and Scheffer & Schachtschabel (2010).*

Notably, most redox reactions are kinetically sluggish, i.e., the electron transfer is often very slow and may only move forward when catalysed by bacterial activity or by the interdependent redox activity of other organic (oxalate, ascorbate, citrate etc.) and inorganic components (Fe, Mn, S, etc.). In aqueous solutions, the spontaneous oxidation rate of Fe^{2+} by O_2 for instance is pH and speciation dependent. At pH ≥ 4, aqueous Fe^{2+} is dominant and only oxidizes moderately slowly, whereas at pH ≥ 6 and elevated pO_2 the more readily oxidised $Fe(OH)^0$ species determines the significantly accelerated oxidation rate (Morgan & Lahav, 2007). Iron reduction, in contrast, is mostly dependent on the reductive reactivity of ferric iron minerals and the reductant involved in the reaction, often accelerated by organic substances (Zinder et al., 1986; Sulzberger et al., 1989; Stumm & Sulzberger, 1992; Postma, 1993). Notably, biogeochemical redox processes are a rather complex interdependent network of reactions in which products of one or more parallel, competitive redox reactions induce one or more subsequent reactions that may or may not involve microbial catalysis, which can only be tackled by kinetic reaction transport modelling (Hunter et al., 1998).

The solubilities of minerals containing structurally bound redox species such as Fe as a major component may be strongly affected by the interaction with reductants or oxidants. In

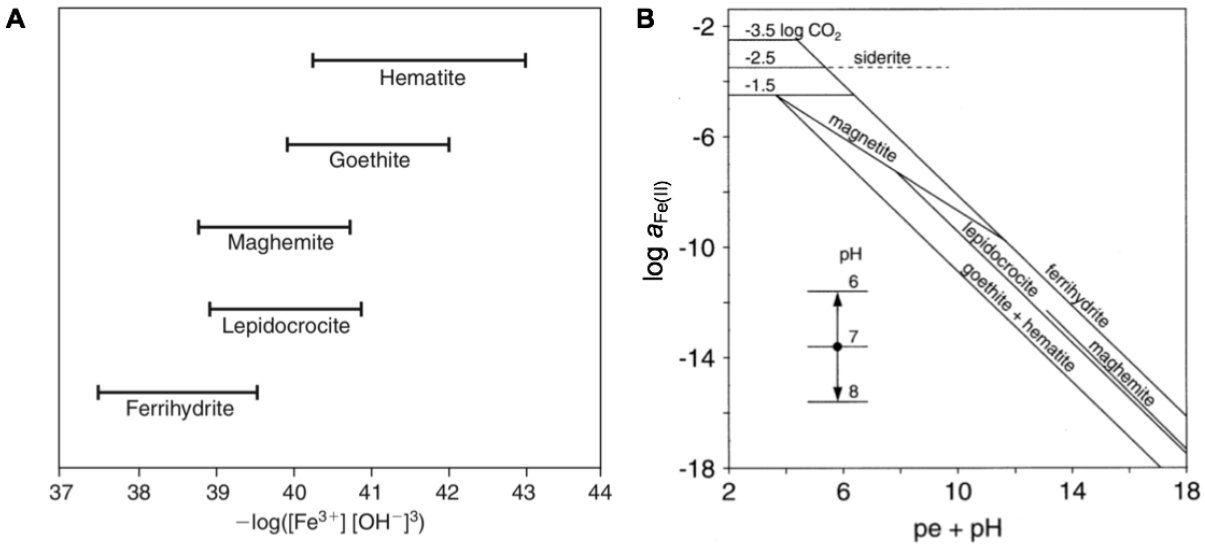

Figure 1.12. Stabilities of ferric (oxyhydr)oxides commonly found in natural environments at 25 °C and 1 atm, i.e., hematite (α-Fe_2O_3), maghemite (γ-Fe_2O_3), goethite (α-FeOOH), lepidocrocite (γ-FeOOH) and ferrihydrite ($Fe_5O_8H{\cdot}H_2O$), magnetite (Fe_3O_4), and siderite ($FeCO_3$). (A) solubility product (ranges); *taken from Appelo & Postma (2005), based on data given in Cornell & Schwertmann* (*2003*), (B) Log Fe^{2+} activity of the aqueous solution in equilibrium with the iron phases as a function of p*e* + pH and pCO_2. Note that the pH dependency of log $a_{Fe(II)}$ changes by the order of 10^2 for each pH unit; *taken from Cornell & Schwertmann (2003) after Lindsay (1979) and Lindsay & Sadiq (1983).*

aqueous environments, such redox processes are surface-controlled, i.e., electron transfer and subsequent reactions are dependent on complexation reactions at the mineral–water interface (Sulzberger et al., 1989; Hering & Stumm, 1990; Stumm, 1997). The surface morphology-dependent redox reactivity of the ferric iron (oxyhydr)oxides plays an important role in the (bio)geochemical redox cycling of iron. Surface complexation of a reductant such as Fe(II), which may become available from microbial respiration, induces **reductive dissolution** over a wide pH range (acidic to neutral) of the otherwise nearly insoluble ferric iron (oxyhydr)oxides (Figure 1.12). The adsorption of Fe(II) induces an electron transfer to the bulk crystal Fe(III) centre ion of the surface group, reducing it to Fe(II), while the adsorbed reductant is oxidised (Williams & Scherer, 2004). Outer-sphere redox reactions are much slower than inner-sphere redox reactions because the electron transfer between a redox couple is diffusion controlled and slow. For an inner-sphere sorption complex, however, the electron transfer is facilitated by ferromagnetic coupling of adjacent Fe ions in the edge–sharing sorption coordination typical for many divalent metals on hydrous oxides, where the orbitals of the adsorbing Fe(II) and the surface Fe(III) overlap (Sherman, 1987). Hence, if chemically sorbed to a mineral surface, Fe(II) can act as a much stronger reductant than free aqueous Fe^{2+} (e.g., Wehrli et al., 1989; Williams & Scherer, 2004).

Ferric iron (oxyhydr)oxide dissolution upon inner-sphere adsorption of Fe(II) and electron transfer is assumed to occur by the formation of an activated complex between the now reduced surface central ion and oxidised sorbent ions in the form of $>Fe(II)_{surface}–O–Fe(III)_{adsorbed}^{+}$. The Fe(II)–O bond is less stable in the crystal structure than the Fe(III)–O bond due to the difference in ionic radii, so that the oxidised Fe complex easily detaches from the surface upon hydration (Sulzberger et al., 1989; Wehrli et al., 1989; Boland et al., 2014). The detachment of the reduced surface Fe(II) is the rate determining step in the reductive dissolution reaction (Sulzberger et al., 1989; Wehrli et al., 1989). The electron transfer can be facilitated by bridging ligands, such as surface OH^{-}-groups on hydrous mineral surfaces or organic ligands like oxalate (Wehrli et al., 1989), and can be catalysed by the formation of a ternary complex with aqueous Fe(II) (Zinder et al., 1986; Sulzberger et al., 1989).

An alternative theory, based on the semiconducting properties of iron minerals, assumes that surface-mediated reductive dissolution occurs via two distinct but coupled processes at separate surface sites determined by the different surface site reactivities with Fe(II): (1) oxidative Fe(II) adsorption and homoepitaxial growth, and (2) internal bulk electron conduction driven by the development of a potential gradient across the crystal leading to reduction of

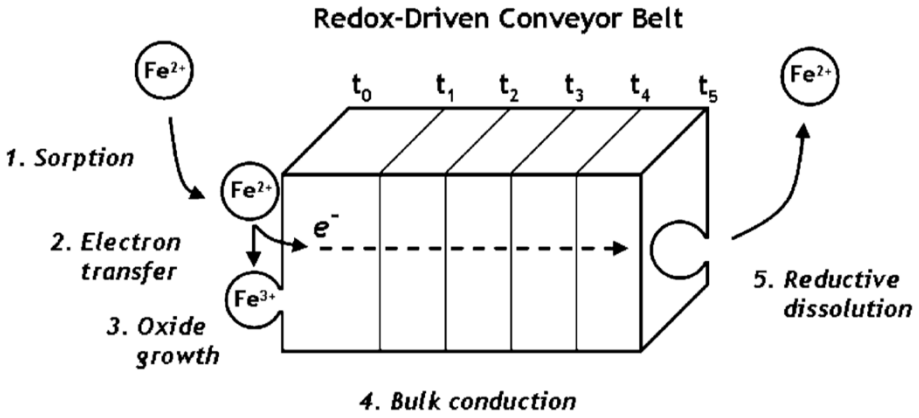

Figure 1.13. Illustration of the redox-driven conveyor belt mechanistic model. Upon sorption (1) of aqueous Fe(II) to a goethite surface at time t_0 (reference plane), electron transfer (2) induces Fe(II) oxidation and growth at the reference plane (3). The liberated electron travels through the bulk crystal (4) and causes reductive dissolution at a separate surface plane (5). Over time, and continuous succession of (1) to (5), the reference plane will migrate from t_0 to t_5 and thus until complete mixing of bulk goethite Fe(III) atoms and aqueous Fe(II) has occurred. *From Handler et al. (2009)*.

surface-structural Fe(III) at a different surface site and liberation as Fe(II) into solution (Figure 1.13; Yanina & Rosso, 2008). This electron transfer-induced atom exchange has been supported by ^{57}Fe isotope tracer studies in the presence and absence of biotic catalysts (Handler et al., 2009; Rosso et al., 2010; Handler et al., 2014), providing additional confirmation that Fe reduction and atom exchange *can* occur abiotically within measurable time frames. The mineral-specific crystal structure, surface coordination environment, and particle size distribution decisively affect the reductive dissolution rates of hydrous iron oxides, also in the presence of an organic ligand (Larsen & Postma, 2001). It is concluded, for example, that despite hematite being a much better electric conductor than goethite, a higher abundance of more reactive hydroxyl surface groups and its nano-size may compensate for the lower conductivity of goethite, suggesting that the bulk conduction model may apply similarly to both minerals (Handler et al., 2009).

The interaction with Fe(II) may affect the fate of metals or metal contaminants when adsorbed to or incorporated in ferric (oxyhydr)oxides. Most (transition) metal ions form strong inner-sphere complexes with iron (oxyhydr)oxide surfaces and may mediate electron transfer at the iron mineral surface. Whereas alkali ions adsorb electrostatically in outer-sphere complexes, these ions impede rapid electron transfer and thus reductive dissolution of the ferric component through their intact hydration shells (Wehrli et al., 1989). The adsorption of Fe(II), however, is consistent with divalent metal sorption to ferric (oxyhydr)oxides and may compete

with divalent metal ions for sorption sites as shown for hematite and goethite (Jeon et al., 2003; Frierdich & Catalano, 2012a). This is important as Fe(II) associated with ferric (oxyhydr)oxides can facilitate the release of redox-active and -inactive adsorbed and structurally incorporated metals through reductive dissolution of the ferric (oxyhydr)oxides (e.g., Davranche & Bollinger, 2000; Pedersen et al., 2006). More specifically, the cycling of incorporated metals has been demonstrated to result from electron transfer induced Fe atom exchange reactions, mediated by the Fe(II)–goethite and Fe(II)–hematite redox couple (Frierdich et al., 2011; Frierdich & Catalano, 2012a,b; Latta et al., 2012). The extent to which a metal may be liberated depends on the crystal chemistry of the iron mineral it is associated with, the pH and redox conditions of the system, and on the metal ion properties such as ionic radius and redox potential, as ions of similar ionic size to octahedrally coordinated Fe(III) tend to be more stable within the ferric iron oxide crystal structure (e.g., Coughlin & Stone, 1995; Manceau et al., 2000; Alvarez et al., 2008; Frierdich & Catalano, 2012b).

The association of Fe(II) with a mineral surface plays a key role in these reactions. Notably, homogeneous redox reactions in aqueous solution are much slower than heterogeneous redox reactions, i.e., when aqueous Fe(II) is associated with the iron mineral surface (e.g., Coughlin & Stone, 1995; Buerge & Hug, 1997; Buerge & Hug, 1999; Liger et al., 1999), supporting the assumption that structural Fe(II) is a stronger reductant than aqueous Fe(II) (e.g., Wehrli et al., 1989; Coughlin & Stone, 1995; White & Peterson, 1996). More specifically, it is the mineral surface-associated Fe(II) – either adsorbed, incorporated, or structural – that provides for the most favourable electron transfer pathways via orbital overlap (c.f., Sherman, 1987; Williams & Scherer, 2004) or superexchange via coordinating oxygens (Taylor et al., 2017). Chemically adsorbed ions can thence be reduced by intrasurface electron transfer even on insulating mineral surfaces, as shown for example for Se(IV) and U(VI) reduction by adsorbed Fe(II) at the montmorillonite (Charlet et al., 2007) and Al_2O_3 (Taylor et al., 2017) surfaces, respectively.

The adsorption and/or incorporation of reductants such as Fe(II) or organic ligands can further affect the stability of the ferric (oxyhydr)oxides as effective sinks for dissolved metals by inducing the **transformation among the iron oxides**. Such transformations may potentially release pre-adsorbed metals from the transforming iron host mineral or incorporate them into the transformation product (e.g., Pedersen et al., 2005; Marshall et al., 2014). However, transformation associated with increasing crystallinity and thus decreasing surface area and fewer available reactive surface sites affects the sorption capacity of the resulting iron oxide, which decreases in the order of ferrihydrite > goethite > hematite (e.g., Cornell & Schwertmann,

2003; Usman et al., 2012). The poorly crystalline ferric hydroxide ferrihydrite naturally occurs as nanoparticulate mineral and as such has been proven an excellent metal sorbent due to its large reactive surface area (e.g., Swallow et al., 1980; Schultz et al., 1987; Fuller et al., 1993; Waite et al., 1994; Raven et al., 1998; Arthur et al., 1999; Scheinost et al., 2001). Ferrihydrite is generally the first solid form of oxidised Fe to precipitate from Fe-containing aqueous systems. At 25 ºC and circumneutral pH, ferrihydrite can form within minutes at high rates of hydrolysis and supply of dissolved aqueous Fe^{3+} species (e.g., $Fe_2(OH)_2^{4+}$ dimers as "growth units"; Cornell & Schwertmann, 2003). However, ferrihydrite is the thermodynamically least stable iron oxide and converts into the more crystalline phases lepidocrocite (γ–FeOOH) and goethite (α–FeOOH) via (reductive) dissolution–reprecipitation (Hansel et al., 2005; Pedersen et al., 2005; Liu et al., 2007; Boland et al., 2014; Perez et al., 2019).

The presence of Fe(II) plays a critical role in these transformation reactions (Pedersen et al., 2005; Liu et al., 2007; Larese-Casanova et al., 2012; Perez et al., 2019). The growth of a structurally similar Fe(III) surface layer on reacted iron oxyhydroxides upon Fe(II) adsorption and electron transfer to the structural Fe(III) (Williams & Scherer, 2004), implies that the recrystallisation of ferrihydrite into the more stable lepidocrocite and goethite is induced by the breakdown of the ferrihydrite crystal lattice as the electrons travel further into the bulk crystal (Pedersen et al., 2005). This dissolution–reprecipitation reaction occurs even at very low Fe(II) concentrations (Hansel et al., 2005). The FeOOH modification into which ferrihydrite transforms depends on the available Fe(II) concentration and adsorption rate, leading to preferential formation of goethite at higher and of lepidocrocite at lower Fe(II) concentration and uptake (Hansel et al., 2005; Boland et al., 2014). The two FeOOH modifications thereby follow different and competitive formation pathways. Lepidocrocite precipitates directly from low concentrations of $Fe(OH)_2^+$ and $Fe(OH)^{2+}$ that become available in solution as ferrihydrite dissolves, whereas goethite requires polymerisation and dehydration of these aqueous species (Liu et al., 2007). Lepidocrocite is the thermodynamically less stable FeOOH modification and readily transforms into goethite and/or magnetite at increased pH and Fe(II) concentrations (Hansel et al., 2005; Boland et al., 2014). Ferrihydrite may also transform into hematite (Fe_2O_3) via inter-structural rearrangement (Schwertmann & Murad, 1983; Schwertmann et al., 1999), and/or into mixed-valent spinels (e.g., magnetite Fe_3O_4) driven by increased electron transfer and delocalisation (Cornell & Schneider, 1989; Tronc et al., 1992).

In the presence of sulphate, chloride, or carbonate, the transformation of ferrihydrite to lepidocrocite and goethite may proceed via the formation of an intermediate Fe(II)/Fe(III)

hydroxy salt of the green rust group (Carlson & Schwertmann, 1990; Schwertmann & Fechter, 1994; Perez et al., 2019). Because of the Fe(II) component, green rust minerals are attractive metal reductants (e.g., Loyaux-Lawniczak et al., 2000; O'Loughlin et al., 2003a,b; Thomas et al., 2018). The transformation of ferric oxides into mixed-valent green rusts is facilitated by the reducing interaction with Fe(II) (Usman et al., 2012), and accelerated by microbial reduction and organic compounds (Ona-Nguema et al., 2002). Under reducing conditions, metastable green rust (carbonate-type) may also convert into the more stable mixed-valent iron oxide magnetite and the ferrous iron carbonate siderite (Ona-Nguema et al., 2002).

Natural environments are extremely complex, and reductants such as Fe(II) and the presence of microbes or organic substances may strongly affect the stability of the otherwise sparingly soluble iron oxides that may act as effective sinks for metal contaminants. Furthermore, the presence of common soil and water components such as reactive anions and other redox-sensitive elements like S, N, and C may additionally affect the stabilities of iron minerals and metal partitioning to different extents in dynamic redox environments (e.g., Carroll et al., 1998; O'Day et al., 2004; Appelo & Postma, 2005; Sahai et al., 2007).

2 Microanalytical tools to study mineral–water interaction

State-of-the-art microscopic and spectroscopic techniques provide the crucial evidence for the thermodynamics-based geochemical theories on molecular reactions at the mineral surface in aqueous systems. They are particularly powerful tools to investigate and ‘visualise’ mineral–water interfacial processes and are thus essential to thoroughly study metal sorption complex geometries, surface speciation, mineral dissolution and precipitation, and nucleation and growth reactions.

Most of our early understanding of sorption reactions is based on empirical aqueous solution thermodynamics (solubility) and kinetic mineral–water interaction studies. This experimental data was fitted with surface complexation models, however, at first lacking the microscopic and spectroscopic evidence of the actual sorption process. Sposito (1990) noted:

"*Traditional adsorption experiments are notoriously insensitive to surface mechanisms and speciation, leading to a vast set of concepts that may all explain the same phenomenon. Spectroscopic methods are the only source of information about surface speciation*".

To determine the surface structure of chemisorbed species is challenging. Bulk crystal or powder X-ray diffraction methods are redundant because the surface species do not exhibit the required periodicity and long-range order as bulk crystals. Also, neutron diffraction does also not apply due to its penetration through the material, therefore being insensitive for surface structures. Electrons, however, have a relatively short penetration depth in solid materials in the order of 5–10 Å at energies of 20 to ~1000 eV, whereby the mean free path increases with increasing acceleration voltage. Therefore, incident electron and photon beam microscopic and spectroscopic techniques that use particle scattering, emission and absorption render most powerful for surface structure and speciation analyses (Brown, 1990). The rather traditional scanning and transmission electron microscopies (SEM, TEM) allow *visualisation* of the surface micromorphology and near-surface crystallographic structure, whereas the synchrotron radiation-based X-ray absorption fine structure (XAFS) and photoelectron spectroscopies (XPS) allow for the identification of the surface speciation (composition) and therewith the distinction between surface reaction mechanisms (e.g., Brown, 1990; Hochella, 1990).

All of these methods are principally based on the interaction of induced energy with the sample material and are evaluated by the resulting energy output of this interaction. Distinctive characteristics are the energy intensity and analytical depths resulting in the very specific application ranges of the various methods. There are many more techniques that can be used to investigate the surface microtopography, composition and structure, e.g., scanning tunnelling and atomic force microscopy (AFM), auger electron and secondary ion mass spectroscopy, nuclear magnetic resonance and Mößbauer spectroscopy, and low energy emission diffraction to name a few (c.f., Brown, 1990; Hochella, 1990; O'Day, 1999). This chapter focuses only on methods applied in this study.

2.1. Electron microscopy – visualisation at the nanoscale

2.1.1. Scanning electron microscopy (SEM)

SEM is a traditional electron beam microscopic imaging technique commonly used to study the morphology of a mineral and its surface topography. In combination with an energy dispersive X-ray spectroscopic detector (EDS or EDX), it allows for locally resolved qualitative chemical analyses of the sample. Interaction of the electron beam with the atoms of a solid material results in the emission of various electrons and X-rays from different penetration depths, as a function of which the energy of the beam decreases (Figure 2.1). The penetration depth is directly dependent on the energy of the incident beam (keV) and the density of the sample but may range between several tens of nanometres to a few micrometres. At low energy ($\leq$ 50 eV), secondary and auger electrons are generated from the atomic orbitals near the surface (nm range), and depending on the angle towards the incident beam, shadowing effects and penetration depth, surface topographies appear photographically (Figure 2.2A; Hochella,

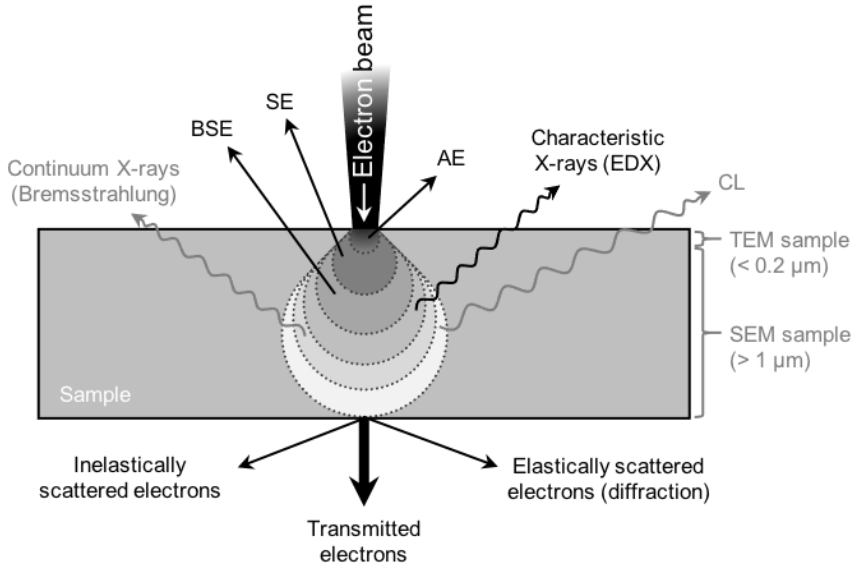

Figure 2.1. Schematic of the signals produced upon incident electron beam interaction with a solid sample in the SEM; penetration plume width ~1-2 µm (not to scale). Resulting emissions include Bremsstrahlung, backscattered electrons (BSE) which are sensitive to element densities (atomic number) and phase differences, and secondary electrons (SE) which provide topographic information. Characteristic X-rays are element specific and can be detected with an EDX device for qualitative chemical analysis. Auger electrons (AE) and cathodoluminescence (CL) provide further atomistic information, and inelastically scattered electrons (absorption) can provide information on composition and bond states, however, all of which require specific detectors which common SEM instruments are rarely equipped with. Transmitted and elastically scattered (diffracted) electrons allow for structural investigations and are the basis for high-resolution imaging and electron diffraction techniques (e.g., TEM). *Modified from Peacor (1992) and Buseck (1992).*

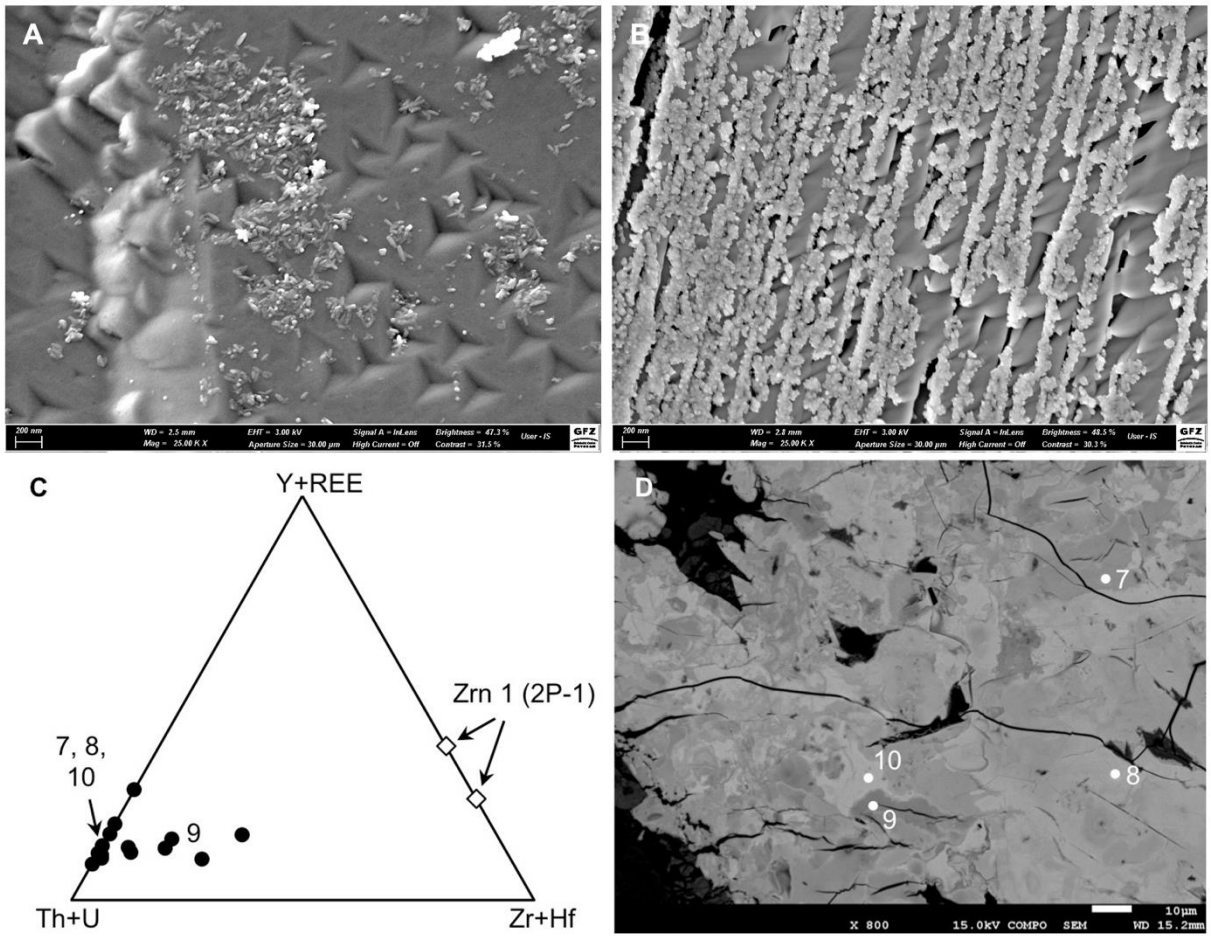

Figure 2.2. Examples for the use of high-resolution SEM imaging. (A) and (B): topographic information provided by secondary electron detection captured with a FE-SEM, showing etch pits and nano-scale surface precipitates formed on a siderite crystal reacted in an acidic aqueous solution (*this work*). (D) Micrograph of a metamict Th-silicate captured in the backscattering electron (BSE) mode: darker areas indicate the dominant presence of relatively lighter elements (here: more Zr; point 9), whereas areas of predominantly heavier elements appear brighter (here: more Th; points 8 and 10). Simultaneously detected X-rays allow qualitative chemical characterisation of the sample, as exemplary shown in (C); this is however limited to the micron-scale by the excitation range of the electron beam. The points in the BSE image refer to the compositions plotted in (C). *Data in (C) and (D) are taken from my master thesis; Zrn 1 (2P-1) refers to a zircon sample therein.*

1990). For imaging, the micro- to macroscopic sample is scanned by a highly focused electron beam in a vacuum chamber. The imaging resolution of most field emission (FE) electrode SEM's ranges within the tens to hundreds of nanometre scale, with advanced devices allowing resolutions down to the range of Ångströms (~ 0.3 nm). At higher energies and thus greater sample penetration depths (< 1 µm), backscattering electrons (BSE) are generated by elastic backscattering (reflection) of incident beam electrons from the interaction sphere. Heavier atoms are stronger backscatterers than lighter atoms, which results in more intense, brighter appearing signals in the detected BSE image known as the atomic number contrast (Figure

2.2D). Inelastic scattering of high-energy incident electrons (absorption) results in the emission of element-characteristic X-rays, the intensities of which are dependent on the chemical composition of the sample (Buseck, 1992; Peacor, 1992). The X-rays can be detected by EDX devices commonly connected to the SEM, providing local information of relative elemental compositions (Figure 2.2C). Note, however, that this is a qualitative approach and does not allow the identification of chemical species. Here, SEM analyses is therefore primarily used for solid characterisation, e.g., to investigate surface precipitate morphology at the nano to micron scale (c.f., Figure 2.2A–B). The high penetration depth, however, makes SEM analysis insufficient to identify surface species and can neither resolve nor distinguish between sorption, incorporation and/or (co)precipitation.

2.1.2. Transmission electron microscopy (TEM)

High-resolution (HR)TEM is a powerful tool to investigate crystal structures at the sub-nanoscale. This technique allows the detection of early-stage formation of crystalline phases such as nanoparticulate metal-precipitates upon metal–mineral interaction in aqueous solutions (e.g., O'Loughlin et al., 2003a,b), and in some cases helps to visualise metal distribution on/in the reacted mineral (e.g., Lu et al., 2020; Perez et al., 2020). As the identity and formation pathway of secondary phases plays an important role in metal retention, HRTEM can be essential. The simultaneous imaging and diffraction at the near-atomic level can shed light on nanoparticulate structure and morphology of phases that are notoriously difficult to determine such as that of ferrihydrite (Janney et al., 2000; Hiemstra, 2013), and may indicate crystallisation pathways such as aggregation-based nanoparticle attachment (e.g., Penn & Banfield, 1998; Banfield et al., 2000; Burleson & Penn, 2006; De Yoreo et al., 2015), providing insights to overarching mineral–water interaction mechanisms.

TEM is based on the same principles of monochromatic electron beam interaction with a sample as shown for SEM in Figure 2.1, with the important difference that the beam penetrates – *is transmitted* – through the entire sample. There are two major applications of transmission electron microscopy: high-resolution imaging and electron diffraction (structural analysis). For high resolution imaging, the electrons are highly focused to produce a two-dimensional projection of the scattering material, basically analogous to optical imaging. As the resolution is a function of the very small radiation wavelength of electrons, electron microscopy allows image resolutions at the sub-Ångström scale, which is within the order of crystallographic

lattice distances. This however requires acceleration voltages above 100 keV (McLaren, 1991). Electrons are readily absorbed and scattered at these energies, so that the sample thickness for this technique is usually below 0.5 µm (Figure 2.1).

Imaging occurs via two stages: (1) (elastic) scattering of the incident beam electrons by the sample, which are collected and focused by the objective lens onto the focal plane producing the first "image" (*diffraction pattern*), which is (2) subsequently magnified as the diffracted beams pass through additional lenses that allow for the high-resolution in HRTEM (Figure 2.3; McLaren, 1991; Buseck, 1992). Amorphous objects produce continuous electron scattering, i.e., a diffuse diffraction pattern, and can thus be readily distinguished from the distinct arrays or grids of spots in diffraction patterns produced by crystalline materials: the interference of electron diffraction waves from atoms within the crystal planes produces a constructive interference pattern of diffraction maxima (i.e., diffracted beams that are in phase). The distance between the resulting spots in the diffraction pattern (*d*-spacing) is reciprocally related to the spacing of the real crystal planes, and the direction of the arrays of spots is normal to the direction of the lines of the lattice (Figure 2.4). At high resolution, the structural information contained in the electron diffraction pattern thus allows detailed characterisation of a crystal dimension and atomic structure, as it represents a projection of the reciprocal lattice (Figure 2.5). To obtain crystal structure information from the diffracted beam projection (imaging), the "recombination" of the diffracted beams is achieved mathematically by fast Fourier transformation (FFT; McLaren, 1991), which is commonly used to produce FFT "diffraction spot" images from high-resolution lattice fringe images (Figure 2.6). Such lattice fringes are

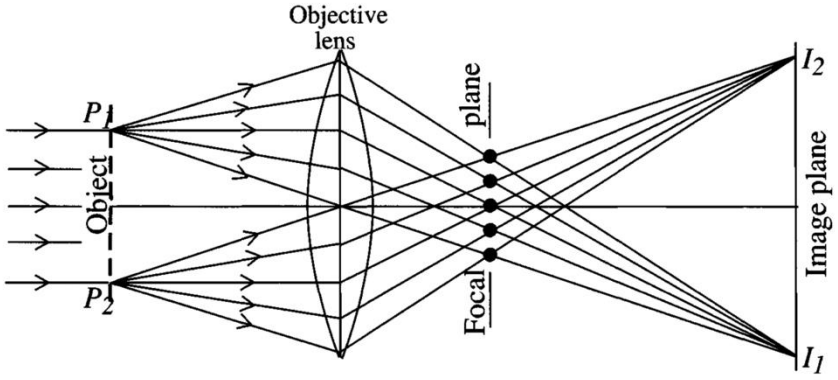

Figure 2.3. Schematic of image formation by electron diffraction: the scattered electron beams are collected by the objective lens producing a diffraction pattern on the focal plane of the objective lens, and then recombined to form the (inverse) image on the image plane. *From McLaren (1991).*

interference patterns produced between two diffraction spots and represent the periodicity of the diffracting crystal structure normal to the crystallographic direction (Buseck, 1992).

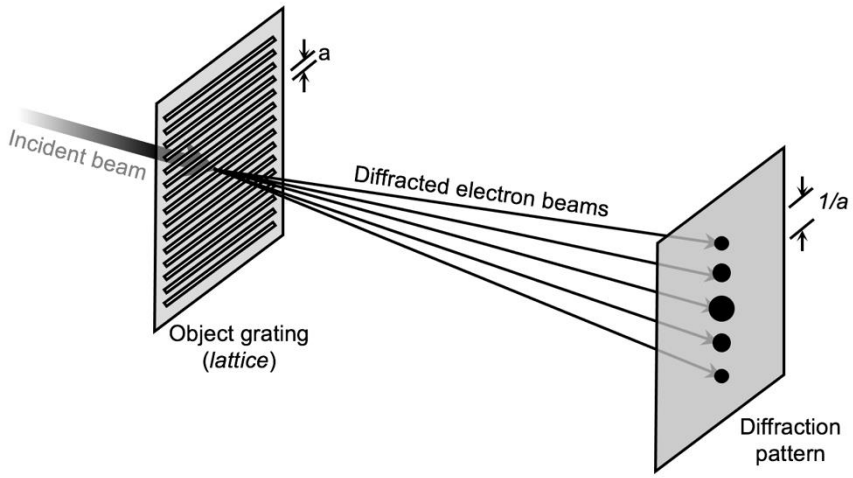

Figure 2.4. Schematic of optical diffraction pattern formation from a simplified one-dimensional object grating analogous to electron diffraction; *a* is the spacing between the slits and 1/*a* the reciprocal spacing between the diffraction spots. Such a vertical single line pattern may also result from a slit aperture that only allows a single row of vertically diffracted beams to pass through. *Modified after McLaren (1991).*

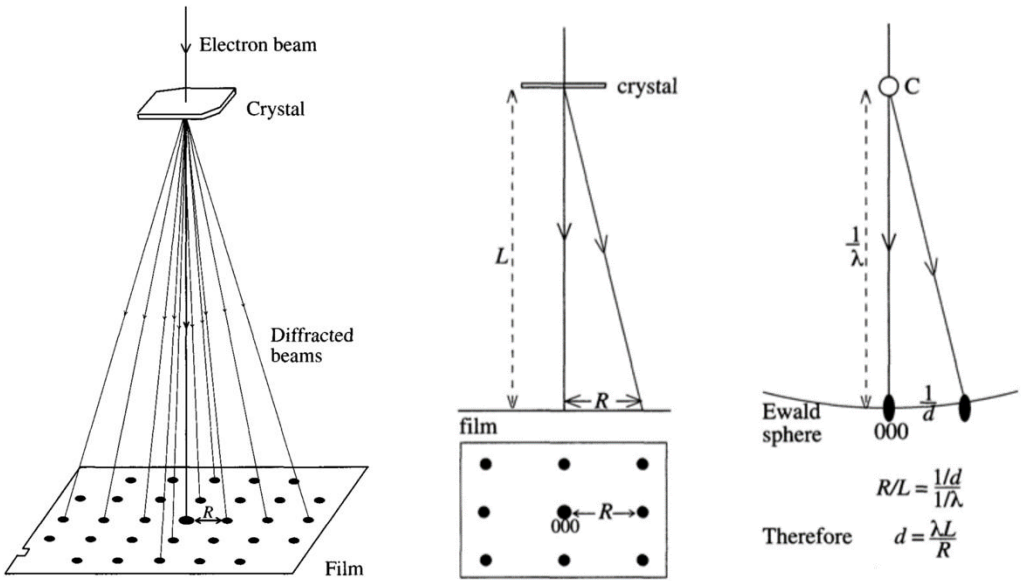

Figure 2.5. Representation of the simple geometry relating the real lattice electron diffraction pattern and the projection of the reciprocal lattice section in the crystal plane normal to the electron beam. The lattice spacing *d* is derived from the distance *R* in the real diffraction pattern, where *λ*L is the camera constant of the TEM. This relationship allows the determination of lattice distances and indexing of the diffraction pattern, relating every spot *hkl* in the projection to the (*hkl*) lattice planes of the crystal. *From McLaren (1991).*

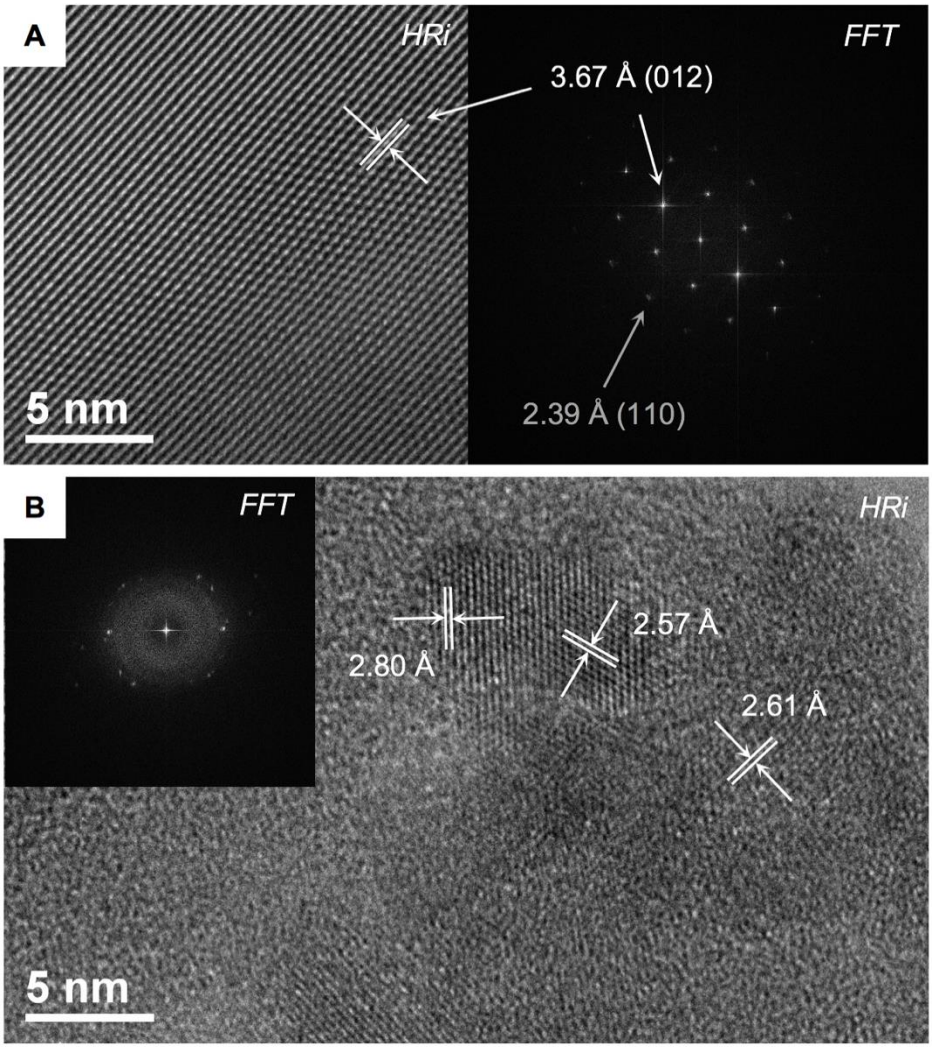

Figure 2.6. Examples for HRTEM imaging (HRi) with respective FFT images. (A) Perfect lattice fringes captured from a natural siderite crystal; measured distances given in Å between the dominant fringes correspond to the reciprocal distances between the calculated diffraction spots in the FFT image, which match the lattice distances between the (012) planes in siderite. Less obvious fringes of the (110) planes still produce diffraction points in the FFT (grey). (B) Crystalline clusters exhibiting lattice fringes in the HRi are identified as goethite (2.6 Å) particles growing from a dissolved (remnant) siderite particle (2.8 Å); these clusters produce distinct diffraction spots in the FFT and are thus distinguishable from the amorphous matrix that exhibits blurry rings in the FFT. *Data shown from this work.*

In this work, HRTEM imaging and electron diffraction is used to morphologically and structurally characterise nanoprecipitates, and to detect changes in mineral surface and host–precipitate interface structure after metal–mineral–water interaction, such as surface structure relaxation upon dissolution or large ion incorporation. Electron diffraction is particularly useful, as it provides structural information of nanoprecipitate phases at a scale that allows detection of well-ordered (crystalline) nanoclusters in an amorphous matrix which would otherwise not be detectable by common powder XRD or visible in FESEM analyses (Figure 2.6B).

2.2. X-ray spectroscopy – speciation and bonding environment

X-ray spectroscopy has been fundamental to provide evidence for metal ion interaction with mineral surfaces. Stipp and colleagues (1991; 1992), for example, provided the spectroscopic basis for metal interaction with calcite surfaces on which SCMs of ion adsorption to carbonate surfaces were developed (Van Cappellen et al., 1993; Wolters et al., 2008). The type of bonding with a mineral surface determines whether or not a metal may be readily released under changing geochemical conditions (*see* section 1.2). The geometry of metal ion complexation on mineral surfaces can be revealed by X-ray spectroscopic techniques. Supporting early SCM (e.g., Hiemstra et al., 1989a,b; Sulzberger et al., 1989), synchrotron-based spectroscopy studies demonstrated that many transition metals form strong inner-sphere sorption complexes on iron (oxyhydr)oxide surfaces (e.g., Venema et al., 1996; Bargar et al., 1997b; Ostergren et al., 2000a; Trivedi et al., 2003; Ponthieu et al., 2006).

2.2.1. X-ray photoelectron spectroscopy (XPS)

XPS has been widely used in materials sciences before it gained increasing interest in the Earth sciences to study mineral surfaces. The excitation depth of the soft X-rays impinging on a solid material surface can range from below 1 up to over 10 nm. Upon interaction of outer shell and core level electrons of (near-) surface atoms with the induced X-rays (photons), photoelectrons can be emitted if the photon energy exceeds the binding energy of the electron

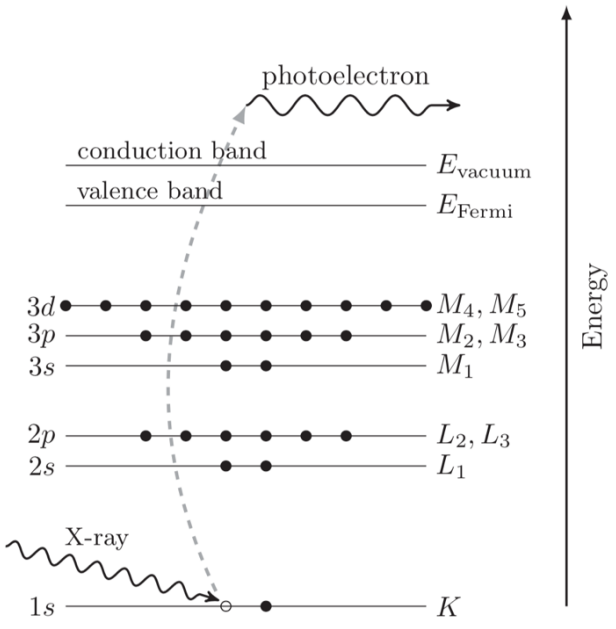

Figure 2.7. Schematic of the photoelectric effect where an incident X-ray (energies between 0.5 to 500 keV) is absorbed by an electron in a quantum core level (or shell) of an atom. For a particular electronic core level to absorb the X-ray, the X-ray energy must exceed the binding energy E_B of the electron, which is then removed from its quantum level. The energy of the absorbed photon is transferred to the resulting photoelectron that is ejected from the atom leaving behind a hole in the core electron level. *From Newville (2014).* Note that the first principal atomic levels are referred to in terms of shells (K, $L_{1\text{-}3}$, $M_{1\text{-}5}$ etc.) in XAFS literature, and in terms of quantum numbers (1s, 2s, 2p etc.) in XPS literature, although they relate to the same thing (c.f., Hochella, 1988).

(Figure 2.7). The absorbing atom is in an excited state containing one core hole left behind by the emitted photoelectron. This state decays within femtoseconds by either the (1) *X-ray fluorescence effect*, in which the core hole is filled by a higher energy core-level electron (e.g., a *L* level electron dropping into the *K* shell), thereby emitting atom-characteristic fluorescence X-rays that can be used for chemical quantification, or by the (2) *Auger effect*, in which the core hole is filled by a higher shell electron (e.g., a *M* level electron dropping into the *K* shell), thereby emitting a second (Auger) electron into the continuum (Figure 2.8). For XPS, which uses lower X-ray energies, Auger emissions are commonly used to measure the photoelectric effect (Newville, 2014). The characteristic, element-specific kinetic energies E_K of the photoelectrons are thus defined by the difference of the injected photon energy $h\nu$ and the binding energy E_B of the electron in its orbital and a spectrometer constant ϕ_{sp}:

$$E_K = h\nu - \left(E_B + \phi_{sp}\right) \qquad \text{(eq. 2.1).}$$

The relative intensities of the detected element-specific electron binding energies are used to identify the valence state of elements and molecular compositions near or at a mineral surface. The great advantage of using XPS for elemental analysis is that all elements from Li to U can be detected and unambiguously identified (H and He simply do not have enough electrons to undergo Auger transitions). This is because the characteristic electron configuration and energy of each element correspondingly produce characteristic photoelectron spectra upon photon irradiation. The only very small overlap of elemental spectral lines additionally facilitates the analysis of chemically complex samples (Hochella, 1988; 1990).

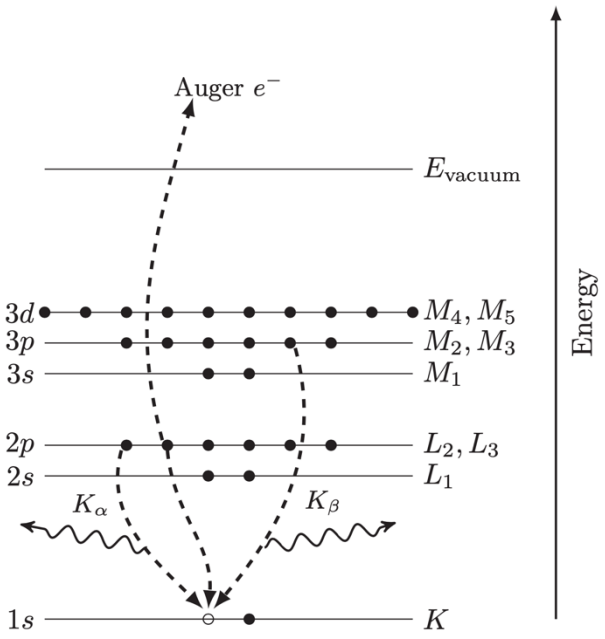

Figure 2.8. Schematic of the Auger (e^-) and X-ray fluorescence (photon) emissions during electronic relaxation. *From Newville (2014).* Both result from electron transitions from higher-level electrons filling the core-level hole upon inner-shell ionisation. The energy difference between these levels is imparted to the emitted particle (Auger electron or photon). Only if the higher-level vacancy is filled again by another electron, an Auger e^- is emitted resulting in *two* electron vacancies in the final state (*core-core-core* notation, e.g., $L_3M_{2,3}M_{2,3}$). In contrast, photon emission results in *one* vacancy in the final state (e.g., $2p_{3/2}$ or L_3). The probability of either de-excitation process depends on the atomic number Z and energy level of the absorbing atom (Hochella, 1988).

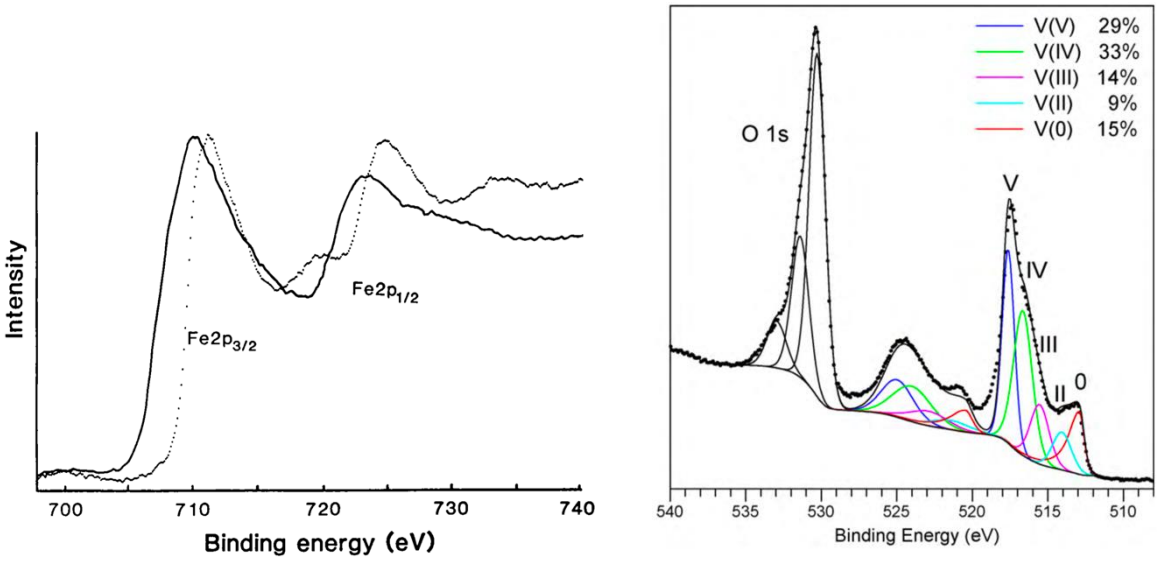

Figure 2.9. Left: XPS spectra of the Fe 2p region. Shown are the main Fe 2p lines for ferrous iron in fayalite (solid curve) and for ferric iron in hematite (dotted curve). The characteristic peak shift between these lines can be used to determine iron oxidation states near the surface. *From Hochella (1988)*. Right: Example of the V 2p (and O 1s) lines of a quantified mixed-valent vanadium oxide sample. *From Biesinger et al. (2010).*

X-ray photoelectron spectroscopy is thus a powerful tool to characterise mineral surface chemistry, i.e., to identify the chemical state and speciation of an element within the top 10 nm of a sample. Shifts and relative distances between binding energy peaks also allow for the quantification of the chemical state of a metal within a surface structure, which can be used to detect and determine the degree of oxidation (e.g., Figure 2.9; Hochella, 1988; Biesinger et al., 2010). The additional inspection of the oxygen O 1s spectra of the same samples further provides information on the oxygen coordination of the surface metal, as structural O^{2-} reveals relatively lower binding energies than structural OH^{-} (Figure 2.10; e.g., Junta & Hochella, 1994; Duckworth & Martin, 2004b; Biesinger et al., 2010). Similarly, peak shifts by approximately +0.3 eV in the Ca $2p_{3/2}$ spectrum of calcite may be indicative for a structural change towards its polymorph aragonite, as electron binding strengths differ between structural units (Pederson, 1982; Godelitsas et al., 2003). X-ray photoelectron spectroscopic evidence of Me-carbonate speciation on reacted calcite surfaces (Figure 2.11; e.g., Stipp et al., 1992) were fundamental in supporting theoretical surface complexation models for Me(II)–carbonate interaction proposed by Van Cappellen and co-workers (1993). More recently, XPS is particularly used as a complementary tool to the visualising techniques such as SEM, TEM, and AFM. For example, Godelitsas et al. (2003) provided evidence for aqueous Pb^{2+} binding to the surface CO_3^{2-} groups of the calcium carbonate substrate before precipitation of secondary carbonate phases were observed in electron microscopic imaging, presenting Pb $4f_{7/2}$ and $4f_{5/2}$

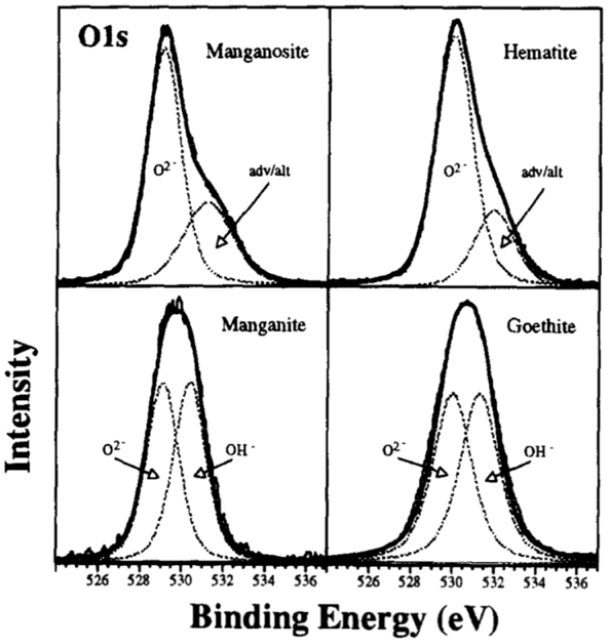

Figure 2.10. XPS spectra of the O 1s photoelectron lines from pure Mn and Fe (oxyhydr)oxides can be used as reference materials for oxygen coordination. The spectra attributed to structural O^{2-} in the oxides show a major peak with a shoulder that is associated with adventitious oxygen species and/or an additional phase. The O 1s spectra of the oxyhydroxides exhibit two congeneric peaks, one corresponding to structural O^{2-} and one corresponding to structural OH^{-} with a +1.3 eV higher binding energy (*from Junta & Hochella, 1994*).

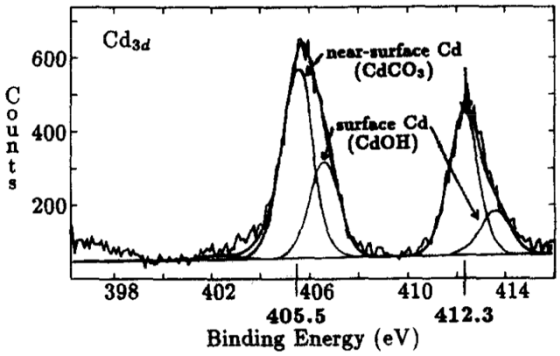

Figure 2.11. XPS spectrum of the Cd 3d photoelectron line providing evidence of near-surface Cd-carbonate formation. Presented in an early study on the interaction of aqueous Cd with the calcite surface by Stipp et al. (1992).

binding energies characteristic for Pb in $PbCO_3$ (at 138.6 and 138.8 eV; Fulghum et al., 1988; Feng et al., 2016).

The determination of the chemical state particularly of some transition metals contained in mixed-valent compounds can be challenging. Strong overlaps of the binding energy lines of the individual species make accurate peak assignments difficult (e.g., *see* V 2p lines in Figure 2.9). In such cases, the characteristic kinetic energies of the Auger transitions can be used to determine the *Auger parameter* which allows for a more accurate identification and quantification of peak contributions. The (modified) Auger parameter a' is derived from the emitted kinetic energy of the Auger electron E_K, which is composed of the three atomic levels (C_1, C_2, C_3) contributing to the Auger transitions in the de-excitation process (c.f., Figure 2.8), and the binding energy E_B of the ejected core electron (C):

$$a' = E_K(C_1C_2C_3) + E_B(C) \qquad \text{(eq. 2.2).}$$

(This form of the Auger parameter is the currently the most used and has therefore been indicated as "modified" from the early stages of its development; Wagner, 1972; Gaarenstroom & Winograd, 1977; Hochella, 1988; Biesinger et al., 2012 *and references therein*). Usually, *C*

and C_1 describe the same electronic state. In the Auger transition example given in Figure 2.8, the core level from which the photoelectron was emitted is L_3 (or $2p_{3/2}$), and the corresponding Auger kinetic energy would be written as $E_K(L_3M_{2,3}M_{2,3})$. Because the relation of the kinetic energy of the photoelectron to the incident X-ray energy $h\nu$ (eq. 2.1), and the apparent Auger binding energy is dependent on E_B, in practice, the Auger parameter is commonly determined by known and measured maximum peak energies:

$$\alpha' = E_B(\text{photoelectron}) - E_K(\text{Auger electron}) + h\nu \qquad \text{(eq. 2.3).}$$

The maximum peak energy value (E_K) of the Auger line can further be displayed in a chemical state scatter plot (*Wagner Plot*) against the corresponding photoelectron binding energy of the compound. The position of the compound provides additional information on (1) the relaxation energy, which can be an indicator for the chemical bonding type (covalent vs. ionic), and on (2) initial state effects, i.e., the chemical shift induced by changes in the ground state electronic structure of the absorbing atom, which in turn depends on the valence state of its bonding neighbouring atoms (Hochella, 1988; Biesinger et al., 2012).

The Auger parameter, in combination with the peak shape and position of the Auger and photoelectron lines can be particularly helpful to distinguish between Cu species in mixed-valent compounds (e.g., Poulston et al., 1996; Goh et al., 2006; Biesinger et al., 2010; Biesinger, 2017). In this study, XPS was used to determine the oxidation states and surface speciation of Cu (using both photoelectron and Auger electron energies), Fe and Pb. Additional XPS spectra of the O 1s and C 1s lines were used to confirm the type of metal bonding at the reacted mineral surface.

2.2.2. X-ray absorption fine structure (XAFS)

X-ray absorption spectroscopy or *fine structure* is a synchrotron-based method particularly expedient for short-range structural and (surface) speciation analyses. The very high intensity of the hard X-ray beam (> 10 keV) and the adjustability of the wavelength allow for the investigation of a large number of elements at very dilute (trace amounts) to pure element concentrations under a wide range of experimental conditions. Similar to XPS, this technique is based on the photoelectric effect, where monochromatic X-rays are used to interact with the sample, producing photoelectrons from the atomic shells of the absorbing atom (Figure 2.7; Newville, 2014). The much higher photon energies applied in XAFS, however, result in a

predominance of the fluorescence effect upon excited atom relaxation, which allows for simultaneous chemical analyses of the sample material, e.g., in 2-dimensional X-ray fluorescence (elemental) maps of the same area (Sutton et al., 2002).

In principle, upon absorption, the propagation of the photoelectron away from the absorbing atom can be treated as a radial wave function with a wavenumber $k = 2\pi/\lambda$ and its wavelength described by $\lambda \sim 1/\sqrt{E - E_0}$, where E is the X-ray energy and E_0 is the binding energy of the core level electron (equivalent to E_B in XPS terminology). The probability of X-rays to be absorbed at a core electron shell is described by the *absorption coefficient* μ, which is a function of the atomic number and mass, the sample density, and of the X-ray energy. Absorption occurs at an X-ray energy of $E \approx E_0$. If the energy increases just above E_0, there will be a sharp increase in the absorption coefficient, known as the *absorption edge* (Figure 2.12; Newville, 2014). Because each element has a specific energy value for E_0 and therefore the absorption edge, XAFS analyses can only be conducted for one element at a time (thus the notation of the absorbing shell edge of an element, e.g., Fe K-edge).

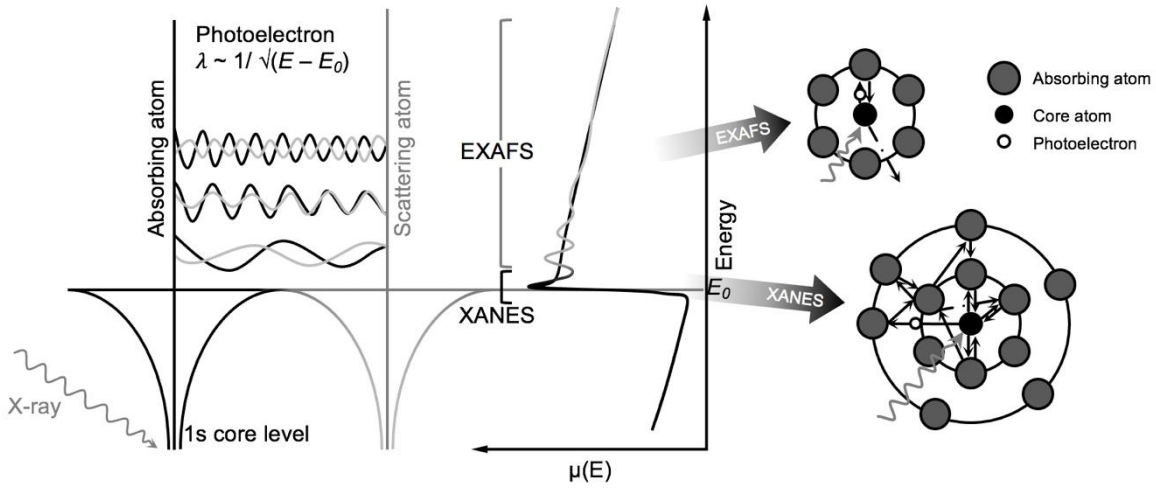

Figure 2.12. Schematic of the X-ray absorption process based on the photoelectric effect and resulting scattering mechanisms. At X-ray energies just above E_0 of an element, absorption occurs, visible as a sharp increase in the absorption coefficient $\mu(E)$, the absorption edge. Upon absorption, the photoelectron propagates away from the absorbing atom in form of a wave function (black oscillating lines) and scatters between the absorbing atom and its nearest neighbours (XANES). The radial wavefunction of the scattering photoelectron is partially backscattered to the absorbing atom, which causes characteristic alterations in the amplitude of the oscillating wave function (grey) and therefore in $\mu(E)$ at higher energies beyond the absorption edge (EXAFS). *Modified from Newville (2014) and Brown & Parks (1989).*

Key to XAFS is the consideration of atoms in a three-dimensional space surrounded by other atoms. Emitted photoelectrons scatter between the nearest neighbouring atoms of the absorbing atom. As a bulk sample method, XAFS provides information of the *average* nearest neighbour environment, i.e., atoms in the nearest two to three (rarely more than 4) coordination shells around the adsorbing atom within a radius of approximately 6 to 10 Å (Brown, 1990; Kelly et al., 2008). There are two distinct areas of the absorption spectrum (Figure 2.12): (1) the *X-ray absorption near edge structure* (XANES) at energies of approximately –50 to +200 eV around E_0, and (2) the *extended X-ray absorption fine structure* (EXAFS), which extends over energies of 50 to 1000 eV beyond E_0. These two spectral regions provide different information about the coordination environment of the absorbing atom (example spectra are given in Figure 2.13):

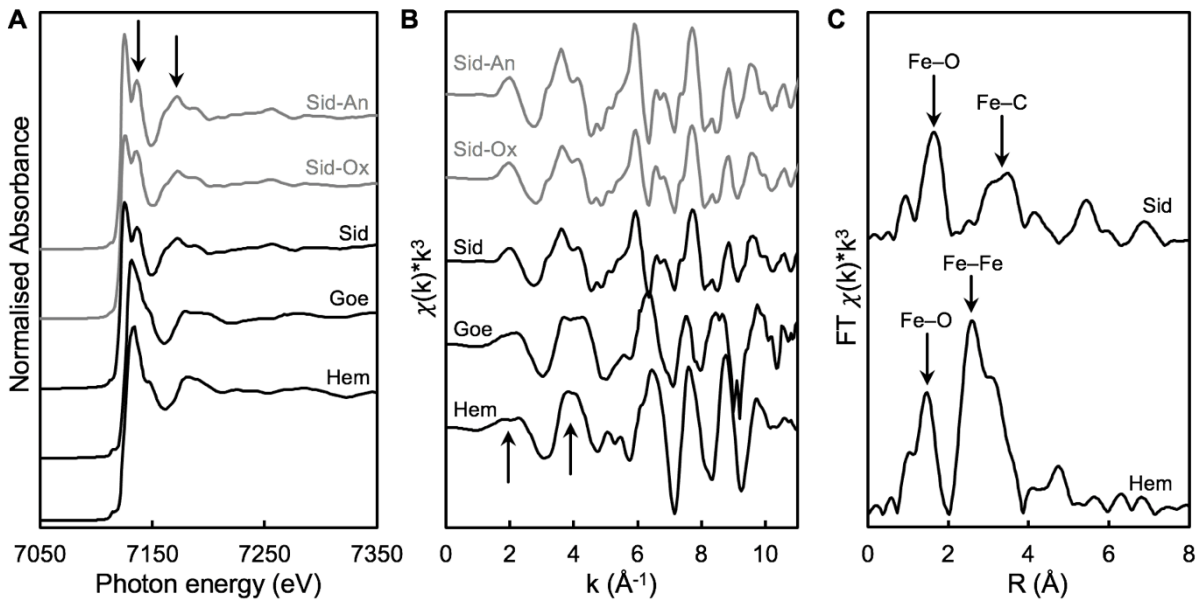

Figure 2.13. Example XAFS spectra of the Fe K-edge. (A) Normalised absorbance ($\mu(E)$) as a function of X-ray energy E (eV) of reference materials hematite (hem), goethite (Goe) and siderite (Sid) and two sample spectra (grey). Note the characteristic features of the single-peak ferric and split-peak ferrous iron (left arrow) within the XANES region of the absorption spectra. The right arrow indicates the feature that distinguishes the oxygen and carbonate coordination of the absorbing Fe atom in the respective structure. These features show that sample Sid-Ox is partially oxidised while Sid-An closely resembles the siderite reference. (B) Extracted EXAFS of the same spectra shown in (A). The weighting of the EXAFS function $\chi(k)$ by k^3 is common practice to emphasise the oscillations. Distinctive features that distinguish the ferric iron (oxyhydr)oxides from the ferrous carbonates are indicated by arrows. (C) The Fourier transform (FT) of the isolated EXAFS shown in (B); arrows highlight the contributions from the Fe–O, Fe–Fe and Fe–C scattering paths. *Data from this study.*

(1) The XANES signal results from multiple photoelectron scattering paths that can exceed distances farther than the second or third coordination sphere of the absorbing atom. The near edge structure is related to the electron configuration and thus to the orbital symmetry of the absorbing atom. That is, electron transitions between the orbitals upon X-ray absorption differ between element oxidation states, which shows as distinct features in the absorption edge (Figure 2.13A). The XANES spectrum therefore provides information on oxidation state, speciation, and binding geometry of the absorbing atom (Kelly et al., 2008) and thus allows, for example, for the assessment of the Fe oxidation state in iron-bearing minerals (Bajt et al., 1994; Wilke et al., 2001; Petit et al., 2001; O'Day et al., 2004), and to determine the metal speciation in mixed component solids such as soils (Manceau et al., 1996, 2002; Walker et al., 2005).

(2) The EXAFS signal results from all individual backscattering paths of the ejected photoelectron between the absorbing atom to the first two or possibly three neighbouring atoms before it propagates away from the absorbing atom. The interference between outgoing and scattering photoelectron waves gives rise to the oscillations well above the adsorption edge (Figure 2.13B; Brown, 1990; Newville, 2014). These oscillations, that is, the Fourier transform of the oscillatory part of the EXAFS function (Figure 2.13C), contain the information required to describe the nearest neighbour coordination environment of the absorbing atom. More specifically, the EXAFS signal χ represents the sum of all scattering path contributions of the photoelectron as a function of the wavenumber *k*:

$$\chi(k) = \sum_i \chi_i(k) \qquad \text{(eq. 2.4).}$$

Each individual scattering path $\chi_i(k)$ can be described by

$$\chi_i(k) = \frac{\left(N_i S_0^2\right) F_{\mathrm{eff}_i}(k)}{kR_i^2} \cdot \sin\left(2kR_i + \varphi_i(k)\right) \cdot e^{-2\sigma_i^2 k^2} \cdot e^{-2R_i/\lambda(k)} \qquad \text{(eq. 2.5),}$$

where *i* stands for identical scattering paths or each group of coordinating atoms at the same radial distance *R* from the absorbing atom referred to as "shell" (Kelly et al., 2008). The Fourier transform of the EXAFS equation (eq. 2.5) is typically used to model the measured EXAFS signal with the help of analytical software packages such as ARTEMIS (Ravel & Newville, 2004). In principle, equation 2.5 consists of four parts that describe the EXAFS signal (Kelly et al., 2008; the most important parameters for the theoretical model are highlighted in **bold**):

The first term, $\frac{\left(N_i S_0^2\right) F_{\mathrm{eff}_i}(k)}{kR_i^2}$, describes the amplitude of the signal by the reduction factor $\mathbf{S_0^2}$, which accounts for the relaxation of electrons upon excitation of the photoelectron. It is entirely correlated with the number of atoms within a coordination shell, $\mathbf{N_i}$. The amplitude term further includes the effective scattering amplitude $F_{\mathrm{eff}_i}(k)$ of the photoelectron, which accounts for the k-dependent specific scattering properties of elements. That is, at higher wavenumbers, heavier elements (more electrons) are stronger photoelectron scatterers than lighter elements (fewer electrons). Additionally, scattering contributions of atoms abate with increasing distance $\boldsymbol{R_i}$ from the absorber as accounted for in the expression $\frac{1}{kR_i^2}$.

The second term, $\sin\left(2kR_i + \varphi_i(k)\right)$, describes the oscillatory part of the EXAFS signal. Interatomic distances R_i, or more specifically, the half lengths of the photoelectron scattering path, can be derived from the Fourier transform of this sine function (Figure 2.13C). The scattering path ($2kR_i$) is thereby corrected for the phase shift $\varphi_i(k)$ of the photoelectron that results from its interaction with the absorbing and the scattering atoms. This shift is typically around –0.5 Å and is the reason why R_i differs from the peak position in the Fourier transform.

In the third term, $e^{-2\sigma_i^2 k^2}$, the mean-square displacement of the bond length $\boldsymbol{\sigma^2}$ accounts for dynamic (thermal) and static (structural) disorder in the averaged interatomic distances between the absorber and coordination atoms.

The last term, $e^{-2R_i/\lambda(k)}$, accounts for the distance a photoelectron travels upon excitation. This mean free path $\lambda(k)$ of the photoelectron typically ranges between ~5 to 30 Å and thus constrains the EXAFS signal to be local probe, dominated by the scattering contributions of atoms/shells within a radial distance of ~10 Å (Kelly et al., 2008 *and references therein*; Newville, 2014).

From the theoretical model of the Fourier transformed EXAFS signal, average coordination numbers N_i can be obtained within an approximate error of 10 to 20%, and average interatomic distances R_i determined at an accuracy of about 0.02 Å (Brown, 1990). These values provide necessary information to describe the immediate coordination environment of the absorbing atom. In the particular case of metal sorption studies, the XANES part of the absorption spectrum provides more reliable information of the sorption speciation, whereas the EXAFS region is generally used complimentarily to distinguish between structural incorporation

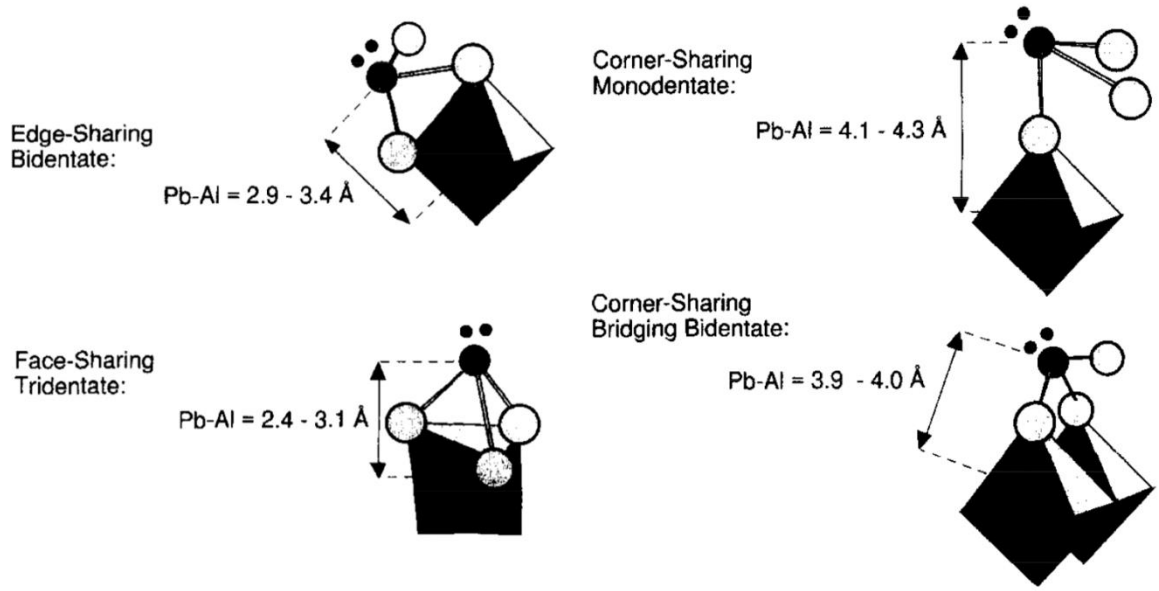

Figure 2.14. Examples of Pb(II) sorption geometries, here on AlO_6 octahedra in Al-oxides. The interatomic distances represented by Pb–Al scattering path lengths given in (Å) were obtained from the FT of the Pb L_3-edge EXAFS (not shown; *from* Bargar et al., 1997a). All geometries show mononuclear complexes, except of the corner-sharing bridging bidentate complex, which is binuclear. Edge-sharing bidentate complexation is also typical for Pb(II) adsorption onto goethite and other iron (oxyhydr)oxides.

(usually indicated by higher coordination numbers) and surface complexation geometries (generally lower coordination numbers; examples shown in Figure 2.14).

A limiting factor to XAFS is its analytical constraint to the near-range order of the sample structure, so that complementary XRD analysis for the long-range order confirmation of the structural information is recommended. Additionally, as the X-ray absorption intensity of an element is strongly dependent on the atomic number, lighter elements with atomic numbers < 22 yield adsorption edges at energies below 5 keV, which coincides with the strong X-ray absorption by water and thus excludes the analyses of these elements (Brown, 1990).

There are numerous examples of how XAFS has advanced our understanding of sorption mechanisms and the coordination chemistry of sorption complexes, ion incorporation and speciation. In an early solution chemistry study on the adsorption mechanisms of Zn(II) from an aqueous solution in equilibrium with calcite and undersaturated with respect to Zn carbonate, Zachara and co-workers (1988) suggested outer-sphere complexation of Zn(II) onto calcite. Their interpretation was based on the instability of the sorption complex which pointed at incomplete dehydration of the adsorbed Zn ion. The independence on surface charge, however, hinted at a partially covalent character of the surface bond indicating that Zn was at least in part

dehydrated upon adsorption. This ambiguity of the sorption behaviour of Zn was clarified by Elzinga and Reeder (2002), who provided EXAFS spectroscopic evidence for a mononuclear tetrahedral inner-sphere surface complexation of Zn onto calcite under comparable study conditions. Further excellent examples are studies using XAFS to identify metal sorption complexation in groundwaters, soils, tailings and even house dust (Manceau et al., 1996; Brown et al., 1999; Carroll et al., 1998; O'Day et al., 1998; Manceau et al., 2002; McLean et al., 2011; Finlay et al., 2020). These studies greatly contribute to our understanding of the partitioning of metals in mixed component systems, which is essential to predict the geochemical behaviour of potential contaminants in a wide range of different environments.

In this study, XAFS is used in two ways: high-resolution µXANES combined with µXRF mapping is used to locally identify the oxidation state and first-shell coordination of Fe, Cu, and Pb to assess redox products and assess the relationship between reacted siderite grains, secondary mineral phases and solid-associated metal species. In addition, XAFS bulk spectra of the same samples are used to identify the predominant speciation of Fe in the secondary phases, and of solid-associated Cu and Pb. And specifically, the EXAFS region of the bulk XAFS spectra is used to determine the first to third shell structural coordination of solid-associated Cu and Pb in order to distinguish between metal (ad)sorption, incorporation, or (co)precipitation.

3 Metal–mineral interactions in aqueous solutions

The aqueous geochemical behaviour and surface properties of minerals play a key role in metal–mineral interactions. The specific characteristics of iron (oxyhydr)oxides and divalent metal carbonates have been extensively studied and are reviewed with regards to dissolved metal immobilisation from aqueous suspensions.

It follows the formulation of the research objectives of this thesis to investigate siderite as potential candidate material for metal immobilisation purposes. Siderite is an attractive reagent for metal uptake from contaminated aqueous systems as it combines properties of both iron-bearing and carbonate minerals. A review is presented reflecting on its mineral–geochemical properties and metal-uptake potential.

3.1. Metal sorption to iron oxides

Iron (oxyhydr)oxides are naturally abundant and mostly occur as nano-sized crystallites. Their large reactive surface areas make them excellent sorbents for ions and molecules. Hematite (α–Fe_2O_3), the FeOOH modifications goethite (α–FeOOH) and lepidocrocite (γ–FeOOH), and the poorly crystalline ferrihydrite (often given as $Fe_5O_8H \cdot 4H_2O$ although its exact formula varies; e.g., Cornell & Schwertmann, 2003; Hiemstra, 2013) are among the most excessively studied ferric iron (oxyhydr)oxides for metal sorption of, e.g., Pb, Cd, Co, Cr, Cu, Ni, Zn. The group of the mixed-valent green rust nano-minerals (roughly $Fe^{2+/3+}{}_3(OH)_7$, often with intercalated anions) have been of increasing interest due to the potential of their ferrous iron component to undergo redox reactions with metal sorbates, e.g., As, Cr, Se, and U. Notably, sorption efficiency varies considerably with experimental parameters such as pH, solution composition, study conditions (e.g., ambient or oxygen-free), and sorbate and sorbent type and concentration, all of which notoriously differ between studies. However, some generalisations have been formulated based on numerous macro- and microscopic analyses and/or in combination with surface complexation studies on metal sorption to various (iron) oxide minerals. Ten aspects are elucidated below (modified after Brown & Parks, 2001):

(1) The **high dielectric constants** of iron oxides in comparison to other mineral sorbents facilitates the destabilisation of the hydration shell surrounding dissolved metals in close approximation to the iron oxide mineral surface, promoting sorption via ligand exchange reactions. Consequently, divalent transition and heavy metal cations show high sorption affinities for iron oxide mineral surfaces (e.g., Brown & Parks, 2001; Fischer et al., 2007) and tend to form strong inner-sphere complexes with the sorbents. Numerous XAFS studies show the specific complexation of metals, e.g., for Cd(II) on goethite (Venema et al., 1996), Zn(II) on goethite and hematite (Trivedi et al., 2001; Ha et al., 2009), and As(V) and Pb(II) on goethite, hematite and ferrihydrite (e.g., Manceau et al., 1992; Bargar et al., 1997b; Sherman & Randall, 2003; Trivedi et al., 2003; *reviewed by* Waychunas et al., 2005).

(2) **Adsorption is reversible**. Even dominantly inner-spherically adsorbed adions may be rapidly and almost completely recovered if the solution pH is significantly decreased or lowered well below the pH_{PZC} of the sorbent (e.g., Schultz et al., 1987; Gunneriusson et al., 1994).

(3) **Ionic size and redox state matter**. Competition between cations for sorption sites can be expected for metal cations that show preferences for similar surface sites and to form similar surface complexes (e.g., Cu(II) and Fe(II); Swallow et al., 1980). The ion oxidation state

directly effects the ionic radius and aqueous speciation of the metal sorbate. Some metals occur as oxyanions or free ions that form either weaker outer-sphere or stronger inner-sphere complexes on the same substrate depending on their oxidations state. Studies on Cr sorption onto iron oxides using XAFS, for example, show that Cr(VI) preferentially occurs as chromate oxyanions (CrO_4^{2-}) which attach to all FeOOH polymorphs via electrostatic attraction (Wu et al., 2016), whereas the reduced form Cr(III) forms inner-sphere complexes with goethite and hematite (Waychunas et al., 2005; Wu et al., 2016) or even coprecipitates as (Fe^{III},Cr^{III})OOH due to its similar ionic radius to Fe(III) in octahedral coordination (0.615 Å $^{[6]}$Cr(III) *vs.* 0.645 Å $^{[6]}$Fe(III); Shannon, 1976; Eary & Rai, 1988; Manceau et al., 2000; Bibi et al., 2018). Similarly, using XAFS it was possible to demonstrate that Se(VI) is commonly present as selenate (SeO_4^{2-}) in aqueous solutions and sorbs only weakly onto goethite as outer-sphere complex, whereas Se(IV) in the form of selenite (SeO_3^{2-}) adsorbs chemically onto goethite as inner-sphere complex (Hayes et al., 1987). Ionic radii determine the stability of an ion in specific crystallographic metal sites (the following values are taken from Shannon, 1976). For example, the ionic radii of octahedrally coordinated Mn(III) (0.645 Å) and Cr(III) are equal and very similar to that of Fe(III), respectively, and are thus generally highly compatible with the $^{[6]}$Fe(III) site in any of the ferric iron oxide structures. In comparison, slightly larger ions of similar sizes, e.g., Co(II) (0.745 Å), Ni(II) (0.69 Å), and Zn(II) (0.74 Å), are more compatible with the more open goethite structure than with the hematite structure, while the much larger Mn(II) (0.83 Å) ion is generally less compatible with either (Manceau et al., 2000; Frierdich & Catalano, 2012b). Hence, the incorporation of slightly larger ions such as Cu(II) (0.73 Å) and Zn(II) (0.74 Å) is more common in goethite than in hematite. However, the incorporation of Cu(II) into goethite for example results in considerable distortion of the $^{[6]}$Fe(III) site due to the Jahn-Teller effect. This distortion can be better compensated for by relaxation and compliance effects in the goethite structure compared to in hematite (Manceau et al., 2000), but this also facilitates liberation of these ions (e.g., Frierdich & Catalano, 2012b; Stegemeier et al., 2015).

(4) **Redox conditions play a crucial role in metal retention by iron minerals**. From the sorbent perspective, the redox activity of the major metal component of the mineral such as Fe(II) and Mn(II) greatly affects the sorption behaviour of redox-sensitive adions such as As, Co, Cr, Se, and U. For example, Mn oxides are less favourable sorbents for Cr(III), as the Mn(II/IV) component would oxidise Cr(III) rapidly to Cr(VI), which is more soluble and forms less stable sorption complexes than Cr(III) (Manceau et al., 1992; Wu et al., 2016). Therefore, the reduction of Cr(VI) and U(VI) by the Fe(II) component upon adsorption on mixed-valent green rust minerals is much more favourable for immobilisation of these elements (e.g.,

Williams & Scherer, 2001; O'Loughlin et al., 2003). Despite their exceptionally low solubility in neutral to moderately alkaline natural waters (e.g., K_{sp}(goethite) ≈ 10^{-40}; Hsu & Marion, 1985), the stability of the amphoteric ferric iron oxides is affected by extreme changes in the pH towards very acidic or alkaline regimes, and by changes in the redox state of the system (*see* section 1.2.4.2.). Consequently, adsorbed or incorporated metals may be liberated upon reductive dissolution of the ferric sorbents under reducing conditions. In other words, as pe and pH decrease, the activity of Fe(II) in solution increases, for example, by a factor of hundred for each unit change in pH (*see* Figure 1.12; Cornell & Schwertmann, 2003). The effect of Fe(II) on metal retention has become of increasing interest, as Fe(II) is an abundant reductant in natural systems irrelevant of biogenic or non-biogenic origin. The interaction of Fe(II) with Fe(III) oxide minerals in the presence of metal (ad)ions have been reported with various results. Coughlin & Stone (1995) showed that goethite with pre-adsorbed Me(II) exhibited increased sorption upon interaction with added Fe(II) to the oxygen-free system. Upon adsorption, Fe(II) induces electron transfer and conduction through the bulk crystal lattice (Yanina & Rosso 2008) and thus a change in surface Fe(II)/Fe(III) distribution; this reworking of the surface potential resulted in enhanced adsorption of both redox-active Mn(II), Co(II), Cu(II), and less redox-active Ni(II), Pb(II) metal ions (Coughlin & Stone, 1995). However, bulk electron conduction, which leads to reduction of structural Fe(III) at separate "exit" site of the electron and resulting liberation of Fe(II) into solution without net reduction of the mineral (Yanina & Rosso, 2008; Handler et al., 2009; Handler et al., 2014) was also reported to cause Me(II) cycling through and release from goethite and hematite upon reaction with Fe(II) under anoxic conditions (Frierdich et al., 2011; Frierdich & Catalano, 2012a,b).

(5) **Sorption initially occurs rapidly** (within seconds) at high-energy surface sites (e.g., kink and step edges; Hochella, 1990) followed by a slower reaction involving lower-energy sites (e.g., terraces) and eventually by the formation of three-dimensional complexes and precipitates once all reactive sites are occupied (e.g., Strawn et al., 1998; Brown & Parks, 2001 *and references therein*; Jeon et al., 2001).

(6) **Surface site densities determine the reactivity of mineral surfaces**. For iron oxides, surface sites can be described by the coordination geometry of the surface oxygen groups, which can be singly (>$FeOH^{-1/2}$, "A-type"), doubly (>Fe_2OH^0, "B-type") and triply (>$Fe_3OH^{+1/2}$, "C-type") coordinated (*see* Figure 1.4; Hiemstra et al., 1989a,b; Cornell & Schwertmann, 2003). Protonation and ion adsorption behaviour thus varies for each type of surface site and is generally pH dependent: the neutral hydroxyl group of the doubly

coordinated oxygen, for example, is considered inert over a wide pH range, thus ion adsorption is mostly attributed to the charged singly and triply coordinated sites. As the abundances of the different reactive surface sites are mineral specific and vary for crystallographic faces, surfaces of the same sorbent can show different reactivities for proton and/or cation sorption on goethite (Hiemstra et al., 1989a,b; Hiemstra & Van Riemsdijk, 1996). The specific surface site distribution of a crystal is a function of its morphology: while the surface geometry of goethite nanoparticles is dominated by a combination of (101) and (001) faces containing mostly A- and C-type reactive surface sites, larger goethite particles also exhibit (010) and (210) faces with high surface densities of reactive A- and B-type oxygen coordination sites (Villalobos et al., 2009). Earlier SCM, XAFS and combined studies confirmed that such different surface structure and bonding geometries on the goethite surface offer differently stable sorption sites based on the charge distribution that may or may not satisfy Pauling's bond valence rule (e.g., Spadini et al., 1994; Venema et al., 1996; Bargar et al., 1997a,b). For example, Pb(II) was found to form different inner-sphere complexes with the $Fe(O,OH)_6$ octahedra on different surface sites: Either bidentate or tridentate edge-sharing complexes were identified at triply coordinated sites on the (110) and on doubly and singly coordinated sites on the (021) faces of acicular goethite crystals. Bidentate corner-sharing complexes, however, were attributed to singly coordinated sites on the (110) face rather than on the relatively smaller (021) face, where repulsive interactions were expected to be stronger (*see* Figure 2.14 for comparable geometries; Ostergren et al., 2000a). Similarly, the (001) plane of hematite predominantly contains "inert" doubly coordinated hydroxyls but also underlying higher-coordinated terminal Fe groups, which preferentially interact with anions. Based on the different site characteristics on this plane, Yanina & Rosso (2008) demonstrated that a potential gradient can develop across a hematite crystal as a result of the selective adsorption of potential-determining ions onto the differently reactive surface sites on the (001) hematite basal plane, and charge-accumulating adsorption on singly and triply coordinated sites on lower-index (*hk*0) faces.

(7) **Sorbent crystallinity and phase transformations affect ion sorption**. According to SCM studies, highly crystalline phases such as goethite and magnetite are expected to exhibit lower sorption capacities compared to less crystalline iron oxides because of their relatively lower specific surface areas and thus relatively lower sorption site densities (e.g., Dixit & Hering, 2003). For example, demonstrating the effect of substrate crystallinity on the adion sorption geometry, Trivedi et al. (2001) showed in an XAFS study that Zn(II) retained its hydration shell upon adsorption on amorphous iron oxide forming outer-sphere complexes, but formed inner-sphere sorption complexes upon adsorption on the more crystalline goethite

surface. As the overall crystal surface structure varies with particle size, this is a contributing factor determining the abundance of available reactive sorption sites (e.g., Lasaga, 1984; Waychunas & Zhang, 2008; Ha et al., 2009; Villalobos et al., 2009; Jung et al., 2016). Therefore, transformations between poorly crystalline, typically nanoparticulate phases to highly crystalline iron oxides may have considerable effects on metal adsorption and retention. Upon phase transformation reactions, metals may be released (c.f., (4)) or incorporated: Aging and thermal treatment of poorly crystalline ferrihydrite at alkaline pH, for example, may enhance entrapment of metal ions in more crystalline iron oxide structures, as shown for Cd(II) and Zn(II) coprecipitated with ferrihydrite (Martinez & McBride, 1998), for pre-adsorbed Ba and Sr (Arthur et al., 1999), for Pb(II) which got partially incorporated into defects and nanopores of goethite and hematite during early stages of ferrihydrite crystallisation (Vu et al., 2013), and U(VI) incorporation into hematite upon transformation from ferrihydrite (Marshall et al., 2014). Increased relative concentrations of divalent metals (e.g., Co, Cu, Zn) may in turn retard the transformation kinetics by stabilising ferrihydrite, leading to the formation of metal-substituted goethite at lower and of hematite or spinel at higher relative metal concentrations (*see* section 1.2.4.2.; Cornell, 1988; Cornell & Giovanoli, 1988).

(8) **Ionic strength affects ion adsorption**. Ionic strength effects are minor to negligible for metal ions that form strong sorption complexes (e.g., Cu, Pb, Ni, Cd etc.), but considerable for alkali earth ions (e.g., Mg, Ca, Ba) and oxyanions (e.g., of Cr, Se) that form weak sorption complexes by retaining their hydration shell (Hayes & Leckie, 1987). However, high ionic strength may cause coagulation and nanoparticle aggregation. Although aggregation reduces surface charge and reactive surface area and thus potentially decreases ion adsorption, aggregation also enhances entrapment of metals sorbed to the particles. Desorption of Zn(II), Cu(II) and U(VI) adsorbed to nanoparticulate iron (oxyhydr)oxides, for example, was found to be partly inhibited and slowed upon increased aggregation (Gilbert et al., 2009; Stegemeier et al., 2015; Dale et al., 2015; Jung et al., 2016).

(9) **Inorganic ligand effects on metal adsorption are various**. The presence of high relative concentrations of inorganic ligands such as chloride, phosphate, sulphate, and carbonate, may inhibit sorption of metals that form oxyanions and/or strong complexes with these ligands by competitive formation of aqueous or surface sorption complexes. The adsorption of carbonate, for example, was suggested to outcompete arsenate (As(V)) and strongly reduce the sorption capacity of ferrihydrite for arsenate and arsenite (As(III)) in carbonate-rich groundwaters (Appelo et al., 2002), whereas arsenate was found to outcompete

phosphate adsorption onto goethite, particularly at pH below 6 (Liu et al., 2001). While metal anions such as chromate (Cr(VI)) may compete with carbonate anions for the same sorption sites on goethite (Van Geen et al., 1994; Villalobos et al., 2001), the sorption of some metal cations may be enhanced or facilitated in the presence of moderate to low concentrations of inorganic ligands by the formation of ternary metal-bridging complexes. A combination of bond-valence based SCM with XAFS and Fourier transform infrared spectroscopy studies showed that the total amount of Pb(II) and Cd(II) sorption on goethite was enhanced in the presence of carbonate, sulphate, and chloride (Gunneriusson et al., 1994; Ostergren et al., 1999, 2000a,b; Villalobos et al., 2001). Similarly, U(VI) readily forms U(VI)-carbonate complexes which were found to bind in an inner-sphere metal-bridging complex on hematite and ferrihydrite at atmospheric CO_2 concentrations (Waite et al., 1994; Bargar et al., 2000; Villalobos et al., 2001). Naturally, as the speciation of dissolved carbonate species varies with pH, the sorption behaviour of carbonate onto goethite varies accordingly. In natural waters at neutral pH and moderate dissolved CO_2 concentrations of 1 to 6 mM, a considerable fraction of goethite sorption sites is thus expected to be occupied by adsorbed carbonate species (Villalobos & Leckie, 2000), which in turn may affect metal sorption (Villalobos et al., 2001).

(10) And last, though not further addressed in this study, is the presence of organic coatings on mineral surfaces. Such coatings may affect sorption of metals with high affinity for organic ligand complexation (e.g., Cu(II) and Hg(II)) but is expected to have little effect on other divalent metals. Organic acids, however, may promote desorption by metal complexation with the organic component (e.g., Coughlin & Stone, 1995; Liu et al., 2001).

3.2. Metal–carbonate mineral interaction

The divalent metal carbonates ($Me^{II}CO_3$) have high affinities to sorb heavy metals such as Cd, Co, Cu, Pb, and Zn which tend to form inner-sphere sorption complexes on carbonate mineral surfaces (e.g., Terjesen et al., 1961; Kornicker et al., 1985; Davis et al., 1987; Zachara et al., 1991; Van Cappellen et al., 1993; Salem et al., 1994; Gutjahr et al., 1996a; Elzinga & Reeder, 2002; Elzinga et al., 2006). In contrast to the iron (oxyhydr)oxides, however, the high reactivity of carbonates is manifested in their much higher solubility and fast reaction rates in natural aqueous systems. This is also why carbonates in the form of soda (Na_2CO_3), limestone, and abiogenic or biogenic calcium carbonate are used as effective neutralisers and reagents for the remediation of contaminated acidic aqueous environments with dynamic redox and thus

fluctuating acidity conditions (e.g., *acid mine drainage*; Johnson & Hallberg, 2005; Moon et al., 2011; Macías et al., 2012; Skousen et al., 2019). The dissolution of carbonate minerals is thereby used to neutralise the system through alkalinity production, promoting precipitation of secondary phases. Instead of adsorption, the coprecipitation of metals in less soluble solid carbonates is the aspirational target. However, not all heavy metals form carbonate minerals or incorporate easily into the calcite or aragonite structures, and the relatively high solubility of these minerals potentially facilitates metal release upon moderate changes in the aqueous conditions. The surface properties, crystallographic and geochemical relationships governing these reactions are therefore key factors in terms of metal uptake efficiency by carbonate minerals and will be elucidated in more detail over the following paragraphs.

3.2.1. Mineralogic chemical properties of the divalent metal carbonates

Carbonate minerals are highly abundant, either as rock-forming components in limestone and marble, or as sedimentary cements, metamorphic or metasomatic veins, skarns, as detritus, mostly originating from (fossil) biogenic carbonate material. The rock-forming carbonate minerals calcite, aragonite (both $CaCO_3$), dolomite ($CaMg(CO_3)_2$) and magnesite ($MgCO_3$), however, are very reactive and have relatively high solubility products K_{sp} ranging from $10^{-8.3}$ to $10^{-17.1}$ (at 25 ºC and 1 atm; Plummer & Busenberg, 1982; Langmuir, 1997 *and references therein*). Since limestones and dolomites often form aquifers of good porosity and permeability, circulating groundwater can vastly interact with these minerals. Thus the higher reaction rates of carbonate minerals compared to for example oxides or silicates has a prevailing or *regulating* effect on the groundwater and soil chemistry even if present as minor components (e.g., Appelo & Postma, 2005; Scheffer & Schachtschabel, 2010). The stability relations between phases in the Me(II)O–CO_2–H_2O system are pivotal for the regulatory effect of carbonate minerals in soils and aquatic systems, with Me(II) representing primarily Ca(II) and Mg(II) for the rock-forming carbonates, but also Mn(II) and Fe(II) for the most common minor carbonates rhodochrosite ($MnCO_3$) and siderite ($FeCO_3$) particularly found in anaerobic environments.

The solubility and reaction kinetics of the divalent metal carbonates are strongly related to the CO_2 partial pressure and the proton (H^+) concentrations in the aqueous system (Plummer et al., 1978; Pokrovsky & Schott, 2002). This is important as the pCO_2 can vary by several orders of magnitude from atmospheric concentrations of $10^{-3.5}$ atm in surface waters, to $10^{-2.5}$ atm in calcareous aquifers, and up to $10^{-1.5}$ atm in soil fluids where increased CO_2 concentrations arise

from root respiration and microbial degradation of organic matter (c.f., Langmuir, 1997; Appelo & Postma, 2005; Scheffer & Schachtschabel, 2010). In general, carbonate mineral dissolution is surface reaction-controlled and proceeds rapidly at far from equilibrium and acidic pH conditions according to

$$MeCO_3 + H^+ \rightleftharpoons Me^{2+} + HCO_3^- \qquad \text{(eq. 3.1).}$$

This reaction is governed by the protonation of the $>CO_3^-$ surface site, and becomes independent of pH at circumneutral and alkaline pH ranges, following

$$MeCO_3 + H_2O \rightleftharpoons Me^{2+} + HCO_3^- + OH^- \qquad \text{(eq. 3.2)}$$

(Figure 3.1; Pokrovsky & Schott, 2002; Duckworth & Martin, 2004a). The presence of CO_2 in most natural waters interacts with metal carbonate minerals and water following the reaction

$$MeCO_3 + CO_2(g) + H_2O \rightleftharpoons Me^{2+} + 2HCO_3^- \qquad \text{(eq. 3.3).}$$

At acidic pH < 4, when the divalent metal carbonate dissolution is proton-promoted, the forward reaction rate of equation 3.3 is relatively unaffected by increased pCO_2, while it becomes enhanced at higher to circumneutral conditions when dissolution is independent of pH but dependent on pCO_2. The backward reaction towards carbonate precipitation is in turn favoured under neutral to alkaline pH and at reduced pCO_2 conditions (e.g., Plummer et al., 1978; Bruno et al., 1992; Pokrovsky & Schott, 2002).

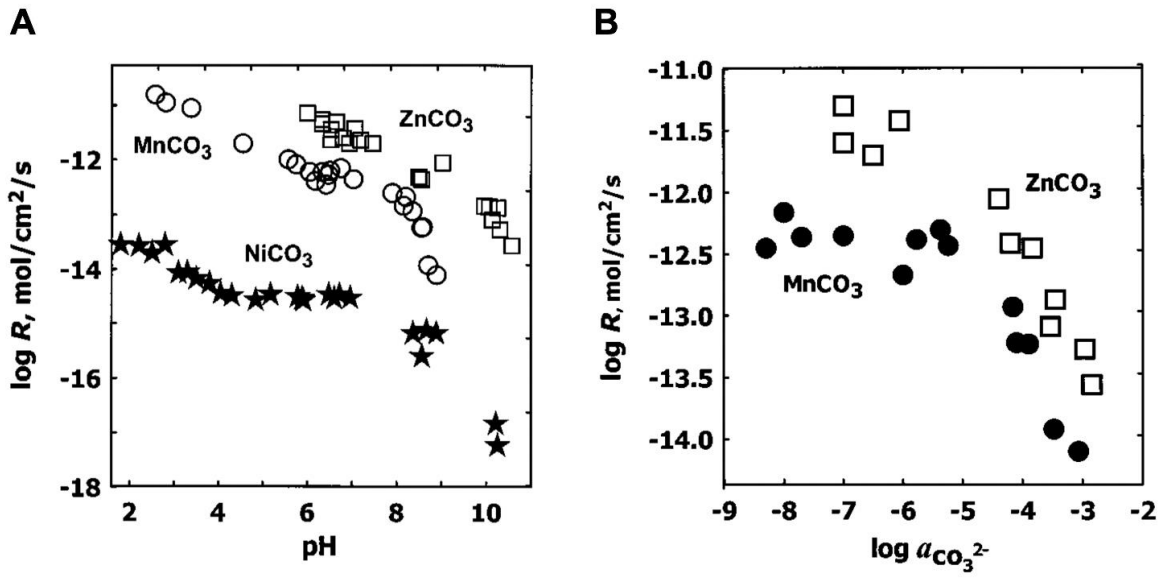

Figure 3.1. Examples of $MeCO_3$ dissolution rates at 25 ºC and I = 0.01 M as a function of (A) solution pH, and (B) dissolved carbonate ion activity over a pH range of 6 to 10.3. *From Pokrovsky & Schott (2002).*

This dependency of carbonate mineral solubility and reaction kinetics on pCO_2 at above neutral pH can be explained by speciation of CO_2(g) dissolved in water: upon dissolution, CO_2(g) becomes CO_2(aq) which, in part, associates with H_2O molecules to form carbonic acid (H_2CO_3):

$$CO_2(aq) + H_2O \longrightarrow H_2CO_3 \qquad \text{(eq. 3.4).}$$

Note that by convention, the sum of the two coexisting species CO_2(aq) and H_2CO_3 may be given as H_2CO_3* (although CO_2(aq) is much more abundant). At pH ≤ 6.3, H_2CO_3* is the dominant species and continuous replenishment of CO_2, for example in a system open to constant CO_2(g) exchange, enhances carbonate mineral dissolution by consumption of CO_2 according to equation 3.3. With increasing pH, H_2CO_3* dissociates into bicarbonate (HCO_3^-) which becomes the dominant species in the pH range of 6.3 ≤ pH ≤ 10.3 (Figure 3.2). Within this pH range, when carbonate mineral dissolution rates are independent of pH, high pCO_2 concentrations lead to enhanced interaction of the dissolved metal cation in the bulk solution with aqueous HCO_3^-, driving the formation of aqueous $MeCO_3^0$ species and thus increasing the solubility of the carbonate mineral (Plummer et al., 1978; Bilinski & Schindler, 1982; Bruno et

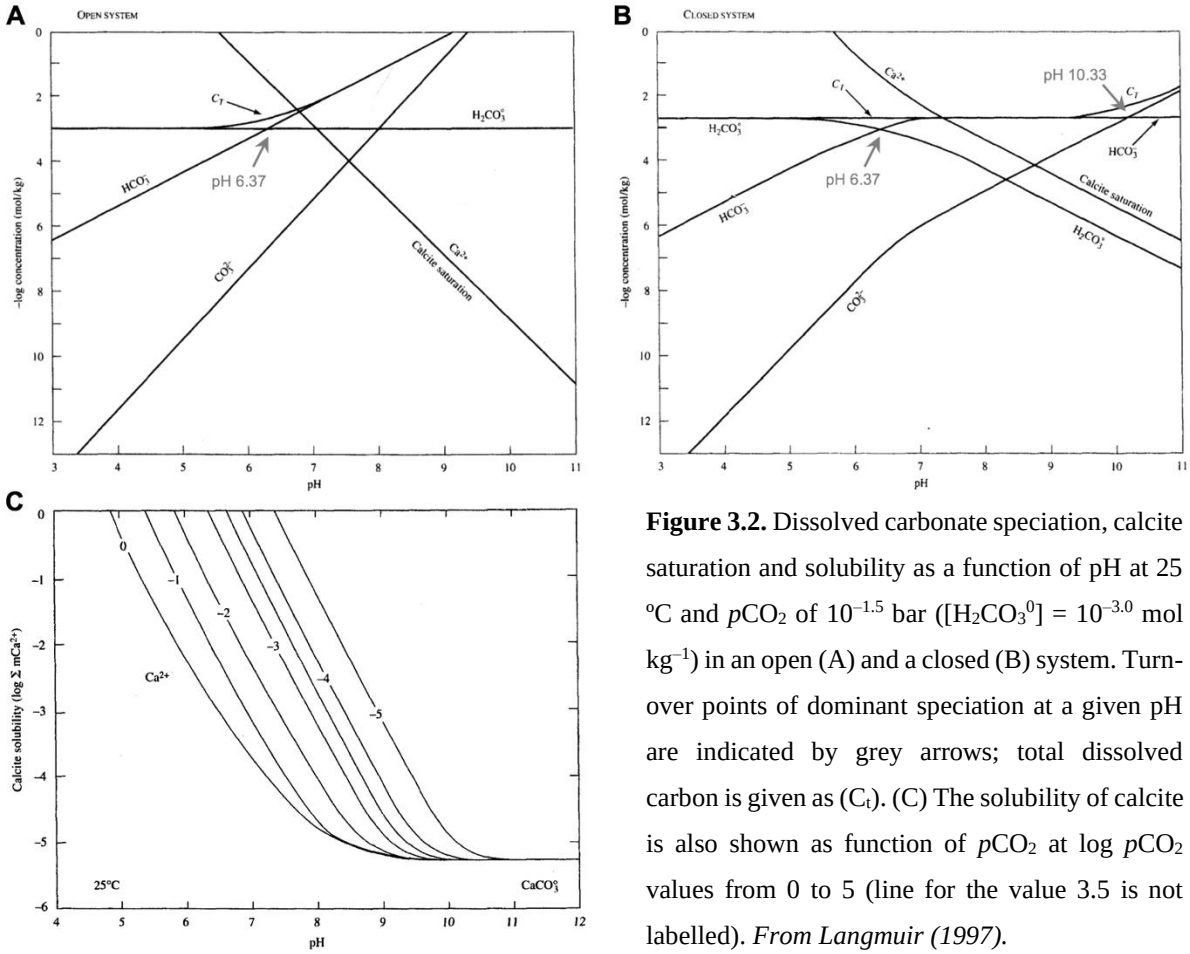

Figure 3.2. Dissolved carbonate speciation, calcite saturation and solubility as a function of pH at 25 °C and pCO_2 of $10^{-1.5}$ bar ($[H_2CO_3^0] = 10^{-3.0}$ mol kg^{-1}) in an open (A) and a closed (B) system. Turn-over points of dominant speciation at a given pH are indicated by grey arrows; total dissolved carbon is given as (C_t). (C) The solubility of calcite is also shown as function of pCO_2 at log pCO_2 values from 0 to 5 (line for the value 3.5 is not labelled). *From Langmuir (1997).*

al., 1992; Langmuir, 1997). As pH increases further, bicarbonate dissociates into carbonate (CO_3^{2-}) which becomes the dominant species at pH ≥ 10.3 and again promotes carbonate mineral dissolution under the formation of negatively charged metal–carbonate aqueous complexes such as $Me(CO_3)_2^{2-}$ (Plummer et al., 1978; Bilinski & Schindler, 1982; Bruno et al., 1992). Notably, surface complexation models suggest that at strong undersaturation with respect to the carbonate mineral at alkaline pH, the presence of HCO_3^- and CO_3^{2-} may inhibit dissolution upon carbonation of the rate-controlling surface species $>MeOH_2^+$ by the formation of less reactive $>MeHCO_3^0$ and $>MeCO_3^-$ (Pokrovsky et al., 1999; Pokrovsky & Schott, 2002; Pokrovsky et al., 2009).

The metal (Me^{II}) component of the $MeCO_3$ minerals affects their dissolution/precipitation behaviour. For example, the solubilities and dissolution rates of the redox-sensitive Mn and Fe carbonates rhodochrosite ($MnCO_3$) and siderite ($FeCO_3$) are additionally affected by the presence of oxidants such as molecular oxygen. The provoked oxidation of the reduced Mn(II) and Fe(II) structural components particularly at circumneutral to alkaline pH conditions causes precipitation of secondary Mn and Fe (oxide) phases directly on the dissolving mineral surface. Such surface precipitates complicate the assessment of dissolution rates but are thought to explain the relatively lower rates measured under oxic *vs.* anoxic conditions (Duckworth & Martin, 2004b).

Carbonate reaction rates may be further affected by the interaction with dissolved ions in aqueous solution. That is, these ions may form aqueous complexes with the dissolved carbonate species and thus alter the saturation state of the solution with respect to the carbonate mineral, or ions may adsorb to high energy reactive surface sites (steps, kinks), thereby influencing dissolution and growth rates (Terjesen et al., 1961; Reeder, 1983; Pokrovsky & Schott, 2002; Schott et al., 2009). Chemically, metals preferentially sorb to the $>CO_3H^0$ site (Van Cappellen et al., 1993). However, the structural and thus morphological properties of the different reactive surface sites also influence metal sorption and incorporation, as well as the dissolution and growth rates and mechanisms of the carbonate (MacInnis & Brantley, 1992; Paquette & Reeder, 1995; Reeder, 1996; Elzinga & Reeder, 2002; Duckworth & Martin, 2004a,b; Alexandratos et al., 2007; Pérez-Garrido et al., 2007; Tang et al., 2007). Such interactions will be detailed in the following.

3.2.2. Metal–carbonate mineral interaction in aqueous systems

Generally, the ionic size of an aqueous divalent metal cation plays a significant role in its sorption affinity and the tendency to form anhydrous solid carbonates, which require the dehydration in part or in whole of the aqueous metal cation. As hydration energy increases with decreasing ionic radius, sorption affinity – the ease of dehydration – decreases with decreasing radius of the dehydrated divalent metal ion which increases with atomic number from Mn to Cu (e.g., Kornicker et al., 1985; Davis et al., 1987; Zachara et al., 1988; Zachara et al., 1991). Thus, smaller metal ions with high hydration energies that only slowly exchange water molecules from their first hydration sphere (Mg, Co, Ni, Cu, ± *Zn*) tend to form hydrous carbonates and mononuclear inner-sphere surface complexes that maintain a higher degree of partial hydration (e.g., Reeder, 1996; Elzinga & Reeder, 2002). These metals are also more prone to desorption, i.e., sorption of the most tightly hydrated metals such as Zn, Co and Ni is easily reversed (Figure 3.3; Zachara et al., 1991). Larger metal ions of Mn, Fe, Cd, Zn, Ca, Pb, Sr and Ba with lower hydration energies, however, exchange waters from their first hydration sphere rather rapidly and tend to form stronger, dehydrated inner-sphere surface complexes and

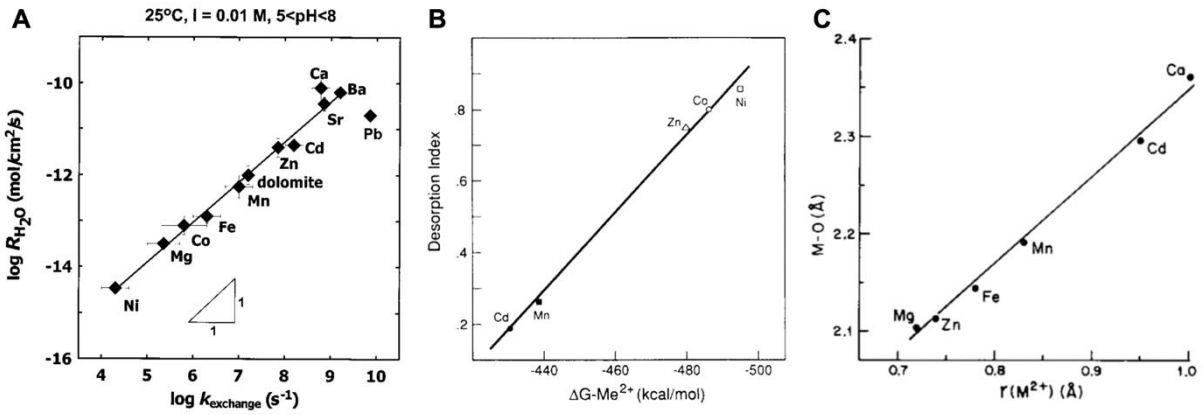

Figure 3.3. Examples of ion size effects on divalent metal–carbonates. (A) Linear relationship between the water-promoted dissolution rates at 25 ºC, constant $[CO_2] = 10^{-4}$ M, and at pH 5 to 8 as a function of the first-order rate constant $k(s^{-1})$ for water exchange between solvent and the hydration sphere of the dissolved metal. *From Pokrovsky & Schott (2002).* (B) Desorption index (< 1) as a function of the hydration energies of the respective dissolved metal cation. *From Zachara et al. (1991).* (C) Bond length of the Me–O bond in calcite–type structured anhydrous $MeCO_3$ minerals shown as a function of the ionic Me^{2+} radius in octahedral coordination. *From Reeder (1983).* Note that the different bond lengths in (C) correlate well with the dissolution behaviour of the metals that form anhydrous metal carbonates shown in (A), and that metals with higher desorption indices in (B) are those with higher hydration energies and tend to form hydrous carbonates. Zn is somewhat ambiguous as it forms both hydrous (hydrozincite) and anhydrous (smithsonite) carbonates.

individual anhydrous carbonate minerals such as otavite ($CdCO_3$), smithsonite ($ZnCO_3$), cerussite ($PbCO_3$), strontianite ($SrCO_3$) and witherite ($BaCO_3$) of decreasing solubility (e.g., Grauer, 1999; Pokrovsky & Schott, 2002; Rouff et al., 2004; Duckworth et al., 2004). The ionic radius-dependent stability of the surface species therefore affects the (initial) metal adsorption behaviour and geometry on the carbonate sorbent (Zachara et al., 1988, 1991; Reeder, 1996; Elzinga & Reeder, 2002; Elzinga et al., 2006) as well as the likelihood to form and the properties of the anhydrous solids. Over a pH range of 5 to 8, the dissolution rates of anhydrous $MeCO_3$ again correlate with the water exchange rates into the hydration sphere of the corresponding dissolved cation and thus decreases in the order of Pb ≈ Ba ≈ Ca ≥ Sr > Cd > Zn ≥ Mn > Fe > Co > Mg > Ni (Figure 3.3; Pokrovsky & Schott, 2002; Duckworth & Martin, 2004a). In fact, since even strong chemical metal adsorption is reversible (e.g., Rouff et al., 2005, 2006), the tendency to form separate solid phases decreases the risk of desorption/release. The aqueous metal concentration is then controlled by the solubility of the less soluble metal-carbonate phase, particularly by those yielding lower solubilities relative to the calcium and calcium-magnesium carbonates (Plummer & Busenberg, 1982; Grauer, 1999; Köhler et al., 2007).

Incorporation during growth or upon coprecipitation of carbonate minerals is an important removal mechanism for a wide range of divalent heavy metal cations. The calcium carbonates have been most extensively studied, reporting on the removal of metals from suspensions of circumneutral pH that are undersaturated with respect to the heavy metal carbonate. The metals thereby show element (and ionic size) dependent preferences for distinct surface sites (Paquette & Reeder, 1995; Reeder, 1996), and may form solid solutions with the host mineral surface (Stipp et al., 1992; Chada et al., 2005). Notably, charge balance constrains the calcite and aragonite structures to divalent cations as major elements (Reeder, 1983). Metals that do not form solid carbonates (e.g., Sb, Se, U, As, Cr) can form mixed (Ca,Me)-oxide precipitates upon carbonate dissolution (Renard et al., 2015; Renard et al., 2019) or, as shown for uranyl (UO_2^{2+}) and the As(V) and Cr(VI) oxyanions, can be incorporated during calcite growth (Reeder et al., 2001; Alexandratos et al., 2007; Tang et al., 2007; Renard et al., 2015). The large Ba and Pb cations were even shown to substitute for the octahedrally coordinated host Ca(II) in the calcite structure despite considerable degrees of local relaxation and distortion due to their much larger ionic radii compared to Ca (Reeder et al., 1999), which is in contrast to their otherwise 9-fold coordination in witherite and cerussite (Speer, 1983; Chevrier et al., 1992).

The ionic size of the metal cation determines the crystallographic structure in which an anhydrous $MeCO_3$ or solid solution crystallises (Reeder, 1983; Zachara et al., 1991). There are

two major crystallographic groups: the *calcite-type* and the *aragonite-type*. For metal cations with ionic radii smaller or equal to that of $^{[6]}$Ca(II) ($^{[6]}$Me(II) ≤ 1.00 Å; Shannon, 1976) including Fe, Mn, Zn, Ni, Co, and Cd, the respective carbonate mineral crystallises in the rhombohedral, *calcite-type* structure where the metal cation is octahedrally coordinated (Effenberger et al., 1981). Metal cations with ionic radii larger than $^{[6]}$Ca(II), such as Pb, Sr and Ba, crystallise in the orthorhombic, *aragonite-type* structure where the metal cation is 9-fold coordinated ($^{[6]}$Me(II) ≈ $^{[9]}$Ca(II) = 1.18 Å; Shannon, 1976; Reeder, 1983; Speer, 1983).

The **$MeCO_3$ crystal structure-type** influences dissolution-coupled metal–carbonate interactions. Particularly in low temperature environments, carbonate–water reactions in the presence of dissolved metal species are controlled by local thermodynamic equilibria at and in close proximation to the carbonate mineral surface (Renard et al., 2019). Thus, surface precipitates are generally directly coupled with simultaneous dissolution reactions of the carbonate host mineral, generally $CaCO_3$. In suspensions that are initially undersaturated with respect to the host and the metal carbonate, the dissolution of the host mineral provides Ca^{2+} and more importantly CO_3^{2-} which may induce supersaturation and thus precipitation of a secondary (Me,Ca)CO_3 or $MeCO_3$ phase (Prieto et al., 2003; Köhler et al., 2007; Renard et al., 2019). In the presence of various dissolved metals, the individual removal rates are controlled by competitive precipitation of metal carbonates of decreasing solubility (Köhler et al., 2007). The different crystallisation tendencies of the metal carbonates additionally affect the dissolution and growth rates of the substrate and also govern the overall metal uptake efficiency (Terjesen et al., 1961; Bischoff & Fyee, 1968; Salem et al., 1994; Gutjahr et al., 1996a,b; Pokrovsky & Schott, 2002; Prieto et al., 2003; Duckworth et al., 2004; Cubillas et al., 2005a,b; Di Lorenzo et al., 2020). More specifically, upon rapid metal adsorption and heterogeneous nucleation of a secondary carbonate phase, crystallisation and growth may continue in the same crystallographic orientation as the host mineral (epitaxial growth), or in an orientation independent of the host.

Epitaxial growth can occur when the underlying substrate acts as structural template for the overgrowing phase. The lower activation barrier facilitates the formation of a crystalline layer that grows in a well-defined orientation relative to the host. This *epitaxial layer* formation is promoted among isostructural phases. Such coatings tend to form vast thin films leading to passivation of the substrate surface and therefore inhibiting further interaction of the latter with the aqueous solution. Prominent examples are the interactions of Pb and Cd with the $CaCO_3$ polymorphs:

Pb–aragonite: Aragonite acts as perfect template for the isostructural Pb-carbonate cerussite. This template promoted interface-coupled nucleation, however, leads to surface passivation and consequently to reduced reaction kinetics and a decrease in the overall Pb uptake efficiency of aragonite (Godelitsas et al., 2003; Di Lorenzo et al., 2020). ***Cd–calcite:*** The same is true for the interaction of Cd with calcite, which forms perfect dislocation-free epitaxial coatings of calcite-type structured mixed $(Cd,Ca)CO_3$ or nearly pure otavite on calcite surfaces (Xu, M. et al., 2014). Thin epitaxial growth layers of < 0.01 µm already decrease the dissolution rates of calcite by two orders of magnitude; thicker layers prevent further dissolution and thus limit the amount of Cd removed from solution (Prieto et al., 2003; Cubillas et al., 2005b; Pérez-Garrido et al., 2007). The inhibiting effect of Cd on calcite dissolution has also been shown for reactions with natural limestones, suggesting limited uptake of this metal (Sdiri et al., 2012). Dissolution-induced epitaxial growth of $(Cd,Ca)CO_3$ on dolomite was found to be similarly self-limiting, indicating that this phenomenon may be generalised to other carbonate systems of the calcite-type group (e.g., Mn, Fe, Zn; Callagon et al., 2017). This is supported by another study reporting heteroepitaxial overgrow of a mixed $(Mn,Ca)CO_3$ phase on calcite despite considerable structural deviation (Xu, M. et al., 2017). However, a strong lattice mismatch as is the case between $CoCO_3$ and calcite results in non-epitaxial precipitation of a mixed Co-hydroxy-carbonate phase instead of pure $CoCO_3$ precipitates upon Cd interaction with calcite (Xu, M. et al., 2015).

In the case of **structural dissimilarity** of substrate and precipitate, the substrate does not serve as a template for nucleation. Thus, heterogeneous nucleation and growth will occur independently of the substrate structure, resulting in randomly oriented crystal growth on the substrate surface. This type of overgrowth tends to result in micron-sized crystallites and mineral replacement including considerable pore space development. Using the same prominent examples of Pb and Cd interaction with the $CaCO_3$ polymorphs:

Pb–calcite: The dissolution-induced reaction of high concentrations of Pb (0.048 to 4.8 mM) with both polymorphs results in rapid Pb consumption through the formation of cerussite and hydrocerussite surface precipitates (Godelitsas et al, 2003). However, the structurally independent dissolution–precipitation reaction between trigonal calcite and orthorhombic cerussite leads to extensive replacement (Yuan et al., 2016; Di Lorenzo et al., 2020). This is because calcite does not function as a template for cerussite precipitation which leads to randomly oriented growth of micron-sized crystallites of cerussite on the calcite surface. The development of (nano)pores during the replacement reaction provides the required permeability

for continued fluid penetration into the calcite host, progressing solvent-mediated phase transformation (Yuan et al., 2016; Di Lorenzo et al., 2020). Cerussite precipitation was further reported to promote calcite dissolution in natural limestone, emphasising that calcite is much more efficient for Pb uptake than aragonite (Sdiri et al., 2012; Di Lorenzo et al., 2020). ***Cd–aragonite****:* Similarly, the structural mismatch of mixed (Cd,Ca)CO_3 and otavite precipitates on both biogenic and abiogenic aragonite results in the formation of randomly oriented crystals of up to micrometre size and a higher consumption of total Cd compared to interaction with calcite under the same experimental conditions (Prieto et al., 2003). Again, the non-epitaxial growth of 3–10 µm thick otavite coatings on aragonite was shown to allow continuous dissolution of aragonite as the reactive fluid penetrates through pore space. Although aragonite dissolution rates were found to be decreased by about one order of magnitude, the slowing effect of the Cd coatings were much more significant for the much thinner coatings on calcite, which lowered the dissolution rates by two to three orders of magnitude (Cubillas et al., 2005b). Consequently, structural dissimilarity between substrate and expected metal-carbonate precipitate is favourable in terms of metal removal efficiency by the $CaCO_3$ polymorphs.

Overall, metal-carbonate solubility controlled (co)precipitation and incorporation into carbonate minerals upon adsorption are key processes in CO_2-containing aqueous systems with metal concentrations even below or near saturation with respect to the metal carbonates (e.g., Davis et al., 1987; Fulghum et al., 1988; Stipp et al., 1992; Reeder, 1996; Elzinga & Reeder, 2002; Rouff et al., 2004). Equally controlled by their – in contrast – very low solubility in many natural environments, the interaction of dissolved metals with the ferric iron (oxyhydr)oxides predominantly occurs via adsorption. The different tendencies of the transition and heavy metal cations to form (an)hydrous carbonates explains the co-existence of both carbonate- and iron oxide-associated metals in contaminated environments (e.g., Carroll et al., 1998; O'Day et al., 1998; Gankhurel et al., 2020).

3.3. Summary of metal uptake by iron and carbonate minerals

Key factors on metal uptake by iron and carbonate minerals are the aqueous solution chemistry including the *Eh*, pH, pCO_2, dissolved metal speciation and concentrations, sorbent to sorbate ratio, and the distance from equilibrium of solid phases (saturation state, solubility, reaction rates). The binding strength of metal sorption and likelihood of incorporation into sorbents are dependent on the ionic size and charge of the dissolved metal ion as well as on the surface properties of the sorbent.

Dissolved metal cations can be captured by adsorption, incorporation and (co)precipitation. As even strong chemisorption is readily reversible, the most sustainable form of uptake is the (co)precipitation of metals in separate solid mineral phases of lower solubility. Additional particle aggregation, phase transformation, and incorporation upon mineral growth can enhance the retention efficiency of a nanoparticulate sorbent.

Ferric iron (oxyhydr)oxides are effective sorbents for metal cations and nearly insoluble over a wide range of pH and oxic conditions. A change from oxidising to reducing conditions may lead to reductive dissolution of the ferric iron phases and the potential release of adsorbed metals. Redox-active metals may redox-interact with Fe to either induce ferric iron precipitation by simultaneous metal reduction or vice versa.

Major anhydrous calcium carbonate minerals have high affinities for (divalent) metal interaction, but their solubility is strongly affected by the aqueous pH and pCO_2 conditions. Particularly divalent metal cations (Me^{2+}) may form strong surface sorption complexes. Due to the typically lower solubilities compared to calcite and aragonite, Me^{2+} ions may also be captured by $MeCO_3$ (co)precipitation. However, changes in the pH and/or pCO_2 conditions may result in carbonate mineral dissolution and metal release. Though the corresponding increase of alkalinity may stabilise other phases that may capture the released metal ions.

3.4. Research objectives

There is simply no jack-of-all-trades when it comes to metal remediation from geochemically complex systems that may undergo redox fluctuations. From what is known about iron and carbonate minerals, the ferrous iron carbonate siderite ($FeCO_3$) may prove an excellent candidate material to capture heavy metals from aqueous systems over a wide range of geochemical conditions because it combines the advantageous properties of its two key components:

(a) the reducing capability of ferrous iron under anoxic conditions, and the high stability and sorption capacity of the ferric iron oxidation products that form under oxidising conditions (*see* sections 1.2.4.2. and 3.1.), and

(b) the reactivity of carbonate, which acts as an acidity regulator and as a source for metal-carbonate precipitation under either redox condition (*see* section 3.2.).

This leads to the **hypothesis** that **by allowing siderite to dissolve, the induced coupled metal–iron–carbonate–water interactions will effectively remove heavy metals from both oxic and anoxic acidic aqueous environments**.

To test this hypothesis, a series of dissolution–precipitation batch experiments are designed to study the siderite dissolution-controlled uptake mechanisms of two heavy metals with very different chemical properties under oxic and anoxic conditions as a function of time:

(1) Lead (Pb) is chosen as a representative for relatively redox-insensitive metals that tend to form anhydrous carbonate minerals. Lead is one of the most common and highly toxic pollutants particularly found in areas affected by mining activities, waste disposals, and landfills. Lead readily interacts with both ferric iron (oxyhydr)oxides and the calcium carbonate minerals which has been intensively studied in terms of Pb removal from aqueous solutions.

(2) Copper (Cu) is chosen to investigate the behaviour of a redox-sensitive metal which does not readily form anhydrous carbonate solids. Copper is less toxic but is often found in high concentrations accompanying Pb in areas affected by industrial discharge, mining, and landfills. Dissimilar to Pb, Cu readily redox-interacts with iron, forms hydrous carbonate phases and highly distorted Cu sorption complexes on ferric iron (oxyhydr)oxide and carbonate sorbents.

The aim is to determine the nature of the mechanisms responsible for the metal uptake by thorough investigation of the reaction products. More specifically, it is aimed to distinguish whether metal uptake is primarily achieved through adsorption, incorporation, (co)precipitation or by a combination of these, and whether iron or carbonate play a dominant role for each metal under the different study conditions. Understanding the metal uptake and bonding mechanisms is crucial to evaluate the efficacy of siderite as reagent to sustainably remove metal contaminants from polluted aqueous environments.

To identify and characterise the solid reaction products and determine the speciation of solid-associated metals including oxidation state and type of bonding, the reacted solids recovered from the siderite dissolution experiments are analysed by:

- Scanning electron microscopy coupled with an EDS device to investigate the morphology of the reacted siderite surfaces and the secondary phases formed thereon, and to qualitatively assess the presence of Pb and Cu on reacted siderite surfaces,
- High-resolution transmission electron microscopy to characterise the nano-particulate reaction products and the siderite–precipitate interface morphologically and structurally at the nanoscale;
- X-ray photoelectron spectroscopy to quantitatively assess the speciation of surface bound Pb and Cu (oxide, carbonate or other) and the oxidation state of Fe and Cu at the reacted siderite surface;
- Synchrotron-based X-ray absorption fine structure spectroscopy to identify the speciation and coordination geometry of solid-bound Pb and Cu to distinguish between various forms of sorption and (co)precipitation in a separate solid phase, and to determine redox-induced changes in Cu and Fe speciation associated with the reacted solids. The unique combination of simultaneous detection of the X-ray fluorescence signal is used to spatially resolve and ‘visualise’ the metal distribution on the reacted solids at the micron-scale.

Following a review on siderite and its dual potential as a reagent to remove metals from aqueous systems in the final part of this chapter, the experimental and analytical results of this study are presented and discussed in chapter 4 (Pb) and chapter 5 (Cu). The results of the interaction of siderite with aqueous Pb are published in Füllenbach et al. (2020), *ACS Earth and Space Chemistry*.

3.5. Siderite as reagent for metal immobilisation

3.5.1. Occurrence and geochemical properties

Siderite ($FeCO_3$) forms under moderately low temperature conditions in reducing freshwater environments that are low in sulphur and rich in Fe^{2+}, such as swamps (Postma, 1981, 1983) and peat areas (Linke & Gíslason, 2018), whereby microbial reduction of ferric iron may be important for siderite formation in recent subsurface and marine sediments (Roh et al., 2003). Diagenetic occurrences of siderite are usually related to hydrothermal activities and recrystallisation of calcite and dolomite, such as in large stratiform, massive or vein orebodies in metasomatic carbonate rocks of marine origin (Cortecci & Frizzo, 1993; Laube et al., 1995; Bouzenoune & Lécolle, 1997; Martin et al., 2017) and in skarns (Burt, 1977), or hydrothermal alteration of felsic volcanic rocks (Morton & Nebel, 1984), and replacement of carbonate sedimentary cements by reductive fluids during burial (Stel, 2009). Siderite is also an important component of Archaean and Proterozoic sedimentary successions that were deposited in the yet anoxic oceans of early Earth and during periods of the evolving oxygenation of the Earth's atmosphere (Holm, 1989; Bekker, et al., 2010; Konhauser et al., 2017; Rasmussen et al., 2021). Siderite has further been found to form from iron oxyhydroxide reduction and carbonisation by reaction with sulphide and bicarbonate under CO_2-sequestration relevant conditions (Lammers et al., 2011). Oxidative alteration of siderite results in the formation of ferric iron (oxyhydr)oxides such as ferrihydrite, goethite, hematite, and magnetite (Postma, 1983; Senaki et al., 1986; Duckworth & Martin, 2004b; Rasmussen & Muhlig, 2018).

Siderite contains octahedrally coordinated Fe^{2+} (0.78 Å; Shannon, 1976) as a major cation, thus crystallises in the rhombohedral calcite-type structure. Due to the similar ionic size, siderite often bears Mn^{2+} impurities (Graf, 1961; Effenberger et al., 1981), but was also found to host Ni^{2+} substituted for Fe^{2+}, as confirmed by XAFS on siderite from a lateritic Ni-deposit in Southern New Caledonia (Dublet et al., 2014). The solubility product K_{sp} of siderite at 25 ºC ranges between $10^{-10.8}$ and $10^{-11.0}$, which is similar to the solubilities of the anhydrous (transition) metal carbonates, but two to three orders of magnitude lower than the solubility products of calcite ($10^{-8.48}$), and aragonite ($10^{-8.34}$; Table 3.1). Siderite solubility is highest under acidic pH conditions, plateaus around circumneutral pH and increases again in the presence of high dissolved carbonate concentrations at above neutral to alkaline pH conditions (Figure 3.4A; Bruno et al., 1992).

Table 3.1. Solubility products of some anhydrous divalent metal carbonates generally determined according to the reaction $MeCO_3(s) + 2H^+ \rightleftharpoons Me^{2+} + CO_2(g) + H_2O$ at 25 ºC.

Mineral $Me^{2+}CO_3$	**logK_{sp}**	**Reference**
Calcite $CaCO_3$	–8.48	Plummer & Busenberg (1982)
Aragonite $CaCO_3$	–8.34	Plummer & Busenberg (1982)
Siderite $FeCO_3$	–10.4	Jensen et al. (2002) (wet crystals)
	–10.8	Bruno et al. (1992); Greenberg & Tomson (1992)
	–10.9	Silva et al. (2002); Bénézeth et al. (2009)
	–11.0	Braun (1991); Jensen et al. (2002) (dried crystals)
Smithsonite $ZnCO_3$	–10.8	Grauer (1999) *after* Schindler et al. (1969)
Cobaltite $CoCO_3$	–11.2	Grauer (1999) *after* Reiterer, 1980
Gaspeite $NiCO_3$	–11.2	Grauer (1999) *corrected after* Bruno et al., 1992
Rhodochrosite $MnCO_3$	–11.4	Jensen et al. (2002) (dried crystals)
	–12.5	Jensen et al. (2002) (wet crystals)
Otavite $CdCO_3$	–12.1	Stipp et al. (1993)
Cerussite $PbCO_3$	–12.1	Bilinski & Schindler (1982)
	–13.2	Grauer (1999)* *after* Bilinski & Schindler (1982)

*Corrected for $I = 0$

Generally, at far from equilibrium conditions, siderite dissolution rates exceed its much slower precipitation rates (Greenberg & Tomson, 1992; Jensen et al., 2002), which may explain why reduced aqueous environments are often supersaturated with respect to siderite (Postma, 1981). Siderite dissolves stoichiometrically and in accordance with the surface-controlled dissolution behaviour reported for other divalent metal carbonates (Pokrovsky & Schott, 2002). Siderite dissolution rates at 25 ºC rank somewhere between the more slowly dissolving carbonates of Ni, Mg, and Co that form stronger ionic structures than Fe, and the ionically less strongly bonded carbonates of Mn, Zn and Ca that dissolve more rapidly (*see* Figure 3.3A; Pokrovsky & Schott, 2002; Duckworth & Martin, 2004a). At acidic pH and far from equilibrium conditions, siderite dissolution rates (R) are proton-promoted and decrease monotonically with increasing pH from $10^{-6.4}$ (microscopic) and $10^{-9.1}$ (macroscopic) mol m^{-2} s^{-1} at pH around 1, up to $10^{-7.5}$ (microscopic) and $10^{-10.8}$ (macroscopic) mol m^{-2} s^{-1} at pH 4 (Figure 3.4B–C; Duckworth & Martin, 2004a, for microscopic rates; Golubev et al., 2009, for macroscopic rates). At circumneutral to alkaline pH 5.5 to 12, dissolution rates decrease to $10^{-8.65}$ mol m^{-2} s^{-1} and become independent of pH (Duckworth & Martin, 2004a; Pokrovsky &

Schott, 2002). Generally, increasing temperatures were found to increase the solubility and dissolution rates of siderite (Figure 3.4B; Bénézeth et al., 2009; Golubev et al., 2009). Accelerated transport of protons to the reacting siderite surface, determined by increased rotation speeds of the polycrystalline rotation disk of reacting siderite, increased dissolution rates at pH 1 to 4, whereas dissolution rates of powdered materials normalised to their surface area were found to be one to three orders of magnitude lower relative to those measured for the

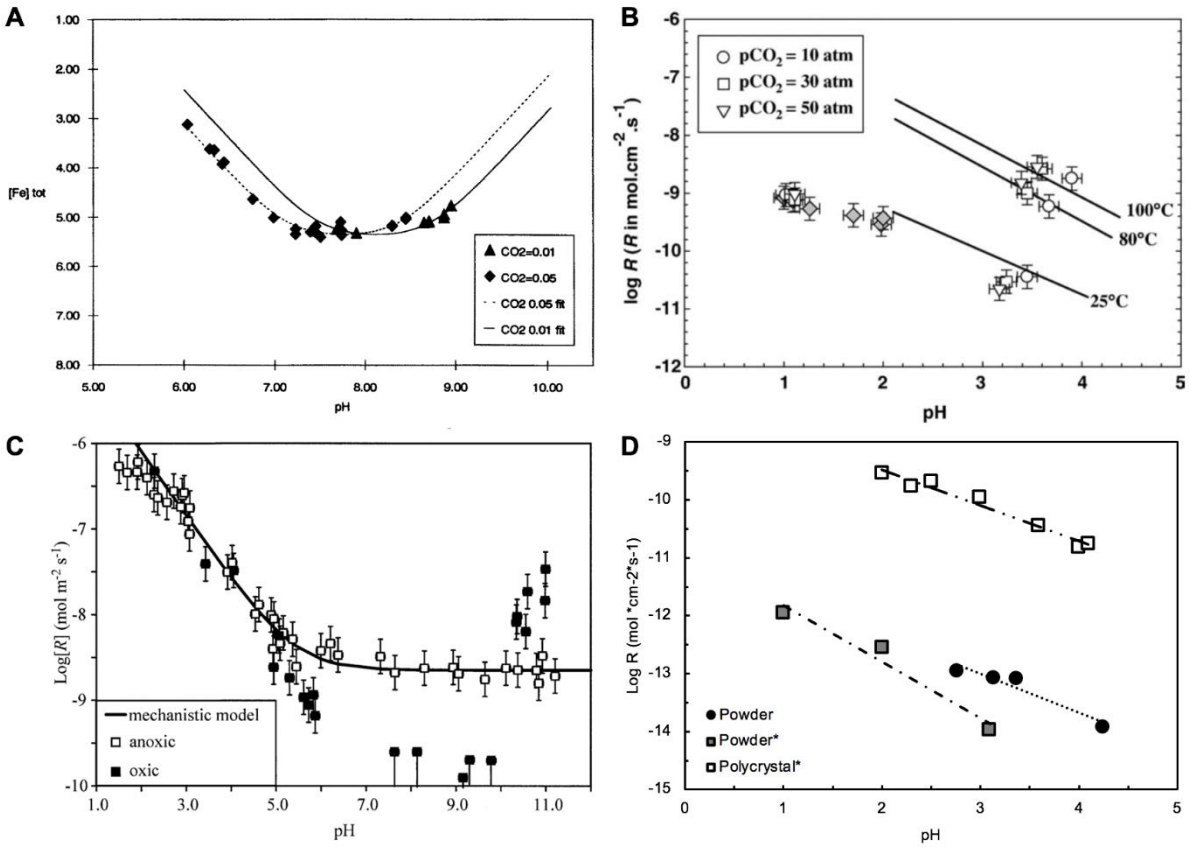

Figure 3.4. Overview of siderite solubility and dissolution kinetics as a function of pH at 25 ºC under anoxic conditions. (A) Solubility in a 1.0 M $NaClO_4$ solution at different pCO_2 pressures of 0.01 atm (triangles) and 0.05 atm (diamonds); lines represent modelled solubilities indicating possible dissolution behaviour at conditions not measured. *From Bruno et al. (1992)*. (B) Siderite dissolution rates at different temperatures and pCO_2 determined from rotation (crystal) disk experiments in a 0.1 M electrolyte solution. Grey filled diamonds represent dissolution rates obtained from pH ≤ 2, CO_2-free solutions. Note that temperature appears to have a greater influence on the kinetics than pCO_2. *From Golubev et al. (2009)*. (C) Comparison of dissolution rates under oxic (filled symbols) and anoxic (open symbols) conditions. Notably, the rates obtained under oxic conditions are much more error prone due to ferric iron precipitate formation. *From Duckworth & Martin (2004b)*. (D) Effect of surface area and properties. Despite the high surface areas of fine powders, rates obtained from a polished thin disk of a polycrystal, which likely contains numerous surface defects and intergranular boundaries, cause the much faster dissolution rates. The rotation disk method may additionally enhance dissolution by accelerated transport of protons to the siderite surface. *Squares: data from Golubev et al. (2009), indicated by an asterisk; filled circles: data from this study.*

rotation disks (Figure 3.4D; Golubev et al., 2009). Increased pCO_2 seems to only have a subsidiary inhibiting effect on the dissolution rates at pH 3.5, but no effect at lower acidic conditions where the pH effect is predominant (Figure 3.4B; Golubev et al., 2009). Although increased concentrations of dissolved (bi)carbonate species may be expected to inhibit siderite dissolution at higher pH as reported for Ca and Mg carbonates (Pokrovsky et al., 2009).

The presence of oxygen considerably affects siderite dissolution rates. At acidic pH conditions, when rates are pH-dependent and increase as a function of proton activity $a_{H^+}{}^{0.75}$ for pH < 5.5 (Figure 3.4C; Duckworth & Martin, 2004b; Golubev et el., 2009), siderite dissolution rates and reactions are identical for both oxic (R_{ox}) and anoxic (R_{anox}) conditions. At $5.5 \leq pH \leq 12$, dissolution rates under anoxic conditions stabilise at $10^{-8.65}$ mol m^{-2} s^{-1}. Under oxic conditions, however, Fe^{2+} released during dissolution oxidises in the presence of oxygen at around pH ≥ 4 (Morgan & Lahav, 2007). Resulting surface precipitation of ferrihydrite at step sites (confirmed by AFM, XPS) slows siderite dissolution rates to < 10^{-10} mol m^{-2} s^{-1} over the range of pH 6 to 10.3. Above pH 10.3, dissolution rates exceed those measured under corresponding anoxic conditions ($10^{-7.5}$ mol m^{-2} s^{-1}) which is linked to rapid electron transfer between dissolved oxygen and surface structural Fe^{2+} (Duckworth & Martin, 2004b). Pokrovsky et al. (2009) noted that no conclusion could be drawn on the effect of CO_2 on the dissolution at alkaline conditions, as the reported experimental conditions were kept CO_2-free to accurately study the effect of oxygen on siderite dissolution rates.

3.5.2. Siderite interaction with metal(loid)s

Over the past twenty years, siderite has been subject to a number of studies investigating its potential to remove dissolved metal(loid)s from contaminated waters. A compilation of the experimental conditions and results of 24 studies is given in Tables 3.2a and 3.2b.

Generally, three major aspects were considered as potential mechanisms for metal uptake upon reaction with siderite: (1) sorption, (2) sorption and metal(loid) reduction, and (3) dissolution-coupled redox reactions. Despite the greatly varying conditions used in the reviewed studies, a brief summary of their outcome in consideration of these three categories is given in the following.

(1) Simple **sorption** or **removal efficiency** was primarily investigated in studies on As uptake from circumneutral waters, such as As-spiked tap or groundwaters under oxic

conditions. In contrast to many other redox-sensitive metal(loid)s, inorganic As becomes more mobile upon reduction, thus unless otherwise feasible, As(III) oxidation to As(V) is commonly sought. Guo and co-worker (2007a,b) found that sufficient removal of both As(III) and As(V) could be achieved upon interaction with siderite and hematite coated quartz sands. The authors, however, noted that visually observed ferric oxidation products as well as the presence of Mn(IV) and Fe(III) may facilitate As(III) oxidation and therefore likely contributed to the overall uptake of As, as As(V) was found to be preferentially removed (Guo et al., 2009). Complementary As sorption studies on natural and synthetic siderite from tap water and pure aqueous solutions suggested both coprecipitation with observed ferric oxyhydroxides, and direct sorption of both As(III) and As(V) to siderite (Guo et al., 2007c, Guo et al., 2010). The oxidation of As(III) to As(V), and the uptake mechanism by coprecipitation with and adsorption to the reaction products goethite and lepidocrocite was later supported by XANES analyses (Guo et al., 2011). Similar results were found for As sorption to and oxidation by calcinated siderite (Zhao et al., 2014). Interestingly, Jönsson & Sherman (2008) similarly found higher sorption yields and coprecipitation of As(V) over As(III) on colloidal synthetic siderite upon reaction under anoxic conditions, however, reported no change in the As redox state.

(2) Many redox-sensitive metals become increasingly mobile upon oxidation. The reducing potential of the ferrous iron component in siderite has thus been an important focus of the reviewed studies. Simple **sorption-induced reduction** studies under oxic conditions suggest that U(VI) and Cr(VI) can be reduced upon reaction with siderite (Wang & Reardon, 2001; Erdem et al., 2004; Ithurbide et al., 2009, 2010), and with siderite containing mineral compounds (Hu et al., 2019). By excluding oxygen as potential oxidant, the reducing potential of synthetic siderite was demonstrated by several studies conducted under anoxic conditions. The reduction of Cr(VI) to Cr(III) was confirmed by Bibi et al. (2017), who provided XAFS spectroscopic evidence for Cr(VI) reduction coupled to colloidal siderite dissolution induced Fe(II) release and Cr(III)-Fe(III) coprecipitation. Scheinost and Charlet (2008) reported XAFS results confirming the reduction of Se(IV) to Se(-II) and precipitation of secondary Se-bearing solids of lower solubility upon interaction with microcrystalline siderite in circumneutral aqueous solutions. Similarly, Np(V) was reduced to Np(IV) at the nanoparticulate siderite surface under comparable experiment conditions but formed NpO_2 nanoparticles and Np(IV) pentacarbonate rather than surface sorption complexes (Scheinost et al., 2016). At slightly lower, near-neutral pH and anoxic conditions, Hg(II) was reduced to gaseous Hg(0) upon adsorption to high surface area siderite (Ha et al., 2017).

(3) The general observation of ferric iron (oxyhydr)oxide by-products indicates that some dissolution of siderite occurs at circumneutral pH conditions, inducing ferrous iron oxidation and reprecipitation. Only two of the here reviewed studies emphasised the effect of the **siderite dissolution-coupled redox reactions** as primary mechanism of the metal(loid) uptake. Both studies used *in situ* AFM on fresh cleavage planes of siderite crystals under oxic and a wide range of pH conditions. Tang and Martin (2011) proposed that during siderite dissolution, the released Fe(II) oxidises by Cr(IV) reduction and reprecipitates as mixed Cr(III)-Fe(III) hydroxide. Renard et al. (2017) proposed a similar mechanism for As uptake from acidic aqueous solutions, in which siderite dissolution induced the precipitation of ferric iron oxyhydroxide, namely ferrihydrite and goethite, that were identified as the predominant sorbents of As rather than siderite. Special emphasis was laid on a near-surface reaction or boundary layer, pointing out the potential passivation of the siderite surface upon continued reaction which might limit the overall reactivity and metal removal potential of siderite. In both studies, however, the authors noted that siderite dissolution rates were not considerably affected by the dissolution-coupled redox and precipitation reactions at pH < 5.5.

From these last-mentioned two studies it becomes particularly clear that there is a close link between metal uptake and siderite dissolution. However, surprisingly few studies acknowledged this link in their discussion of metal uptake mechanisms. For example, although it was not discussed in this respect, findings reported by Erdem et al. (2004) nicely illustrated the connection between Cr(VI) reduction yield and the dissolution behaviour of siderite: reduction yield increased with smaller particle size, increasing temperature, and decreasing pH, all of which enhance siderite dissolution rates. The mention of possible coprecipitation of Cr with ferric hydroxides supports this hypothesis.

Another important aspect is the siderite dissolution-induced release of carbonate and the possible effect on metal uptake. More specifically, some heavy metals tend to form strong complexes or even minerals upon reaction with dissolved carbonate, which may have an inhibiting or enhancing effect on the uptake of a metal. For example, Ithurbide et al. (2009) found that U(VI) was reduced to U(IV) upon interaction with synthetic siderite at various pH conditions. However, since uranium readily complexes with carbonate in solution, the authors proposed an inhibiting effect of increased carbonate concentrations on the sorption-coupled U(VI) reduction based on their geochemical modelling results. In contrast, Ostergren et al. (2000a) suggested an enhancing effect of carbonate on Pb(II) adsorption on goethite by metal-bridging complexation. In their experiments designed to investigate the sorption behaviour of

Pb(II) to siderite under oxic and acidic pH conditions, Erdem & Özverdi (2005) noted some neutralisation of the acidity and possible precipitation of Pb-carbonate. Clearly induced by siderite dissolution, these findings indicate the greater potential of siderite as reactant rather than a mere sorbent.

At last, surprisingly few studies provide analytical confirmation of the nature of the observed ferric (oxyhydr)oxides, therefore providing incomplete evidence for the proposed sorption mechanisms which were mostly considered to involve the Fe(II) oxidation products rather than siderite.

In this work, this gap is addressed by focusing on the reaction products, and, more specifically, on the dyadic properties of siderite: its redox potential as a source of ferrous iron, and its high reactivity as a carbonate.

Table 3.2a. Compilation of studies using siderite to remove dissolved metal(loid)s from aqueous solutions: Experimental parameters. C_0 refers to the initial metal(loid) concentrations, whereas the speciation refers to the initial form and changes of the redox state if given in the study.

Siderite		Metal			Conditions		
Type of siderite	Dosage g L^{-1}	C_0 10^{-3} mol kg^{-1}	Speciation	Evidence	Redox	$pH_{initial}$	Reference
Natural	sludge	0.013 As 0.036 Cd	As, Cd; Cr(VI) to Cr(III)	–	oxic	5.2	Wang & Reardon 2001
Compound	10	0.013	As(III), As(V)	FIAS-AAS[c]	oxic	7.3	Guo et al. 2007a
Compound	10	0.003 - 0.007	As(III), As(V)	FIAS-AAS[c]	oxic	7.3	Guo et al. 2007b
Thin film	0.325	0.025	U(VI) to U(IV)	XPS	oxic	7, 9[a]	Ithurbide et al. 2009
Calcinated	10	0.067	As(III), As(V)	XANES	oxic	2 - 10	Zhao et al. 2014
Tailing	10	0.007 - 0.13	As	–	n.d.	n.d.	Wang et al. 2018
Natural	10	0.12 - 0.965	Pb(II)	–	oxic	1.5 - 4.5	Erdem & Özverdi 2005
Natural	2	0.003 - 0.026	As(III), As(V)	FIAS-AAS[c]	oxic	7.3	Guo et al. 2007c
Compound	10	0.003 - 0.033	As(III), As(V)	GF-AAS[d]	oxic	neutral	Guo et al. 2009
Coated	1	0.16 - 1.6	Cu(II)	–	oxic	5	Danková et al. 2015
Synthetic	2	0.007 - 0.80	As(V)	–	oxic	2 - 10	Guo et al. 2010
Synthetic	1	0.026 - 0.53	As(III) to As(V)	XANES	oxic	2 - 9.6	Guo et al. 2011
Thin film	0.325	0.025	U(VI) to U(IV)	XPS	oxic	7, 9[a]	Ithurbide et al. 2010
Natural	20	0.962	Cr(VI) to Cr(III)	UV-VIS[f]	oxic	1.9 - 3.2	Erdem et al. 2004
Compound	1	0.084	U(VI) to U(IV)	XPS	oxic	3 - 9	Hu et al. 2019
Compound	20	1.53 As 0.2 Cr	As(III), As(V); (Cr)	XANES, EXAFS	oxic	7.7	Hajji et al. 2019
Synthetic	~10	0.024	As(III), As(V)	XANES, EXAFS	anoxic	6 - 10	Jönsson & Sherman 2008
Synthetic	~20	71 - 710	Se(IV) to Se(-II)	XANES, EXAFS	anoxic	8 - 8.3	Scheinost & Charlet 2008
Biogenic	0.6	0.5	U(VI) to U(IV)	XANES, EXAFS	anoxic	7.1 - 7.2	O'Loughlin et al. 2010
Synthetic	1	0.02	Np(V) to Np(IV)	XANES, EXAFS	anoxic	7 - 12	Scheinost et al. 2016
Synthetic	0.2	552[b]	Hg(II) to Hg(0)	XANES, CV-AAS[e]	anoxic	6.5 - 7.5	Ha et al. 2017
Synthetic	5	0.5 - 10	Cr(VI) to Cr(III); Fe(II) to Fe(III)	XANES; Phen.[g] (Fe)	anoxic	4 - 10	Bibi et al. 2018
Natural	crystal	1	Cr(VI) to Cr(III)	XPS; GF-AAS[d]	*an*oxic[h]	1 - 11.5	Tang & Martin 2011
Natural	crystal	0.667 - 6.67	As(III), As(V)	–	oxic	1 - 5.5	Renard et at. 2017

[a]Solution contained 6.25 x10^{-6} mol kg^{-1} CO_3^{2-}. [b]Concentration in 10^{-9} mol kg^{-1}. [c]Flow Injection Analysis System. [d]Graphite Furnace. [e]Cold Vapour Atomic Absorption Spectroscopy (AAS). [f]Ultraviolet-visible spectroscopy. [g]Phenanthroline method (colorimetric). [h]Used deoxygenated water in reaction cell.

Table 3.2b. *Continued from Table 3.2a.* Compilation of studies using siderite to remove dissolved metal(loid)s from aqueous solutions: Metal uptake mechanisms and reaction products. *Italics* indicate uncertain or poor evidence provided for the reaction products reported in these studies. Some studies do not provide a discussion on any reaction products (–), despite reported redox reactions upon interaction with siderite.

Main mechanism	Reaction products	Evidence	Reference
Removal efficacy (sorption, redox)	Goethite, otavite	XRD	Wang & Reardon 2001
Removal efficacy (sorption)	*Ferric hydroxides*	–	Guo et al. 2007
Removal efficacy (sorption)	*Ferric oxides*	*visual observation*	Guo et al. 2007
Removal efficacy (reduction)	Ferric compounds	XPS	Ihurbide et al. 2009
Removal efficacy (sorption)	Hematite (calcination product)	XRD, SEM	Zhao et al. 2014
Removal efficacy (sorption)	Ferric oxyhydroxides	XPS	Wang et al. 2018
Sorption	*$PbCO_3$*	XRD *(not shown)*	Erdem & Özverdi 2005
Sorption	Goethite and ferrihydrite coating	TEM imaging	Guo et al. 2007
Sorption	*Fe-oxide coating*	–	Guo et al. 2009
Sorption	–	–	Danková et al. 2015
Sorption kinetics	Goethite, lepidocrocite	XRD	Guo et al. 2010
Sorption kinetics	*Goethite, lepidocrocite*	*"believed to be"*	Guo et al. 2011
Sorption kinetics and reduction	Ferric compounds, $UO_{2.67}$	XPS	Ithurbide et al. 2010
Sorption and reduction	*Ferric hydroxides (pH < 2)*	*visual observation*	Erdem et al. 2004
Sorption and reduction	–	–	Hu et al. 2019
Adsorption and redox	–	–	Hajji et al. 2019
Adsorption (no redox)	*Symplesite*	XRD *(not shown)*	Jönsson & Sherman 2008
Adsorption and reduction	*Se-Magnetite*	*below detection*	Scheinost & Charlet 2008
Adsorption and reduction	U(VI) incorporation into biogenic siderite	XANES, EXAFS	O'Loughlin et al. 2010
Adsorption and reduction	$Np(IV)O_2$ nanoparticles or hydrous precursor phase	EXAFS, HRTEM	Scheinost et al. 2016
Adsorption and reduction	–	–	Ha et al. 2017
Adsorption and reduction	Ferrihydrite, goethite, lepidocrocite	XANES	Bibi et al. 2018
Dissolution-coupled redox reaction	Ferric hydroxides (pH < 5)	AFM, XPS	Tang & Martin 2011
Dissolution-coupled redox reaction	Goethite, ferrihydrite	Raman, SEM	Renard et at. 2017

4 Pb uptake coupled to siderite dissolution

The interaction of natural siderite with a redox-inactive metal is expected to show very different reaction pathways under oxidising and reducing conditions. Lead (Pb) is one of the most toxic and common anthropogenic pollutants and primarily occurs in its Pb(II) oxidation state in near-surface aqueous environments. As Pb tends to form (an)hydrous carbonates and forms strong sorption complexes on ferric iron (oxyhydr)oxides, it is investigated whether dissolved Pb can be effectively removed from both oxic and anoxic aqueous solutions upon the interaction with siderite. A particular focus is laid on the expectedly different uptake mechanisms under oxic vs. anoxic conditions that will determine the type of bonding upon this interaction and thus the retention efficacy of Pb. Therefore, the solid reaction products are thoroughly investigated using a series of high-resolution analytical techniques to assess the speciation of solid-associated Pb.

The work presented in the following chapter has been published in Füllenbach et al. (2020), *ACS Earth and Space Chemistry*. For more details, the reader is kindly referred to this publication. Contributions made by others are gratefully acknowledged and include supervisory support from Eric Oelkers (UCL), and Liane Benning (GFZ), and helpful discussions, instrument handling, technical and analytical support from Jeffrey Paulo Perez (SEM, TEM, ICP-OES, and XRD; GFZ), Helen Freeman (TEM; GFZ), Sathish Mayanna (SEM; GFZ), Andrew Thomas (EXAFS; KIT), Julia Parker (μ-XRF and μ-XANES at I14, DLS), Jörg Göttlicher and Ralph Steininger (XAFS at SUL-X, ANKA-KIT), Jörg Radnik (XPS; BAM), Ian Wood (XRD; UCL).

4.1. Introduction

Industrial and agricultural use of land and mineral resource exploitation are common sources of heavy metal contamination of soils and aqueous environments. The divalent metal lead (Pb) is among the most common pollutants, reaching toxic levels of 0.4 to 93.3 × 10^{-3} mol kg^{-1}, e.g., in floodplain soils and industrial wastewaters (e.g., Gäbler & Schneider, 2000; Wong et al., 2003; Chen et al., 2012). The speciation and binding form of Pb thereby controls its biogeochemical behaviour, and hence its mobility and bioavailability in soils, rivers, aquifers, and other aqueous systems. Efforts to remove Pb from contaminated soils and waters include phytoremediation (e.g., *summarised in* Bolan et al., 2014; Khalid et al., 2017), and chemical remediation through precipitation as scarcely soluble minerals such as pyromorphite (e.g., Ma et al., 1995; Chrysochoou et al., 2007) and chemical sorption to soil components such as clays (Strawn & Sparks, 1999), aluminium and iron (oxyhydr)oxides (e.g., Bargar et al., 1996; Strawn et al., 1998; Ostergren et al., 2000), and carbonates (e.g., Rouff et al., 2002). In carbonaceous environments, Pb may interact with and also form carbonate minerals (Bilinski & Schindler, 1982; Taylor & Lopata, 1984; Godelitsas et al., 2003; Köhler et al., 2007). Particularly in areas affected by mining, Pb immobilisation is associated with both adsorption to ferric oxyhydroxides and Pb-carbonate formation (Carroll et al., 1988; Gankhurel et al., 2020). The retention efficacy, the uptake reaction kinetics, and the potential release of Pb are critically controlled by the phase stabilities of the mineral sorbents and precipitates, which may be strongly affected by changes in pH and the redox potential of the (aqueous) system.

In this study, siderite was tested for its promising efficacy to immobilise dissolved Pb from acidic aqueous solutions. Providing both carbonate reactivity and ferrous iron for oxidative ferric iron oxide precipitation to interact with dissolved Pb, the dissolution of siderite was explored in a series of batch experiments under both oxidising and reducing conditions. A particular focus is laid on the partitioning of dissolved Pb between carbonate and the ferric (oxyhydr)oxide precipitates upon reaction with siderite under the different redox conditions. A range of high-resolution microscopic and spectroscopic analytical techniques was used to identify solid reaction products, solid-bound Pb speciation and type of bonding. The results of this study and the interpretation of the proposed uptake mechanisms are published in Füllenbach et al. (2020).

4.2. Experimental design and analytical methods

Starting material. For siderite dissolution experiments, natural polycrystalline siderite from the Peyrebrune Quarry, France (Bénézeth et al., 2009) was ground and sieved to a size fraction of < 63 µm. The cleaned material had a specific surface area of 9.95 m^2 g^{-1} determined by BET multipoint krypton adsorption (Quantachrome Autosrob-1MP; GET) and consisted of > 98% siderite with minor impurities of fluorite, quartz and traces of calcite detected by powder X-ray diffraction (XRD; PANalytical X'Pert). Bulk chemical impurities totalling < 6.4 wt.%, as detected by inductively coupled plasma optical emission spectroscopy (ICP-OES, Varian 720ES / Agilent Technologies 5110), included minor amounts of Mn, Ca, Mg, and traces of S, K, Na, Si, Cu and Cr.

Experimental design. Equivalent sets of experiments were conducted under ambient laboratory oxic and anoxic conditions. Anoxic experiments were performed in a CO_2-free anaerobic chamber (97% N_2, 3% H_2; COY Laboratory Products Inc.; GFZ). Aqueous solutions were prepared from reagent or analytical grade chemicals that were used as received from Honeywell Fluka and VWR. For Pb-bearing starting solutions, lead nitrate ($Pb(NO_3)_2$) was dissolved in ultrapure deionized water (Milli-Q, resistivity ~18 MΩ cm) to contain 0.48×10^{-3} mol kg^{-1} Pb. The initial aqueous solution pH was adjusted to 3.0 ±0.1 by adding 15 M HNO_3. The ionic strength of the solutions was adjusted with $NaNO_3$ to 2-5 × 10^{-3} mol kg^{-1}. For the preparation of the anoxic solutions, ultrapure deionised water was deoxygenated by boiling while bubbling with Ar gas for at least 4 h prior to solution preparation. All anoxic aqueous solutions were prepared, and aliquots were taken, in the anaerobic chamber.

The experiments were designed in three series to allow monitoring of the dissolution–precipitation reactions in both aqueous solution and solid samples at selected times: (1) In a series of six duplicate batch experiments, fluid aliquots were collected at six isochronous time steps, while reacted solids were collected upon termination of the experiments after 6, 12, 36, 72, 288, and 1008 h. The set of batch reactors terminated after 1008 h is referred to as the long-term (LT) experiment. High-resolution analyses were performed on the reacted solids collected from these batches. (2) In a series of fifteen duplicate batch experiments, aliquots and solid samples were collected upon termination after 0.5, 1, 2, 3, 6, 12, 20, 28, 36, 48, 72, 96, 144, and 240 h of reaction. This series of sacrificial batches is referred to as the short-term (ST) experiments. (3) Siderite dissolution control experiments (CS) in the absence of Pb were performed in duplicate following the ST experimental protocol in acidic Pb-free solutions and under otherwise identical study conditions to assess whether and how siderite dissolution was

affected by the presence of Pb. Experiment specifications are compiled in Tables A2 and A3. The reacted solids were collected through vacuum filtration using 0.2 µm mesh nylon filters.

Aqueous solution analysis. The total Fe and Pb concentrations in aqueous solution samples were determined by ICP-OES. Additional assessment of the ferrous component using the colorimetric Ferrozine method (Stookey, 1970) in a segmented flow analyser (SFA; SEAL AutoAnalyser 3HR) indicated that the Fe^{total} measured by ICP-OES analyses correspond to the Fe^{2+} concentrations detected via SFA (*see* Figure A2). Hence, Fe^{total} concentrations reported in the following are considered representative for Fe^{2+} concentrations in the reactive solutions.

Solid sample analysis. The solid reaction products were analysed in bulk powder XRD using a PANalytical X'Pert PRO MPD with monochromatic Co radiation (λ = 1.879 Å), equipped with a X'celerator detector. Field emission-SEM imaging using a ZEISS Ultra Plus Gemini (GFZ) equipped with an In-lens secondary electron and energy dispersive X-ray (EDX) spectroscopy detectors (UltraDry SDD) was used for morphological and qualitative chemical analyses of the reacted solids. For high-resolution imaging and additional qualitative chemical analysis, a FEI Tecnai G2 F20 X-Twin TEM (GFZ) was used equipped with a Schottky field emitter electron source, a Gatan Imaging Filter (Tridiem™), and a Fishione high-angle angular dark-field (HAADF) detector. High-resolution (HR) imaging was combined with fast Fourier transformation (FFT) to determine the local structure of the secondary particles and complimented by simultaneous energy dispersive area X-ray (EDAX) spectroscopic elemental analysis. The local distribution and speciation of Pb and Fe were determined by synchrotron-based combined XANES- and XRF-mapping of the Fe K- and Pb L_3-edges, performed at beamline I14 at Diamond Light Source on the reaction products collected from the oxic LT experiment. Complementary bulk XAFS analyses of the Fe K- and Pb L_3-edges on both oxic and anoxic LT experiment solid reaction products were conducted at the SUL-X beamline at the ANKA-KIT synchrotron facility to identify the local bonding environment of Pb and the oxidation state of Fe. Metal speciation was determined by both linear combination fitting of reference and sample material XANES spectra at the respective absorption edges, and by shell-by-shell fitting of the EXAFS region of the Pb L_3-edge to theoretical scattering paths calculated in FEFF6 (Newville, 2001) using the DEMETER software package (ATHENA and ARTEMIS; Ravel & Newville, 2005). Additional XPS analyses using a KRATOS Axis Ultra DLD and the UNIFIT analytical software (BAM) performed on the reacted siderite samples collected from the anoxic LT experiment provided supporting information on the surface speciation of Pb. Complementary geochemical modelling of the aqueous system was used to calculate mineral

saturation indices using the PHREEQC v.3 code (Parkhurst & Appelo, 2013) and the Lawrence Livermore National Laboratory database (2017) modified with thermodynamic data from the CarbFix database (Voigt et al., 2018). More detailed information on the respective sample preparation, instrumentation and measurement specifications, and analytical parameters are provided in the appendix, sections A.1. and A.3.

4.3. Results

4.3.1. Pb uptake coupled to siderite dissolution

Siderite dissolution commences rapidly under acidic pH conditions, resulting in an increase in the reactive fluid pH from initially 3.0 to 5.3 and 6.9 after 1008 h of reaction under oxic and anoxic conditions, respectively (Figure 4.1A–B). Under oxic conditions, the released ferrous iron oxidises and precipitates as ferric (oxyhydr)oxides as soon as the solution pH reaches ≥ 4 within the first 2 h of reaction (Figure 4.1A). In contrast, under anoxic conditions, oxidative Fe precipitation is precluded and aqueous Fe^{total} concentrations continue to increase until 168 h of reaction (Figure 4.1B), while the reactive solution reaches a pH of > 6. Thereafter, the pH and Fe concentrations changed by only ~0.6 pH units and 0.05×10^{-3} mol kg^{-1} Fe^{total} over the remaining period of 840 h of the experiment.

Under oxic and anoxic conditions, about 9 and 13% of the initial dissolved Pb concentrations are removed from the aqueous solutions within the first 2 and 0.5 h of siderite dissolution, respectively (Figure 4.1C-D). Under oxic conditions, Pb concentrations continue to decrease steadily over the remaining experimental period until 90% of the initial Pb concentrations are removed after 1008 h of reaction. Lead removal hence occurred in two stages, apparently coinciding with the oxidative precipitation behaviour of Fe in solution. Under anoxic conditions, Pb removal from the reactive solution is completed (100%) within 96-144 h of reaction and shows a near-linear relationship with increasing dissolved Fe^{total}, which peaks around the same time as Pb removal is complete.

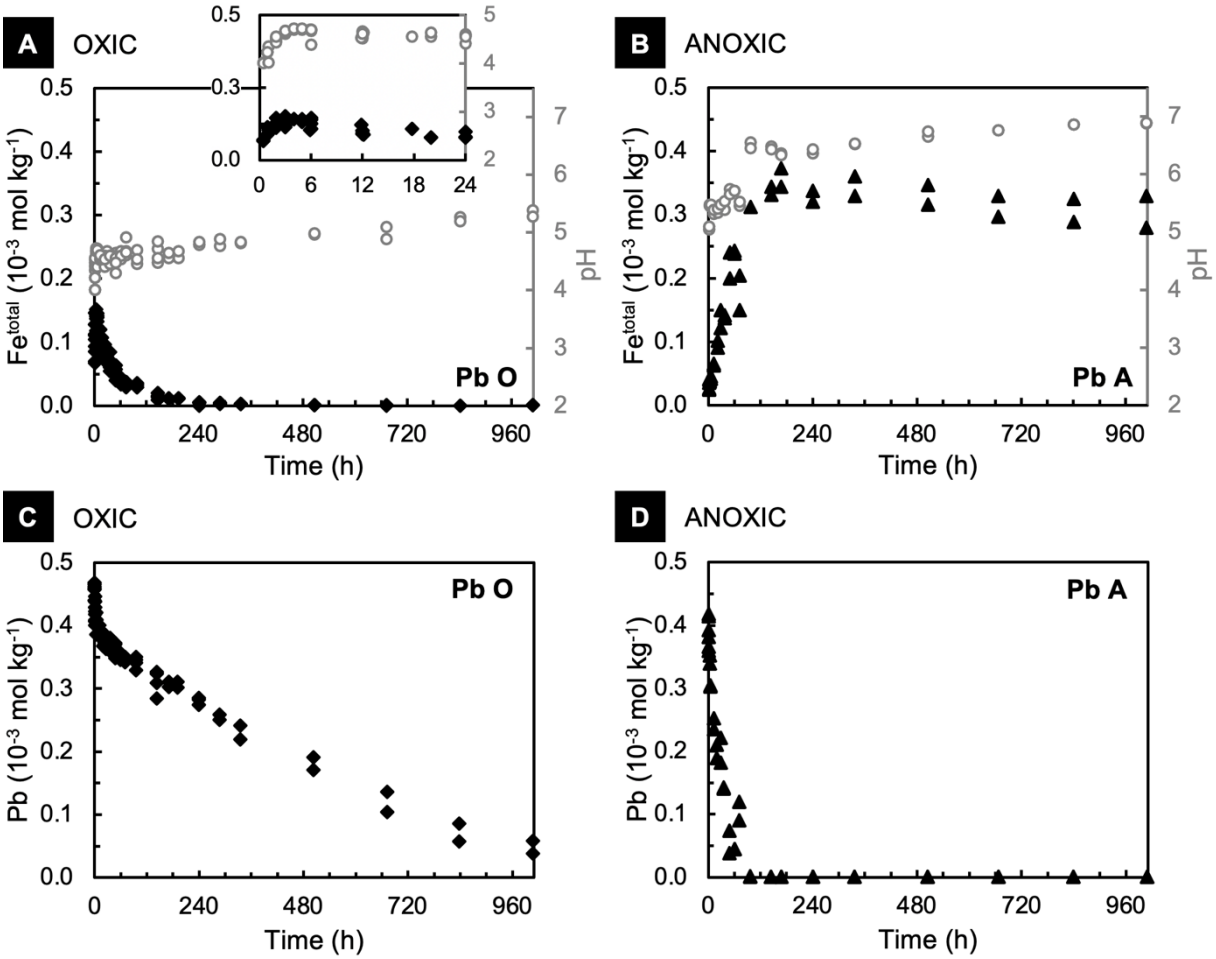

Figure 4.1. Measured total Fe and Pb concentrations (black) and reactive solution pH (grey open circles) over time during siderite interaction with Pb(II) under oxic (A and C; diamonds) and anoxic conditions (B and D; triangles). Error bars are smaller than the symbols. Standard error of the pH probe was ±0.01 units, RSD of the ICP-OES analyses was 0.29 to 1.23 %. The insert in (A) shows Fe^{total} concentrations and pH measured during the first 24 h of the oxic experiment for clarity. The plots include data from all ST and LT experiment series.

4.3.2. Characterisation of the solid reaction products

Siderite dissolution under oxic conditions in the presence of Pb leads to rapid formation of nanoscale surface precipitates within the first hours of reaction (Figure S7 in Füllenbach et al., 2020). After 1008 h of reaction, vast areas of the reacted siderite surface are covered with spherulitic and often six-radially twinned rod-shaped nanoprecipitates (Figure 4.3A–B). Bulk XRD analysis identifies goethite as the only crystalline reaction product (Figure 4.2A; Table A4). High resolution electron microscopy shows that the nanoprecipitates are clumped particles and rods growing out of the clusters via particle attachment. Both phases produce point

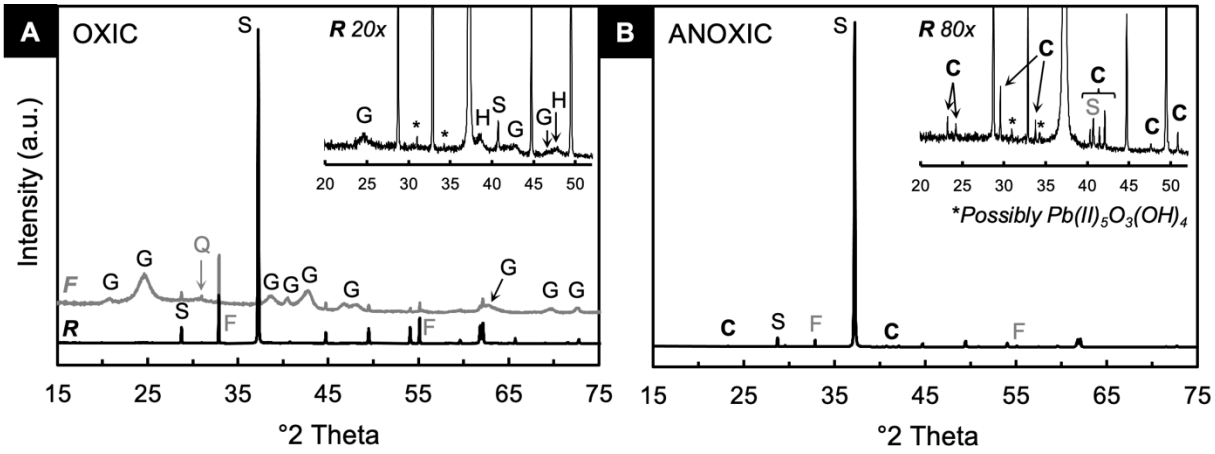

Figure 4.2. X-ray powder diffraction patterns of the reacted siderite samples collected after 1008 h of reaction with aqueous Pb(II) under oxic (A; Pb O LT) and anoxic (B; Pb A LT) conditions. The heavy precipitation under oxic conditions allowed for separate recovery of reacted siderite grains (*R* = 'residue') and ultrafine grained particles (*F* = 'fines'); the latter containing relatively higher quantities of the secondary reaction product goethite. Insets show magnifications of the diffraction patterns (*R*) to highlight the identified secondary phases. S = siderite; Q = quartz, F = fluorite, G = goethite, H = hematite, C = cerussite.

diffraction patterns with *d*-spacings of 2.26 (121) and 2.56 ±0.02 Å (021) characteristic of goethite, confirming the XRD results (Figure 4.3C–E). Some scattered crystalline precipitates show a distinct cerussite resembling morphology (Figure 4.3B; c.f., Godelitsas et al., 2003), but are, however, too scarce to be detected in bulk XRD and HRTEM analyses.

High-resolution TEM imaging of the interface between the reacted siderite surface and the surface precipitates shows that the precipitates grow in a random orientation relative to the siderite surface, resulting in interparticle nanopores (Figure 4.4A). The immediate reaction front at the siderite surface shows a widened lattice with *d*-spacings of 2.89 Å (104) towards the surface, suggesting lattice relaxation upon dissolution or possibly early-reaction stage Pb–carbonate formation. It follows an up to 20 nm wide zone of narrower (104) *d*-spacings of 2.86 Å, possibly indicating surface Fe oxidation ($^{[6]}Fe^{III}$ = 0.645 Å < $^{[6]}Fe^{II}$ = 0.78 Å; Shannon, 1976). This transition zone is followed by a different phase grown at random orientation to the siderite (104) lattice plane and with *d*-spacings of 2.58 Å, indicative of goethite (021) (Figure 4.4B).

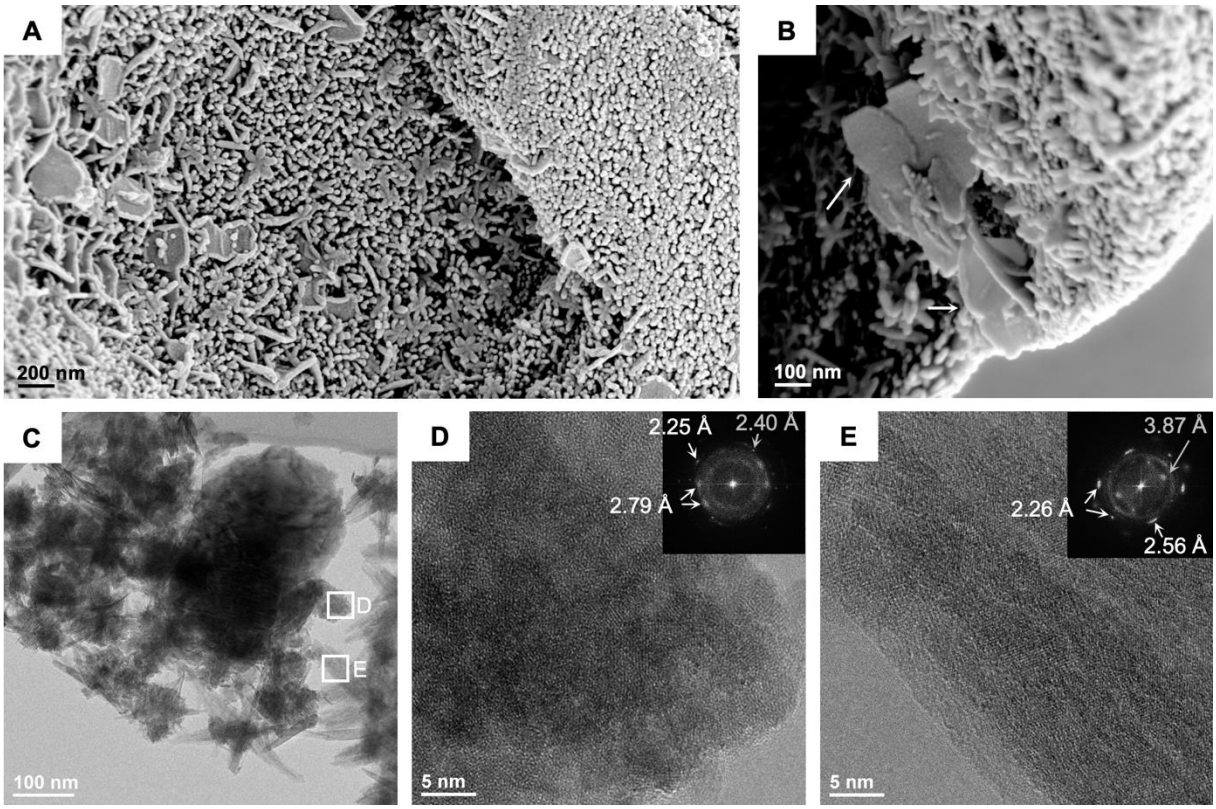

Figure 4.3. Scanning and transmission electron micrographs of siderite reaction products recovered from Pb-bearing solutions after 1008 h of reaction under oxic conditions (Pb O LT). Vast areas of reacted siderite surfaces are covered by rod-shaped and intercalated pseudo-hexagonal tabular precipitates (A–B). Ultra-fine reaction products consist of remnant, nearly completely reacted siderite fragments overgrown and replaced by nanoparticulate precipitates (C) and (D). Particles possibly grew over time via particle attachment (E). Point diffraction patterns in the inserted FFT images in (D–E) identify the nanoparticles as goethite (2.25-2.26 Å (121), 2.56 Å (021)), traces of hematite (3.87 Å (012)) and residual siderite (2.40 Å (110), 2.79 Å (104)).

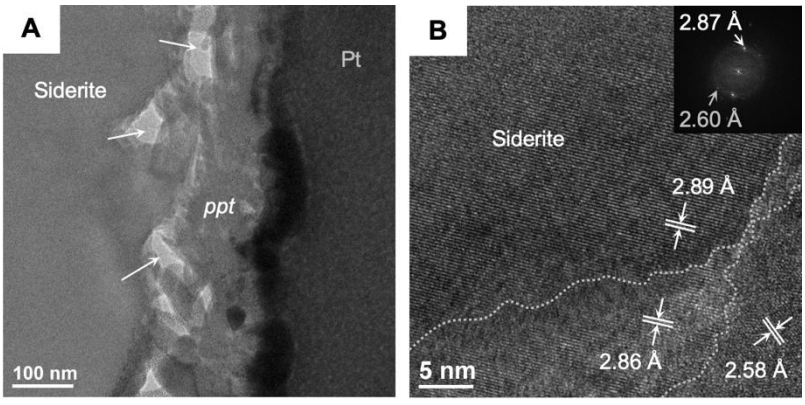

Figure 4.4. Transmission electron micrographs of siderite surface–precipitate interface of reacted siderite grains collected after 1008 h (A) and 240 h (B) of reaction in Pb-bearing solutions under oxic conditions. (A) The surface precipitates (ppt) formed at random orientation relative to the parent siderite substrate, leaving pore spaces at the interface (arrows; Pt = platinum from samples preparation). (B) The slightly narrower lattice distances in a transition zone at the reaction front (dotted lines) possibly indicate surface oxidation (replacement of Fe^{2+} by smaller Fe^{3+}). Lattice spacings of the precipitates are indicative for goethite (2.58-2.60 Å (021)).

Solids recovered from the anoxic experiment after 1008 h of reaction primarily show dissolution features and lack Fe oxidation products (Figure 4.5A). Only scarce occurrences of nano- to micro-crystallites with cerussite-like pseudo-hexagonal morphology are observed on the otherwise smooth reacted siderite surface (Figure 4.5B). Bulk XRD analysis identifies cerussite ($PbCO_3$) as the only crystalline reaction product (Figure 4.2B; Table A4). High-resolution TEM analyses of the nanoprecipitates and the reacted siderite surface reveal crystalline structures with *d*-spacings of 2.63 ±0.03 Å and 2.92 ±0.05 Å, confirming the presence of cerussite (lattice planes (102) and (012); Figure 4.5D–E). This finding is additionally supported by the detection of Pb in EDX analyses of reacted siderite grain surfaces (Figure 4.5C). Notably, distinct phase boundaries are rarely observed. However, a widening of the siderite (104) *d*-spacings from 2.83 Å within the bulk siderite crystal to 2.90 Å towards the

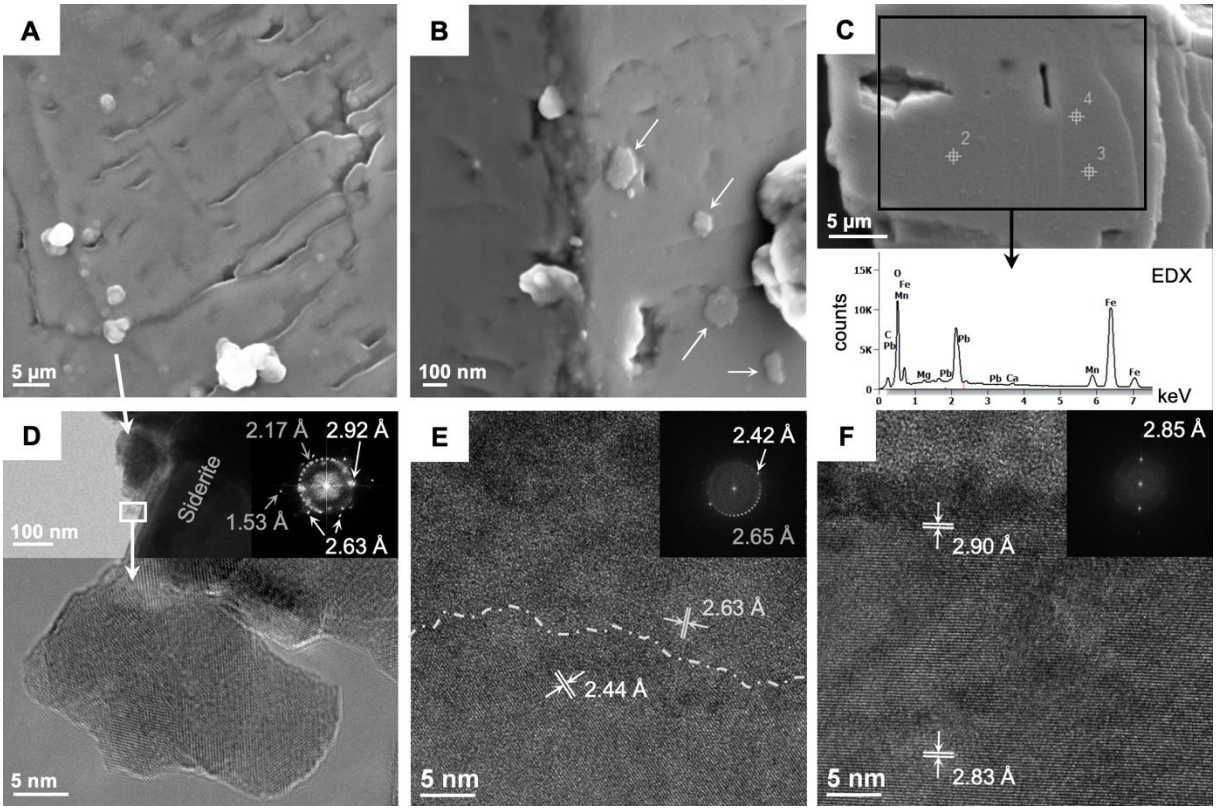

Figure 4.5. Scanning and transmission electron micrographs of reacted siderite recovered after 1008 h of reaction in Pb-bearing solutions under anoxic conditions (Pb A LT). The reacted surfaces show only few dispersed (sub)micron scale nodular and pseudo-hexagonal surface precipitates and etch-features (A–B). The clear enrichment of Pb in areas with surface precipitates (C) and point diffraction patterns (FFT, insets in D) of HRTEM images (D–E) identify the precipitates as cerussite (2.63-2.65 Å (102), 2.92 Å (012); D) attached to the reacted siderite (1.53 Å (122), 2.17 Å (113); D). Cerussite formation at a different angle relative to the reacted siderite surface (2.44 Å (110); E) suggests non-epitaxial growth, whereas widening of the siderite crystal lattice (2.83 Å (104)) towards the reacted surface (F) may result from lattice relaxation during dissolution and/or indicate some degree of replacement by cerussite (2.90 Å (012)).

reacted near-surface suggests surface relaxation due to dissolution, or, potentially, due to some incorporation of Pb into the relaxed dissolution surface structure (Figure 4.5F).

4.3.3. Pb speciation and local bonding environment

To determine the speciation and bonding environment of solid-associated Pb in the solid reaction products retrieved from the long-term experiments after 1008 h of reaction under both oxic and anoxic conditions, complementary XAFS analyses were employed.

High-resolution XRF-maps of the oxic samples indicate a mostly homogeneous distribution of Pb on the reacted siderite grains, with some grains exhibiting areas of low amounts or no Pb at the surface (Figure 4.6A–C). These low-Pb areas likely represent cleavage or fracture plains of the reacted siderite, or precipitate-free areas. Linear combination fitting (LCF) of the XANES Fe K- and Pb L_3-edge spectra obtained from the bulk sample with spectra of reference materials indicate that approximately 5% of the Fe associated with the reacted siderite grains is oxidised, while solid-associated Pb is present as Pb(II) and predominantly coordinated with oxygen and subordinately with carbonate species (Table 4.1). On a more local scale, areas of heterogeneous Pb distribution (Figure 4.6C) show a predominance of Pb-carbonate coordination (ca. 61%) associated with mostly reduced Fe (ca. 79% Fe^{2+}; compared to ~17% Fe^{2+} where the XRF signal for Pb is markedly lower), suggesting Pb is directly associated with the siderite surface. In contrast, in areas of homogeneous Pb distribution (Figure 4.6D) Pb is primarily coordinated with hydroxide groups (ca. 75%) which coincided with a high degree of Fe oxidation (ca. 85%), suggesting that Pb is in this case predominantly associated with secondary ferric precipitates. Additional shell-by-shell fitting of the Pb L_3-edge EXAFS region of the spectra collected from the bulk sample confirms Pb adsorption to the oxidised Fe precipitates (Figure 4.7; Table 4.2). Interatomic distances of $R_{Pb–O}$ = 2.31 Å to two first shell neighbouring oxygen atoms, and $R_{Pb–Fe}$ = 3.31 Å to one second shell Fe neighbouring atom are in close agreement with published distances suggesting a bidentate edge-sharing inner-sphere adsorption complex of Pb to the $Fe(O,OH)_6$ surface groups of ferric iron (oxyhydr)oxides (e.g., $R_{Pb–O} \leq 2.35$ Å and $R_{Pb–Fe}$ = 2.91 to 3.49 Å; Bargar et al., 1997b; Bargar et al., 1998; Ostergren et al., 2000a; Trivedi et al., 2003; Liu et al., 2018).

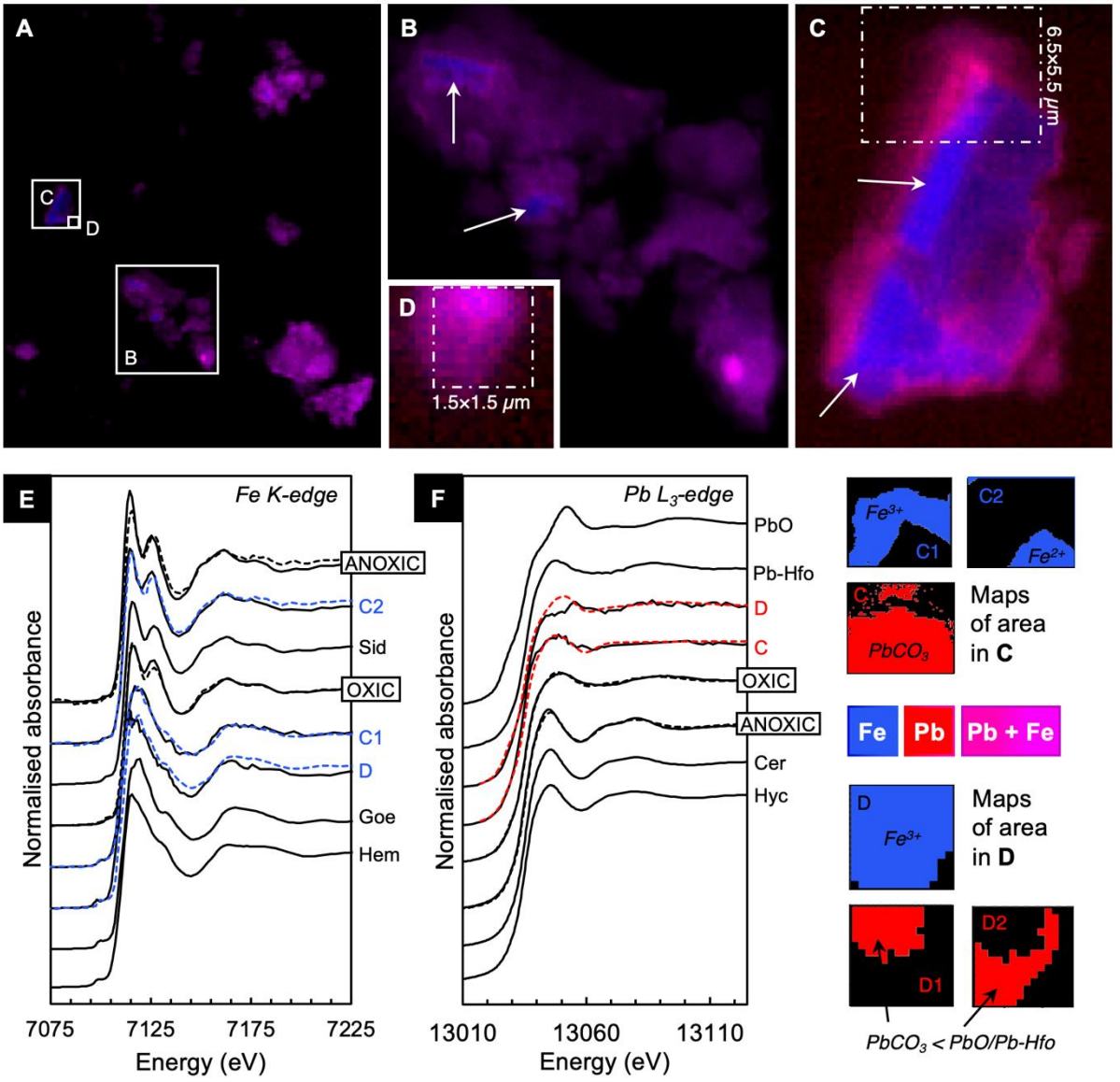

Figure 4.6. Complementary bulk and micro-mapping XANES and XRF analyses of reacted siderite grains recovered after 1008 h of interaction with Pb under oxic and anoxic conditions. High-resolution elemental Pb and Fe XRF maps of siderite grains reacted under oxic conditions (Pb O LT) show a mostly homogeneous distribution of Pb on the grain surfaces (magenta colour), with some areas of low Pb signal (A–D). Corresponding XANES Fe K- and Pb L_3-edge spectra (E–F and illustrated in blue (Fe) and red (Pb) coloured maps) collected from areas outlined by white broken-lined boxes in (C) and (D) indicate a spatial correlation between advanced Fe oxidation and relatively higher contributions of Pb-oxide coordination, whereas areas of low Pb X-ray fluorescence signal show a predominance of Pb-carbonate speciation. 'OXIC' (Pb O LT) and 'ANOXIC' (Pb A LT) indicate bulk sample analyses. Reference spectra are shown for: Sid = siderite, Goe = goethite, Hem = hematite, Pb-Hfo = Pb-adsorbed to hydrous ferric oxide, Cer = cerussite, Hyc = hydrocerussite. Dashed lines represent linear combination fits; coloured lines correspond to mapped areas in C and D (resolution 100 × 100 nm pixel). Note that the Pb distribution varies only slightly and locally; strongly blue (Fe-rich) areas likely indicate precipitate-free surfaces or fracture planes (white arrows). Image dimensions: (A) 165 × 145 µm, (B) 45 × 38 µm, (C) 18 × 13 µm, (D) 2.5 × 2.5 µm. Corresponding linear combination fit results are given in Table 4.1

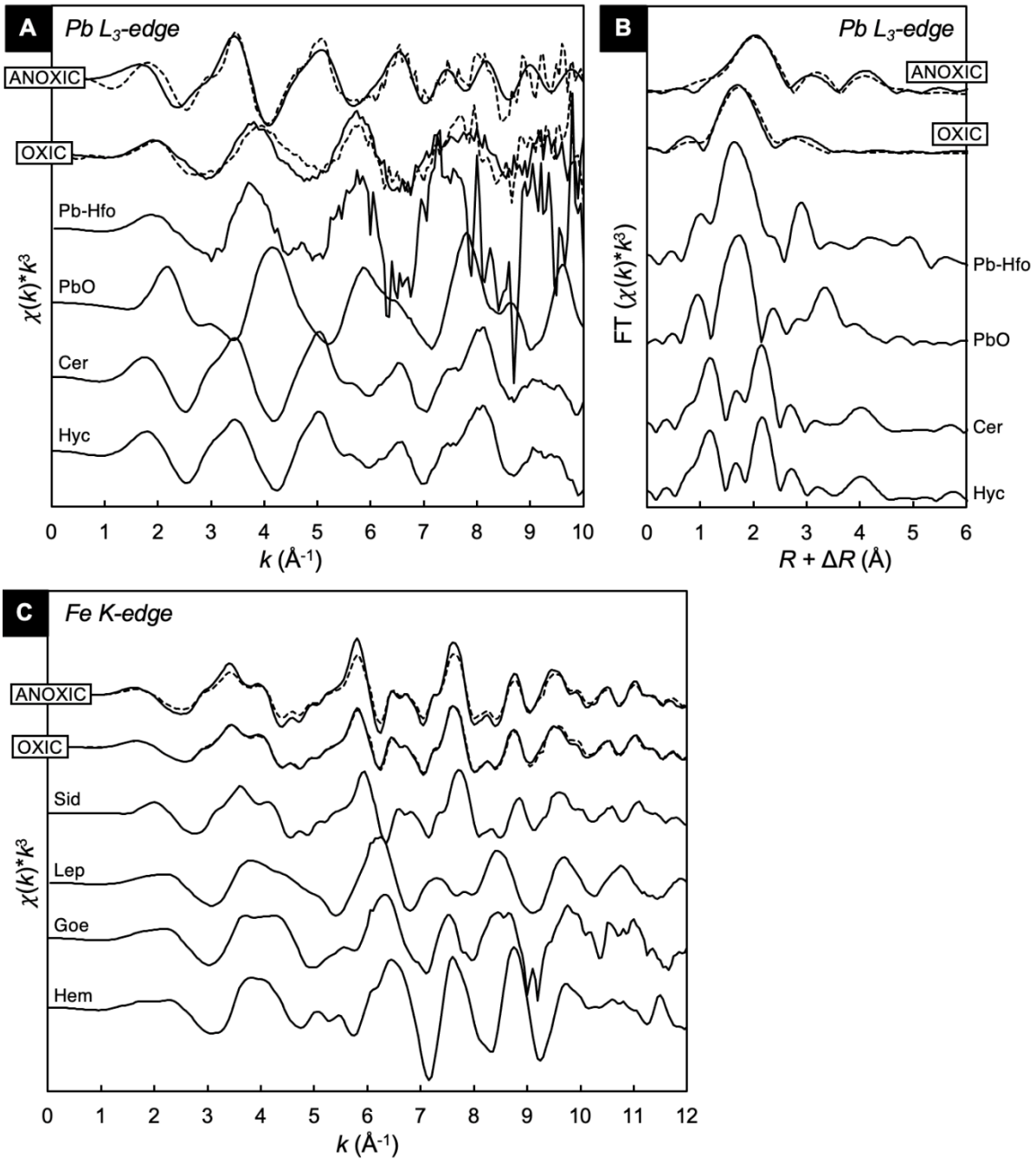

Figure 4.7. Stacked and normalised Pb L_3-edge (A–B) and Fe K-edge (C) spectra of the EXAFS region collected from the bulk reacted solid samples recovered from the oxic and anoxic experiments after 1008 h of reaction (corresponding to the bulk XANES spectra shown in Figure 4.6E–F). Dashed lines in (A) and (C) represent the linear combination fit results of the data to reference spectra also shown (*see* Table 4.1). Dashed lines in (B) represent the shell-fit results of the Fourier transformed (FT) EXAFS data (*see* Table 4.2). Reference spectra: Pb-Hfo = Pb-adsorbed to hydrous ferric oxide, Cer = cerussite, Hyc = hydrocerussite; Sid = siderite, Goe = goethite, Hem = hematite.

Linear combination fit results of the XAFS Fe K- and Pb L_3-edge spectra of the solid bulk samples collected from the anoxic long-term experiments after 1008 h of reaction confirm that

all solid-associated Pb is coordinated with carbonate, while siderite remains completely reduced with no indication of Fe oxidation (Table 4.1; Figure 4.6E–F). This finding is supported by shell-by-shell fit results of the corresponding EXAFS region of the Pb L_3-edge spectrum, indicating the characteristic 9-fold oxygen coordination of Pb in the orthorhombic cerussite structure (c.f., Chevrier et al., 1992; Table 4.2; Figure 4.7).

Table 4.1. Linear combination fit results of the k^2-weighted XANES spectra of the Fe K- and Pb L_3-edge obtained from the bulk samples and micro–XANES mapping (see Figure 4.6). Fitting range for normalised absorbance spectra was –20 to +70 eV from the absorption edge. Fitting of the k^3-weighted EXAFS spectrum over a *k*-range of 3 to 12 (Fe K-edge) and 1 to 9 (Pb L_3-edge) of the bulk samples is also listed in comparison in *italics*.

Sample	R-factor	Reduced χ^2	Standard material*		
Fe K-edge					
OXIC[a]			**$Fe^{II}CO_3$**	**$Fe^{III}_2O_3$**	
Bulk	0.003	0.0006	95.1	4.9	
	0.020	*0.105*	*89.0*	*5.7*	
Map C1[c]	0.038	0.0095	16.9	83.1	
Map C2	0.006	0.0013	79.2	20.8	
Map D	0.004	0.0007	14.9	85.1	
ANOXIC[b]					
Bulk	0.022	0.0040	100.0	–	
	0.104	*0.957*	*100.0*	–	
Pb L_3-edge					
OXIC[a]			**$PbCO_3$**	**PbO**[d]	**Pb-Hfo**[e]
Bulk	0.0003	0.0001	18.7	25.4	55.9
	0.841	0.239	34.2	65.8[f]	–
Map C	0.005	0.0008	61.4	38.6	–
Map D	0.008	0.0012	26.6	54.4	19.0
ANOXIC[b]					
Bulk	0.0008	0.0001	100.0	–	–
	0.180	*0.072*	*100.0*	–	–

The goodness-of-fit is represented by the R-factor and reduced χ^2; additional uncertainties of the fit originate from mathematical scaling and summation of the fitted spectra in Athena and range within approximately ±10%. Note that the XAFS signal represents a short-range coordination of the absorbing atom, thus alignments with reference materials indicate speciation rather than a long-range crystal structure. [a]Pb O LT and [b]Pb A LT (long-term experiments). [c]See Figure 4.6 for mapped areas and corresponding XANES spectra. [d]Massicot. [e]Hfo = hydrous ferric oxide. [f]Pb-Hfo was not included in fit.

Table 4.2. EXAFS fit parameter of the Pb L_3-edge spectra obtained from the solid reaction products collected after 1008 h of reaction under oxic and anoxic conditions. Values in *italics* were fixed during the fitting procedure.

Sample	Shell	N	R (Å)	σ^2 (Å^2)	Possible geometry
OXIC[a]	Pb–O	2.24 (0.17)	2.31 (2)	*0.01*	*– distorted trigonal pyramidal*
bulk	Pb–Fe	0.55 (0.25)	3.31 (4)	*0.01*	*– bidentate edge-sharing*
ANOXIC[b]	Pb–O	8.4 (2.91)	2.65 (4)	0.027 (6)	*cerussite*
bulk	Pb–C	*3*	3.15 (15)	0.027 (6)	*(fitted to crystal structure;*
	Pb–Pb	*6*	4.15 (6)	0.014 (4)	*Chevrier et al., 1992)*

[a]oxic = Pb O LT; [b]anoxic = Pb A LT. N = coordination number (degeneracy). R = interatomic distance (half path length). σ^2 = Debye-Waller disorder term. Fitting range in R-space was 1.2 to 4.0 Å (oxic) and 1.5 to 5.0 Å (anoxic), respectively. The energy shift ΔE_0 is -6.7 ±2.1 (oxic) and -0.05 ±3.5 eV (anoxic), respectively. The amplitude reduction factor (S_0^2) was set to 0.9 in all fits. Uncertainties are given in brackets.

In addition to XAFS, the speciation of surface bound Pb in solids recovered from the long-term anoxic experiment was examined by bulk XPS analysis (Figure 4.8; Table A5). A clear Pb $4f_{7/2}$ line detected at 138.6 eV with a Pb $4f_{5/2}$ line at +4.9 eV towards higher binding energies indicates Pb-carbonate as in $PbCO_3$ (Pederson, 1982; Feng et al., 2016), Pb-calcite (Fulghum et al., 1988), and Pb-aragonite (Godelitsas et al., 2003). Notably, shifts towards higher binding energies by +0.3 and +0.4 eV observed in the O 1s and C 1s spectra suggest a change in the (near-)surface structure from a trigonal calcite-type as in siderite to an orthorhombic aragonite-type structure as in cerussite (Godelitsas et al., 2003).

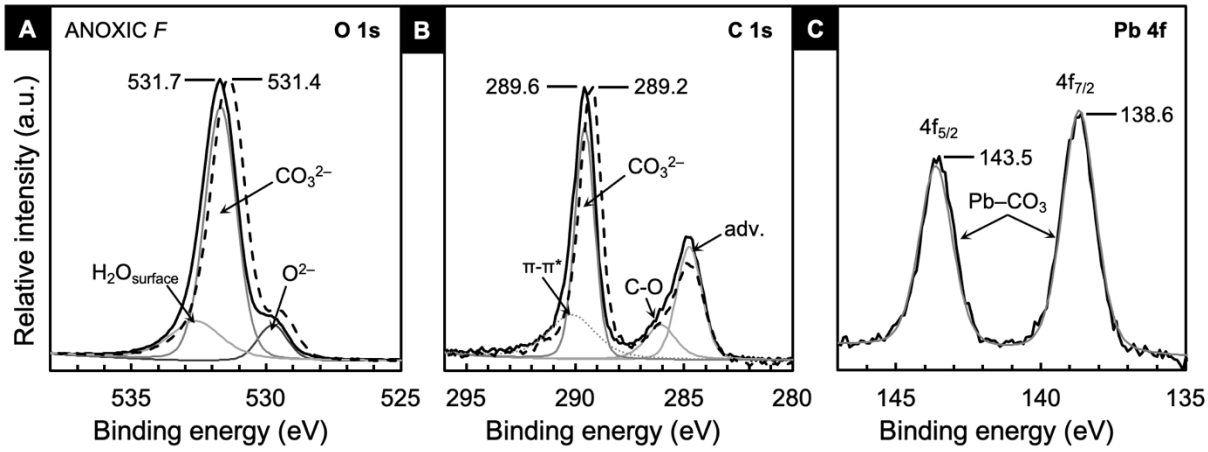

Figure 4.8. X-ray photoelectron spectra of the O 1s (A), C 1s (B) and Pb 4f (C) photoelectron lines obtained from the bulk siderite sample collected after 1008 h of reaction in Pb-bearing aqueous solution under anoxic conditions (Pb A LT; *F* = 'fines'). Solid black lines present the sample data, dashed lines show spectra obtained from the unreacted siderite sample for comparison. Grey lines show the best fit results of the spectra, indicating the intact carbonate surface with only minor contamination due to sample handling and storage (e.g., surface H_2O, ethanol (C–O), adventitious carbon (adv.); *see* Table A5).

4.4. Mechanisms of Pb removal coupled to siderite dissolution

4.4.1. Summary of Pb uptake under oxic and anoxic conditions

The dissolution of natural siderite in acidic, Pb-bearing oxic and anoxic aqueous solutions for a total of 1008 h readily commences upon immersion and increases the solution pH to ≥ 4.5 within 0.5 to 2 h of reaction under both redox conditions. Under oxic conditions, the Fe(II) component of siderite is oxidised, resulting in ferric (oxyhydr)oxide precipitation. Simultaneously, Pb gradually declines until 90% of the initially dissolved Pb concentrations are removed from the oxic solution after 1008 h of reaction. In the anoxic system, released Fe(II) remains in solution as no oxidation occurs, while Pb uptake is completed within 96–144 h of reaction. Bulk solid reaction products recovered from the experiments after 1008 h of reaction are identified as nanocrystalline goethite precipitated in the oxic system, and cerussite in the anoxic system.

The considerable difference in the rate of Pb removal and cerussite precipitation, and the strong effect of oxygen on the siderite dissolution products suggest that different mechanisms are responsible for Pb removal under the two study conditions. More specifically, the lack of separate solids containing Pb as major component suggests that adsorption likely dominates Pb uptake from the oxic system, whereas cerussite precipitation controls Pb removal from the anoxic system. Indeed, in the oxic reaction products recovered after 1008 h of reaction, solid-bound Pb is predominantly associated with the ferric (oxyhydr)oxide precipitates and to a minor extent coordinated with carbonate species at the siderite surface. Locally, however, solid-bound Pb–carbonate coordination reaches up to 61% of the scattering contributions to the XANES spectra in areas of heterogeneous coverage of the siderite surface by ferric (oxyhydr)oxide precipitates. Bulk EXAFS shell-fitting indicates a coordination geometry typical for Pb sorption to ferric (oxyhydr)oxides, while any potential Pb–C scattering paths are likely overshadowed by the stronger Pb–Fe scattering. In contrast, XANES analyses of the anoxic reaction products collected after 1008 h of reaction confirm that no Fe oxidation had occurred and all Pb is associated with carbonate. This finding is confirmed by EXAFS shell-fitting, indicating a 9-fold oxygen coordination of Pb as in cerussite. Supported by XPS results, and HRTEM and SEM imaging, cerussite most likely forms directly at the siderite surface.

These results demonstrate that siderite dissolution can be used to effectively remove Pb from acidic oxic and anoxic aqueous solutions. To predict the efficacy of Pb retention, however, understanding the mechanisms of uptake is key. Hence, a more detailed discussion addressing the uptake pathways leading to the observed results follows. Proposed reactions describing the siderite–Pb interactions under both redox conditions are given in Table 4.3.

Table 4.3. Proposed chemical reactions describing the interaction of siderite with dissolved Pb in acidic oxic and anoxic aqueous solutions leading to the observed results reported in section 4.3. Gibbs free energies (ΔG^o_r) were calculated based on the standard state Gibbs free energies of formation (ΔG^o_f) of the mineral and aqueous species included in the reactions at 25 ºC given in Tables A16–A17.

	Reaction	Remarks
	OXIC	
1	$\mathbf{FeCO_3} + 2H^+ \longrightarrow Fe^{2+} + H_2CO_3$	*Siderite dissolution*
2	$\mathbf{Pb^{2+}} + H_2CO_3 \longrightarrow \mathbf{PbCO_3} + 2H^+$	*Cerussite precipitation*
3	$Fe^{2+} + \mathbf{¼O_2} + H^+ \longrightarrow Fe^{3+} + ½H_2O$	*Homogeneous oxidation* (0.46 V)[a]
		$\Delta G^o_{r3} = –77.0$ kJ mol$^{–1}$
3’	$FeCO_3 + ¼O_2 + 3H^+ \longrightarrow Fe^{3+} + ½H_2O + H_2CO_3$	*Heterogeneous oxidation*
		$\Delta G^o_{r3'} = –110.7$ kJ mol$^{–1}$
4	$Fe^{3+} + 3\mathbf{H_2O} \longrightarrow Fe(OH)_3 + 3H^+$	*Ferrihydrite formation*[b]
5	$Fe(OH)_3 + H^+ \longrightarrow Fe(OH)_2^+ + H_2O$	*Ferrihydrite dissolution*
6	$Fe(OH)_2^+ \leftrightarrow Fe_2(OH)_4^{2+} \leftrightarrow$ polymerisation $\longrightarrow \boldsymbol{\alpha}\mathbf{\text{-}FeOOH} + H^+$	*Transformation to Goethite*
7	$\mathbf{FeCO_3 + ¼O_2 + Pb^{2+} + 1½H_2O \longrightarrow \alpha\text{-}FeOOH + PbCO_3 + 2H^+}$	$\Delta G^o_{r7} = –54.5$ kJ mol$^{–1}$
		$Eh_{r7} = 0.21$ V[c]
	ANOXIC	
	Only reactions 1 and 2 occur, leading to	*Dissolution–precipitation*
8	$\mathbf{FeCO_3 + Pb^{2+} \longrightarrow PbCO_3 + Fe^{2+}}$	$\Delta G^o_{r8} = –11.8$ kJ mol$^{–1}$

[a]Standard redox potential (E^0) of the full cell reaction. [b]2-line Fhy. [c]Redox potential of the reactions (Eh_r).

4.4.2. Siderite dissolution coupled iron (oxyhydr)oxide precipitation

As siderite dissolves under oxic conditions, ferrous iron is rapidly oxidised by oxygen (reactions 1 and 3; Table 4.3) resulting in the precipitation of ferric (oxyhydr)oxide as soon as the reactive solution reaches pH ≥ 4 within the first 2 h of reaction (reaction 4; Table 4.3; Morgan & Lahav, 2007). Nanoscale ferric precipitates formation at or near the siderite surface agrees well with findings reported in AFM studies on siderite dissolution in the presence of

molecular oxygen (Duckworth & Martin, 2004b; Renard et al., 2017). Thermodynamic considerations based on the presented analytical results suggest that the ferric iron precipitates preferentially form directly at the reacting siderite surface from heterogeneous oxidation of the (surface)structural Fe(II) component, which is thermodynamically more favourable than homogenous oxidation of aqueous Fe^{2+} by dissolved O_2 (reaction 3 vs. 3';Table 4.3). Consequently, some surface Fe oxidation likely occurs before the observed drop in aqueous Fe^{2+} concentrations indicating the precipitation of ferric (oxyhydr)oxides. Additionally, relatively narrower lattice spacings observed in HRTEM images suggest the presence of smaller Fe(III) atoms in a near-surface transition zone between the bulk siderite crystal and the surface precipitate (Figure 4.4B). This early-stage (near-surface) oxidation very likely produced metastable ferrihydrite ($Fe(OH)_3$; Duckworth & Martin, 2004b; Renard et al., 2017), which rapidly transforms into thermodynamically more stable goethite (reaction 4–6; Table 4.3). Goethite formation is indicated by a colour change of the reactive suspension from grey to ochre within 2 h of reaction and is identified as the dominant reaction product.

Neither the presence of Pb nor the vast but heterogeneous nucleation of ferric (oxyhydr)oxides markedly affect the apparent siderite dissolution process under oxic conditions as previously reported in the literature (e.g., Duckworth & Martin, 2004a,b; Renard et al., 2017). However, although previous findings of dissolution–precipitation-based formation of ferrihydrite and goethite at the dissolving siderite surface agree well with the results presented herein, there is no convincing evidence suggesting siderite surface passivation as proposed by Renard et al. (2017). Notably, surface precipitates in this study grow at a random orientation relative to the underlaying siderite lattice, and the structural dissimilarity between dissolving siderite substrate (trigonal) and goethite secondary precipitate (orthorhombic) indicates non-epitaxial growth (c.f., Kleber et al., 2010). Such structurally independent overgrowths allow continuous fluid percolation through nanopores and thence have no significant effect on the dissolution rate (Figure 4.4A; *see* section A.3.2. Figure A5, Table A6; e.g., Hudson, 2003; Cubillas et al., 2005b). Additionally, the reactive solution pH continues to increase by ~0.8 units over about 1005 h of reaction, despite the simultaneous proton-releasing Fe oxidation–precipitation–transformation reactions that continued throughout the duration of the oxic long-term experiment. Hence, the proton-consuming reaction of siderite dissolution outcompetes the proton-producing reactions, but at a slowed rate of siderite dissolution, which generally declines considerably at pH > 5.5 (Duckworth & Martin, 2004a,b; Golubev et al., 2009).

4.4.3. Siderite dissolution coupled cerussite precipitation

The formation of the Pb-carbonate cerussite ($PbCO_3$) controls the removal of Pb from the anoxic system and may also precipitate during the very early stages of siderite dissolution under oxic conditions. At acidic pH ≤ 3, regardless of the redox conditions, siderite dissolution occurs stoichiometrically, releasing Fe^{2+} and CO_3^{2-} into the aqueous solution where carbonate further reacts with protons to form H_2CO_3 (reaction 1; Table 4.3). Dissolved H_2CO_3 may also readily react with the divalent Pb(II) to form $PbCO_3$ (reaction 2; Table 4.3). Under both redox conditions, ca. 9 and 13% of the initially dissolved Pb is removed from the aqueous solutions within < 0.5 and 2 h of reaction, respectively (Figure 4.1). Notably, at this point in the reaction, oxidative Fe precipitation in the oxic system is very limited if not negligible. Thermodynamic calculations based on the measured aqueous solution compositions indicate that cerussite becomes saturated as soon as siderite dissolution commences (within < 0.5 h of reaction) – and carbonate is available near the dissolving siderite surface regardless of the redox condition (*see* Table A8). Early-stage (near-)surface precipitation of cerussite is very likely, as cerussite solubility at 25 ºC and low pH conditions is much lower ($K_{sp} = 10^{-13.2}$; Bilinski & Schindler; 1982; Grauer, 1999) than that of siderite ($K_{sp} = 10^{-10.9}$; Bénézeth et al., 2009).

Preferential partitioning of Pb into the solid phase is additionally supported by the strongly negative Gibbs free energy of the overall reaction summarising successive siderite dissolution–cerussite precipitation–oxidative goethite precipitation under oxic conditions (reaction 7; Table 4.3). Notably, such dissolution–precipitation reactions likely occur very close to the reacting siderite surface, where mineral saturation may be reached sooner than in the bulk solution (c.f., 'boundary layer'; Renard et al., 2017). This reaction sequence may in part explain the considerable scattering contributions of about 19% Pb–carbonate in the bulk and up to 60% in the high-resolution XANES spectra obtained from the solid reaction products collected from the oxic LT experiment. The near-surface saturation and precipitation is also supported by the pseudohexagonal tabular crystallites of cerussite morphology (c.f., Godelitsas et al., 2003) observed on reacted siderite grains recovered from both oxic and anoxic experiments after 1008 h of reaction (Figures 4.3A–B and 4.4B).

Before saturation of cerussite is reached near the dissolving siderite surface, some Pb likely adsorbs onto the siderite surface within the first minutes of reaction, despite the acidic solutions and regardless of the redox condition (e.g., Erdem & Özverdi, 2004). Divalent metal carbonates of the form $MeCO_3$ (Me = Ca, Mn, Fe; *see* section 1.2.3) show high sorption affinities for metals that tend to form complexes or (hydrous) minerals with carbonate, such as Zn(II) (Zachara et

al., 1988; Reeder et al., 1999; Elzinga et al., 2006), Cd(II) (Stipp & Hochella, 1991; Prieto et al., 2003), Cu(II) (Reeder et al., 1999; Elzinga & Reeder, 2002; Elzinga et al., 2006), and Pb(II) (Fulghum et al., 1988; Rouff et al., 2002; Erdem & Özverdi, 2004; Rouff et al., 2004). The coordination surface sites $>Me^+$ and $>CO_3^-$ of the $MeCO_3$ minerals promptly protonate when exposed to water. Thus, upon immersion of siderite into acidic Pb-bearing aqueous solutions, dissolved Pb ions likely compete with H^+ for the $>CO_3^-$ surface sites to form $>CO_3H^0$ and $>CO_3Pb^+$ (c.f., Van Cappellen et al., 1993; Pokrovsky & Schott, 2002). From this first sorption reaction, near-surface saturation and subsequent cerussite precipitation likely follows (possibly contributing to widening of the near-surface siderite crystal lattice; Figure 4.4B and 4.5F). Such initial adsorption thus may explain the early and rapid Pb uptake from both oxic and anoxic aqueous solutions, and the carbonate scattering contributions to the locally resolved XANES spectra collected from the oxic reaction products.

In contrast to the oxic system, cerussite formation controls Pb uptake from the anoxic system and drives siderite dissolution at pH > 5 (reaction 8; Table 4.3). Crystalline cerussite is confirmed by XRD, TEM, XPS, and XAFS analyses as the only solid reaction product after 1008 h of siderite–Pb interaction under anoxic conditions. Besides (near-surface) precipitation as cerussite crystallites, local dissolution–reprecipitation based replacement of the dissolving siderite surface by cerussite is likely. Notably, siderite is of trigonal calcite-type structure, whereas cerussite crystallises in orthorhombic, aragonite-type structure. This structural dissimilarity results in a non-isotype replacement (c.f., Prieto et al., 2003; Yuan et al., 2016; Di Lorenzo et al., 2020), characterised by a random near-surface crystal lattice orientation of the surface precipitate relative to the siderite surface and lattice widening as observed in HRTEM imaging (Figure 4.5E–F). Near-surface replacement and/or cerussite precipitation is further supported by the change in carbonate structure indicated by a shift towards higher binding energies in the O and C 1s XPS spectra (Figure 4.8). In contrast to studies reporting Pb incorporation into the octahedral metal site of trigonal $CaCO_3$ ($^{[6]}$Ca(II) = 1.0 Å; Shannon, 1976; e.g., Reeder et al., 1999; Elzinga et al., 2006), such metal exchange into the much smaller metal site in isostructural siderite is much less likely due to the large ionic size difference between $^{[6]}$Pb(II) (1.19 Å; Shannon, 1976) and $^{[6]}$Fe(II) (0.78 Å; Shannon, 1976; Effenberger et al., 1981). In addition to the microscopic indication, the 9-fold coordination of Pb as in orthorhombic cerussite as indicated by EXAFS shell-fitting rather implies solvent-mediated transformation of the carbonates than atom exchange, which would be characterised by a lower Pb coordination number and greater distortion of the coordination sphere.

4.4.4. Pb adsorption to goethite

As the siderite surface becomes increasingly covered by continuous ferric (oxyhydr)oxide precipitation and growth upon ongoing siderite dissolution–Fe(II) oxidation under oxic conditions, Pb adsorption to the ferric (oxyhydr)oxides becomes the dominant uptake mechanism. Ultimately, 90% of the initial Pb concentration is consumed by the end of the oxic experiments. Locally, advanced degrees of near-surface Fe oxidation (ca. 85% Fe^{3+} oxide) correlate with a predominantly oxygen-coordination of solid-bound Pb (ca. 54% PbO, and 19% Pb-Hfo) and minor Pb–carbonate contributions (ca. 27% $PbCO_3$; Table 4.1). Bulk sample EXAFS shell-fitting of the Pb L_3-edge indicating interatomic distances of $R_{Pb–O}$ = 2.31 Å and $R_{Pb–Fe}$ = 3.31 Å (Table 4.2) agree well with first and second shell coordination distances reported for inner-sphere bidentate edge-sharing Pb adsorption to ferric (oxyhydr)oxides (Bargar et al., 1997b; Bargar et al., 1998; Ostergren et al., 2000a; Trivedi et al., 2003; Liu et al., 2018). The LCF of locally resolved XANES Pb L_3-edge spectra suggests that Pb is both trigonally and tetragonally coordinated with first-shell oxygens in a distorted pyramidal geometry characteristic for both Pb sorption to iron (oxyhydr)oxides (Bargar et al., 1997b) and for Pb coordination in orthorhombic PbO (Hill, 1985; Bargar et al., 1997a). This additional oxygen atom in the distorted adsorption coordination sphere of solid-bound Pb may explain the slightly longer first shell Pb–O distance compared to a purely trigonal sorption geometry ($R_{Pb–O}$ ~ 2.25 to 2.28 Å; Bargar et al., 1997a; Liu et al., 2018).

A distorted trigonal oxygen coordination is also suggested by scattering contributions to the bulk sample XANES Pb L_3-edge spectra, implying a prevalence of the typical inner-sphere Pb adsorption geometry as also reflected in the low coordination number of 2.24 ±0.18 of the Pb–O shell. In contrast, the scattering contributions indicative of distorted tetragonal first-shell oxygen coordination are particularly prominent in the locally resolved XANES mapping spectra. This higher coordination potentially indicates dehydration and entrapment of sorbed Pb ions during transformation and advanced aggregational growth of the iron oxyhydroxide surface precipitates. Structural incorporation is, however, unlikely due to the absence of second-neighbour oxygen atoms and the low coordination number (Bargar et al., 1997a; Liu et al., 2018). Similarly, despite the potentially increased CO_2 concentrations near the dissolving siderite surface, there is no indication for third shell scatterings and thus for ternary carbonate adsorption (Ostergren et al., 2000a). Instead, the strong Pb-carbonate scattering contributions to all XANES Pb L_3-edge spectra support some degree of early cerussite precipitation.

4.5. Conclusions and environmental impact

Siderite effectively removes elevated concentrations of aqueous Pb from acidic solutions regardless of the redox condition. In contrast to previous studies using siderite as reductant and sorbent for potentially toxic metal(loid)s (*see* section 3.4, Table 3.2), the dissolution of siderite was specifically and successfully used as a key initial mechanism to ensure Pb immobilisation despite changing redox and pH conditions.

Upon siderite dissolution, 90 and 100% of the initial of 0.48 x 10^{-3} mol kg^{-1} Pb are effectively captured from acidic oxic and anoxic solutions within 1008 h and ~96 h of reaction, respectively. Though to different extents, three main mechanisms control the metal uptake under the two redox conditions: (1) rapid pH increase within the first 0.5 to 2 h of reaction, (2) Pb adsorption and cerussite precipitation at the siderite surface, and (3) near-surface iron oxidation leading to ferric iron (oxyhydr)oxide precipitation and Pb adsorption. While the entire reaction sequence occurs under oxic conditions, cerussite precipitation controls Pb uptake under anoxic conditions. Importantly, heterogeneous (non-isotype) cerussite and goethite precipitation thereby prevent passivation of the reacting siderite surface, allowing the crucial dissolution of siderite to continue throughout the 1008 h of experiment duration under both redox conditions.

Environmental implications. In nature, metal contaminated environments may undergo fluctuations in redox conditions, potentially causing metal mobilisation through desorption and/or dissolution of their mineral sink (Calmano et al., 1993; Pedersen et al., 2006). However, the dissolution of siderite is favourable to promote Pb uptake under either redox condition. Generally, siderite dissolution lowers acidity, thus allowing for stabilisation of secondary solid phases. The partitioning of aqueous Pb from acidic solutions into cerussite is thereby most favourable, as this mineral is sparingly soluble over a wide pH-range (Bilinski & Schindler, 1982; Taylor & Lopata, 1984) and is rarely affected by the presence of reductants or oxidants. Oxidising conditions provoke oxidative siderite dissolution and nanoparticulate ferric (oxyhydr)oxide precipitation, which are nearly insoluble sorbents under the experimental study and comparable natural conditions (c.f., solubility products K_{sp} of the iron oxides at 25 ºC range from $10^{-37.7}$ to $10^{-42.75}$; *see* section 1.2.4, Figure 1.12; Cornell & Schwertmann, 2003). Notably, these phases remain stable for the entire experiment duration of up to 6 weeks, while no Pb is released during ferric (hydr)oxide transformation into goethite.

The observed processes coupled to siderite dissolution under both redox conditions are complementary with respect to Pb retention in environments prone to potential redox fluctuations. In oxic environments, the strong bonding within specific Pb adsorption to ferric (oxyhydr)oxide nanoprecipitates may be additionally promoted by entrapment during nanoparticle aggregation or incorporation during advanced crystal growth over time (c.f., Gilbert et al., 2009; Stegemeier et al., 2015). Although ferric (oxyhydr)oxides are nearly insoluble in most natural oxygenated environments, reductive dissolution may occur in strongly reducing environments and in the presence of unoxidised aqueous Fe^{2+} (e.g., Wehrli et al., 1989; Zinder et al., 1996; Pedersen et al., 2005; Frierdich & Catalano, 2012). Reductive dissolution may lead to desorption and remobilisation of adsorbed and/or incorporated Pb (e.g., Strawn et al., 1998; Pedersen et al., 2006; Frierdich & Catalano, 2012a). However, under reducing acidic, and above neutral pH at increased pCO_2 conditions, siderite dissolution is enhanced and Pb readily precipitates as sparingly soluble cerussite or hydrocerussite (Bilinski & Schindler, 1982; Taylor & Lopata, 1984; Bruno et al., 1992). Generally, moderate conditions that provoke siderite dissolution also promote one form or another of Pb removal from solution. This versatility of metal removal pathways implies that siderite dissolution may be a promising effective remediation method of Pb-contaminated aqueous systems under oxic and anoxic, and/or potentially fluctuating redox condition.

5 Cu uptake coupled to siderite dissolution

The interaction of natural siderite with a dissolved redox-active metal is expected to lead to some form of redox-interaction between the ferrous iron component in siderite and the redox-active metal regardless of the environmental redox condition. Copper is a redox-active metal and micronutrient which becomes toxic at the often very high concentrations found in anthropogenically polluted sites. The redox interaction and uptake mechanisms of dissolved Cu(II) coupled to siderite dissolution are explored. The type of bonding upon this interaction determines the retention efficacy of Cu. A particular focus is hence laid on the solid reaction products and the speciation of solid-associated Cu, which are thoroughly investigated using a series of high-resolution analytical techniques.

The work presented in the following chapter is aimed to be published in *Geochimica et Cosmochimica Acta*. Supervisory support by Eric Oelkers (UCL) and Liane Benning (GFZ) are gratefully acknowledged, as well as the helpful discussions, instrument handling and technical support by Ian Wood (XRD; UCL), Jeffrey Paulo Perez (SEM, TEM, ICP-OES and XRD; GFZ), Helen Freeman (TEM; GFZ), Sathish Mayanna (SEM; GFZ), Andrew Thomas (EXAFS; KIT), Julia Parker (μ-XRF and μ-XANES at I14, DLS), Jörg Göttlicher and Ralph Steininger (XAFS at SUL-X, ANKA-KIT), and Jörg Radnik (XPS; BAM).

5.1. Introduction

Copper (Cu) is one of the most widely occurring heavy metal contaminants (Irwin, 1997). It is found in high dosages of 0.43 up to 14.7 × mol kg^{-1} in soils and sediments in and around mining districts (e.g., Gäbler & Schneider, 2000; Pan & Li, 2016), in areas affected by landfill leakage, industrial and agricultural use of land (e.g., Li et al., 2009; Sun et al., 2013). The fate and mobility of Cu in soils and sediments is particularly determined by pH, the redox-potential, and the organic matter concentrations (Irwin, 1997). However, most remediation efforts of Cu(II) contaminated soils are based on adsorption, precipitation of Cu-bearing carbonates and oxyhydroxides, and phytoremediation (e.g., Kumpiene et al., 2008; Bolan et al., 2014), disregarding its redox-activity. This property, however, is important as Cu forms strong redox couples with iron and sulphur in natural environments (e.g., the primary Cu ores are chalcopyrite ($CuFeS_2$) and chalcocite (Cu_2S); Garrels, 1954; Cornwall, 1956; Stumm & Lee, 1961; Irwin, 1997; Matocha et al., 2005).

The stability of solid-bound Cu(II) is thus strongly affected by the phase stabilities of iron oxide and sulphur minerals (e.g., Aquino et al., 2020), which are common acid-producers upon oxidation (Nordstrom, 2011a; Dold, 2016). If liberated into surface and/or groundwaters, however, dissolved Cu speciation is controlled by complexation with hydroxyl and carbonate ions (Flemming & Trevors, 1989) or with organic molecules (Irwin, 1997). Trace amounts of dissolved Cu(II) may adsorb to or incorporate into iron (oxyhydr)oxides such as goethite and ferrihydrite over a wide range of pH ≥ 4 (e.g., Manceau et al., 2000; Peacock & Sherman, 2004; Gilbert et al., 2009; Moon & Peacock, 2012). Thermodynamically, under oxic and low pCO_2, conditions, Cu remains dissolved as Cu^{2+} ions at pH < 3. As the pH increases to circumneutral, Cu may form cupric (Cu(II)) oxide, and Cu(II) hydroxides may precipitate as the pH becomes alkaline. At additionally high pCO_2, Cu(II) may precipitate as hydrous copper carbonate (malachite or azurite; Kiseleva et al., 1992). Under reducing conditions, Cu may precipitate as cuprous (Cu(I)) oxide at pH ≤ 4.5 or native copper (Cu(0)) at any pH and strongly reducing conditions (Puigdomenech & Taxén, 2000).

Siderite was used as a source of the reductant Fe(II) and carbonate to test whether the inorganic redox interaction between Cu(II) and Fe(II) as well as the potential complexation of Cu with carbonate would effectively remove dissolved Cu(II) from initially acidic oxic and anoxic aqueous solutions. Particular focus lays on Cu speciation and the partitioning between ferric iron and carbonate reaction products upon reaction with siderite. Additional focus lays on the redox couples in the system. The controlling electron donors and acceptors and their

effect on the stability of Fe reaction products are expected to strongly affect the stability of solid-bound Cu species and thus the efficacy of siderite as environmental remediation reagent.

5.2. Experimental design and analytical methods

Starting material. For the siderite dissolution experiments in the presence of Cu(II), the same natural polycrystalline siderite of high purity (> 98% siderite) from the Peyrebrune Quarry, France (Bénézeth et al., 2009) was used as described in chapter 4.2. The macrocrystalline siderite material was ground and sieved to a size fraction of < 63 µm in several batches, thus the relative quantities of quartz, calcite and fluorite impurities determined by bulk XRD analyses (*see* Table A1) may vary among the batches.

Experimental design. Siderite dissolution experiments were conducted under ambient oxidising (oxic) and reducing (anoxic) conditions. All experiments were performed at room temperature in duplicate batch reactors under continuous mixing on a rotary mixer. The anoxic experiments were conducted in a CO_2-free anaerobic chamber (97% N_2, 3% H_2; COY Laboratory Products Inc.). For all aqueous solutions reagent or analytical grade chemicals from Honeywell Fluka and VWR were used as received. For the Cu(II)-bearing aqueous starting solutions, copper nitrate trihydrate ($Cu(NO_3)_2 \bullet 3H_2O$) was dissolved in ultrapure deionised water (Milli-Q; ~18 MΩ cm resistivity) to initial concentrations of $1.54 \pm 0.02 \times 10^{-3}$ mol kg^{-1} before ionic strength adjustment with 0.1 M $NaNO_3$. The initial solution pH was adjusted to 3.04 ±0.02, resulting in a total ionic strength of 2-5 $\times 10^{-3}$ mol kg^{-1}. For the anoxic experiments, aqueous solutions were prepared in the anaerobic chamber using deoxygenated deionised water that was boiled while sparged with argon gas for at least 4 h.

For each experiment, 6 g L^{-1} siderite was reacted with the acidic Cu(II)-bearing oxic and anoxic aqueous solutions. Corresponding experiments were performed in three series to allow monitoring of the reactive solution and collecting solid samples at various stages of the reaction: (1) In a series of four batch experiments, solution aliquots were taken at six isochronous time intervals and experiments were ended after 6, 36, 286, and 1008 h of reaction. High-resolution solid analyses were performed on solids collected from the batches terminated after 1008 h and are referred to as the long-term (LT) experiment. (2) In a series of fifteen sacrificial short-term (ST) batch experiments, fluid aliquots and solid samples were collected upon termination after 0.5, 1, 2, 3, 6, 12, 20, 28, 36, 48, 60, 72, 96, 144, and 240 h of reaction. (3) A series of control

experiments of siderite dissolution (CS) in Cu(II)-free oxic and anoxic aqueous solutions was conducted following the short-term (ST) experimental protocol.

Aqueous solution aliquots were collected through 0.2 µm polyethersulfone syringe filters, acidified and diluted for analysis with 0.3 M HNO_3. Upon termination of the LT experiments two roughly different size fractions of reaction products were recovered from the reacted suspensions by vacuum filtration through 0.2 µm filters (nylon/polycarbonate membrane). The fraction predominantly containing the reacted siderite grains with surface precipitates are referred to as *residue* (*R*; < 63 µm), while the clumped ultrafine particles that formed from very fine-grained siderite fragments or possibly in solution are referred to as *ultrafine* fraction (*F*; ≲ 10-20 µm). Experimental parameters are compiled in Tables A2 and A9. More details on the sampling procedure can be found in section A.1.

Siderite dissolution experiments in the absence and presence of Cu(II) were run in parallel using the same experimental design and type of equipment. Respective aqueous solution and solid analyses were performed on the same analytical instruments and following the same sample preparation and analytical procedures. For instrument specifications, please *see* section 4.2; for sample preparation and analytical specifications *see* A.1. and A.4.

Aqueous solution analysis. The concentrations of total dissolved Fe and Cu were determined by ICP-OES. The assessment of Fe(II) via the colorimetric Ferrozine method (Stookey, 1970) was inhibited because of the similar reactivity of Fe(II) and Cu(II). Both metals form indistinguishable complexes with the Ferrozine compound, causing strong interferences. However, based on previous Fe speciation analyses using the Ferrozine method in a SFA apparatus on samples collected from the siderite dissolution experiments in the presence of Pb (*see* chapter 4.2; Figure A2), the Fe^{total} measured by ICP-OES can be considered a close approximation for aqueous Fe^{2+} concentrations.

Solid sample analysis. The solid reaction products collected from both oxic and anoxic experiments were first characterised in bulk by powder XRD. Morphological dissolution features and precipitates on the reacted solids were examined using a FE-SEM equipped with an EDX detector, which was used for additional qualitative local chemical analyses. For morphology and local structure analysis of the secondary phases, high-resolution TEM and corresponding FFT imaging was used. Synchrotron-based high-resolution XRF-mapping combined with XANES-mapping of the Fe and Cu K-edges was applied to determine the local distribution and speciation of solid-associated Fe and Cu. Complementary bulk XAFS analyses

of the Fe and Cu K-edges were conducted to determine the chemical states and speciation by linear combination fitting of reference with sample XANES spectra. The local bonding environment of Cu was assessed by shell-by-shell fitting of the EXAFS region of the Cu K-edge to theoretical scattering paths calculated in FEFF6 (Newville, 2001). The XAFS spectra were analysed using the DEMETER software package (ATHENA and ARTEMIS; Ravel & Newville, 2005). Copper speciation on the reacted siderite surface was determined by bulk XPS analyses. To distinguish between the chemical state of detected Cu species, the Cu LMM Auger kinetic energy and the modified Auger parameter were determined in addition to the characteristic XPS binding energy peak positions (*see* section A.4.). Additional geochemical modelling was performed to calculate metal speciation and mineral saturation indices using the PHREEQC v.3 code (Parkhurst & Appelo, 2013) and the Lawrence Livermore National Library database (2017) modified with thermodynamic data taken from the CarbFix (Voigt et al., 2018) and the MINTEQ.v4 databases.

5.3. Results

5.3.1. Cu uptake coupled to siderite dissolution

Siderite dissolution commences immediately upon siderite powder immersion into the Cu(II)-bearing acidic aqueous solutions. Under both oxic and anoxic conditions, the reactive solution pH thereupon increases rapidly from initially 3.04 to 4.6 and 5.1 within 0.5 h of the onset of siderite dissolution and stabilises around pH 4.6 and 5.6 ±0.1 over the remaining duration of the experiments, respectively (Figure 5.1A–B). Notably, the dissolved metal concentrations behave differently between the two study conditions. Within 0.5 h of reaction under oxic conditions, Fe concentrations released into the solution start to decline as soon as the solution pH reaches to > 4.5 (Figure 5.1A). Dissolved Cu concentrations decline nearly linearly until 80% of the initial concentration is removed from solution by the end of the experiment (Figure 5.1C). Under anoxic conditions in contrast, dissolved Fe concentrations remain low within the first 0 to ~60-96 h of reaction (Figure 5.1B). These low Fe concentrations coincide with an initially rapid decline in the aqueous Cu concentrations within the first 3 to 60-96 h of the reaction. Thereafter, Fe and Cu behave inversely congruently. That is, as the remaining concentrations of 1.2×10^{-3} mol kg^{-1} aqueous Cu decrease nearly linearly until Cu is consumed after 505 h of reaction (Figure 5.1D), dissolved Fe concentrations simultaneously increase, peaking at 1.2×10^{-3} mol kg^{-1} by 505 h of reaction. This apparent proportionality of

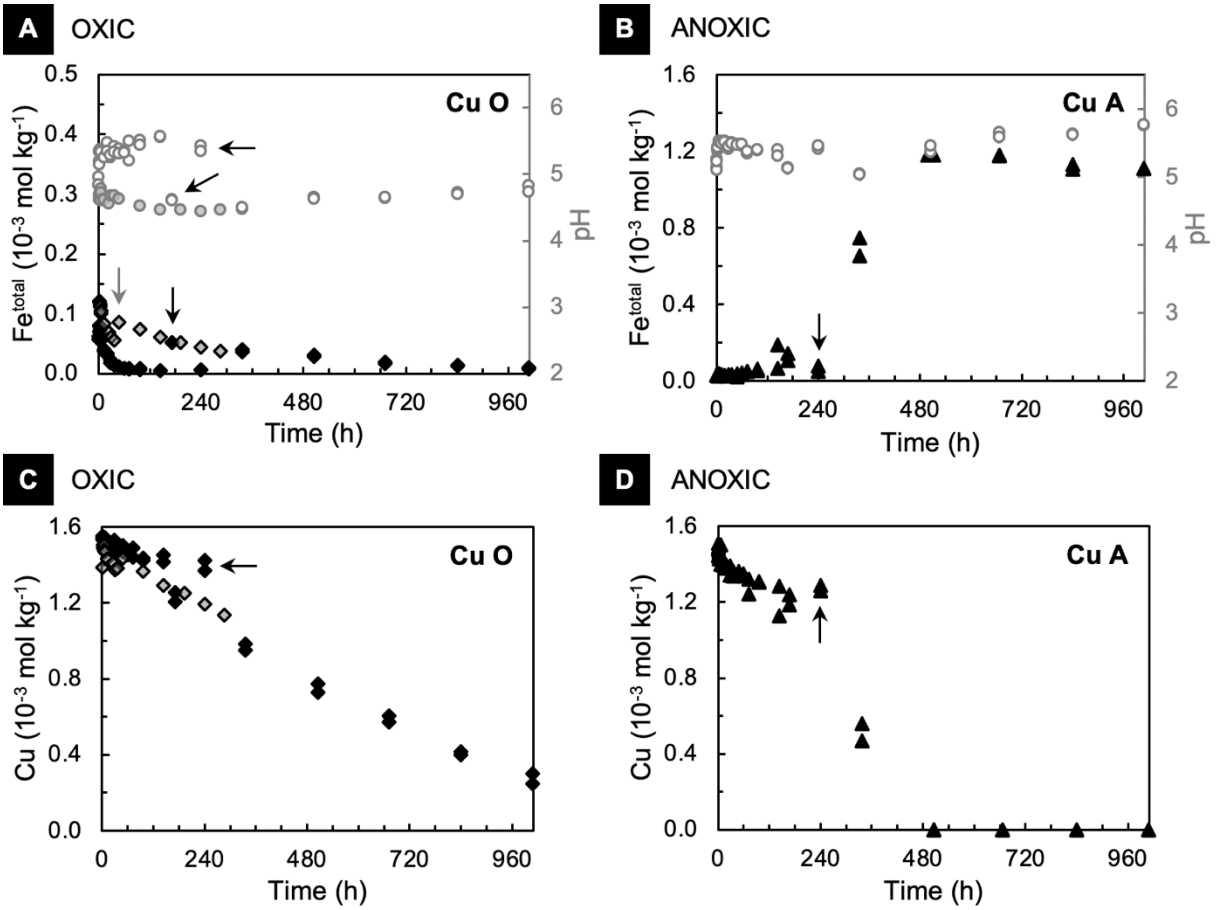

Figure 5.1. Overview of the aqueous Fe^{total} and Cu concentrations as a function of reaction time during siderite dissolution in the presence of Cu(II) under oxic (A, C; black diamonds) and anoxic (B, D; black triangles) conditions. The solution pH over time is plotted on the secondary axis in (A) and (B) (open grey circles). Filled grey symbols show data obtained from preliminary runs of the siderite dissolution experiments in the presence of Cu(II) under oxic conditions run for a total of 286 h; re-runs were conducted to see whether the distinct offsets between individual experiments (indicated by arrows) could be eliminated, however, increased due to the use of a more constrained size fraction of the siderite starting material (38–64 µm instead of < 64 µm).

Cu removal and Fe release suggests a coupling of reactions under some acid production (–0.4 pH units). Thenceforth, siderite dissolution continues at a slower rate (increase in pH to 5.8) while Fe concentrations gradually decrease by 0.08×10^{-3} mol kg^{-1} over the remaining 503 h of reaction.

5.3.2. Characterisation of the solid reaction products

In the course of siderite dissolution in the presence of Cu(II), the precipitation of ferric iron (oxyhydr)oxides is marked by a colour change of both oxic and anoxic suspensions. Pale at first, the colour gradually changes from dark grey to ochre within the first 6 h, to deep reddish-

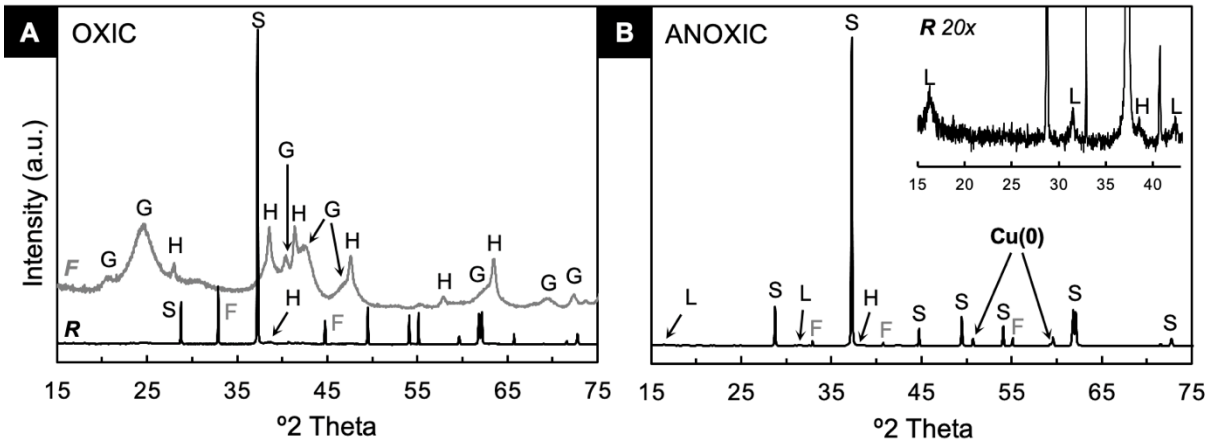

Figure 5.2. Powder XRD of the bulk solids collected from the siderite dissolution experiments after 1008 h of reaction under oxic (A) and anoxic (B) conditions. Ultrafine precipitates (*F*, fines) could be collected and analysed separately from coarser grain fractions (*R*, residue) in from the solids reacted under oxic conditions (A); all unlabelled peaks in (A) result from siderite diffraction. The insert in (B) shows an outcrop of the diffraction pattern at 40x exaggeration for improved visibility of the minor phases. Phases identified are siderite (S), impurities of fluorite (F), secondary goethite (G), hematite (H), lepidocrocite (L) and native copper (Cu(0)).

brown within 240 h of reaction under oxic, and from pale grey to luscious orange within ~96 to 168 h of reaction under anoxic conditions.

Siderite grains recovered after 1008 h of reaction with Cu(II) under oxic conditions are vastly covered with secondary precipitates identified by XRD as nanoparticulate goethite (α-FeOOH) and nanocrystalline hematite (α-Fe_2O_3; Figure 5.2; Table A10). The precipitates form a discontinuous, in part up to ca. 100 to 200 nm thick crust of clustered spherical particles intercalated with randomly orientated ~100 nm small rods. The nano-rods are mostly six-radially intergrown and commonly routed in the nanoparticle clusters (Figure 5.3A–C). Lattice spacings measure 2.26 ±0.01 Å and 2.58 ±0.01 Å in HRTEM and simultaneous FFT images, identifying the rods as goethite (lattice planes (121) and (021), respectively; Figure 5.3C), whereas clumped nanoparticles also exhibit minor diffraction patterns indicative for hematite with *d*-spacings measuring 2.73 ±0.02 Å (104) and 3.78 ±0.07 Å (012) (Figure 5.3B–C; Table A11). No separate Cu phases were observed.

Solid reaction products recovered from the anoxic Cu(II)-bearing aqueous solutions after 1008 h of reaction are identified as lepidocrocite (γ-FeOOH) and native copper (Cu(0); Figure 5.2; Table A10). The lath-shaped crystallites characteristic for lepidocrocite are of up to several hundred nanometres in length and randomly dispersed on the reacted siderite surface and/or aggregated to crust-like chunks in the ultrafine particle fraction (Figure 5.4A–B). This characteristic morphology and lattice spacings of 2.45 ±0.03 Å and 1.74 ±0.01 Å identify these

crystallites as lepidocrocite (lattice planes (031) and (151), respectively; Figure 5.4D, F; Table A11). Spherical nanoparticle clusters associated at random with the lath-shaped crystallites produce diffraction patterns characteristic for lepidocrocite, goethite, and possibly metallic copper (Figure 5.4B–E). The lattice spacings of 2.04 ±0.06 Å observed in both types of precipitates, however, challenge the assignment to Cu(0) (2.09 ±0.10 Å (111)) as they are also within the analytical uncertainty of lattice spacings attributable to goethite (2.19 ±0.11 Å (140)), and/or lepidocrocite (1.94 ±0.10 Å (051); Table A11). Notably, lattice spacings indicative for goethite are commonly observed in the lath-shaped crystallites (Figure 5.4F), suggesting either widening of the lepidocrocite crystal lattice, or some degree of intracrystalline phase transformation.

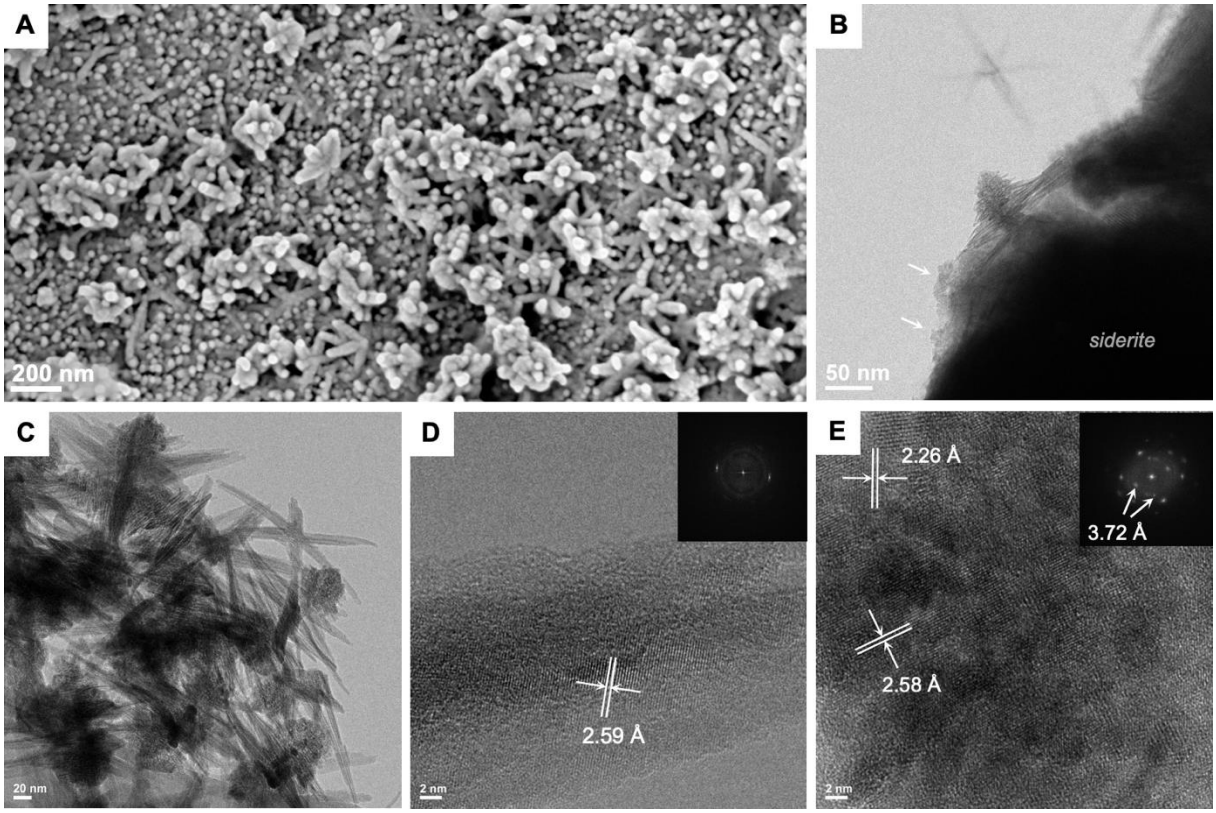

Figure 5.3. High-resolution scanning (A) and transmission (B–E) electron micrographs of solid reaction products collected after 1008 h of siderite interaction with dissolved Cu(II) under oxic conditions. (A) Reacted siderite grain surfaces showing vast but heterogeneous coverage by nanoparticulate precipitates, often forming up to 100-200 nm thick crusts. The precipitates consist of nanocrystalline rods, and rods grown out of nanoparticle clusters in six-radial twining. Nanoparticle clusters grow from the siderite surface (B) or detach, forming loose aggregates (C). (D) and (E) show the most commonly observed *d*-spacings in the rods (D) and clusters (E), which are characteristic for goethite (2.26 ±0.01 Å (121), 2.58 ±0.01 Å (021)) and hematite (3.78 ±0.09 Å (012)). Insets in (D) and (E) show the Fourier transformation images of the calculated diffraction pattern of the crystal phases detected in the HRTEM image area, additionally identifying hematite present in the nanoparticle clusters (E).

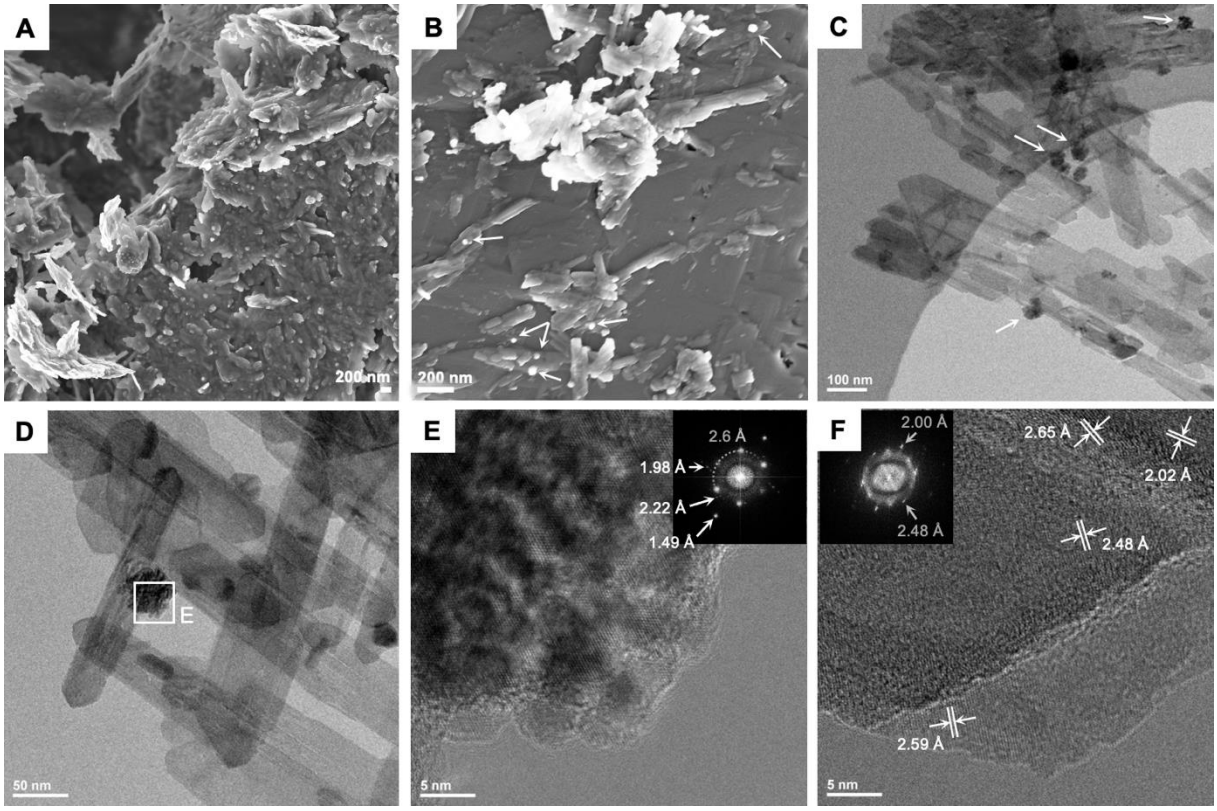

Figure 5.4. High-resolution scanning (A–B) and transmission electron micrographs (C–F) of the solid reaction products collected after 1008 h of siderite interaction with dissolved Cu(II) under anoxic conditions. (A) Nano- to submicron-sized precipitates accumulate in suspension to crust-like aggregates of lath-shaped crystallites and spherical secondary phases. (B) Aggregates of the same type of precipitates are more heterogeneously dispersed on the reacted siderite surfaces, which show distinct dissolution etch pits and terraces. Notably, spherical particles are generally associated with the lath-shaped crystallites (arrows; B-D). At high-resolution, the nanoparticle clusters exhibit *d*-spacings characteristic for goethite (2.58–2.65 Å (021)) and lepidocrocite (1.49 Å (231), 2.48 Å (031); E–F). The exact location of native copper is ambiguous, as the characteristic *d*-spacings of 1.80 and 2.09 ±0.1 Å of Cu (111) and (200), respectively, fall within the 5% uncertainty of less commonly diffracted lattice planes of lepidocrocite (051) (1.94 ±0.1 Å) and goethite (140) (2.19 ±0.1 Å). Blurry rings in the Fourier transform images indicate regions of poor crystallinity (inserts in E and F).

5.3.3. Cu speciation and local bonding environment

A series of complementary X-ray-based analyses including combined µ-XRF and µ-XANES, bulk XAFS and XPS were performed to determine Fe and Cu speciation, and the bonding environment of Cu associated with the reacted solids.

The Fe $2p_{3/2}$ spectra obtained from siderite grains reacted with Cu(II) for 1008 h under both oxic and anoxic conditions show a high degree of near-surface Fe(II) oxidation, indicated by the high contributions of the Fe^{3+} lines to the binding energy peaks at 711.1 and 710.7 eV,

respectively (98% Fe^{3+} in the oxic, and 64% in the anoxic residue (*R*) sample). The predominance of ferric iron surface species in combination with the characteristic binding energy lines of OH^- at 531.0 and 530.8 eV, and of O^{2-} at 529.7 and 529.1 eV in the O 1s spectra, and a reduction of the CO_3^{2-} line at 289.2 and 289.3 eV in the C 1s spectra, suggests advanced surface hydroxylation, or more likely, ferric (hydr)oxide formation (*see* Figure A6, Table A12). Corresponding XPS spectra obtained from the ultrafine reaction products (*F*) show near complete Fe oxidation, indicated by the dominance of Fe^{3+} contributions to the Fe $2p_{3/2}$ lines at 711.7 and 711.3 eV (100% and 95% in the oxic and anoxic *F* samples), respectively. Similar to the spectra collected from the larger reacted siderite grains (*R*), the OH^- lines at 531.0 and 530.9 eV, and the O^{2-} lines at 529.5 and 529.6 eV dominate the O 1s spectra, while carbonate peak contributions at 288.7 and 288.9 eV in the C 1s spectra are very weak. Notably, this is true for spectra recorded from both oxic and anoxic ultrafine samples (*F*), confirming that these fractions predominantly consist of secondary ferric (oxyhydr)oxide reaction products (*see* Figure A6, Table A12).

The Cu $2p_{3/2}$ spectra obtained from samples recovered from the **oxic** experiment after 1008 h of reaction reveal major peaks at 933.7 eV in the residual fraction (*R*), and at 933.2 eV in the ultrafine fraction (*F*). Dominant peak contributions of binding energy lines at 933.9 eV (in *R*) and 934.3 eV (in *F*) are assigned to Cu(II) species, including the characteristic satellite features

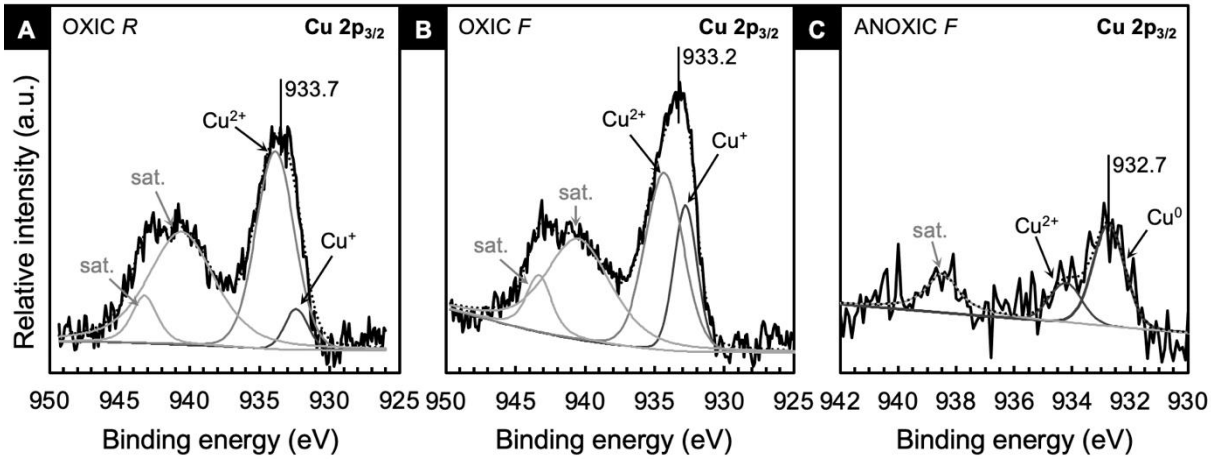

Figure 5.5. X-ray photoelectron Cu 2p spectra obtained from the solid reaction products collected from after 1008 h of reaction under oxic (Cu O LT; A–B) and anoxic conditions (Cu A LT; C). Reacted siderite grains (*R* = residue) and an ultrafine fraction of predominantly ferric precipitates (*F*) were collected separately. No Cu signal was detected on the reacted residual particles collected from the anoxic experiments (anoxic *R*). Minor peaks at 943.3 to 940.5 eV (A–B) and at 938.5 eV (C) are satellite structures ('shake-up lines'). The assignment of the minor peak contributions at 932.4 (A) and 932.8 eV (B) to Cu(I) oxide was based on additional consideration of the Cu LMM Auger parameter (*see* section A.4., Table A13 and Figure A7).

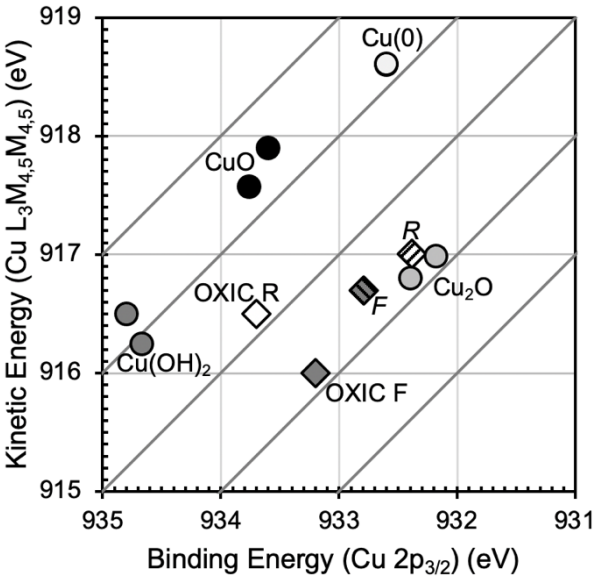

Figure 5.6. Chemical state or Wagner plot showing the Cu $L_3M_{4,5}M_{4,5}$ Auger kinetic energy as a function of the XPS Cu $2p_{3/2}$ binding energy of literature values (Table A12) and sample data obtained from the solids collected after 1008 h of reaction under oxic conditions ('OXIC' = Cu O LT; *R* = residue, open diamonds; *F* = ultrafine particles, grey diamonds). Solid open/filled diamonds represent data of the main peak values, whereas pattern open/filled diamonds show data of the reduced Cu peak contributions (c.f., Figure A7 and Table A12). Compounds of the same oxidation state generally have similar Auger Parameter values *or* similar binding energy values and thus plot within a similar region of this diagram (Biesinger, 2017). Here, this is demonstrated by the main peak data plotting between cupric and cuprous species indicating mixed Cu^{2+}/Cu^{+} oxidation states, while the individual peak contribution data plot closely to Cu(I) oxide indicating a predominance of the Cu^{+} oxidation state (vs. Cu^{0}).

at ~6 eV towards higher binding energies (Figure 5.5A–B and Table 5.1; D'Huysser et al., 1981; Biesinger et al., 2010). These species are potentially coordinated with OH^{-} groups, which may contribute to the 531.1 eV peak of the $Fe(O,OH)_6$ in the corresponding O 1s spectra (c.f., $Cu(OH)_2$, 531.2 eV; Biesinger et al., 2017; *see* Figure A6; Table A12). Minor peak contributions to the Cu $2p_{3/2}$ spectra at 932.4 eV (in *R*) and 932.8 eV (in *F*) indicate the partial reduction of Cu(II) associated with the reacted siderite surface and/or surface precipitates (*R*) by about 11%, and of about 33% to in the ultrafine fraction (*F*) dominated by ferric (oxyhydr)oxide precipitates (Table 5.1). Notably, the characteristic binding energies of the reduced Cu species overlap in the XPS spectrum (D'Huysser et al., 1981; Brabers, 1983; Tobin et al., 1983; Poulston et al., 1996; Biesinger et al., 2007, 2010; Biesinger, 2017). The assignment of these peak contributions to Cu(I) is reasoned by complementary analyses of the Cu $L_3M_{4,5}M_{4,5}$ Auger parameter (*see* section A.4., Table A13, and Figure A7) and the lack of metallic copper in all other solid analyses of the same (oxic) sample. The partial reduction of Cu(II) to Cu(I) in the oxic residue and ultrafine samples is further supported in a chemical state

(or Wagner) plot, where the sample data plot between Cu(II) hydroxide and Cu(I) oxide (Figure 5.6). The lack of Cu–carbonate species and the higher intensity of the Cu $2p_{3/2}$ signal in the ultrafine fraction suggest that by the end of the oxic experiment, Cu is primarily associated with the ferric (oxyhydr)oxide precipitates.

Table 5.1. Quantification of Cu species of the **Cu $2p_{3/2}$** lines in **XPS** spectra obtained from the solids collected after 1008 h of reaction under oxic and anoxic conditions.

Sample	Binding energy (eV)	FWHM (eV)	Relative area (%)	Peak assignment	Cu reduction
OXIC *R*[a]	**933.7**			**Cu(II)**	
	932.38	1.96	5.3	Cu(I)	11%
	933.89	3.24	42.02	Cu(II)	
	940.58	*5.59*	*44.9*	*Satellite*	
	943.22	*2.16*	*7.78*	*Satellite*	
OXIC *F*[a]	**933.2**			**Cu(II)/Cu(I)**	
	932.79	1.96	17.8	Cu(I)[c]	33%
	934.34	3.24	35.48	Cu(II)	
	940.5	*5.59*	*38.02*	*Satellite*	
	943.32	*2.16*	*8.71*	*Satellite*	
ANOXIC *F*[b]	**932.7**			**Cu(0)**	
	932.74	1.29	51.92	Cu(0)[d]	71%
	934.22	1.32	20.81	Cu(II)	
	938.48	*1.35*	*27.27*	*Satellite*[e]	

Solid reaction products recovered from the [a]oxic (Cu O LT) and [b]anoxic (Cu A LT) long-term experiments. *R* = 'residual', defined as reacted siderite grains including surface precipitates; *F* = 'ultrafine', defined as ultrafine reaction products recovered from the suspension. [c]More likely to be Cu(I) based on XAFS results. [d]Assigned as Cu(0) because of the evidence for metallic Cu in the samples by XRD and XAFS. [e]Satellite (or shake-up) lines are indicative for Cu(II) present in the sample; these features result from the interaction of the outgoing photoelectron with a valence electron, which becomes excited to a higher-energy level.

The residual fraction (*R*) of the solids reacted for 1008 h under anoxic conditions produce no detectable Cu $2p_{3/2}$ signal in the XPS spectrum, whereas a weak signal was obtained from the ultrafine sample fraction (*F*; Figure 5.5C). This suggests that by the end of the experimental interaction of siderite with dissolved Cu(II) under anoxic conditions, (1) only small amounts of

Cu are bound within the outermost 10 nm of any solid in the system, and (2) Cu is predominantly associated with the ultrafine particles. In fact, the weak Cu $2p_{3/2}$ peak at 932.7 eV detected in the ultrafine sample fraction is indicative for reduced Cu (71%; Table 5.1). Notably, the signal was insufficient to produce an Auger line. The assignment to metallic Cu(0) is reasoned based on the evidence for native copper provided by XRD, TEM, and XAFS analyses of the same (anoxic) samples. The main peak also includes minor contributions of hydrous oxide coordinated Cu(II), indicated by the line at 934.2 eV and the corresponding satellite structure at 938.5 eV (e.g., D'Huysser et al., 1981; Biesinger et al., 2010).

Iron and copper speciation were also studied using XAFS on the bulk granular solids recovered from the oxic and anoxic experiments collected after 1008 h of reaction. For the local distribution and speciation of Cu on the reacted solids, combined µ-XRF and µ-XANES maps of the Cu and Fe K-edges were complementarily collected of the same samples.

Linear combination fitting (LCF) of the XANES spectra recorded at the Fe and Cu K-edges from the bulk solids reacted under oxic conditions to reference spectra suggest that ca. 35% of the iron, and roughly 76% of solid-associated Cu is present as oxidised hydroxyl-coordinated species, while the remaining 24% of Cu(II) is coordinated with hydroxy carbonate groups (Tables 5.2 and 5.3). At higher spatial resolution, XRF-maps of the reacted siderite grains show a predominantly homogeneous distribution of Cu (Figure 5.7A), with sporadically occurring patches of locally increased Cu signal intensity (Figure 5.7B, D). Corresponding Fe and Cu K-edge XANES spectra LCF results of areas of homogeneous Cu distribution (Figure 5.7C, H–J) suggest a predominance of Cu(II) in hydroxyl-coordination. Minor scattering contributions to the first derivative of the Cu K-edge spectrum suggest some carbonate coordination, which is, however, uncertain (Table 5.3). Corresponding Fe K-edge spectra of this area indicate complete oxidation of the (near-surface) Fe to Fe^{3+} in goethite and hematite coordination (Figure 5.7I; Table 5.2). XANES-maps of areas of heterogeneous Cu distribution indicate a spatial correlation between the different Fe and Cu phases (Figure 5.7B and I–J; Tables 5.2 and 5.3 B4). That is, regions of homogeneous Cu distribution are dominated by hydroxyl-coordinated Cu(II) associated with moderate Fe oxidation (50 to 60% ferric (oxyhydr)oxides; 40-50% siderite). Whereas regions of locally increased Cu XRF signal intensities are associated with increasing scattering contributions of reduced Cu and oxidised Fe species in the corresponding µ-XANES Cu and Fe K-edge spectra (up to 30% of Cu(I) associated with ~85% ferric (oxyhydr)oxides). Notably, LCF of the corresponding Fe K-edge map-spectra further suggests that the Fe(III) is mainly present in a lepidocrocite-like coordination (rather than goethite-like;

Table 5.2 B4). Overall, by the end of the oxic LT experiment performed under oxic conditions, Cu is predominantly present as Cu(II) and most likely coordinated with the $Fe(O,OH)_6$ groups of the ferric (oxyhydr)oxides (goethite and hematite). About 24% of the solid-associated Cu(II) Cu is coordinated as hydroxy carbonate, while patchy occurrences of Cu(I) are spatially correlated with most advanced Fe oxidation, possibly in the form of hematite and lepidocrocite.

Linear combination fitting of the bulk XANES Fe and Cu K-edge spectra of the solids reacted for 1008 h under anoxic conditions suggest that both Fe and Cu are completely reduced, while Cu is present as both Cu(I) (ca. 20%) and in its metallic state (ca. 80% Cu(0); Figure 5.7I–J; Tables 5.2 and 5.3). Complementary XRF-maps recorded of the same samples show a distinctly locally constrained distribution of Cu, where Cu is concentrated in irregular patches associated with the reacted siderite grains (Figure 5.7F–H). Notably, the locally resolved XANES Fe K-edge spectra of a high Cu XRF signal intensity area indicate that the associated Fe is nearly completely oxidised (ca. 95% ferric oxyhydroxide with lepidocrocite-like Fe(III) coordination; no Cu K-edge data available; Figure 5.7I). This correlation suggests that, by the end of the anoxic LT experiment, reduced Cu is exclusively associated with the ferric oxyhydroxide precipitates, most likely lepidocrocite.

On the following page: **Figure 5.7.** Combined X-ray fluorescence (µXRF; top) and X-ray absorption near-edge structure (µXANES; bottom) mapping (A–H) and bulk sample XANES spectra (I–J) of solid reaction products collected after 1008 h of reaction under oxic and anoxic conditions. XANES maps of the outlined boxes in (B), (C), and (H) are shown next to the XRF maps; corresponding spectra are indicated by numbering (B0–4; C0–4; H0–1; green = Cu; blue = Fe. In (I–J), solid black lines = sample and reference data, dashed lines = fit data (green = Cu K-edge; blue = Fe K-edge). Corresponding first derivatives of the data and fit spectra are provided for better visibility of characteristic features in the spectra. 'OXIC' = Cu O LT, 'ANOXIC' = Cu A LT, Sid = siderite, Hem = hematite, Goe = goethite, Lep = lepidocrocite. (A) Overview XRF-map of Cu (green) of an area 250 µm across captured from siderite grains reacted with Cu(II) under oxic conditions, showing a predominantly uniform distribution of Cu, whereas some areas show locally increased intensities (B–D, G, and H). Corresponding XANES spectra of the Fe and Cu K-edges were collected from areas indicated by broken-line boxes in (B) and (C) shown in (I) and (J). For comparison, spectra collected from the bulk solid samples and reference materials are also shown (I–J). In contrast to the Cu distribution observed in the oxic sample, representative Cu–Fe XRF maps of siderite grains reacted with Cu(II) under anoxic conditions shown in (G) and (H) indicate a local concentration of solid-bound Cu, seemingly independent of the detected Fe distribution (blue). The Fe K-edge spectra obtained from the mapped area in (H) are shown in (I). Corresponding Cu K-edge spectra of this sample could not be collected due to technical difficulties at the beamline.

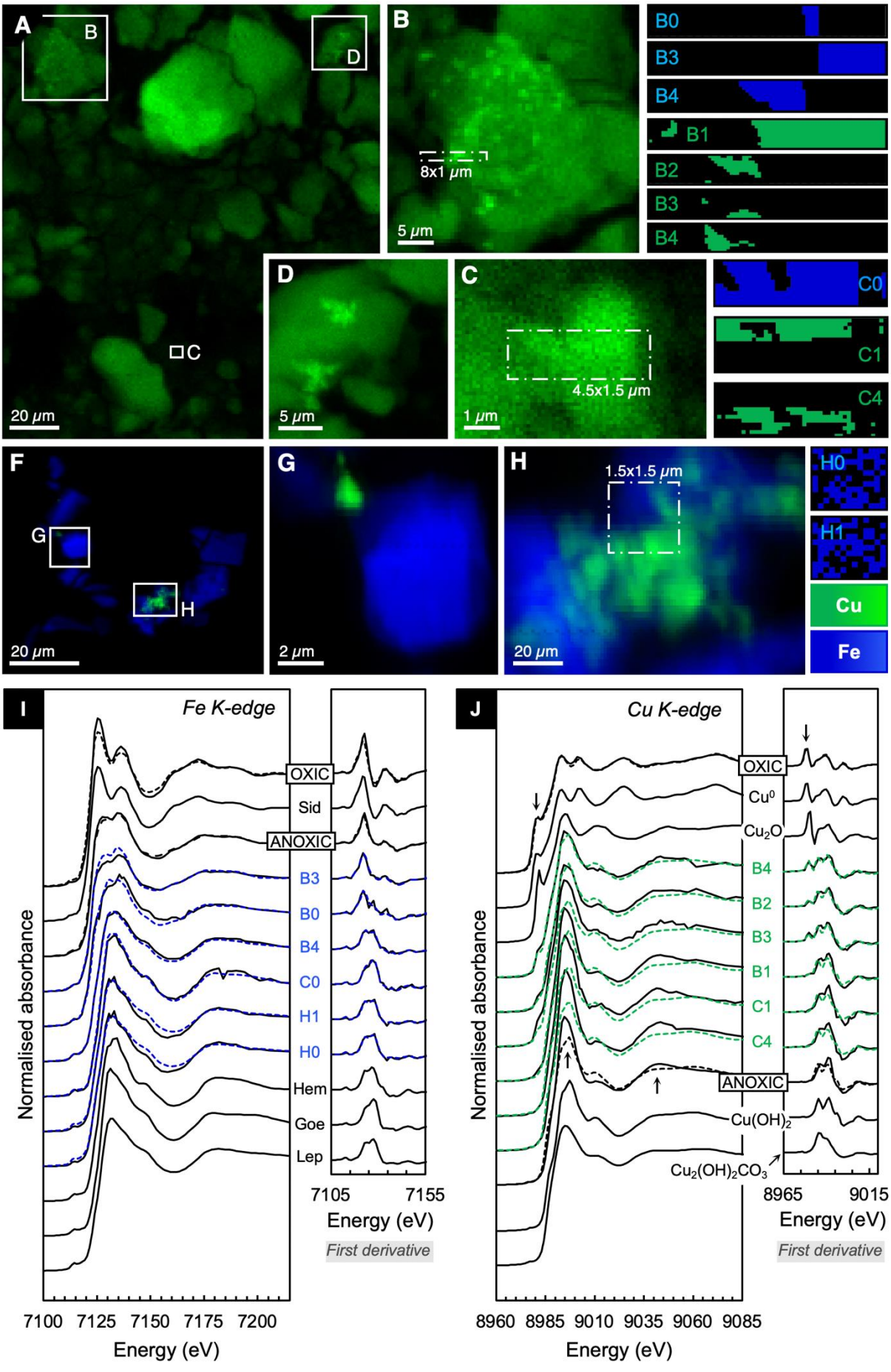
A
B
D
C
20 μm
B
8x1 μm
5 μm
B0
B3
B4
B1
B2
B3
B4
D
5 μm
C
4.5x1.5 μm
1 μm
C0
C1
C4
F
G
H
20 μm
G
2 μm
H
1.5x1.5 μm
20 μm
H0
H1
Cu
Fe
I
Fe K-edge
OXIC
Sid
ANOXIC
B3
B0
B4
C0
H1
H0
Hem
Goe
Lep
Normalised absorbance
7100 7125 7150 7175 7200
Energy (eV)
7105 7155
Energy (eV)
First derivative
J
Cu K-edge
OXIC
Cu⁰
Cu₂O
B4
B2
B3
B1
C1
C4
ANOXIC
Cu(OH)₂
Cu₂(OH)₂CO₃
Normalised absorbance
8960 8985 9010 9035 9060 9085
Energy (eV)
8965 9015
Energy (eV)
First derivative

Table 5.2. Linear combination fit results of the k^2-weighted XANES Fe K-edge spectra obtained from the bulk samples collected after 1008 h of reaction under oxic and anoxic conditions. Bulk sample spectra and locally resolved spectra from µXANES-mapping are listed separately and labelled according to Figure 5.7. Fit results of the first derivative of µ(E), and of the k^3-weighted EXAFS spectrum of the bulk samples are also listed in comparison (second and third row, *italics*). Fitted proportions are given in percent (%), uncertainties in brackets.

Sample		Fe K-edge		R-factor	reduced χ^2	Siderite	Hematite	Goethite	Lepidocrocite
		E_0	ΔE_0			$Fe^{(II)}CO_3$	$Fe_2^{(III)}O_3$	α-$Fe^{(III)}OOH$	γ-$Fe^{(III)}OOH$
OXIC[a]									
Bulk		7122.8	0	0.002	0.00033	62.7 (1.9)	37.3 (1.0)	–	–
		first derivative		*0.019*	*0.00004*	*65.5 (1.7)*	*34.5 (1.3)*	–	–
			EXAFS	*0.066*	*0.248*	*67.7 (1.2)*	–	*14.7 (2.4)*	*17.5 (1.2)*
Map B	0	7122.1	3.08	0.006	0.00122	47.1 (1.9)	–	52.9 (13.8)	–
		first derivative		*0.072*	*0.00012*	*52.9 (3.7)*	–	*47.1 (2.1)*	–
	3	7122.1	3.08	0.004	0.00075	60.9 (1.9)	39.1 (1.6)	–	–
		first derivative		*0.016*	*0.00003*	*63.0 (1.1)*	*37.0 (4.7)*	–	–
	4	7123.5	3.08	0.001	0.00028	11.8 (1.0)	15.8 (5.8)	–	72.4 (5.9)
		first derivative		*0.012*	*0.00002*	*14.5 (1.0)*	*35.7 (6.8)*	–	*49.8 (6.7)*
Map C	0	7127.0	3.08	0.003	0.00051	–	46.1 (14.0)	53.9 (9.5)	–
		first derivative		*0.019*	*0.00005*	–	*40.7 (8.4)*	*59.3 (8.4)*	–
ANOXIC[b]									
Bulk		7122.8	-0.01	0.008	0.00140	100.0 (0.0)	–	–	–
		first derivative		*0.041*	*0.00016*	*100.0 (0.0)*	–	–	–
			EXAFS	*0.063*	*0.462*	*100.0 (0.0)*	–	–	–
Map H	0	7128.1	3.08	0.006	0.00103	7.3 (2.2)	–	–	92.7 (1.8)
		first derivative		*0.015*	*0.00003*	*6.4 (1.3)*	–	–	*93.6 (1.3)*
	1	7128.1	3.08	0.006	0.00107	5.1 (2.2)	–	–	94.9 (1.9)
		first derivative		*0.013*	*0.00003*	*4.1 (1.2)*	–	–	*95.9 (1.2)*

The goodness-of-fit is represented by the R-factor and reduced χ^2; additional uncertainties of the fit originate from mathematical scaling and summation of the fitted spectra in Athena and range within approximately ±10%. [a]oxic = Cu O LT; [b]anoxic = Cu A LT. Fitting range of the normalised absorbance spectra was –20 to +70 eV from the Fe K-edge; fitting *k*-range of the EXAFS was 3 to 12.

Table 5.3. Linear combination fit results of the k^2-weighted XANES Cu K-edge bulk sample spectra and locally resolved spectra from µXANES-mapping spectra (Figure 5.7) obtained from the bulk samples collected after 1008 h of reaction under oxic and anoxic conditions. Fit results of the first derivative of µ(E) are also listed in comparison (second row, *italics*). Fitted phase contributions are given in percent (%), uncertainties in brackets.

Sample	Cu K-edge		R-factor	reduced χ^2	Cu metal	Cu_2O	$Cu(OH)_2$	$Cu_2(OH)_2CO_3$
	E_0	ΔE_0			Cu^0	Cu^+	Cu^{2+}	Cu^{2+}
OXIC[a]								
Bulk	8991.0	-0.05	0.133	0.00034	–	–	76.0 (21.9)	24.0 (15.4)
	first derivative		*0.133*	*0.00034*	–	–	*76.0 (21.9)*	*24.0 (15.4)*
Map B 1	8991.5	1.46	0.033	0.00599	–	0.0 (6.8)	100.0 (9.3)	–
	first derivative		*0.134*	*0.00041*	–	*6.6 (6.4)*	*93.4 (6.4)*	–
2	8991.5	1.46	0.008	0.00127	–	8.7 (3.1)	91.3 (3.1)	–
	first derivative		*0.086*	*0.00017*	–	*23.4 (4.0)*	*76.6 (13.0)*	–
3	8990.5	1.46	0.046	0.00786	–	17.1 (7.8)	82.9 (11.0)	–
	first derivative		*0.077*	*0.00018*	–	*27.2 (4.2)*	*72.8 (8.8)*	–
4	8991.5	1.46	0.005	0.00073	–	28.3 (3.5)	71.7 (2.4)	–
	first derivative		*0.073*	*0.00012*	–	*37.3 (3.4)*	*62.7 (9.9)*	–
Map C 1	8991.5	1.46	0.042	0.00891	–	–	100.0 (0.0)	–
	first derivative		*0.138*	*0.00045*	–	–	*78.9 (19.3)*	*20.2 (19.3)*
4	8991.5	1.46	0.047	0.01021	–	–	100.0 (9.7)	0.0 (9.7)
	first derivative		*0.152*	*0.00050*	–	–	*76.2 (20.4)*	*23.8 (45.6)*
ANOXIC[b]								
Bulk	8979.0	-0.09	0.001	0.00018	78.0 (2.9)	22.0 (2.0)	–	–
	first derivative		*0.011*	*0.00001*	*88.8 (1.5)*	*6.8 (1.5)*	*4.4 (7.2)*	–

The goodness-of-fit is represented by the R-factor and reduced χ^2; additional uncertainties of the fit originate from mathematical scaling and summation of the fitted spectra in Athena and range within approximately ±10%. [a]oxic = Cu O LT; [b]anoxic = Cu A LT. Fitting range of the normalised absorbance spectra was –20 to +70 eV from the Fe K-edge; fitting *k*-range of the EXAFS was 3 to 12.

For more detailed information on the short-range bonding environment of Cu, i.e., to distinguish between sorption, incorporation, and co-precipitation of a separate phase, complementary shell-by-shell fitting was performed on the EXAFS region of the bulk sample Cu K-edge X-ray absorption spectra (Figure 5.8B; Table 5.4). A compilation of fitting parameters of possible coordination geometries is provided in Table A14 with corresponding references given in Table A15.

In the solids collected from the oxic LT experiment, Cu is coordinated by four equatorial oxygens at an interatomic distance of $R_{Cu–Oeq}$ = 1.98 Å, and one axial oxygen at $R_{Cu–Oax}$ = 2.25 Å in its first coordination shell. This closely agrees with reported Cu(II) sorption geometries to iron oxides (Bochatay et al., 1997; Parkman et al., 1999; Alcacio et al., 2001; Scheinost et al., 2001; Peacock & Sherman, 2004; Gräfe et al., 2008; Gilbert et al., 2009; Moon & Peacock, 2012; Dale et al., 2015; Stegemeier et al., 2015) and calcite (Elzinga & Reeder, 2002; Elzinga et al., 2006) described as distorted octahedral oxygen coordination or trigonal bi-pyramidal hydroxo complexes (Oswald et al., 1990; Bowron et al., 2013; Persson et al., 2020). A full octahedral coordination is not supported by the shell fit results. Hence some tetrahedral components may be contained in this geometry as proposed for the hydration structure of Cu^{2+} (Bowron et al., 2013). Including second shell hydrogen scattering contributions at 2.69 Å significantly improved the fit statistics. Although it is not unreasonable to find hydroxyl groups associated with adsorbed Cu (Peacock & Sherman, 2004; Bowron et al., 2013), it is unusual to see hydrogen contributions in an EXAFS spectrum as hydrogen is a very weak scatterer; hence this part of the fit might be argued to be mathematical.

Second shell neighbouring metal atoms are found at interatomic distances of $R_{Cu–Me(1-3)}$ = 2.99 Å, 3.19 Å, and 3.86 Å, respectively. Note that because of their similar atomic number and hence very similar scattering properties, ^{29}Cu and ^{26}Fe are indistinguishable as their shells become as close as 0.05 Å of each other, which is within the fitting error (Newville, 2014). From what is known about the sample, it can be assumed that the nearest metal atom at a distance of $R_{Cu–Me1}$ = 2.99 Å is a Cu atom, likely in the form of a bidentate monomeric neighbouring Cu sorption complex (c.f., Peacock & Sherman, 2004). Scattering contributions of carbonate ligands may also be possible at this distance (2.9 to 3.0 Å; c.f., Süsse, 1967; Elzinga & Reeder, 2002). However, although some carbonate speciation of Cu was suggested by LCF results of the XANES Cu K-edge spectra of this sample, any such scattering contributions are most likely overshadowed by the much stronger scatterings from neighbouring metal atoms. Further scattering contributions from about four to five neighbouring metal atoms are found at a distance of $R_{Cu–Me2}$ = 3.19 Å. Considering that no separate crystalline Cu phase was detected by any other analytical techniques applied on the oxic samples, it is reasonable to assume that Cu is adsorbed to siderite and/or the ferric (oxyhydr)oxide precipitation products. Thus, the scatterers at 3.19 Å distance are likely Fe centres in a bi- and/or tridentate corner-sharing complex coordination with Cu (c.f., Peacock & Sherman, 2004). A third shell neighbouring metal atom is found at $R_{Cu–Me3}$ = 3.86 Å. This distance is too far for comparable Cu sorption complexes on crystalline ferric (oxyhydr)oxides

(c.f., Bochatay et al., 1997; Parkman et al., 1999; Alcacio et al., 2001; Scheinost et al., 2001; Peacock & Sherman, 2004; Gräfe et al., 2008), but agrees well with interatomic distances of $R_{Cu–Fe} \approx 3.88 \pm 0.03$ Å that have been reported for dimeric intraparticulate sorption geometries of Cu(II) within nanopores of ferric oxyhydroxide nanoparticle aggregates (Gilbert et al., 2009; Dale et al., 2015; Stegemeier et al., 2015). Alternatively, the measured $R_{Cu–Me3}$ distances also match the reported distance of $R_{Cu–Ca} \approx 3.9 \pm 0.04$ Å for Cu adsorbed to calcite (Elzinga & Reeder, 2002). Although the Fe site in siderite is much smaller compared to the Ca site in calcite (c.f., $^{[6]}Fe^{2+}$ = 0.78 Å; $^{[6]}Ca^{2+}$ = 1.0 Å; Shannon, 1976), and therefore the distance between the adsorbed Cu and the structural Fe atom is expected to be shorter, this difference may fall within the uncertainty of the EXAFS shell fitting. As suggested by the XPS and XANES bulk analyses, and the rapid removal of Cu(II) from the aqueous solution prior to ferric (oxyhydr)oxides precipitation, some Cu(II) adsorption to siderite may contribute to this scattering path. Sorption to siderite would require a bidentate complexation of Cu that is linked to the surface via carbonate ligands (Elzinga & Reeder, 2002; Elzinga et al., 2006). This coordination is likely but cannot be unambiguously confirmed due to the expected overlap of the carbonate scattering by the much stronger scattering of the neighbouring metal atoms at 2.9 Å.

The high coordination numbers of about two or three (Cu–Me_1) to approximately four (Cu–Me_2) and five (Cu–Me_3) neighbouring metal atoms suggest a complex sorption geometry or a mixture of such. Note that the absorption fine structure represents an average of all scattering contributions of neighbouring atoms around the absorbing atom. Hence, there may be more than one type of sorption complex. That is, Cu seems to be complexed predominantly with the $Fe(O,OH)_6$ groups of ferric (oxyhydr)oxide precipitates, but possibly also with the siderite surface via carbonate ligands (Figure 5.9). This mixed complexation may explain the high coordination numbers and suggests that hydrated Cu(II) sorption complexes were enclosed within ferric (oxyhydr)oxide nanoparticles during continuous precipitation, aggregation, and crystallite growth over the duration of the long-term experiment (e.g., Gilbert et al., 2009; Dale et al., 2015; Stegemeier et al., 2015).

In contrast, the LCF and the shell-by-shell fitting of the Cu K-edge EXAFS region of the spectra recorded from the bulk anoxic sample unambiguously indicates that after 1008 h of reaction, Cu is predominantly coordinated with neighbouring Cu atoms agreeing with the structure of metallic Cu (Figure 5.8A–B; Table 5.4; Wyckoff, 1963). Notably, contributions of minor or locally resolved occurrences of other Cu species, e.g., the presence of Cu(I) oxide as

indicated by XANES and XPS results, are likely overshadowed by the strong metallic Cu–Cu scatterings.

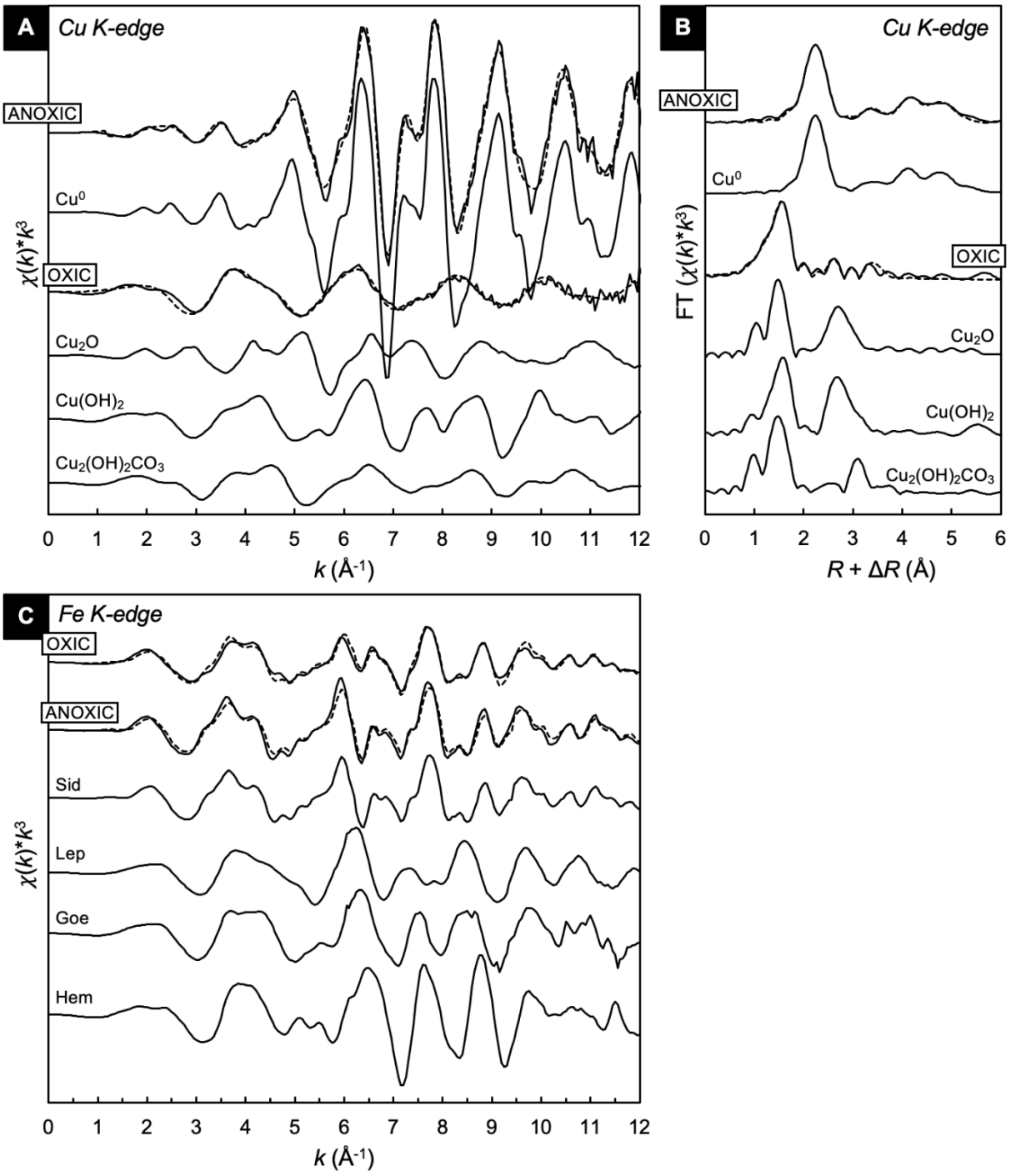

Figure 5.8. Extended X-ray absorption fine structure (EXAFS) spectra collected from reference materials and from bulk solid reaction products recovered from the oxic (Cu O LT) and anoxic (Cu A LT) experiments after 1008 h of siderite interaction with aqueous Cu(II). (A) and (C) show the Cu and Fe K-edge spectra of samples and reference compounds in *k*-space. (B) Fourier transformed EXAFS of samples and reference material Cu K-edge spectra in *R*-space. Solid lines = measured data; dashed lines = LCF fit (A, C) and shell-fit model (B); Sid = siderite; Lep = lepidocrocite; Goe = goethite; Hem = hematite.

Table 5.4. EXAFS shell-by-shell fit parameters of the Cu K-edge spectra obtained from the solid reaction products collected after 1008 h of reaction under oxic and anoxic conditions. Values in *italics* were set to best fit values obtained during the fitting procedure. Structural geometries are referred from literature values (Tables A14–15).

Sample	Shell	N	R (Å)	σ^2 (Å^2)	Possible geometry
OXIC[a]	Cu–O_{eq}	4.3 (2)	1.98 (03)	*0.007*	*– distorted Cu(II) octahedral*
	Cu–O_{ax}	1.1 (2)	2.25 (1)	*0.007*	*or trigonal bi-pyramidal*
	Cu–H*	7.7 (2.4)	2.69 (3)	*0.003*	*hydroxo-complex*
	Cu–Me_1	2.8 (4)	2.99 (1)	*0.010*	*– bi/tridentate edge-sharing*
					Me-O complex / CO_3 ligand
	Cu–Me_2	4.8 (8)	3.19 (1)	*0.015*	*– bi/tridentate corner-sharing*
					Me-O complex ($Fe(O,OH)_6$)
	Cu–Me_3	4.2 (6)	3.86 (1)	*0.015*	*– Me site of siderite*
ANOXIC[b]	Cu–Cu_1	*12*	2.54 (03)	0.008 (03)	*Cu metal*
	Cu–Cu_2	*6*	3.62 (1)	0.013 (2)	*(fitted to crystal structure;*
	Cu–Cu MS_1	*48*	3.83 (03)	0.004 (2)	*Wyckoff 1963)*
	Cu–Cu MS_2	*48*	4.37 (1)	*0.010*	
	Cu–Cu_3	*24*	4.42 (1)	0.012 (1)	
	Cu–Cu MS_1	*48*	4.76 (03)	0.004 (2)	
	Cu–Cu MS_3	*96*	4.77 (1)	0.025 (21)	
	Cu–Cu_4	*12*	5.15 (07)		
	Cu–Cu MS_4	*24*	5.15 (07)	0.005 (03)	
	Cu–Cu MS_4	*12*	5.15 (07)	0.005 (03)	

[a]oxic = Cu O LT (*bulk*); [b]anoxic = Cu A LT (*bulk*). N = coordination number (degeneracy), uncertainty ca. 15%; R = interatomic distance (half path length of the scattering photoelectron between the absorbing and the scattering atom); σ^2 = Debye-Waller disorder term. Me = metal neighbouring atom. MS = multi-scattering path. *Including this shell significantly improved the fit (Kelly, 2008; *see* appendix A.4.1.), despite an uncertainty of ±2.4 (~30%). Amplitude reduction factor S_0^2 was 0.9 (oxic; set to best fit value which agrees well with literature values, *see* Table A14 and references in Table A15) and 0.65 (anoxic), respectively. Energy shift ΔE_0 was -1.0 (oxic; set) and 5.36 eV (anoxic), respectively. Fitting range in *R*-space was 1 to 3.5 Å (oxic) and 1 to 5.2 Å (anoxic), respectively.

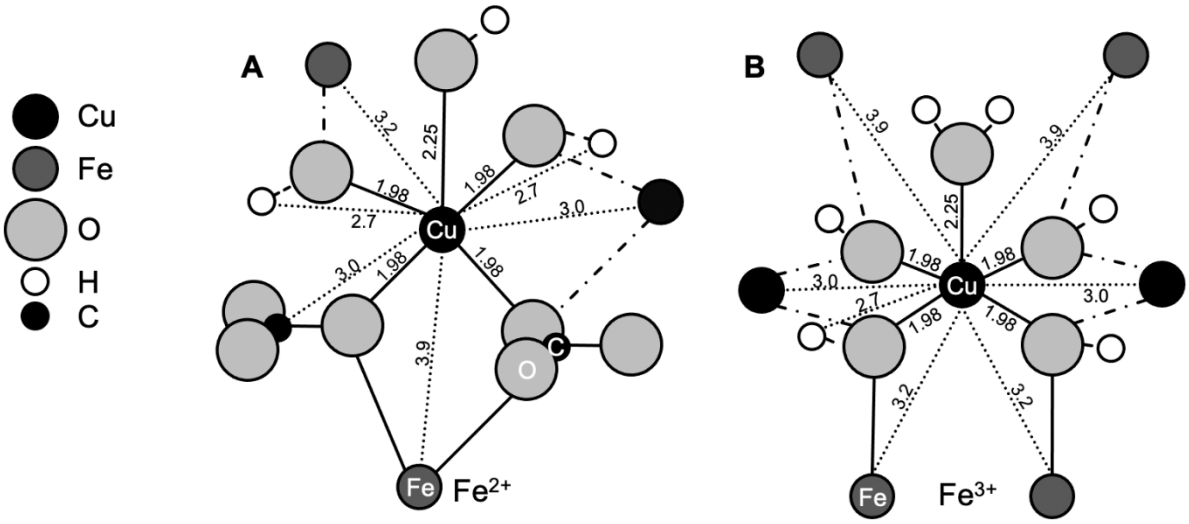

Figure 5.9. Schematic of possible of Cu sorption complex geometries in the solid samples collected after 1008 h of reaction under oxic conditions (c.f. Table 5.4). (A) Sorption to the siderite surface as inner-sphere bidentate complex sharing corners with FeO_6 octahedra via carbonate ligands (*after* Elzinga & Reeder, 2002; Elzinga et al., 2006). Neighbouring atoms of sorbed Cu and possible coordination with Fe atoms from the ferric (oxyhydr)oxide precipitates are also shown. (B) Inner-sphere bidentate sorption complex sharing edges with ferric oxyhydroxide $Fe(OH,O)_6$ octahedra (*after* Peacock & Sherman, 2004), including neighbouring Cu atoms of sorption clusters and possible coordination to Fe atoms of surrounding ferric (oxyhydr)oxide nanoprecipitates as in interparticle nanopores (*after* Stegemeier et al., 2015). A mixture of both variations likely contributed to the EXAFS spectrum. Bond lengths, angles and atom sizes are not to scale.

5.4. Redox-coupled Cu removal and siderite dissolution

5.4.1. Summary of Cu uptake under oxic and anoxic conditions

The reaction of natural siderite in acidic, Cu(II)-bearing oxic and anoxic aqueous solutions over a total duration of 1008 h results in the uptake of 80% of the initially dissolved Cu(II) from oxic, and complete Cu(II) removal within ~505 h from anoxic aqueous solutions. The uptake of Cu(II) is closely related to the dissolution of siderite, marked by immediate Fe(II) release and an increase of the solution pH from 3.0 to 4.6 and 5.1 within the first 0.5 h of reaction under oxic and anoxic conditions, respectively. Under both redox conditions this pH increase and the presence of O_2 and/or Cu(II) as oxidation agents allows secondary ferric iron phases to stabilise from the first 0.5 h of reaction onwards. The solid reaction products recovered from the solutions after 1008 h of reaction are nanoscale goethite and hematite in the oxic, and microcrystalline lepidocrocite and nanoscale native copper in the anoxic system.

Copper is removed from the aqueous solutions by coupled adsorption and reduction reactions. High-resolution and bulk sample spectroscopic X-ray absorption and photoelectron analyses of the final solid reaction products show that after 1008 h of reaction under oxic conditions, Cu(II) is bound as inner-sphere sorption complex on the ferric (oxyhydr)oxide precipitates and, possibly, at the siderite surface. Locally, as well as in bulk, approximately 10 to 30% of solid-bound Cu is reduced to Cu(I) species in association with oxidised iron oxyhydroxides; higher degrees of Cu reduction are thereby correlated with higher degrees of Fe oxidation. No separate solid phases containing Cu as a major component were detected in the oxic reaction products. The same analyses performed on the final solid reaction products show that after 1008 h of reaction under anoxic conditions, approximately 80% of the initially dissolved Cu(II) species are completely reduced and precipitated as nanocrystalline metallic copper (the only solid Cu-phase). Notably, despite the evidence of nanocrystalline Cu metal in the XRD patterns and XAFS and XPS spectra, particulate Cu(0) could not be unambiguously identified microscopically. However, based on high-resolution TEM imaging and XPS analyses native copper is interpreted to be closely associated with and possibly entrapped within the ferric (oxyhydr)oxide nanoprecipitate clusters. Approximately 20% of the solid-bound Cu is reduced to Cu(I) as indicated by LCF of XANES spectra collected from the bulk sample. These reduced Cu species and trace amounts of Cu(II) hydroxide-coordinated species in the XPS spectrum of the ultrafine reaction products are associated with the ferric precipitates and thus interpreted as remnants of early reaction stage sorption species.

These results demonstrate the efficacy of Cu(II) uptake from initially acidic aqueous solutions during siderite dissolution under oxidising and reducing conditions. It is, however, fundamental to understand the mechanisms leading to these observations to evaluate the applicability of siderite for remediation purposes of metal-contaminated natural environments exposed to fluctuating redox conditions.

5.4.2. Siderite dissolution in the presence of oxidants

The presence of oxidants such as oxygen and/or Cu(II) strongly affects the dissolution of siderite and its precipitation products. Siderite dissolution in acidic aqueous solutions is controlled by the protonation of the carbonate surface site. At pH 3, proton promoted dissolution commences readily at a fast rate ($R \approx 10^{-9.1}$ to $10^{-10.0}$ mol cm^{-2} s^{-1}; Golubev et al., 2009) leading to a sharp increase of the reactive solution pH independent of the redox condition

(Figure 5.1A and C; Duckworth & Martin, 2004b). Dissolution rates slow substantially with increasing pH of ≥ 5.5 until becoming pH independent at circumneutral conditions (Pokrovsky & Schott, 2002; Duckworth & Martin, 2004a). Around pH 5, the interaction with oxidants such as O_2 and/or redox-active metals leads to oxidative precipitation of hydrous ferric oxide precipitates near or at the siderite surface (e.g., Duckworth & Martin, 2004b; Tang & Martin, 2011; Renard et al., 2017; Bibi et al., 2018). Such (surface) precipitation occurred in both oxic and anoxic solutions during the first hours of siderite interaction with Cu(II) (Figure 5.1A and C). Differences in the dissolution–precipitation processes and reaction products in the oxic vs. anoxic systems resulted from the different oxidants present in the two study systems, namely O_2 + Cu(II) (oxic) and Cu(II) alone (anoxic).

5.4.2.1. Homogeneous versus heterogeneous redox reactions

Siderite dissolution is a surface-controlled process hence surface reactions play a key role in the dissolution-coupled precipitation of oxidised ferric iron. Although the homogeneous interaction of the aqueous Fe^{2+}–Cu^{2+} redox couple may result in ferric and cuprous precipitates within minutes of interaction in anoxic pH 5.5 aqueous solutions (Matocha et al., 2005), the redox processes observed in this study are more likely surface related (heterogeneous). The absence of separate Cu_2O solids though presence of Cu(I) in close association with the ferric surface precipitates in both study systems (Figures 5.5 and 5.7), and the carbonate associated Cu(II) in the oxic system (Figure 5.7), suggest that the redox reactions responsible for the Fe(III) precipitation–Cu reduction occurred at the dissolving siderite surface. This assumption is supported by the Gibbs free energies of reactions (ΔG_r^o) describing the overall processes of the oxic and anoxic systems, calculated based on the standard state Gibbs free energies of formation (ΔG_f^o) of the reagents and products identified after 1008 h of reaction (Tables 5.5 and 5.6; thermodynamic data in Tables A16–18). The ΔG_r^o of reactions considering structural Fe^{II} as reductant are lower compared to the ΔG_r^o of reactions considering aqueous Fe^{2+} as reductant. This suggests that heterogeneous reduction of Cu(II) via the Cu^{2+}–$Fe^{II}CO_3$ redox couple is thermodynamically more favourable than homogeneous reduction by the Fe^{2+}–Cu^{2+} redox couple in aqueous solution. This is very important because (1) it confirms solid-associated Fe^{II} as reductant and that the Cu^{2+}–$Fe^{II}CO_3$ couple determines the redox reaction (c.f., White & Peterson, 1996; Liger et al., 1999; Williams & Scherer, 2004; Pedersen et al., 2005; Gorski et al., 2016; Taylor et al., 2017; Stewart et al., 2018; Perez et al., 2019), and because (2) it implies that Cu(II) sorption to the siderite surface is required to initiate the reduction of Cu(II) under both redox conditions. Consequently, this explains the partial reduction of up to 30% solid-

bound Cu to Cu(I) species detected by XPS and (local) XANES analyses in the samples reacted for 1008 h under both oxic and anoxic conditions (reaction 4; Table 5.5 and 5.6).

Table 5.5. Proposed reactions describing the observations made on siderite interaction with aqueous Cu(II) under oxic conditions. Gibbs free energies (ΔG_r^o) were calculated based on the standard state Gibbs free energies of formation (ΔG_f^o) of the mineral and aqueous species for the reactions at 25 °C given in Tables A16–A17.

	Reactions under oxic conditions	**Remarks**
1	**$FeCO_3$** + $2H^+ \longrightarrow Fe^{2+}$ + **H_2CO_3**	*Siderite dissolution*
2a	Fe^{2+} + ¼**O_2** + $H^+ \longrightarrow Fe^{3+}$ + ½H_2O	*Fe^{2+} oxidation by O_2* (0.46 V)[a]
2b	Fe^{2+} + **Cu^{2+}** ⟶ **Cu^+** + Fe^{3+}	*Cu reduction by Fe^{2+}* (–0.61 V)[a]
3	Fe^{3+} + 3**H_2O** ⟶ $Fe(OH)_3$ + 3**H^+**	*Ferrihydrite formation*[b]
4a	**$FeCO_3$ + Cu^{2+} + 3H_2O ⟶ $Fe(OH)_3$ + Cu^+ + H_2CO_3 + H^+**	ΔG^o_{r4a} = 45.5 kJ mol^{-1}
4b	**$FeCO_3$ + ¼O_2 + 2½H_2O ⟶ $Fe(OH)_3$ + H_2CO_3**	ΔG^o_{r4b} = –58.0 kJ mol^{-1}
	Goethite formation (within first hours of reaction)	
5	$Fe(OH)_3$ + $H^+ \longrightarrow Fe(OH)_2^+$ + H_2O	*Ferrihydrite dissolution*
6	$Fe(OH)_2^+ \longleftrightarrow Fe_2(OH)_4^{2+} \longleftrightarrow$ polymerisation ⟶ **α-FeOOH** + H^+	*Transformation to Goethite*
7a	**$FeCO_3$ + Cu^{2+} + 2H_2O ⟶ α-FeOOH + Cu^+ + H_2CO_3 + H^+**	ΔG^o_{r7a} = 27.1 kJ mol^{-1}
		Eh_{r7a} = 0.65 V[c] *(after 1 h)*
7b	**$FeCO_3$ + ¼O_2 + 1½H_2O ⟶ α-FeOOH + H_2CO_3**	ΔG^o_{r7b} = –76.4 kJ mol^{-1}
		Eh_{r7b} = 0.92 V[c] *(after 1 h)*
	Transformation to Hematite (after ~240 h)	
8	2$Fe(OH)_3$ ⟶ α-Fe_2O_3 + 3H_2O	ΔG^o_{r8} = –747.2 kJ mol^{-1}
9	2α-FeOOH ⟶ α-Fe_2O_3 + H_2O	ΔG^o_{r9} = –1.9 kJ mol^{-1}
10a	**2$FeCO_3$ + 2Cu^{2+} + 3H_2O ⟶ α-Fe_2O_3 + 2Cu^+ + 2H_2CO_3 + 2H^+**	ΔG^o_{r10} = 53.1 kJ mol^{-1}
		Eh_{r10} = 2.06 V[c]
10b	**2$FeCO_3$ + ½O_2 + 2H_2O ⟶ α-Fe_2O_3 + 2H_2CO_3**	ΔG^o_{r11} = –153.8 kJ mol^{-1}
		Eh_{r11} = 0.91 V[c]

[a]Standard redox potential (E^0) of the full cell reaction. [b]2-line Fhy. [c]Redox potential of the reactions (Eh_r) was calculated assuming a pH dependence of the redox reaction, and thermodynamic equilibrium between the *Eh* and E^0 of the redox reactions involving aqueous Fe^{2+} and Fe^{III} (oxyhydr)oxides (Gorski et al.; 2016; Stewart et al.; 2018). Note, however, that these are approximate values as the system has not reached equilibrium.

5.4.2.2. Enhanced oxidative siderite dissolution by O_2 and Cu adsorption

Upon immersion of siderite into the acidic Cu(II)-bearing **oxic** aqueous solution, siderite dissolves via three parallel reactions: (1) protonation, (2) oxidation induced by O_2, and (3) oxidation induced by Cu(II). At pH < 4, *protonation* of the $>CO_3^-$ and $>Fe^{II}O^-$ coordinative surface sites to $>CO_3H^0$ and $>Fe^{II}OH^0$ controls the dissolution (Pokrovsky et al., 1999; Pokrovsky & Schott, 2002). Under oxic conditions, aqueous *oxygen* in close proximity to the siderite surface also reacts with the hydrated surface sites, whereby electron transfer may occur either via the surface hydroxyl groups or, subsidiarily, via the carbonate groups acting as bridging ligands (e.g., Sulzberger et al., 1989; Wehrli et al., 1989; Duckworth & Martin, 2004b). The either way resulting $>Fe^{III}(OH)_2^+$ surface species are less stable in the surface structure and dissociate into the solution (rate-controlling step; Pokrovsky & Schott, 2002; Duckworth & Martin, 2004b). The more stable aqueous $Fe^{3+}(OH)_2^+$ species most likely represent the initial growth units for the observed ferric (hydr)oxide surface precipitates, particularly at pH ≳ 4.5 when oxidised Fe species may become dominant (reaction 4a,b; Table 5.5; Cornell & Schwertmann, 2003; Morgan & Lahav, 2007). Simultaneously, *Cu(II)* sorption to the siderite surface likely occurred, providing a favourable electron transfer pathway via overlapping d-orbitals of the transition metals $Fe^{II}(s)$ and $Cu^{2+}(aq)$ (Sherman, 1987; Coughlin & Stone, 1995; Liger et al., 1999; Williams & Scherer, 2004; Taylor et al., 2017). Although the initial Cu(II) concentrations exceeded the dissociated proton concentrations (1.53×10^{-3} mol kg^{-1} Cu(II) vs. pH 3.04, equivalent to $[H^+] \approx 0.91 \times 10^{-3}$ mol kg^{-1}), proton consumption (pH increase) was three orders of magnitude higher than the consumption of dissolved Cu(II) species within the first 0.5 h of reaction. In other words, surface protonation initially outcompeted Cu(II) sorption, causing the immediate and sharp increase in dissolved Fe^{total} concentrations at the start of the experiments. This is supported by the fact that protons rapidly and equally adsorb to both the metal and the carbonate sites, whereas aqueous Cu^{2+} first needs to partially loose its hydration shell to then preferentially sorb to the carbonate sites (e.g., Van Cappellen et al., 1993; Pokrovsky & Schott, 2002; Elzinga & Reeder, 2002; Schott et al., 2009), which makes the sorption process of hydrated Cu^{2+} slower compared to H^+ sorption. Consequently, siderite dissolution in the presence of O_2 was not significantly affected by the sorption of Cu(II). However, the resulting Cu^{2+}–$FeCO_3$ redox couple likely enhanced surface-Fe^{II} oxidation in addition to the oxidative action of O_2 (Stumm & Lee, 1961). At pH ≥ 4.5 (after 0.5 h), as proton promoted dissolution starts to slow markedly, dissolution is hence driven by Fe oxidation and consumption by (near-)surface precipitation of ferric iron (hydr)oxides (c.f.,

Duckworth & Martin, 2004b; Tang & Martin, 2011; Renard et al., 2017), which can be described by the successive reactions

$$>Fe^{II}OH_2^+ + O_2(aq) + 2H^+ \longrightarrow >Fe^{III}(OH)_2^0 + H_2O$$

$$\rightleftharpoons >[Fe^{III}(OH)_2]^* + H_2O \longrightarrow Fe^{III}(OH)_3(s) + H^+ \qquad \text{(eq. 5.1)},$$

$$>Fe^{II}OH_2^+ + Cu^{2+} + H_2O \longrightarrow >[Fe^{III}OCu^{I}OH]^0* + 3H^+$$

$$\rightleftharpoons >[Fe^{III}OCu^{I}OH]^0 + H_2O \longrightarrow Fe^{III}(OH)_3–Cu^+ \qquad \text{(eq. 5.2)}.$$

Note that in this notation one charge is considered to be associated with the surface (the charge of $>Fe^{II}OH_2^+$ is +1; Pokrovsky & Schott, 2002). The asterisk indicates a metastable transition (or activation) complex, and "$–Cu^+$" indicates sorption to $Fe(OH)_3$. This series of surface reactions likely describes the early mechanism of Cu(II) uptake and reduction coupled to siderite dissolution under oxic conditions, whereby Fe^{II} oxidation by O_2 is spontaneous and thus thermodynamically more favourable than the oxidation reaction by Cu(II) (c.f., reactions 4a,b in Table 5.5).

The removal of dissolved Cu(II) from oxic aqueous solutions occurs via two pathways: (1) adsorption and reduction at the siderite surface, and (2) adsorption and entrapment within the ferric nanoprecipitates. The initial sorption of Cu(II) to the siderite surface (equation 5.2 and reaction 4a in Table 5.5) results in the partial reduction of 10 to 30% of solid-bound Cu(II) to Cu(I) closely associated with the ferric (hydr)oxide nanoprecipitates. Notably, solid-bound Cu(I) species are heterogeneously dispersed and concentrated in infrequent patches (Figure 5.7B and D), which might suggest some form of segregation (Martínez & McBride, 1998) of what most likely are surface (sorption) species rather than precipitates. Additionally, as the siderite surface becomes progressively covered by ferric iron precipitates as a result of continued siderite dissolution–precipitation reactions, less 'fresh' siderite surfaces are available for Cu(II) reduction. Consequently, adsorption to the ferric surface precipitates soon dominates Cu(II) uptake (*see* section 5.3.3., EXAFS), resulting in a predominantly homogeneous distribution of the remaining 70 to 80% of solid-bound Cu(II) sorption species (Figure 5.7 A and C).

In contrast to other studies on siderite interaction with redox-active metals such as Cr (e.g., Tang & Martin, 2011; Bibi et al., 2018) and As (e.g., Renard et al., 2017), coprecipitation of mixed Cu–Fe (oxyhydr)oxides or incorporation into goethite (e.g., Manceau et al., 2000; Frierdich & Catalano, 2012b) or siderite is not supported by the EXAFS fit results. That is, the

assessed coordination of Cu by about 4.3 oxygens does not agree with the typical distorted octahedral 6-fold coordination of Cu in (hydr)oxides and carbonates (e.g., Süsse, 1967; Oswald et al., 1990; Manceau et al., 2000; Elzinga & Reeder, 2002; Elzinga et al., 2006). However, aggregation, aging, and growth of the nanoprecipitates to clusters and rods likely enclosed the Cu sorption complexes within the interparticle nanopores, which would explain the relatively high coordination number for an adsorbed species (Table 5.4; Gilbert et al., 2009; Stegemeier et al., 2015). The adsorption of Cu to siderite and the Fe precipitates is further supported by the mixed character of oxide- and carbonate-coordinated Cu sorption geometries indicated by the XAFS results, which strongly suggest partial scattering contributions of carbonate coordination (~24%) in addition to the prevalent coordination with hydroxyl groups (~75%; Figure 5.7–5.9, Table 5.4).

5.4.3. Cu reduction by siderite in the absence of O_2

Heterogeneous reduction of Cu(II) determines the reactions under anoxic conditions. As discussed in section 5.4.2.1., the Cu^{2+}–$Fe^{II}CO_3$ redox couple is thermodynamically favourable over homogeneous Cu(II) reduction by aqueous Fe^{2+}, hence Cu(II) sorption to the siderite surface is required for the Fe(II) oxidation–Cu(II) reduction observed in the anoxic system. At the initial pH of 3, proton promoted dissolution outcompetes Cu(II) sorption leading to a sharp increase in pH up to 5.1 within 0.5 h of reaction (Figure 5.1B). Also, Cu(II) is a much weaker oxidant than O_2 and the detachment of the oxidised $>Fe^{III}OH_2^+$ surface groups from the reacting siderite surface is the rate limiting step. Hence in the absence of molecular oxygen, the relatively slower electron transfer between sorbed Cu^{2+} and structural Fe^{II} likely retards the detachment and therewith the dissociation of Fe species into solution. This may explain the extremely low Fe^{total} concentrations of 0.038×10^{-3} mol kg^{-1} measured in the anoxic solution up until about 60 h of reaction. As this early-stage dissolution–precipitation process is essentially very similar to the oxic system, one would expect (1) a continuous and steady uptake of dissolved Cu and Fe species from the aqueous solution, leading to (2) a mostly homogeneous distribution of Cu associated with siderite and ferric precipitates, and (3) predominantly Cu(I) species, possibly with some remnant Cu(II) occurrences. In contrast, over the course of 1008 h of reaction there is (1) an apparent change in seemingly strongly coupled behaviour of dissolved Fe and Cu, leading to (2) heterogeneous distribution of Cu closely associated with clusters of sub-microcrystalline lepidocrocite, and (3) near complete reduction to metallic Cu(0) associated with the ferric precipitates rather than with the siderite surface.

Key to understanding the mechanisms controlling these observations is the sudden and coupled behavioural change of the dissolved metals in the anoxic aqueous solution observed between ≲168 h and 505 h of reaction (*see* Figure 5.1B and D). Up to ~60 h of reaction, measured Fe^{total} concentrations increase nearly linearly before starting to increase twice as rapidly until about 168 h of reaction. From then on, Fe concentrations increase nearly six times as rapidly until peaking after 505 h of reaction while dissolved Cu concentrations decrease simultaneously at reverse rates. As soon as all Cu is removed from solution, dissolved Fe concentrations start to drop at slowed rates. This synchronous behavioural change of Fe and Cu in the reactive solution strongly suggests that the previously accelerated Fe release is closely linked and crucial to Cu uptake.

In other words, this coupled behaviour of the dissolved metals suggests that siderite dissolution is driven by the interaction with Cu, which in this case is further linked to Fe oxidation (c.f., reactions 1–4; Table 5.6). Notably, during the early period of relatively constant Fe release up to ~60 h of reaction, spherical precipitates become increasingly prominent at the reacting siderite surface (*see* Figure A8). These precipitates can be interpreted as ferric (hydr)oxides that result from the oxidation of *one* (near)surface Fe(II) by *one* adsorbed Cu(II) (equation 5.2; reaction 1–4; Table 5.6). As there is no molecular oxygen in the anoxic system to accelerate the process of oxidative Fe precipitation, the redox reaction is controlled by the sorption behaviour of Cu(II), which shows the typical trend of initially fast followed by slower sorption until about 168 h of reaction. As a result, approximately 20% of the dissolved Cu(II) is reduced to Cu(I) species found in close association with ferric (oxyhydr)oxide (Figure 5.7; Table 5.4). However, after 1008 h of reaction under anoxic conditions, > 70% of solid-associated and 100% of crystalline Cu is present as Cu(0). Thus, equation 5.2 is insufficient to explain the near complete Cu(II) reduction and increase in Fe(II) release observed in the anoxic system. Reactions 1–4 in Table 5.6 are furthermore insufficient to explain the formation of lepidocrocite as main reaction product found in close association with (fully) reduced Cu in the anoxic and in part in the oxic solid samples after 1008 h of reaction (e.g., Figure 5.4 and 5.7). Neither do reactions 4a and b in Table 5.5 suffice to explain the formation of goethite and hematite as main reaction products in the oxic system.

Table 5.6. Proposed reactions describing the observations made on siderite interaction with aqueous Cu(II) under anoxic conditions. Gibbs free energies (ΔG_r^o) were calculated based on the standard state Gibbs free energies of formation (ΔG_f^o) of the mineral and aqueous species for the reactions at 25 ºC are given in Tables A16–A17.

	Reaction under anoxic conditions	**Remarks**
	Reaction phase I	*Reaction up to ~168 h*
1	$\mathbf{FeCO_3} + 2H^+ \longrightarrow Fe^{2+} + \mathbf{H_2CO_3}$	*Siderite dissolution*
2	$Fe^{2+} + \mathbf{Cu^{2+}} \longrightarrow \mathbf{Cu^+} + Fe^{3+}$	*20% Cu red.*, E^0 = –0.61 V[a]
3	$Fe^{3+} + 3\mathbf{H_2O} \longrightarrow \mathbf{Fe(OH)_3} + 3\mathbf{H^+}$	*Ferrihydrite formation*
4	$\mathbf{FeCO_3 + Cu^{2+} + 3H_2O \longrightarrow Cu^+ + Fe(OH)_3 + H_2CO_3 + H^+}$	ΔG^o_{r4} = 45.5 kJ mol^{-1} Eh_{r4} = –0.03 V[c]
	Reaction phase II	*Reaction ~144 to 1008 h*
1	$\mathbf{FeCO_3} + 2H^+ \longrightarrow Fe^{2+} + \mathbf{H_2CO_3}$	*Siderite dissolution*
5	$Fe^{2+} + \mathbf{Cu^+} \longrightarrow \mathbf{Cu^0} + Fe^{3+}$	*Complete Cu red.*, E^0 = –0.25 V[a]
3	$Fe^{3+} + 3\mathbf{H_2O} \longrightarrow Fe(OH)_3 + 3H^+$	*Ferrihydrite formation*
6	$Fe(OH)_3 + H^+ \longrightarrow Fe(OH)_2^+ + H_2O$	*Ferrihydrite dissolution*
7	$Fe(OH)_2^+ \longrightarrow \boldsymbol{\gamma}\mathbf{\text{-}FeOOH} + \mathbf{H^+}$	*Reprecipitation as lepidocrocite*
8	$\mathbf{FeCO_3 + Cu^+ + 2H_2O \longrightarrow \gamma\text{-}FeOOH + Cu^0 + H_2CO_3 + H^+}$	ΔG^o_{r8} = 1.9 kJ mol^{-1} Eh_{r8} = 0.07 V[c]
	Overall reaction of stages I+II	
4	$\mathbf{FeCO_3} + \mathbf{Cu^{2+}} + 3H_2O \longrightarrow Cu^+ + Fe(OH)_3 + \mathbf{H_2CO_3} + H^+$	*Sid. dissolution, Cu reduction*
6	$Fe(OH)_3 + H^+ \longrightarrow Fe(OH)_2^+ + H_2O$	*Ferrihydrite dissolution*
7	$Fe(OH)_2^+ \longrightarrow \gamma\text{-}FeOOH + H^+$	*Reprecipitation as lepidocrocite*
8	$FeCO_3 + Cu^+ + 2\mathbf{H_2O} \longrightarrow \boldsymbol{\gamma}\mathbf{\text{-}FeOOH} + \mathbf{Cu^0} + H_2CO_3 + \mathbf{H^+}$	*Complete Cu reduction*
9	$\mathbf{2FeCO_3 + Cu^{2+} + 4H_2O \longrightarrow 2\gamma\text{-}FeOOH + Cu^0 + 2H_2CO_3 + 2H^+}$	ΔG^o_{r9} =38.7 kJ mol^{-1} Eh_{r9} = 0.61 V[c]
	$2Fe^{2+} + Cu^{2+} \longrightarrow Cu^0 + 2Fe^{3+}$	E^0 = 0.34 V – 0.77 V = –0.43 V[a]

[a]Standard redox potential (E^0) of the full cell reaction. [b]2 line-Fhy. [c]Redox potential of the reactions (Eh_r) were calculated based on the proposed thermodynamic agreement of the *Eh* and E^0 values of the aqueous Fe^{2+} and mineral (oxyhydr)oxides, and the pH dependence of the redox reaction noted by Gorski et al. (2016) and Stewart et al. (2018). Note, however, that these are approximate values as the system has not reached equilibrium. Sid. = siderite; red. = reduction.

5.4.3.1. Stepwise Cu(II) reduction

Redox reactions including Fe and Cu are strongly influenced by the concentrations of the reductant, oxidant, and protons in the system (e.g., Coughlin & Stone, 1995; White & Peterson, 1996). The pH of the reactive anoxic solution remained relatively stable at pH 5.4 to 5.7 from 2 h of reaction onwards, suggesting that the pH effect may be negligible for the majority of the experiment duration. In contrast, changes of dissolved metal concentrations through continuous Fe release and Cu uptake may have a much more significant effect. That is, depending on the initial Fe^{2+}/Fe^{3+} concentrations, traces of Cu(II) can increase Fe(II) oxidation rates via *stepwise reduction* of one Cu(II) ion by two Fe(II) ions (*see* reactions 2 and 5; Table 5.6; Stumm & Lee, 1961). Similarly, Cu(II) concentrations exceeding 10^{-4} mol kg^{-1} may strongly promote the reduction of Cu(II) by structurally bound Fe(II) (shown for magnetite; White & Peterson, 1996). Coughlin & Stone (1995) further reported that a "threshold" concentration of 1.0×10^{-3} mol kg^{-1} Fe(II) was required for an observed gradual but significant increase of 5.0×10^{-6} mol kg^{-1} Cu(II) uptake by goethite under anoxic conditions. It is thus likely that in the anoxic study system some form of threshold concentration of Fe(II) and/or Cu(II) was reached between 60 and 168 h of reaction, leading to the significant and near-linearly coupled increase in aqueous Fe and decrease in aqueous Cu concentrations until all dissolved Cu was consumed after ~505 h of reaction.

This observed change in aqueous metal concentrations also affects the redox potential (*Eh*) of the suspension (*see* section 1.2.4.). More specifically, a change in the *Eh* may indicate increased complex formation between redox couples such as Cu^{2+}–$FeCO_3$ (Stumm & Sulzberger, 1992). At lower *Eh* conditions, more strongly reduced species are dominant. From the negative *Eh* determined for reaction 4 (Table 5.6), it can be inferred that the heterogeneous reduction of Cu(II) to Cu(I) and thence the decrease in Cu(II) concentrations lowered the redox potential of the suspension. Simultaneous increase of Fe(II) resulting from continuous siderite dissolution likely had the same effect, which is supported by PHREEQC model calculations based on the measured dissolved metal concentrations in the anoxic aqueous solution at selected time steps (*see* Table A20). The model results indicate a drop in the redox potential and a predominance of Cu(I) over Cu(II) aqueous species at 6 h of reaction which agrees with reaction 4 (Table 5.6). Hence, during the first ~60 h of reaction under anoxic conditions, Cu(II) was likely only reduced to Cu(I) (*first reduction step*; c.f., Stumm & Lee, 1961). A subsequent increase in *Eh* indicated by the model at 168 h likely represents the *second reduction step* to Cu(0) which agrees with reaction 8 (Table 5.6). Notably, reaction 8 includes the transformation

of $Fe(OH)_3$ to lepidocrocite. In the presence of aqueous Fe(II), this transformation reaction may be accompanied by changes in pH and *Eh* of the reactive solution because Fe(II) oxidation and precipitation as $Fe(OH)_3$ produces protons and increases the *Eh* (reactions 2–3), whereas during the transformation reaction the pH and *Eh* are buffered (reactions 6–7), before a drop in pH and an increase in *Eh* may indicate the end of the transformation reaction (reaction 8; Table 5.6; c.f. Schwertmann & Fechter, 1994). Therefore, the second reduction step of Cu(I) to Cu(0) was likely associated with lepidocrocite formation, which explains the spatial association between the two phases (e.g., Figure 5.4 and 5.7).

This multistep process is further supported by the morphology of siderite grains after 1008 h of reaction under anoxic conditions, where smooth surfaces show little to no spherical surface precipitates but larger lath-shaped lepidocrocite crystallites (Figure 5.4B). Hence, nucleation and growth of lepidocrocite likely occurred at the expense of the ferric nanoparticle precursors. Consequently, newly exposed siderite surfaces allow further siderite dissolution, increasing Fe(II) release into the reactive solution (Figure 5.1B). This process may also be responsible for the segregation of the reduced Cu phase(s) within ferric nanoparticle clusters and the close association with the lepidocrocite crystallites, respectively (Figure 5.4 and 5.7H; e.g., Martínez & McBride, 1998).

5.4.4. Oxidative Fe precipitation and phase transformations

5.4.4.1. The effect of Cu(II), Fe(II), and O_2 on siderite oxidation products

The stepwise reduction of Cu(II) likely also played an important role in the formation of the crystalline ferric iron reaction products identified in the oxic and anoxic systems. More specifically, the nanoparticulate $Fe(OH)_3$ formed from Fe(II) oxidation by O_2 and/or Cu(II) (reactions 1–4, Tables 5.5 and 5.6) was only observed in SEM images of early-stage solid reaction products (e.g., Figure A10 A–C). This phase was however, absent or below detectable quantities in the samples collected after 1008 h of reaction under either redox condition. Based on the high similarity to ferric iron phases reported to have formed at the siderite surface, these early nanoprecipitates are assumed to be ferrihydrite (simplified as $Fe(OH)_3$; c.f., Duckworth & Martin, 2004b; Renard et al., 2017). Ferrihydrite is a thermodynamically metastable nanoparticulate ferric hydrous oxide that readily transforms into energetically more stable and more crystalline ferric (oxyhydr)oxides (e.g., Schwertmann & Murad, 1983; Schwertmann & Fechter, 1994; Schwertmann et al., 1999; Cornell & Schwertmann, 2003; Hansel et al., 2005;

Pedersen et al., 2005; Liu et al., 2007; Boland et al., 2014; Perez et al., 2019). Hence, both goethite (oxic system) and lepidocrocite (anoxic system) most likely formed from this ferrihydrite precursor via dissolution–reprecipitation transformation pathways (Schwertmann & Fechter, 1994; Liu et al., 2007; Boland et al., 2014; Perez et al., 2019).

This transformation pathway is important because both aqueous Cu(II), but particularly dissolved Fe(II) strongly affect the formation and transformation of the iron oxides (e.g., Cornell, 1988; Cornell & Giovanoli, 1988; Tronc et al., 1992; Martínez & McBride, 1998; Williams & Scherer, 2004; Hansel et al., 2005; Pedersen et al. 2005; Liu et al., 2007; Yang et al., 2010; Larese-Casanova et al., 2012; Boland et al., 2014; Perez et al., 2019). The rate of transformation is thereby limited by ferrihydrite formation from Fe(II) oxidation (Schwertmann & Fechter, 1994), which in turn depends on the oxidant/redox couple (c.f., Stumm & Lee, 1961; Duckworth & Martin, 2004b; Renard et al., 2017). In the oxic study system, Fe(II) oxidation is controlled by oxygen, whereas in the anoxic system it is controlled by Cu(II). Sorption of Cu(II) may stabilise ferrihydrite from dissolution under conditions of increased ferric (oxyhydr)oxide solubility, retarding the transformation to more crystalline phases (Cornell, 1988; Cornell & Giovanoli, 1988). Minor amounts of Fe(II) as low as 0.03 to 0.2 × 10^{-3} mol kg^{-1} in turn preferentially promote – or are required for – the transformation from ferrihydrite into lepidocrocite, particularly under anoxic and slightly acidic pH conditions (Schwertmann & Fechter, 1994; Liu et al., 2007; Boland et al., 2014; Perez et al., 2019). It may hence be assumed that it required about 60 h of reaction under anoxic conditions, to reach sufficiently high Fe(II) concentrations of > 0.038 × 10^{-3} mol kg^{-1} to be released to promote the dissolution of ferrihydrite and therewith the transformation into lepidocrocite. This coincided with a decrease in Cu(II) concentrations down to < 1.34 × 10^{-3} mol kg^{-1} below which inhibition of ferrihydrite dissolution becomes negligible ("threshold" concentrations). Simultaneously, previously singly reduced Cu species likely underwent further reduction coupled to additional $Fe(OH)_3$ formation. As a result, for each Cu(II) ion that interacts with one structural Fe(II), three slightly offset reaction pathways occur in the anoxic system: (1) initial Cu(II) sorption to siderite and Cu(II) reduction-coupled (near)-surface $Fe(OH)_3$ precipitation (reactions 1–4), (2) dissolution–reprecipitation controlled transformation of $Fe(OH)_3$ to lepidocrocite (reactions 6–7), and (3) iron oxide transformation coupled Cu reduction (reactions 1–8; Table 5.6). As the formation of native copper requires a stepwise reduction of Cu(II) by two Fe(II) (e.g., Stumm & Lee, 1961), processes (1) and (2) must have occurred at a ratio of about 2:1. The acidity produced during $Fe(OH)_3$ formation simultaneously fuels siderite dissolution which is increasingly facilitated as more $Fe(OH)_3$ precipitates were consumed at the expense of progressive lepidocrocite

precipitation and growth. This self-accelerating multistep process (summarised in reaction 9; Table 5.6) is reflected in the apparent 1:1 Cu uptake and Fe release into the anoxic solution.

Lepidocrocite is thermodynamically unstable with respect to goethite and hematite, hence a transformation into these more stable minerals is expected over time (Cornell & Schwertmann, 2003). Particularly at high Fe(II) concentrations (2.0 mM) and in the absence of chloride, goethite precipitates at the expense of lepidocrocite (Hansel et al., 2005). Since such high Fe(II) concentrations were not reached throughout the anoxic experiment, the transformation of lepidocrocite to goethite remains very limited – the only indication for this transformation is provided by HRTEM imaging (Figure 5.4F; Table A11). Lepidocrocite is the otherwise only ferric phase found in XRD and XAFS analyses of solids reacted for 1008 h under anoxic conditions. The presence of Fe(II), increased CO_2 to O_2 ratios may hinder the transformation of lepidocrocite to goethite under anoxic conditions (Carlson & Schwertmann, 1990; Hansel et al., 2005), but favour the conversion of ferrihydrite to goethite under oxic conditions through sorption of carbonate to the goethite surface (Ostergren et al., 2000a; Villalobos & Leckie, 2000). As carbonate concentrations in the anoxic system are estimated to be very low ($\lesssim 1.0 \times 10^{-3}$ mol kg^{-1} only originating from siderite dissolution; Table A20), these dependencies additionally explain the predominance of lepidocrocite over goethite in the anoxic reaction products.

Under oxic conditions, in contrast, the rapid oxidation of Fe(II) is dominated by oxygen which promotes the transformation of $Fe(OH)_3$ by producing an excess of $Fe^{3+}(OH)_2^+$ that may more readily polymerise to goethite rather than directly precipitate as lepidocrocite (e.g., Liu et al., 2007; reaction 6; Table 5.6). This transformation may be additionally facilitated by some sorption of dissolved carbonate to the building units of goethite, which allows the assemblage of the corner-sharing double band structure of goethite but hinders the linkage of the edge-sharing double band structure in lepidocrocite (Carlson & Schwertmann, 1990). Yet LCF of Fe K-edge spectra obtained from samples reacted for 1008 h under oxic conditions showed the presence of lepidocrocite, which was associated with heterogeneous occurrences of Cu(I) (Figure 5.7B; Tables 5.2 and 5.3). Lepidocrocite is typically an oxidation product of Fe(II) interaction with ferric iron oxides (Cornell & Schwertmann, 2003; Hansel et al., 2005; Pedersen et al., 2005; Larese-Casanova et al., 2012; Liu et al., 2007; Boland et al., 2014; Perez et al., 2019). This spatial correlation between Cu(I) and lepidocrocite may provide evidence for the partial and limited (initial) Cu(II) reduction–Fe(II) oxidation reaction, while the dominance of goethite (and hematite) is representative for oxygen-induced Fe oxidation. Observed colour

changes of the reactive siderite suspensions from initially pale grey to ochre confirm the early formation of goethite within 1 to 6 h of reaction under oxic conditions, whereas a colour change into luscious orange marked lepidocrocite formation after ~96 to 168 h of reaction under anoxic conditions. This time difference confirms the proposed two different pathways of ferrihydrite transformation under the two study conditions. That is, lepidocrocite formation is linked to the slower stepwise reduction of Cu(II) in the anoxic system, while the faster Fe(II) oxidation rate by O_2+Cu(II) results in a faster transformation of $Fe(OH)_3$ into goethite (and hematite) in the oxic system. Under both redox conditions, the lack of microscopic and spectroscopic evidence for ferrihydrite by the end of the experiments suggests near complete transformation to FeOOH while no Cu was released during any transformation reaction.

Further formation of hematite under oxic conditions results from oxygen-driven Fe(II) oxidation, which is thermodynamically favoured over the oxidation by Cu(II) (reaction 7b and 10b; Table 5.5). However, Cu(II) may additionally promote hematite formation, which is generally a transformation product of ferrihydrite through aging, internal rearrangement, and dehydration at circumneutral pH (Schwertmann & Murad, 1983). The successive colour change of the oxic suspension into deep reddish-brown after 240 h marked advanced hematite formation, most likely via ferrihydrite transformation within the nanoparticulate clusters (reaction 8; Figure 5.3E), or directly from siderite surface oxidation (reaction 10b; Table 5.5).

5.4.4.2. The effect of redox strength on metal uptake mechanisms by siderite

In all presented study systems where an oxidant was present (here, Cu(II)±O_2), spherulitic surface precipitates formed within the first hours of siderite dissolution. This observation agrees with previous studies on siderite–metal interaction in the presence of oxidants such as O_2, As(V), Cr(VI), and/or U(VI), reporting ferrihydrite-like (e.g., Duckworth & Martin 2004b; Erdem et al., 2004; Ithurbide et al., 2009; Ithurbide et al., 2010; Tang & Martin, 2011) and/or goethite (e.g., Guo et al., 2010; Guo et al., 2011; Renard et al., 2017; Füllenbach et al., 2020) and lepidocrocite (Guo et al., 2010; Guo et al., 2011; Bibi et al., 2018; this study) precipitation over a wide range of pH ~3 to 10 and within < 1 to 4 h and 24 h of contact with siderite in aqueous solution.

Some metals are stronger oxidants than others. More specifically, As(III) is more likely oxidised by O_2 than As(V) is reduced upon interaction with siderite (Jönsson & Sherman, 2008; Guo et al., 2010; Guo et al., 2011; Renard et al., 2017). No ferric reaction products have been reported after siderite interaction with As(V) under anoxic conditions (Jönsson & Sherman,

2008) which suggests that As(V)–siderite is a relatively weak redox couple and ferric reaction products reported from studies performed under oxic conditions resulted from siderite oxidation by O_2. In contrast, Cr(VI) is rapidly and completely reduced under all reported pH and regardless of the presence of O_2 (Wang & Reardon, 2001; Erdem et al., 2004; Tang & Martin, 2011; Bibi et al., 2018). The rapid precipitation of ferric (oxyhydr)oxides and sparingly soluble $Cr^{III}_{1-x}Fe^{III}_{x}(OH)_3$ under both redox conditions (Tang & Martin, 2011; Bibi et al., 2018), suggests that Cr(VI)–siderite is a very strong redox couple. Additionally, the formation of goethite and lepidocrocite has only been reported in studies of siderite–metal interaction in the presence of O_2 (Guo et al., 2010; Guo et al., 2011; Renard et al., 2017; Füllenbach et al., 2020; this study) and as oxidation product of Cr(VI)–siderite interaction at low pH and low initial Cr(VI) concentrations (Bibi et al., 2018).

The stepwise reduction of Cu(II) by two Fe(II) suggests that the Cu(II)–siderite redox couple is weaker than the strong and more rapid reduction of one Cr(VI) by three Fe(II), but stronger than As(V)–siderite couple leading to no measurable Fe(II) oxidation. Weakly or not redox-active metals that are primarily captured by sorption to ferric (oxyhydr)oxides, such as As(V), hence are likely more dependent on the oxidation of the ferrous component of siderite (e.g., by O_2) than metals forming strong redox couples with siderite. This may further imply that Cr(VI) may outcompete Cu(II) for Fe(II) oxidation, whereas As may have little effect on this redox reaction but may preferentially adsorb to the resulting ferric precipitates.

The Me–siderite redox couple also affects type and transformation of the Fe reaction products. The oxidation of Fe(II) is the rate limiting step for the initial ferric precipitate formation (c.f., Stumm & Lee, 1961; Duckworth & Martin, 2004b; Renard et al., 2017). Ferrihydrite-like phases are the first to form from moderate to strong siderite oxidation reactions. The formation of the more crystalline phases goethite and lepidocrocite, seems to require strong oxidants such as Cr(VI) (Bibi et al., 2018), Cu(II) (this study), and/or O_2 (Wang & Reardon, 2001; Guo et al., 2007; Guo et al., 2010; Guo et al., 2011; Renard et al., 2017; Füllenbach et al., 2020) to induce ferrihydrite transformation into these phases (e.g., Cornell & Giovanoli, 1988; Schwertmann & Fechter, 1994; Cornell & Schwertmann, 2003; Liu et al., 2007; Perez et al., 2019). Notably, in this study, the transformation into goethite upon siderite interaction with Cu(II) and O_2 occurred within 1 to 6 h of reaction, whereas the transformation into lepidocrocite under O_2-free conditions was indicated after ~96 to 168 h of reaction. This difference in reaction times is furthermore attributed to the faster oxidation rate of ferrous iron

by O_2 compared to, and a potentially retarding effect of Cu(II) (c.f., Cornell, 1988; Cornell & Giovanoli, 1988).

5.5. Conclusions and environmental impact

The oxidation pathways and hence the stability of Fe play a critical role in the fate and mobility of Cu in water-saturated, iron-rich environments prone to redox fluctuations. In this study, the ferrous iron carbonate mineral siderite was used to test its efficacy to remove dissolved Cu(II) from oxic and anoxic acidic aqueous solutions. Under the studied conditions, siderite acts as sorbent and reductant while its dissolution provides acid-neutralising carbonate. Upon interaction with siderite, Cu neither forms separate phases with carbonate nor Fe but precipitates as native copper under anoxic conditions.

The results of this study demonstrate that siderite dissolution effectively removes 80 and 100% of initially dissolved Cu(II) concentrations of $1.54 \pm 0.02 \times 10^{-3}$ mol kg^{-1} from acidic oxic and anoxic aqueous solutions within 1008 and 505 h of reaction, respectively. The major uptake mechanisms include: (1) adsorption-induced (heterogeneous) stepwise Cu reduction and Fe oxidation, (2) Cu adsorption to ferric reaction products, and (3) ferric (hydr)oxide transformation coupled to complete Cu reduction. Under both oxic and anoxic study conditions, proton-promoted siderite dissolution leads to an initial increase in solution pH, stabilising ferric precipitates upon heterogeneous oxidation of the ferrous iron component at or near the siderite surface. The resulting type of ferric (oxyhydr)oxide is influenced by the type of oxidant present in the aqueous system.

Under oxic conditions, both O_2–$Fe^{II}CO_3$ and to a lesser extent Cu^{2+}–$Fe^{II}CO_3$ redox couples play the key role for Cu uptake. The fast Fe oxidation by oxygen is enhanced by additional though weaker oxidation by copper, resulting in rapid precipitation of $Fe(OH)_3$ and subsequent transformation into more crystalline goethite and hematite. Approximately 10 to 30% of solid-bound Cu is initially reduced from Cu(II) to Cu(I) sorption species, while continuous Cu(II) adsorption to and entrapment within interparticle pore spaces of the ferric precipitates dominates the sequestration mechanism until the end of the experiment.

Under anoxic conditions, Cu uptake and reduction are controlled by the formation of the Cu^{2+}–$Fe^{II}CO_3$ redox couple. The lack of oxygen thereby results in slower but ultimately complete reduction of > 70% of solid-bound Cu to Cu(0). Native copper formation is

chemically and spatially linked to metastable ferric (hydr)oxide transformation to lepidocrocite, which is favoured under slightly acidic anoxic conditions and at low ("threshold") concentrations of Fe(II) and Cu(II).

The presence of ferric (oxyhydr)oxide-associated Cu(I) species in the solid reaction products of both redox systems, and the remnant Cu(II) species in the anoxic solid reaction products are evidence for the stepwise (heterogeneous) reduction of Cu under both redox conditions. Dissolved carbonate resulting from siderite dissolution seems to have little effect on the redox reactions but buffers the solution at favourable pH conditions.

The results of this study emphasise the decisive role the type of oxidant(s) play(s) for the type of reaction product formation. A comparison to other studies on siderite interaction with metals under both redox conditions shows that strong oxidants such as Cu(II), Cr(VI) and/or O_2 result in rapid oxidative precipitation of scarcely soluble Fe(III) or mixed metal (oxyhydr)oxides regardless of the experimental redox condition, whereas weaker oxidants such as As(V) seem to require the presence of strong oxidants such as O_2 to induce ferric (oxyhydr)oxide precipitation to provide for the preferential sorption to the oxide surfaces.

Environmental implications. Natural environments may undergo redox changes over time, which may cause the release of metals sorbed to suspended solids (e.g., Calmano et al., 1993; Pedersen et al., 2006). In organic-depleted environments, Cu readily sorbs to the ubiquitously abundant iron oxides (e.g., Scheinost et al., 2001; Peacock & Sherman, 2004) and/or carbonate minerals (e.g., Elzinga & Reeder, 2002; Elzinga et al., 2006). Under both redox conditions, the initial adsorption of Cu to siderite grains (≤ 63 μm, silt fraction) induces Cu–Fe electron transfer reactions leading to oxidative ferric (oxyhydr)oxide precipitation and (partial) Cu reduction. As long as an oxidant is available in solution to promote oxidative dissolution of siderite, this multistep process is self-sustaining, as associated proton production and oxidative Fe(II) consumption perpetuates siderite dissolution and hence Cu uptake. This can be illustrated by a thought experiment:

Under oxic conditions, Cu removal from solution is dominated by adsorption to the ferric iron oxidation products. Over time, aggregation and entrapment of solid-bound Cu captures adsorbed Cu within the ferric (oxyhydr)oxide particles, retaining the entrapped Cu ions from potential desorption induced by changes in the aqueous solution conditions (e.g., Eh, pH, dilution; c.f., Gilbert et al., 2009; Stegemeier et al., 2015). Theoretically, under increasingly reducing conditions and/or in the presence of aqueous Fe^{2+}, metal cycling may result from

reductive dissolution of the ferric iron oxide sorbents (e.g., Wehrli et al., 1989; Stumm & Sulzberger, 1992; Pedersen et al., 2005 and 2006; Frierdich & Catalano, 2012a,b). This may in turn make increasing amounts of reactive Fe(II) available to interact with any released or yet dissolved Cu(II) and/or Cu(I), resulting in the precipitation of Cu(I) oxide and ferric (oxyhydr)oxide via a homogeneous redox pathway (Matocha et al., 2005). Or, as shown in the anoxic experiment, Cu(II) (re)sorption to siderite may form the much stronger heterogeneous Cu^{2+}–$Fe^{II}CO_3$ redox couple which (re)induces ferric (oxyhydr)oxide precipitation and Cu reduction. Low concentrations of dissolved Cu(II) and Fe(II) may additionally enhance the transformation of metastable ferric hydroxide to more stable lepidocrocite and complete reduction to native copper. The stepwise reduction of Cu(II) coupled to the consumption of oxidising Fe(II) by, and the transformation of ferric precipitates to crystalline lepidocrocite, simultaneously drives the continuous dissolution of siderite. A similar phenomenon was observed when siderite dissolved in the presence of Pb(II) in an anoxic aqueous solution. Thereby the consumption of the dissolving carbonate to form $PbCO_3$ drove the dissolution reaction until all available Pb(II) was consumed (*see* chapter 4; Füllenbach et al., 2020). Siderite surface passivation may be avoided as long as non-epitaxial growth of the surface precipitates allows for continuous dissolution of siderite through interparticle pore spaces (e.g., Hudson, 2003; Cubillas et al., 2005b; Yuan et al., 2016). Also, the suggested limiting effect of Cu(II) sorption on ferric (oxyhydr)oxide nanoparticle growth through aggregation or oriented attachment by surface site passivation (Kim et al., 2008; Stegemeier et al., 2015) may be overcome by the continuation of these successive reactions over time, which continuously produce new surface sites by progressive ferric (oxyhydr)oxide precipitation.

This study further demonstrates the dynamic character and the effect of redox active species like O_2, Fe(II), and Cu(II) on the stability of the ferric (oxyhydr)oxides. Such observed redox-induced transformations of the ferric (oxyhydr)oxides may affect their sorption capacity, which increases with decreasing particle size and decreases with increasing crystallinity (*see* section 1.2.3.; e.g., Cornell & Schwertmann, 2003). Notably, the poorly and exclusively nano-crystalline ferrihydrite generally reveals the highest metal(loid) sorption capacity of the ferric (oxyhydr)oxides due to its extremely high surface area and therewith highest availability of sorption sites. Although a decrease in Cu(II) uptake may therefore be expected upon the proposed transformation reactions to more crystalline phases, the lack of Cu re-release under oxic conditions and the accelerated uptake under anoxic conditions demonstrate that ferrihydrite transformations to lepidocrocite, goethite, and hematite ultimately promote Cu retention.

Overall, siderite dissolution proved to be an efficient reactant for Cu(II) removal from aqueous solutions under both redox conditions. Reaction mechanisms observed additionally improve our understanding of abiotic redox behaviour of Cu and Fe, which can be translated to the many other Fe-rich natural environments. The redox-induced reaction dynamics of the Fe-bearing minerals may further encourage research on elemental partitioning during mineral nucleation, growth, and replacement reactions which are of fundamental importance for studies using iron minerals and their isotopic compositions as proxies to reconstruct ancient environmental conditions.

6 Conclusions and future perspectives

The interaction of natural siderite with dissolved redox-active Cu(II) and less redox-active Pb(II) was demonstrated to effectively remove both metals from initially acidic aqueous solutions under both oxic and anoxic conditions. Mechanisms responsible for the metal uptake under the different redox conditions and their environmental implications are summarised. Future work required before potential implementation of siderite as a reagent is outlined and implications of the findings for similar modern and ancient geochemical environments are discussed.

6.1. Metal uptake coupled to siderite dissolution

6.1.1. Conclusions from experimental work

Siderite dissolution was experimentally and microanalytically shown to be an effective strategy to capture dissolved redox-inactive (Pb) and redox-active (Cu) metals from acidic aqueous solutions under oxidising and reducing conditions. Metal uptake pathways differ between the redox settings, though all uptake mechanisms are closely interlinked with the continuous dissolution of siderite, which is in turn fuelled by the formation of less soluble reaction products. Surface reactions are key in all processes under both redox conditions.

6.1.1.1. Metal uptake under oxic conditions

Under oxic conditions, the oxidation of the Fe(II) component in siderite is essential. The oxidised form of iron, Fe(III), is less stable in the siderite structure and preferentially partitions into secondary Fe(III) (oxyhydr)oxide surface precipitates. Iron oxidation by oxygen occurs much more rapidly in the presence of Cu than in the presence of Pb, as Cu(II) additionally oxidises near-surface Fe(II) and therefore enhances oxidative dissolution of siderite while being partially reduced to Cu(I). The initially enhanced oxidative siderite dissolution by Cu(II) and O_2 is further reflected by the more rapid increase in solution pH within 0.5 h of reaction in the Cu-bearing compared to the Pb-bearing oxic system. In contrast, initial metal uptake within the first 2 h of reaction is more effective for Pb through near-surface Pb-carbonate precipitation. Initial Cu uptake occurs via sorption to siderite inducing oxidative Fe(III) precipitation. As the solution approaches pH 5 after ca. 2 h of reaction, Fe(III) precipitation advances in both Cu- and Pb-containing oxic systems and metal adsorption to and likely entrapment within these secondary nanoprecipitates becomes the dominant uptake mechanism until the end of the experiments. Non-epitaxial growth of the surface precipitates prevents siderite surface passivation by allowing continuous siderite dissolution as reactive fluid penetrates through interparticle pore spaces. Siderite dissolution continues at notably slowed rates due to the increased solution pH which is buffered by progressive adsorption and precipitation reactions.

6.1.1.2. Metal uptake under anoxic conditions

Under anoxic conditions, the chemical properties of the dissolved metals play a decisive role in their uptake coupled to siderite dissolution. As redox-inactive metal, Pb uptake is more strongly influenced by its tendency to form (an)hydrous carbonate minerals. Hence, upon initial surface sorption and proton-promoted liberation of carbonate from the dissolving siderite

surface, Pb uptake is dominated by rapid precipitation as sparingly soluble cerussite, while all Fe in the system remains reduced and no ferric (oxyhydr)oxide precipitation occurs. However, as redox-active metal and relatively strong oxidant, the uptake of Cu(II) is strongly influenced by its heterogeneous redox interaction with the Fe(II) component of the dissolving siderite surface. Initial adsorption of Cu(II) to surface structural Fe(II) induces oxidative Fe(III) surface precipitation and partial reduction to Cu(I). Over time, increasing Fe concentrations resulting from simultaneous proton-promoted siderite dissolution and declining Cu concentrations through continued adsorption reactions seem to reach coinciding threshold concentrations upon which Fe(III) precipitate transformation occurs, leading to lepidocrocite precipitation and further reduction to Cu(0). This stepwise reduction coupled to Fe(III) phase transformation is decisive for the complete removal of Cu from solution. In contrast, released Fe concentrations vary with the presence of different metals. In both cases, Pb and Cu enhance Fe(II) liberation over time compared to metal-free solutions.

The metal uptake mechanisms described for the anoxic system also correspond to processes occurring at low pH ≤ 3 regardless of the redox condition, when Fe(II) remains the dominant form of Fe and oxidation by O_2 is negligible or excluded. Consequently, at very acidic pH conditions, siderite dissolution regulates acidity by proton consumption and provides reactive surface sites for metal interaction, forming adsorption complexes that act as precursors for subsequent precipitation of metal carbonates such as cerussite, and/or induce electron transfer and thus Fe(II) oxidation as observed for the heterogeneous single-step Cu(II) reduction to Cu(I).

6.1.1.3. Conclusions

Surface-controlled dissolution–precipitation and adsorption reactions regulate the acidity of both oxic and anoxic aqueous systems to less acidic, near-neutral conditions. Heterogeneous, non-epitaxial surface precipitation of secondary goethite and cerussite on siderite thereby prevents surface passivation, while transformation reactions of the ferric (oxyhydr)oxides additionally create pore spaces and free reactive siderite surfaces, progressing these reactions. The presence of oxidants (O_2, Cu(II)) is an important factor, enhancing the heterogeneous oxidative siderite dissolution–Fe(III) (oxyhydr)oxide precipitation reactions under oxidant reduction, and – in the case of Cu – precipitation as native metal. All captured metal species remained solid-bound throughout the prolonged experimental reaction times, reiterating the efficacy of this method.

The redox activity of the dissolved metal influences the pathways for metal uptake. From the example of Pb and Cu, it may be inferred that under comparable study conditions, redox-inactive metals that readily form carbonate minerals (e.g., Cd) may follow the pathway outlined for Pb which includes the precipitation of Me-carbonate. Metals that do not readily form carbonate minerals but are more strongly redox-active (e.g., Cr, Se, Np) may follow the pathway outlined for Cu which is dominated by the heterogeneous redox interaction with the Fe(II) component of siderite. Metal(loid)s that have lower tendencies to form carbonate minerals and/or are much weaker redox reactants (e.g., As, Zn, Ni) are more likely scavenged in the presence of a strong oxidant such as O_2 or other redox-active metals to induce Fe(III) (oxyhydr)oxide precipitation acting as sorbents. These redox-induced and proton-producing precipitation and transformation reactions buffer the reactive solution pH allowing siderite to continuously dissolve. In the presence of stronger oxidants such as Cr(VI), U(VI), or Se(IV), the electron transfer-induced redox reactions may be accelerated, leading to stronger metal reduction, and buffering of the aqueous system at possibly lower pH conditions promoting continuous siderite dissolution. The presence of CO_2 released from siderite dissolution may additionally aid ternary surface complexation (e.g., for U), while longer reaction periods (aging) promote aggregation and/or transformation of the Fe(III) precipitates, thereby entrapping sorbed metal(loid)s and enhancing metal retention.

Overall, this study demonstrates that siderite dissolution has great potential to immobilise metal contaminants from polluted water-saturated environments without introducing additional harmful substances. The obtained detailed insights into the reaction mechanisms responsible for the uptake of metals with very different chemical properties upon the interaction with siderite allow for more accurate predictions of metal behaviour and the potential application of siderite as remediation reagent to specific polluted sites. This understanding can be translated to other metal contaminants and also to other Fe(II)- and carbonate-rich natural environments.

6.1.2. Using siderite to remediate metal contamination

The uptake of dissolved metals from acidic oxic and anoxic aqueous systems by siderite is directly coupled to the dissolution behaviour of siderite under the investigated study conditions. When considering the application of siderite as a reagent to remediate metal-contaminated aqueous environments that are prone to undergo redox fluctuations, for example by reactive

particle injections, in permeable reactive barriers, or as direct supplement to contaminated soil or drainage treatment systems, several aspects require further testing.

Every contaminated site is unique in its geochemical characteristics which may affect the siderite dissolution behaviour and thus its metal-uptake efficacy in different ways. Primary factors affecting siderite reactivity and reaction kinetics are reasonably well understood and can be inferred for a specific environmental setting. These factors include the aqueous solution composition (e.g., pH, pCO_2, pO_2), temperature, and the availability of reactive surfaces on siderite (i.e., particle size, morphology, and surface roughness; e.g., Mulders et al., 2021). Furthermore, rough estimates can be made on the applicability of siderite to a particular system affected by metal contamination from the number of studies on siderite interaction with metals under various study conditions, including the adsorption behaviour of different metals as a function of pH and initial sorbent–sorbate ratios, and the potential redox interactions between redox-active metals and siderite (*see* section 3.3.2). However, the effects and interaction mechanisms of competitive behaviour of metals and organic and inorganic ligands in multielement aqueous systems are not yet fully understood.

The results presented in this work demonstrate that the metal-uptake mechanisms vary with the type of metal contaminant and the availability of oxidants such as O_2 in the system. The different metals and other chemical components might hence impede or enhance the dissolution and therewith the metal immobilisation efficacy of siderite. Understanding the effects of other chemical constituents on metal interaction with dissolving siderite, particularly of redox-active metal contaminants (e.g., As, Cr, Se, U) and non-metallic constituents (e.g., S, N, P), will be crucial as soils, sediments, and (sub)surface waters are multielement systems and metal contaminants generally occur as assemblages (*see* Table 1.1; e.g., Carroll et al., 1998). To determine the extent to which inorganic and/or organic substances and concentrations may impede or improve siderite reactivity and therefore metal-uptake, the following interrelations should be investigated individually as well as in combination: Siderite interaction with (1) **inorganic substances**, (2) **organic substances**, and (3) siderite reactivity and interaction with other substances under more **flow conditions**.

6.1.2.1. Effects of inorganic substances

Siderite interaction with inorganic substances such as dissolved metals and inorganic ligands under oxic and/or anoxic conditions has been briefly discussed in section 3.5.2.

Inorganic metals and ligands can affect the efficacy of siderite to act as remediation reagent in various ways:

1) **Redox strength of the metal contaminant(s)**. Arsenic, for example, most readily adsorbs to and interacts with ferric iron oxides in the form of As(V), hence oxidation is required. In the absence of an oxidant, siderite does therefore not serve as an effective sorbent for As. However, the combination of siderite+As+oxidant (e.g., O_2, Cu, Cr, or organic oxidants) may help As immobilisation (c.f., Wang & Reardon, 2001; Hajji et al., 2019). Competitive sorption and reduction between metals of more similar redox strength such as Cr, Np, Se, and U, as well as the combinatory effect on the uptake of redox-inactive metals should be investigated.

2) **Tendency to form carbonate complexes or minerals**. The interaction of dissolving siderite with metals that form isostructural metal carbonate minerals of lower solubility such as Cd, Co, Mn, may result in epitaxial surface precipitation in the case of near-surface or solution saturation with respect to otavite, spherocobaltite, or rhodochrosite. Consequently, the reacting siderite surface may become passivated, particularly under anoxic conditions (c.f., Köhler et al., 2007). Under oxic and pH > 4–4.5 conditions, the extremely low solubility of ferric iron (oxyhydr)oxides may outcompete $MeCO_3$ precipitation, thus a mixture of non-epitaxial ferric and epitaxial carbonate precipitation on the reacting siderite surface may maintain a porous texture allowing continuous dissolution of siderite. The passivating effect of epitaxial growth on siderite dissolution should be examined as a function of metal concentrations and siderite grain size.

3) **Effect of inorganic ligands on siderite–Me interaction**. Anionic ligands such as phosphate, sulphate, and chloride may compete with surface sites for metal complexation (e.g., Schindler, 1990; Bargar et al., 1998; Ostergren et al., 2000a,b; Liu et al., 2001). To what extent, and whether metals may be most affected by which ligands, and which ligands may further have the strongest impact on siderite dissolution (inhibiting or promoting) needs to be thoroughly reviewed and experimentally evaluated. Again, both redox conditions will be important. For example, under strongly reducing conditions, the presence of sulphur may result in pyrite precipitation (e.g., Appelo & Postma, 2005), hence removing Fe(II) from solution which could otherwise interact with dissolved metal ions, while possibly accelerating siderite dissolution.

6.1.2.2. Effects of organic substances

This thesis provides an in-depth characterisation of the inorganic/abiotic interaction of siderite with dissolved metals in aqueous systems. Besides inorganic substances, however, soils and aqueous environments can contain large quantities of organics and biota in the form of organic molecules, organic matter, and microorganisms. Organic substances and microbes can affect siderite efficacy to act as remediation reagent in three ways: by (1) **biologically mediated interaction** through direct use of substances for microbial respiration and metabolic activity, (2) **biologically induced interaction** through interaction with organic molecules that are products of microbial activity or degradation products of organic matter, and (3) **surface complexation** through interaction of (a) organic substances with mineral surfaces, and/or (b) dissolved metal interaction with (cell) surface functional groups. In soils, organic-rich sediments, and mine wastes such as tailings, these three ways of direct or indirect interaction may all occur in different redox zones of a system and affect both siderite and dissolved metal species – more specifically, the ferrous iron in siderite and redox sensitive metal(oid)s.

1) **Biologically controlled interaction**. Microbial metabolism can use metals and sulphur as energy source through (extracellular) electron transfer, which may catalyse and thus affect other, abiotic redox reactions. In aerobic environments, acidophilic bacteria can oxidise or reduce mineral-bound Fe, S, but also other (redox active) trace metals, including As, Cu, Cr, Hg, Mn, Mo, and U, which causes mineral dissolution and precipitation cycling and affects the bioavailability of these metal(loid)s (Southam, 2012). Particularly in the case of iron, microbial metabolism may lead to enhanced reductive or oxidative dissolution of iron minerals, often associated with the corresponding redox effect on other redox-sensitive elements such as sulphur, organic carbon, nitrogen, and manganese (Hering & Stumm, 1990; Stumm & Sulzberger, 1992; Konhauser et al., 2011), and metals such as Cr (e.g., Ellis et al., 2002). In anaerobic environments, some microorganisms can enzymatically reduce dissolved metals like As(V), Cr(VI), and U(VI) upon uptake into their cell (Cheng et al., 2012; Lu et al., 2012). Dissimilatory metal reducing microorganisms can reverse the oxidation reactions and use metals as electron acceptors (reduction) and organic compounds and hydrogen as electron donors, leading to reduced metal and Fe(II)-bearing precipitates (e.g., siderite) and soluble reduced metal and Fe^{2+} complexes (oxidation; Lu et al., 2012; Southam, 2012).

In aerobic – oxygen-rich – environments, therefore, the presence of Fe(II) oxidising microbes likely enhances oxidative siderite dissolution and Fe(III) (oxyhydr)oxide precipitation, providing new adsorption sites for dissolved metal ions. However, the reductive effect of siderite may be strongly reduced, depending on the microbe to siderite to metal ratios – high amounts of microbes may outcompete metal sorption, constraining metal uptake to sorption to and/or coprecipitation with secondary ferric (oxyhydr)oxides.

In anaerobic – oxygen-depleted – environments, metal reducing microorganisms may promote the reductive potential of siderite by metabolising ferric (oxyhydr)oxides that may have formed on the siderite surface, while causing additional siderite precipitation. Released metal(loids) adsorbed to ferric (oxyhydr)oxides may either resorb to the nanoparticulate reduction products (e.g., magnetite, vivianite), and/or form (reduced) metal precipitates (e.g., sulphides, carbonates, or native Cu). Notably, these metal precipitates are more susceptible to oxidation due to their nanometre size (Cheng et al., 2012; Southam et al., 2012). Pre-sorbed or coprecipitated metals, such as As(V) in ferric (oxyhydr)oxides, may become reduced and re-associated with the solid reaction products of bioreduction (c.f., Ona-Nguema et al., 2009).

Such biogenic redox effects on siderite and dissolved metals need to be considered and possibly experimentally tested to allow more accurate predictions of the metal uptake efficacy of siderite in microbe-rich sediments or soils. The competitive interaction of metals with either microbes or siderite may be particularly interesting. However, this brief discussion considers microbial metabolism as oversimplified ‘one way’ system by excluding the interaction of metals and minerals with metabolic reaction products, which further affect metal speciation and mineral stabilities.

2) **Biologically mediated interaction.** Microbial metabolism and decay of organic matter produce organic acids. Autotroph microbial communities in low carbon systems, for example, excrete low molecular weight carboxylic acids (LMWCA) that conjugate to acetate, citrate, formate, oxalate, and pyruvate (Dold et al., 2005). These organic molecules can form highly mobile complexes with Fe(III) and thereby lower the saturation states – thus enhance dissolution and prevent precipitation – of ferric (oxyhydr)oxides (Dold et al., 2005). In anaerobic and low sulphuric waters, dissimilatory metal reductors utilising Fe(III) and other metals as electron acceptors can use the LMWCA as electron donors, resulting in high concentrations of aqueous Fe(II)

and metals such as Ni, Cu, As(III) in solution (Dold et al., 2005; Cheng et al., 2012; Southam, 2012), while remediating others such as Cr(III) and U(VI) by reductive precipitation (Southam, 2012).

The interaction with organic acids also strongly affects siderite dissolution behaviour (Mulders, 2021). Under acidic oxic conditions, siderite dissolution is enhanced in the presence of oxalic acid, while the relative amount of oxidised Fe released increases. In contrast, acetic acid seems to slow siderite dissolution (Mulders, 2021). Hence, under both oxic and anoxic conditions, microbial metabolic reaction products enhance the solubility of both metals and mineral-bound Fe by the formation of soluble complexes.

Whether LMWCA inhibit metal-siderite interaction likely depends on the LMWCA to siderite to dissolved metal ratio, the types of LMWCA and dissolved metals, and the physicochemical conditions. These dependencies should be experimentally tested to get a better understanding of the potential impact on the efficacy of siderite as remediation reagent in organic-rich soils and sediments in which LMWCA formation is likely.

3) **Surface complexation** with (cell) surface functional groups. The effect of microorganisms and their metabolic products comes down to the *abiotic* interaction of sorption and surface complexation (e.g., Fein et al., 1997). As discussed above, organic acids enhance mineral dissolution by the formation of ion complexes at the mineral surface, thereby facilitating electron transfer and weakening metal–oxygen bonds (e.g., Dold et al., 2005). Formation of highly soluble organic acid complexes at the siderite surface most likely facilitates its enhanced dissolution (Mulders, 2021).

   Depending on the relative amounts of available surface (sorption) sites and type of ligand, organic ligands (acids) may either promote metal adsorption to oxide surfaces by acting as bridging ligands (ternary complex formation) or facilitate metal release by forming aqueous metal ion–organic complexes (e.g., with oxalate, picolinate, humic acid, organic matter; Sulzberger et al., 1989; Schindler, 1990; Coughlin & Stone, 1995; McBride et al., 1997; Liu et al., 2001; Strawn & Baker, 2009).

   Two aspects of surface complexation can be considered: (a) Sorption of organic substances on mineral surfaces, and (b) metal complexation with (cell) surface functional groups. Note, however, that the core mechanisms of both are very similar.

   (a) **Sorption of organic substances on mineral surfaces.** Besides metabolic respiration, acidic refractory decomposition of organic matter (OM) produces organic molecules. Among the most studied are humic substances, which are very

large molecules containing carboxyl and hydroxyl groups that can adsorb to mineral surfaces (Tipping, 1981). For the sorption to Fe and Mn oxides, the most important of these groups is the carboxyl group (Tipping & Cooke, 1982). Humic substances are primarily negatively charged (the carboxyl group –COOH becomes >COO^- surface functional group upon sorption to mineral surfaces) and thus adsorb to positively charged mineral surfaces. Hence adsorption increases and is favoured at acidic conditions (Tipping, 1981; Scheffer & Schachtschabel, 2010).

Although adsorption of humic substances impedes the crystallisation of poorly crystalline minerals such as ferrihydrite, it also stabilises them against microbial decomposition while lowering their surface charge to negative even at low pH (Tipping & Cooke, 1982; Scheffer & Schachtschabel, 2010). As a result, metal adsorption to more negatively charged metal oxides – i.e., to the sorbed organic moieties – increases. For example, under acidic oxic conditions, Cu(II) sorption to goethite with pre-sorbed humic substances is enhanced over sorption to pure goethite and dissolved humic substances (Tipping et al., 1983; Otero Fariña et al., 2018). Adsorbed bivalent metals in turn increase the number of positively charged surface sites on metal oxides and thus the extent of humic substance adsorption through bridging of organic acid chains (e.g., >Me–COOH–Me; Tipping et al., 1983).

Under oxic conditions, where siderite dissolution induced metal uptake is dominated by adsorption to secondary ferric (oxyhydr)oxides, this doubly enhanced sorption may seem favourable, particularly at pH 4-7. However, the primarily monodentate inner-sphere >Me–COOH and >COOH–Me complexes are less stable than the more commonly bidentate inner-sphere metal sorption complexes on the ferric (oxyhydr)oxide surfaces (e.g., Moon & Peacock, 2011). Although Cu(II) seems preferentially associated with the organic moieties on ferric oxide–organic compounds (Moon & Peacock, 2012; Otero Fariña et al., 2018), if also present, aqueous humic substances may simultaneously compete for complexation with dissolved Cu and Pb in solution (Tipping et al., 1983; Xia et al., 1997).

In natural, chemically more complex systems, competitive sorption of organic substances with anions for sorption sites at mineral surfaces may also increase phosphate and arsenate mobility (Scheffer & Schachtschabel, 2010).

Similar to the interaction with microbially derived carboxylic acids, the impact on siderite as remediation reagent depends on the ratio of humic substances (or OM) to siderite to dissolved metal ratio, the types of humic substances present and the type of dissolved metals. These dependencies should be experimentally tested as a function of various physicochemical conditions (Eh, pH) to better understand the described interactions in organic-rich aqueous environments.

(b) **Metal complexation with (cell) surface functional groups.** Metals can directly interact with (adsorb to) microbial cell walls and/or organic matter (Beveridge et al., 1976; McBride et al., 1997; Manceau & Matynia, 2010). Microbial cell walls contain carboxylic acid surface functional groups, such as carboxyl, phosphoryl, and hydroxyl groups. Hence the sorption mechanisms of metal cations to the primarily negatively charged surface functional groups are similar to organic substances.

Metal sorption to cell walls is often pH dependent and different metals tend to preferentially sorb to specific surface functional groups. For example, at low pH, Cu(II), Cd(II), Fe(III), Ni(II), and Au(III) primarily bind to the carboxyl group in the cell wall of non-Fe metabolising bacterium *Bacillus subtilis* (Beveridge & Murray, 1980; Moon & Peacock, 2012), but Cd(II) also binds to phosphatic sites in isolated cell walls of *Rhodococcus erythropolis* when carboxylic sites are occupied (Ferris et al., 1989). The uranyl cation exclusively interacts with neutrally charged phosphoryl, forming monodentate inner-sphere complexes on the cell walls of *B. subtilis* at pH < 3, while at pH 3-5 uranyl increasingly forms bidentate inner-spherically to carboxyl functional groups (Kelly et al., 2002). Similarly, Zn(II) primarily binds to phosphoryl and much less to carboxyl groups of *Pseudomonas putida* at circumneutral pH (6.9; Toner et al., 2005).

Similar behaviour is found for metal interaction with natural organic matter (NOM). The affinities of NOM for metal binding (sorption to fulvic acid) decreases in the order of Pb > Cu > Ni > Zn > Cd for strong carboxyl complexes (Manceau & Matynia, 2010 *and references therein*).

The different affinities are associated with the formation of metal sorption complexes of various binding strengths. Weakly binding Zn and Cd are readily outcompeted by Cu, which forms stronger inner-sphere chelate complexes with NOM, cell walls, and humic substances (Weng et al., 2002; Claessens & Van

Cappellen, 2007; Manceau & Matynia, 2010), which are likely combinations of carboxyl, carbonyl, or amino functional groups (Karlsson et al., 2006).

The most direct impact on siderite efficacy to take up metals from contaminated oxic solutions in the presence of bacterial or NOM is the competitive sorption of metals to either the organic functional groups or to the mineral surfaces. For example, while Zn(II) and possibly Cd(II) only secondarily bind to organic functional groups as long as mineral surface site are available (Toner et al., 2006), Cu(II) has a much greater affinity to complex with the organic moiety (Du et al., 2018). Also, the solubility versus uptake of Cu, Cd, Zn, Ni, and Pb by OM strongly depends on the relative concentrations of metals and OM in the soil solution (Weng et al., 2002). Hence the concentrations of these metals as well as the total amount of OM need to be assessed before applying siderite to remediate a metal contaminated, organic-rich system.

Notably, most of the metal sorption experiments on cell walls and organic acids and substances have been performed under oxic conditions and disregarding the strong effects of electron transfer reactions between living cells and redox sensitive metals. However, it may be assumed that the siderite dissolution induced metal uptake may be similarly affected by the presence of organics as by strongly redox-active metals under the respective redox condition. The main concern may be the increased solubility of metals that preferentially form aqueous complexes with organic molecules or substances, making them less available to interact with siderite.

Overall, key parameters affecting microbial activity and the stability of organic matter and minerals (siderite and its reaction products) are the physicochemical conditions (Eh and pH), and the relative abundances of nutrients, metals, and organics in the system. For example, high dissolved metal concentrations can be toxic to microorganisms, even more so than to higher plants (Vulkan et al., 2000; Lofts et al., 2004; Dong, 2012). Another important factor influencing the reactivity and reaction rates in an organic-rich system is the particle size of reacting and precipitating minerals. However, the difficulty for more accurate predictions of dissolved metal behaviour in organic-rich aqueous environments is that the relative importance of biotic vs. abiotic effects are still poorly understood. The question remains to what extent mineral reactions are mediated by microbial activity (Dong, 2012).

The influence of organics on the efficacy of siderite to capture dissolved metals from the aqueous fluid may be addressed based on what is now known from the inorganic system

presented in this study. Before addressing a multicomponent system, experimentally assessing the impact of organic substances and microbial activity on the reactivity of siderite under both aerobic and anaerobic conditions will be a crucial first step. When these effects are understood, the combined effects of multicomponent waters could be investigated by reacting well-characterised metal- and organics-containing wastewaters from mine or industrial discharges in a suspension with well-characterised fine-grained siderite. Similarly, the effects of organic substances and organic acids could further be studied by reacting well-characterised, siderite-rich soil or sediment samples with oxic and deoxygenated aqueous solutions containing selected metal ions following a similar experimental protocol as described in this study.

6.1.2.3. Effects of the experimental design

The batch experiments conducted in this study represent a most simplified closed system approach to investigate the interaction of siderite with dissolved metals under controlled laboratory conditions. In natural environments, however, most aquatic systems and wet soils are open to mass transfer, i.e., to the exchange of chemical substances such as gases (e.g., O_2, CO_2), ions, and organic and inorganic molecules. Mass transfer or exchange reactions affect the overall mass balance and therewith the stability of species in a system, as illustrated for the carbonate speciation in open and closed systems in section 3.2.1. One way to experimentally simulate more natural (open system) conditions is to perform experiments that provide a continuous flow of new reactive fluid to the reaction cell in a flow-through setup.

By applying a constant flow rate in approximation to groundwater flow velocities or infiltration rates in soils, the constant influx of fresh reaction fluid will affect the observed dissolution and associated metal uptake mechanisms. For example, under fluid flow, siderite may dissolve more rapidly as consumed protons are constantly replenished, and the reactive solution pH may remain relatively constant even at acidic conditions. Under oxic conditions, metal adsorption to secondary iron (oxyhydr)oxides may be hindered by flow velocities exceeding surface reaction (adsorption and complexation) rates, while lower flow velocities providing a continuous feed of dissolved metal ions adsorbing to the iron (oxyhydr)oxides may lead to a more rapid passivation of available sorption sites. However, simultaneously enhanced dissolution rates of siderite may also promote the precipitation of new iron (oxyhydr)oxides and therewith formation of new reactive surface sites. Under anoxic conditions, a continuous replenishment of protons dissolving siderite, and of weak redox active metals reacting with the dissolving siderite surface may potentially enhance, for example, Pb uptake by driving cerussite precipitation which is coupled to siderite dissolution. Whether or not the enhanced precipitation

of metal carbonates isotypic to siderite, such as otavite, may cause rapid passivation of the siderite surface under anoxic flow conditions, however, strongly depends on the different rates of fluid flow, siderite dissolution, and secondary mineral precipitation.

In addition to the possibility to assess the duality of siderite with respect to metal uptake under more natural conditions, flow-through experiments also allow the quantification of reaction rates. However, some major challenges remain: (1) the immediate re-consumption of Fe(II) released during siderite dissolution through redox reactions in the presence of oxidants such as oxygen, copper, or other redox active metals or organic substances, complicates the quantification of siderite dissolution and iron (oxyhydr)oxide precipitation rates based on the measured Fe concentrations in the reacted outlet solution, and (2) the continuous change in surface characteristics of the reacting siderite during dissolution and secondary surface precipitation, particularly in the presence of oxidants, generally introduces additional uncertainties to the quantification of reaction rates (c.f., Duckworth & Martin, 2004a,b; Mulders, 2021).

Flow-through experiments could furthermore provide valuable insights into the metal uptake efficacy upon interaction with dissolving siderite under slightly more natural 'open system' conditions. These include the potential change in aqueous solution characteristics, such as by dilution or changes in proton and/or dissolved metal concentrations. Although inner-spherically adsorbed metal ions may be released upon dilution and/or acidification of the aqueous solution, it is expected that a fraction of adsorbed metals entrapped within secondary iron (oxyhydr)oxide precipitate aggregates remain captured (c.f., Dale et al., 2015; Stegemeier et al., 2015). This actual efficacy of metal retention upon interaction with siderite could furthermore be tested and quantified in desorption experiments, in which fully (metal-)reacted siderite powder would be exposed to a constant flow of pure water and/or slightly acidic (e.g., pH 3-5) metal-free aqueous solutions and the reacted outlet is measured for potentially released metals.

For specific applications such as injection into contaminated aquifers or use in permeable reactive barriers, physical parameters affecting particle reactivity and dispersibility are additional important constraints to make more informed predictions on the applicability of siderite to remediate metal polluted environments. Initial complementary batch experiments could investigate the reactivity and metal-uptake efficacy of ground natural siderite compared to the finer grained synthesized siderite, which differ considerably in reactive surface properties (Mulders et al., 2021). Flow-through experiments under controlled oxic and anoxic conditions

could further constrain the parameters affecting siderite dissolution rates such as particle size and loading, changes in influx water chemistry, and element transport at flow rates simulating groundwater conditions. Column experiments could provide insights into natural vs. synthetic siderite particle mobility and dispersibility in porous sediments which depend on the particle size, shape, reactivity, and the carrier matrix. If injected, the carrier fluid should increase particle mobility, be inert, and not introduce additional harmful substances to the environment. Carboxymethyl cellulose, for example, has been shown to effectively disperse nanoparticulate zero valent Fe in fine-sand sediment without oxidising the reduced Fe component (nZVI; Reischer et al., 2022), and could thus be tested as potential carrier substance. Before implementation, experiments at increased scale should be conducted, e.g., in tank experiments simulating the prospect application environment.

6.2. Implications for related aqueous environments

The gained understanding of the siderite interaction with redox-active and -inactive metals in aqueous systems under oxidising and reducing conditions provides a more general insight into interrelations within metal bearing, Fe- and CO_2-rich aqueous systems. These interrelations include (1) the oxidative dissolution–precipitation behaviour of the Fe(II) component, (2) the resulting Fe(III) (oxyhydr)oxide formation reactions depending on the (metal) oxidant present, (3) the interaction of dissolved carbonate with metals to form less soluble metal-carbonate minerals, and (4) the acid regulating effect of siderite dissolution. The detailed observations of these interactions can be translated to chemically similar environmental settings. Two examples will be briefly illustrated in the following.

6.2.1. Potential metal release during Enhanced Weathering

The recently emerging carbon sequestration strategy of *Enhanced Weathering* utilises the dissolution–precipitation behaviour of Fe(II)/Mg-SiO_2 phases in airborne CO_2-enriched water. This carbonation of basaltic rocks (c.f., Gíslason & Oelkers, 2014), involves dissolution induced regulation of acidity, and carbonate and (oxidative) iron mineral precipitation. It may therefore be implied that through Enhanced Weathering processes, metals potentially released upon Fe(II)/Mg-SiO_2 dissolution can be re-captured by similar processes of metal adsorption to and carbonation in sparingly soluble secondary minerals as reported in this study.

Enhanced Weathering is a geoengineering concept based on the natural dissolution behaviour (weathering) of silicate rocks for large-scale sequestration of atmospheric CO_2 (Seifritz, 1990; Lackner et al., 1995; Schuiling & Krijgsman, 2006). To accelerate the dissolution or weathering rates of the natural silicate rocks (Oelkers, 2001; Oelkers & Gíslason, 2011), Enhanced Weathering strategies envisage the application of finely powdered olivine (forsterite, Mg_2SiO_4) and olivine–bearing (ultra)mafic rocks on agricultural and forestry lands (Köhler et al., 2010; Moosdorf et al., 2014; Taylor et al., 2015). Bicarbonate formation during forsterite dissolution in CO_2-enriched waters according to

$$(Mg,Fe)_2SiO_4 + 4CO_2 + 4H_2O \longrightarrow 2(Mg,Fe)^{2+} + 4HCO_3^- + H_4SiO_4 \quad \text{(eq. 6.1)}$$

would simultaneously counteract soil and ocean acidification, and act as fertiliser through increased riverine input of nutrients (e.g., P, K), silicic acid, total alkalinity, and dissolved inorganic carbon concentrations (Köhler et al., 2010; Hartmann et al., 2013; Köhler et al., 2013).

The natural chemical weathering of rocks upon interaction with water – terrestrially via meteoric and subsurface circulating waters, while seawater alters marine rocks and sediments – controls various elemental cycles besides the carbon cycle. It also causes the liberation of metals (e.g., Berner et al., 1983). As a consequence, concerns have been raised about potential risks of simultaneous metal leaching from the silicate minerals during Enhanced Weathering implementation (Edwards et al., 2017; Monsterrat et al., 2017). In nature, metals released during basalt dissolution upon interaction with CO_2-rich waters are likely sequestered by carbonate mineral precipitation and/or association with ferric (oxyhydr)oxides, as observed in comprehensive studies combining modelling, experimental and field data from river and groundwaters affected by volcanic activity (Flaathen et al., 2009; Olsson et al., 2014). Specifically designed batch experiments on olivine dissolution in seawater indicate the release of Ni, which is the most common trace element in olivine-bearing rocks, however at concentrations below permitted drinking water levels of 20 µmol L^{-1} (EU Council Directive on Drinking Water, 2015; Monsterrat et al., 2017). Similarly, liberated Cr commonly associated with mafic rocks may readily partition into insoluble chromite minerals (Waychunas et al., 2005; Wu et al., 2016), or coprecipitate with ferric (oxyhydr)oxides under surface water conditions (Eary & Rai, 1988; Manceau et al., 2000; Bibi et al., 2018).

These studies suggest that upon potential release, trace metals like Ni and Cr may be captured by ferric iron and carbonate reaction products of the dissolution of peridotite or mafic

rock dissolution. However, little work has been done to systematically investigate the potential release and re-capture of Ni and Cr from these natural mineral materials applied in Enhanced Weathering strategies. Considering the results presented in this thesis, the capture of CO_2 from air and of potentially harmful metals dissolved in soil fluids could be combined. Although the olivine-rich rocks dunite and harzburgite are preferential for CO_2 sequestration due to their higher Mg contents, basalt may be preferential for the additional capture of metals due to its higher Fe content. A series of batch basalt dissolution experiments in simulated Enhanced Weathering conditions to monitor metal liberation and re-precipitation from olivine and basaltic glass dissolution would provide first insights into the efficacy of combined CO_2 and metal sequestration. A thorough investigation of the reaction products using HRTEM, and X-ray based spectroscopies to identify the solid reaction products, metal distribution, and type of bonding would help to assess whether and which metals are preferentially partitioned into less soluble carbonate or ferric iron phases or form reversible adsorption complexes. Surface interaction of dissolved metals with simultaneously precipitating silica and Al (oxyhydr)oxides is also likely. Notably, due to the exposure to air during the application of Enhanced Weathering strategies on terrestrial lands, conditions are expected to be primarily oxic.

The release and uptake of Ni, Cr, and Co has been monitored a series of corresponding preliminary olivine (forsterite) and basaltic glass dissolution batch experiments under acidic and alkaline oxic conditions (Forsey, 2020; Haynes, 2021). It was found that Cr, Ni, and Co were released from both materials into the aqueous solution upon dissolution but were removed from the reactive fluid upon pH increasing carbonation. This observation suggests that dissolution–precipitation mechanisms similar to those presented in this study may be responsible for the re-immobilisation of the liberated metals. These first insights further suggest that Enhanced Weathering could potentially simultaneously remove airborne CO_2 as well as dissolved metals. Whether the metals were sequestered by carbonate or iron (oxyhydr)oxide precipitation should be subject to future investigations on the reacted solids to determine the distribution, speciation, and bonding, hence the retention of the metals.

6.2.2. Implications for siderite in early Earth environments

Siderite is one of the major components of Archaean to early Proterozoic sedimentary successions known as iron formations (IF). As major Fe(II)-bearing mineral, the strongly redox-dependent formation and decomposition behaviour of siderite plays a key role in deciphering the depositional history of IFs and their response to increasing oxygenation of the early Earth's atmosphere. The herein detailed documentation of oxidative siderite dissolution behaviour upon interaction of siderite with O_2 and/or Cu as oxidant under anoxic conditions may provide insights into possible reaction mechanisms that help unravel the most pressing questions regarding the origin and fate of siderite in these ancient and dramatically changing environments. Possible approaches are discussed in the following.

There are two main depositional types of IFs that are generally linked to the evolutionary changes in the early Earth's atmospheric and oceanic geochemical conditions. The banded iron formations (BIFs) are relatively deep-water sedimentary successions formed in the yet anoxic ocean and linked to suboceanic hydrothermal vent activity before the oxygenation of the Earth's atmosphere during the Great Oxidation Event (GOE) approximately 2.4 Ga ago. The granular iron formations (GIFs) are younger sedimentary successions deposited at shallower depths above the wave-base, post-dating the GOE during the Paleoproterozoic (Bekker et al., 2010). The formation history of IFs is still not unambiguously resolved. Key remaining questions include (1) identifying the primary depositional mineralogy, and (2) understanding the mechanisms responsible for the rise of oxygen in the ocean and atmosphere. As ferrous iron carbonate and major component of IFs, the origin and redox behaviour of siderite play an important role in deciphering the depositional history and rise of oxidative weathering. However, the origin and fate of siderite in IFs remains debated and subject to research.

Opposing approaches set the theoretical framework for the contextual interpretation of the characteristics of ferrous carbonates in IFs and the redox-dependent formation–decomposition behaviour of siderite in corresponding experimental studies. Siderite occurrences in IFs often contain impurities of Ca, Mg, and Mn, and are generally accompanied by other carbonate minerals along the solid solution series of ankerite ($Ca(Fe,Mg{\pm}Mn)CO_3$), dolomite ($CaMg(CO_3)_2$), and calcite ($CaCO_3$), and are commonly associated with magnetite and hematite (Konhauser et al., 2017; Rasmussen et al., 2021). Based on extensive petrographic studies, it is generally agreed that siderite is not a primary, but an early diagenetic phase (Ayres, 1972; Rasmussen & Muhling, 2018; Rasmussen et al., 2021), possibly resulting from the remineralisation of organic matter (Konhauser et al., 2017). There are two fundamentally

different approaches, in which siderite has been proposed to have either been (1) abiotically precipitated on suitable pre-existing substrates, such as greenalite and silica-rich muds (Tosca et al., 2019; Rasmussen et al., 2021; Jiang et al., 2022) or as transformation product of the mixed-valent Fe phase green rust (Halevy et al., 2017), or formed via (2) biotically assisted pathways of initial microbially mediated Fe(II) oxidation inducing primary Fe(III) oxide deposition and subsequent microbial (dissimilatory) Fe(III) reduction linked to organic carbon oxidation to form ferrous carbonate minerals (Bekker et al., 2010; Konhauser et al., 2017).

To unravel the origin of the siderite and associated carbonate minerals, the cation composition and C, O, and Fe isotopic signatures of the ferrous-rich carbonate phases have been used as paleo-environmental proxies and indicators for potential iron and carbon sources. However, the fractionation mechanisms of these elements during siderite formation and oxidative decomposition are not fully understood. The very negative $\delta^{13}C$ values (–5 to –10‰) of generally all Fe(II)-rich carbonate minerals have been interpreted as indicative for complete organic matter oxidation coupled to primary Fe(III) mineral reduction, further explaining the very low contents of organic carbon ($\leq$ 0.01 to 0.5 wt.% total organic carbon in IFs; Konhauser et al., 2017; Tang et al., 2018). However, the proposed cation and ^{13}C (and ^{18}O) isotopic compositions of siderite (Mozley, 1989; Mozley & Wersin, 1992) can be ambiguous as cation incorporation and isotopic fractionation are linked to structural affinities (Sengupta et al., 2020) and can be affected by siderite nucleation and growth kinetics (Jiang & Tosca, 2019). More specifically, the cation composition of ferrous carbonates depends more on the metal cationic radius and coordination in the mineral structure, which require different formation conditions such as increased temperature or homogeneous nucleation, rather than on the water composition (c.f., Sengupta et al., 2020). Hence, the chemical composition in siderite may not directly reflect the cation chemistry of the aqueous solution and thus the depositional environment siderite precipitated from. Carbonate minerals of distinctly different $Me^{2+}CO_3$ composition (with Me^{2+} = Ca, Mg, Mn, and/or Fe) show strong variations in their dissolution–precipitation behaviour as discussed in this thesis (*see* section 3.2.) and should thus instead be distinguished between and viewed separately, e.g., siderite vs. ankerite vs. Ca/Mg-rich carbonates. Furthermore, variations in the $\delta^{13}C$ values in carbonates may result from the mixture of water sources with different ^{13}C isotope compositions, such as shallow seawaters in contact with limestones (~0‰) and deeper, ^{13}C-depleted hydrothermal source vent fluids (–7.0‰; Rasmussen et al., 2021 *and references therein*). The $\delta^{13}C$ values may further vary substantially by up to –4‰ without biological influences through kinetic growth effects (Jiang & Tosca, 2019; Jiang et al., 2022). These various effects on siderite cation and isotopic composition should be considered when

using these features as paleo-environmental proxies. As ^{13}C fractionation occurs during siderite nucleation and growth, further isotopic fractionation may occur during oxidative dissolution of siderite and of secondary carbonate phase precipitation (e.g., ankerite, cerussite, etc.). The detailed documentation of the oxidation–precipitation pathways of siderite under reducing ('pre GOE') and oxidising ('post GOE') conditions presented in this thesis may help constraining cation partitioning and ^{13}C isotopic fractionation factors in future experimental studies. High-resolution solid phase analyses similar to those applied herein such as combined µXRF and XAFS analyses could be used to determine cation distribution and structural bonding. The emerging technique of atom probe tomography analysis on geological samples could further locally resolve C and O isotopic compositions in siderite and the secondary phases allowing for a more accurate interpretation of the isotopic compositions in these minerals used as potential paleo-environmental and geochemical proxies.

Besides the origin of siderite, its decomposition – i.e., oxidative dissolution – may provide insights into the geological history of IFs and the oxygenation of the early Earth's atmosphere during and/or following the GOE. The oxidant-dependent pathways of oxidative siderite dissolution described in this thesis may help improve our understanding of and aid constraining potential mechanisms that may have been responsible for the evolution of our modern oxygen-rich atmosphere. Particularly in the younger GIFs, siderite is considered to be early diagenetic and closely associated with magnetite and hematite (Bekker et al., 2010; Rasmussen et al., 2021). After burial, siderite was likely thermally decomposed and replaced by magnetite which further transformed into hematite during late-stage alteration of pre-GOE iron formations (Rasmussen & Muhling, 2018; Rasmussen et al., 2021). Following the initial rise of atmospheric oxygen after the GOE, it has been proposed that the global occurrence of ^{13}C-enriched limestones and dolostones of the Lomagundi Event (ca. 2.3 to 2.1 Ga) may be linked to the oxidative weathering of siderite (Bachan & Kump, 2015). As demonstrated in this thesis, oxidative dissolution of siderite provides carbon and reduces acidity, while resulting oxidative Fe(III) precipitation buffers the pH. For the early Earth's evolving atmosphere, siderite oxidative dissolution is hence considered a critical source of carbon to comply with the reconstructed measures of pCO_2 in the atmosphere, organic carbon burial and O_2 accumulation in the atmosphere (Bachan & Kump, 2015). This contrasts the commonly proposed oxidative weathering of continental sulphides as source of acidity, which not only consumes much more O_2 than siderite oxidation, but also causes an alkalinity imbalance (Bachan & Kump, 2015).

Oxidative weathering of Fe(II) minerals has been coupled to the biogeochemical behaviour of Cr and Cu as emerging paleo redox proxies. The interaction of such redox-active metals with Fe(II) minerals may vary with the type of metal and oxygen present in the system (c.f., chapter 5). Relative Cr enrichment in sedimentary successions following the GOE has been proposed to be linked to early enhanced oxidative weathering: aerobic continental pyrite oxidation would generate the first 'acid rock drainage' causing primary Cr(III) mineral dissolution and increased Cr(VI) flux into the ocean, while subsequent interaction with Fe(II) would have caused Cr(III)-Fe(III) oxyhydroxide coprecipitation representing a 'first sedimentary cycle of oxidative weathering' (Konhauser et al., 2017 *and references therein*). This interpretation assumes no estuarine mixing or Cr biogeochemical cycling within costal and shelf seas which may affect the δ^{53}Cr values of seawater, reflecting local rather than global processes (Goring-Harford et al., 2020). Although siderite is known to undergo oxidative dissolution upon heterogeneous reduction of Cr (e.g., Tang & Martin, 2011; Bibi et al., 2018), potential Cr isotopic fractionation mechanisms during the redox-induced dissolution–precipitation reactions are poorly understood. Results presented in this thesis indicate that the oxidative effect of a redox-active metal is affected by the redox strength of the metals and the presence of O_2, resulting in different redox-induced pathways of metal removal from the aqueous solution. These effects may further influence metal isotope fractionation and should be investigated experimentally to constrain the isotopic fractionation factors to be considered when using Cr and its isotopic compositions as paleo redox proxy.

Similarly, Cu isotopes have been proposed as biogeochemical and redox proxies. Apparent changes in the Cu isotopic compositions in the Archaean to Proterozoic sediments have been interpreted to be linked to enhanced (aerobic) oxidative weathering, thus recording the GOE (Chi Fru et al., 2016). Copper isotopic compositions can be strongly affected by redox reactions and aqueous, mineral surface, and potentially organic complexation reactions with the greatest fractionation predicted for the oxidation of Cu(I) to Cu(II) (Sherman, 2013; Sherman & Little, 2020). Hence the shift from generally negative to continuously positive δ^{65}Cu compositions has been interpreted to be associated with a removal of ^{65}Cu isotopes during the declining deposition of BIFs and increasing input of continentally derived ^{65}Cu from oxidative (Cu(I)) sulphide weathering (not considering the potential effect of increasing oxidative decomposition of siderite). The coinciding negative δ^{56}Fe and increasing marine sulphate sedimentary compositions coupled to the apparent change in the Cu isotopic composition has thus been interpreted to reflect the atmospheric and oceanic oxidising conditions during and after the GOE (Chi Fru et al., 2016). The heavy ^{65}Cu isotope is generally assumed to be preferentially

associated with ferric oxides and thus seawater would be enriched in the lighter ^{63}Cu isotope. Although abiotic and biotic Cu oxidation cannot be distinguished, the inversely plotting organic $\delta^{13}C$ and $\delta^{65}Cu$ values have been interpreted as covariant Cu and C cycling in ancient oceans (Chi Fru et al., 2016), contrasting the positive correlation in modern sediments (Ciscato et al., 2019 *and references therein*). Additional isotopic fractionation has been observed in native Cu^0 in marine sediments. Though interpreted to reflect redox processes, neither the factors responsible for the variations in the observed fractionation intensities in different marine sedimentary settings, nor whether the oceanic crust is sink and/or source for Cu in seawater is well understood (Dekov et al., 2013). In concert with Cr, Cu partitioning and isotopic fractionation is likely affected by the strength of the redox couple and the presence of O_2 during the redox-induced dissolution–precipitation reactions between Cu(II) and Fe(II)-bearing minerals. These effects on isotopic fractionation are, however, unknown. Considering that Cu(I) oxidation to Cu(II) is linked to the greatest fractionation, the stepwise reduction of Cu(II) to Cu(0) likely has a similar effect. Also, the general difficulty to unambiguously assess the oxidation state of Cu in redox reaction products (c.f., chapter 5; Biesinger, 2017) may additionally complicate the interpretation of Cu isotope signatures. Redox-induced Cu isotope fractionation is commonly linked to organic complexation. However, the results reported in this thesis demonstrate that Cu(II) reduction may also occur abiotically under reducing and oxidising conditions by heterogeneous Fe(II) oxidation. Hence the presented redox-induced partitioning of Cu in reducing and oxidising environments may encourage experimental verification of and help constraining the mechanisms responsible for Cu isotopic fractionation in ancient and modern environments.

Studies using siderite to remove redox-active metals from oxic and anoxic aqueous solutions demonstrate that oxidative siderite dissolution can also be induced abiotically and contribute to isotopic fractionation. Experimental and combined solid phase analytical assessment of the C, O, Fe, and metal (e.g., Cu, Cr) isotopic compositions during the redox-induced dissolution–precipitation reactions of siderite and redox-active metals could shed light on the currently uncertain isotopic fractionation pathways of these elements to verify their use as biological and redox proxies.

Appendix

This appendix contains supplementary information of the siderite material used, siderite dissolution in metal-free aqueous solutions, and of experimental and methodological specifications of the work presented in chapters 4 and 5.

A.1. Starting material and methodological specifications

The natural siderite material used in this work originates from the Peyrebrune Quarry, France (Bénézeth et al., 2009). The polycrystalline material of high purity (> 98%) was ground in an agate mortar and sieved to a size fraction of < 63 µm. The powdered material was washed in ethanol to prevent oxidation; cleansing cycles of washing and sonication to remove ultrafine particles was repeated five times. Until experimental use or pre-experimental characterisation, the cleaned material was stored in ethanol or in the anaerobic chamber to avoid oxidation. Unreacted siderite starting material was characterised by XRD, SEM (*see* below; Table A1; Figure A1), and ICP-OES analyses (*see main text*), prior to experimental use.

Table A1. Relative amounts of phases identified in the unreacted siderite starting material (size fraction <63 µm) by XRD analysis. Note that these are approximate values based on peak width and intensity, given in %.

Mineral	**Chemical Formula**	**Powder Diffraction File (PDF)**	**Siderite**
		Reference	*Bulk material*
Siderite	$FeCO_3$	PDF 01-083-1764 Effenberger et al. (1981)	> 95-98
Fluorite	CaF_2	PDF 01-077-2093 Batchelder & Simmons (1964)	1-5
Calcite	$CaCO_3$	PDF 01-083-1762 Effenberger et al. (1981)	< 1
Quartz	SiO_2	PDF 01-086-2237 Young et al. (1977)	≤ 1
Hematite[a]	Fe_2O_3	PDF 01-089-0598 Sadykov et al. (1996)	< 1

[a]Primary alteration product (likely hydrothermal/igneous; Senaki et al., 1986)

Siderite dissolution experiments in the presence of dissolved Pb and Cu were performed in several series of experiments under oxic and anoxic conditions. Aqueous solution pH and metal concentrations were monitored at each sampling time step. For aqueous solution analysis, solution aliquots were filtered through a 0.2 µm polyethersulfone syringe filter, immediately acidified by adding 1.5 M HNO_3 or 12 M HCl, then diluted with 0.1 M HNO_3 or 0.1 M HCl and stored at 4 to 5 ºC prior to solution chemistry analyses. Solid reaction products were collected after each experiment by vacuum filtration through a 0.2 µm nylon or polycarbonate membrane filter and stored either dry in a desiccator or in ethanol to prevent phase

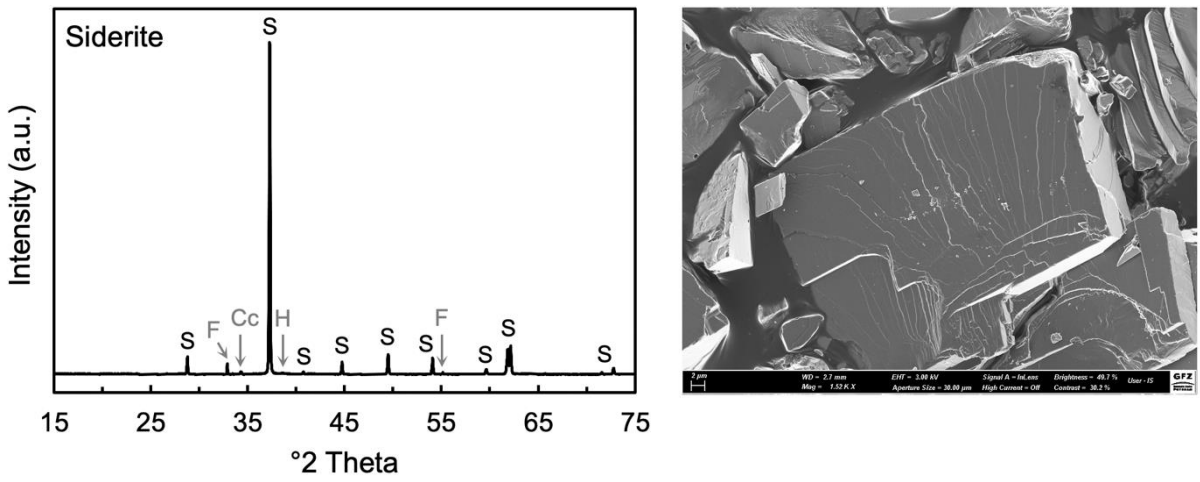

Figure A1. XRD pattern (left) and SEM image (right) of the unreacted siderite. S = siderite, F = fluorite, Cc = calcite, H = hematite.

transformation and oxidation. Solids collected from the anoxic experiments were stored in the anaerobic chamber until used for analyses.

Total Fe, Pb, and Cu concentrations were determined by **ICP-OES** (RSD = 0.29 to 1.23%). To detect possible aqueous Fe oxidation, Fe speciation was determined using the Ferrozine method in a colorimetric segmented flow analysis (**SFA**) apparatus (SEAL AutoAnalyser 3HR). The reagent Ferrozine, a disodium salt of 3-(2-pyrdyl)-5,6-bis(4-phenylsulfonic acid)-1,2,4-triazine (> 98% purity, ACROS organics) forms a bright magenta-coloured complex with ferrous Fe which can be spectrophotometrically identified by its maximum absorption peak at 562 nm (Stookey, 1971). The intensity of this absorption line can then be translated into the

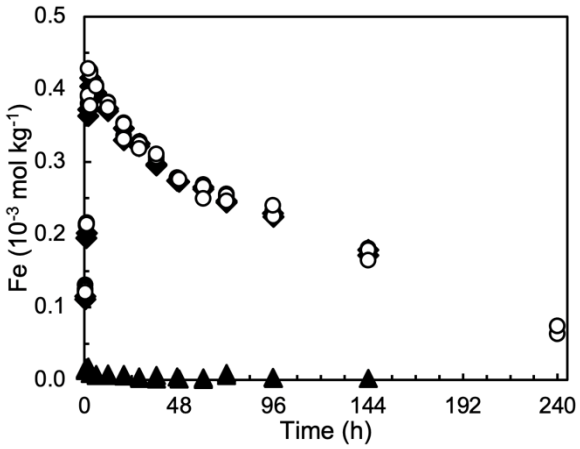

Figure A2. Measured Fe concentrations during siderite dissolution under oxic conditions in the absence of metals in the aqueous solution. Data obtained from ICP-OES shown in empty symbols versus SFA data shown in black symbols. Circles = Fe^{total}, diamonds = Fe^{2+}, triangles = Fe^{3+}. Error bars are smaller than the markers (average RSD(SFA) = 0.35%, RSD(OES) = 0.76%).

ferrous Fe concentration in the analysed aqueous solution. For aqueous solutions in which Cu and Fe are simultaneously present, this method is not applicable because both metals form indistinguishable complexes with Ferrozine, resulting in strong interferences in the detected signal. Total Fe concentrations measured using the ICP-OES were nearly identical to those obtained by SFA, whereby $Fe^{total}_{SFA} \approx Fe^{2+}_{SFA}$ (RSD = 0.35–0.76%; Figure A2). Hence, the Fe^{total} concentrations obtained from ICP-OES measurements can be assumed representative for Fe^{2+}.

For **XRD** analysis of the unreacted and reacted siderite samples, the solids were dispersed in ethanol and mounted dropwise on ultra-thin glass cover slips. The samples were measured at 20 mA and 40 kV over a range of 5 to 105 º2θ with a step size of 0.001 º2θ.

For **SEM** analyses, tiny amounts of granular unreacted and reacted siderite sample dispersed in ethanol were mounted dropwise and/or with a mineral picking needle onto carbon tape stuck on Al SEM sample stubs. Mounted samples were sputter coated with Au or C for sample conductivity. Samples reacted under anoxic conditions were prepared in the anaerobic chamber and transferred to the SEM instrument in an anaerobic box to prevent oxidation.

For high-resolution **TEM** imaging, solid samples were prepared in two ways: (1) Focused ion beam (FIB; Ga beam) technology in a FEI Helios G4 UC Dual Beam SEM was used to cut electron transparent thin foils of 2.5 × 5 × 15 µm from the Au-coated SEM samples. The thin foils were lifted out using Pt as 'glue' and mounted on half Cu TEM grids. (2) Reacted solids dispersed in ethanol were drop-cast onto holey amorphous carbon-coated Cu TEM grids. Due to these sample preparation methods, Ga, Pt, Au, and Cu were detected in TEM-EDX analyses. The FEI Tecnai G2 F20 X-Twin TEM was operated at 200 kV with a Schottky field emitter electron source. Additionally obtained HAADF scanning transmission electron micrographs and FFT patterns were processed and analysed using the Gatan GMS3 software DigitalMicrograph™.

Metal speciation and bonding analysis were performed on solid reaction products collected after 1008 h of reaction under oxic and anoxic conditions, using synchrotron-based **XANES**- and **XRF**-mapping at the beamline I14 at Diamond Light Source. The solid samples were dispersed in ethanol and drop-cast onto 1.5 × 1.5 mm SiN window sample holders that were mounted on a coarse-motion XY sample stage. The nano-focused, monochromatic hard X-ray beam with a beam size of 50 nm was operated at a current of 200 to 300 mA and an acceleration voltage of 8 to 15 keV to generate XANES spectra of the Fe and Cu K-, and Pb L_3-edges. Selected area spectra were collected over an exposure time of 0.05 s pt^{-1} with a Malcom XSP3

detector combined with a 20 mm diode in backscatter or transmission geometry. The raw XANES spectra were pre-processed in the Python-based script MANTIS for initial data reduction and to produce reasonable clusters of mapped XANES spectra. Bulk sample XAFS analyses were conducted at the SUL-X beamline at the ANKA-KIT synchrotron, which features a larger beam size of 10 × 10 µm to 25 × 30 µm. The fine-grained solid samples collected after 1008 h of reaction under oxic and anoxic conditions were further pulverised and homogenised with ultrafine inert, non-absorbing boron nitride (BN) in an agate mortar and pressed into 10- or 13-mm diameter pellets. The software XAFSmass (Klementiev, 2012) was used to calculate the relative mass proportions of sample and BN required to obtain optimal absorption signals. At both beamlines, powdered Fe, Cu, and Pb reference compounds were prepared accordingly, and reference absorption spectra were collected under the same conditions as the samples. At the ANKA-KIT SUL-X beamline, full XAFS spectra (**XANES** and **EXAFS** region) of the Fe and Cu K-, and P L_3-edges were generated at 50 to 100 mA. Multiple (3 to 5) scans of each sample and reference material were collected using a Si(111) monochromator in focused and collimated mode. At both beamlines, absorption edge energies for the Fe K-edge (7112.0 eV), Cu K-edge (8978.9 eV), and the Pb L_3-edge (13035.2 eV) were calibrated by measuring a Fe, Cu, or Pb metal foil, respectively, prior to or simultaneously with the sample or reference material. All XAFS spectra were processed and fitted using the Demeter software package (Ravel & Newville, 2005). From this package, ATHENA was used for initial background correction, absorption edge energy alignment, and normalisation, as well as for linear combination fitting. Uncertainties associated with linear combination fitting originate from the individual steps of the procedure, i.e., from the removal of variations between preparation, absorber concentrations, and thickness effects of the samples and standards during normalisation, from the summation of the individual species in the samples, and from the mathematical scaling factor applied in the software to the standard spectra for best representation of the standard over the defined energy range (Kelly et al., 2008). The resulting uncertainty of the linear combination fitting ranges within ca. ±10%, whereby the statistical goodness-of-fit parameters are similar to those for the EXAFS spectra discussed below.

Theoretical models of the absorbing metal coordination environment were produced using ARTEMIS for shell-by-shell fitting of the Fourier transformed EXAFS Pb L_3- and Cu K-edge spectra. Values for the energy shift (ΔE_0), the coordination number (N), the half path length (R) of the scattering photoelectron, the amplitude reduction factor (S_0^2), and the Debye-Waller disorder factor (σ^2) were determined to best fit theoretical scattering paths generated from mineral structure files by the embedded FEFF6 program (Newville, 2001). The goodness-of-fit

is indicated by a R-factor ≤ 0.05 (given as a percentage of misfit), which is the sum of all squared point-by-point deviations of the theoretical model spectrum. Another important statistical indicator of a good fit is a low value for χ^2_ν (ideally close to 1), which is the sum of squared deviations between model and data values divided by the uncertainties (χ^2) normalised to the degrees of freedom ν in the model (defined as $N_{ind} - N_{var}$, where ind = independent points (data), and var = variants (fit); Kelly et al., 2008). The total number of parameters allowed to vary according to the Nyquist theorem $N_{ind} = 2\Delta k \Delta R/\pi$ was thereby never exceeded (Kelly et al., 2008).

For surface chemical analysis, **XPS** was performed at the Federal Institute for Material Research and Testing (BAM; Berlin). Solid samples collected after 1008 h of reaction under oxic and anoxic conditions (Pb and Cu O/A LT) were mounted on a sample holder with double adhesive tape. A Kratos Axis Ultra DLD spectrometer was used with a monochromatic Al Kα radiation source (1486.6 eV) operated at 150 W. The analytical chamber was kept at a base pressure of ca. 10^{-9} mbar, and a charge neutraliser was used during data collection. Calibration of the binding energy scale of the instrument was carried out following a Kratos Analytical procedure based on ISO 15472 (2010). Survey and high-resolution scans were performed in hybrid lens and slot mode over an analysis area of 300 × 700 µm^2 and pass energies of 80 eV and 20 eV, respectively. Spectra were charge corrected to the main line of the adventitious C 1s peak at 285 eV, which was used as internal reference. Background subtraction was performed after Tougaard (Hesse & Denecke, 2011). The software UNIFIT (Hesse et al., 2007) was used to fit the measured spectra with sum Gaussian functions following a least-squares fitting routine.

A.2. Siderite dissolution under oxic and anoxic conditions

To determine the effects of dissolved metals on the dissolution behaviour and reaction products of siderite in acidic aqueous solutions, **control experiments** (CS) were conducted under oxic and anoxic conditions in parallel to and following the identical experimental protocol as for the short-term (ST) series described in sections 4.2 and 5.2. Experimental specifications are given in Table A2, the results of measured Fe^{total} concentrations in the aqueous solution are shown in Figure A3, and SEM imaging of solids collected at selected time steps are shown in Figure A4.

Table A2. Experimental parameters and selected results from aqueous solution analyses of the control experiments of siderite dissolution in the absence of metals under oxic and anoxic conditions (CS).

Experiment	**Duration**	**Volume**	**Ionic strength**	**Siderite**	**pH**		**Me** (10^{-3} mol kg^{-1})	
	(h)	(g)[d]	(10^{-3} mol kg^{-1})		*initial*	*final*	*initial*	*final*
Siderite dissolution without lead				(± 0.1-1.8)	(± 0.01)			
CS O (ST)[a]	240[c]	10.1	2.37	51.6	2.79	4.45	--	--
CS A (ST)[b]	240[c]	10.0	2.08	51.9	3.08	6.92	--	--

[a]CS O ST = oxic short-term experiments, performed in PE-capped PP tubes; [b]CS A ST = anoxic short-term experiments, performed in butyl rubber aluminum crimp seal glass vials. [c]Series of 15 batches in duplicate run for 0.5, 1, 2, 3, 6, 12, 20, 28, 36, 48, 60, 72, 96, 144, 240 h. [d]Uncertainty ±0.05 to 0.06.

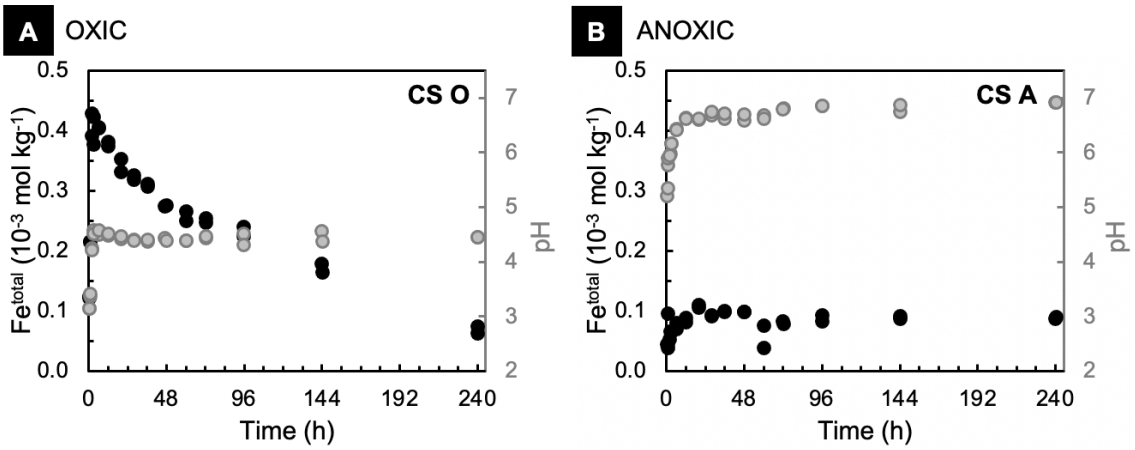

Figure A3. Total Fe concentrations (black) and pH (grey) shown as a function of time during dissolution of siderite in metal-free solutions under oxic (A) and anoxic (B) conditions (CS O and CS A; Table A2). Error bars are smaller than the markers; standard error of the pH probe is ±0.01 pts; RSD(OES) = 0.29–1.23%.

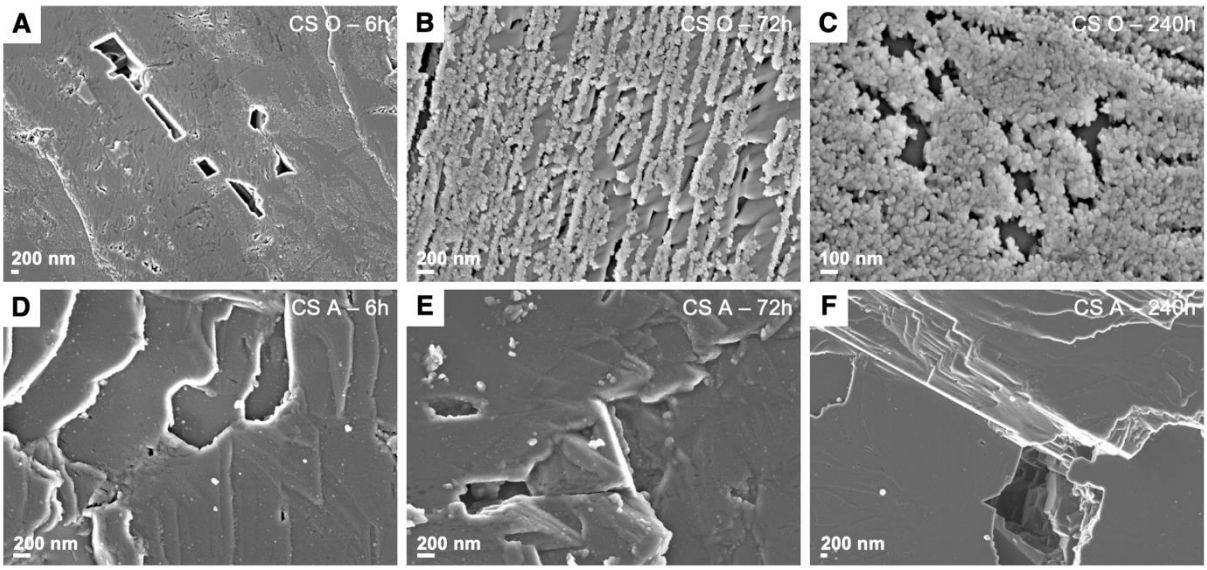

Figure A4. Scanning electron micrographs of reacted siderite grains collected after 6, 72 and 240 h of reaction in metal-free aqueous solution under oxic (CS O) and anoxic (CS A) conditions.

A.3. Siderite dissolution in the presence of Pb (chapter 4)

In chapter 4, the dissolution behaviour and reaction products of siderite dissolved in the presence of Pb under oxic and anoxic conditions was presented and discussed. The initial and final **aqueous solution specifications** are compiled in Table A3.

Table A3. Specifications of initial and final aqueous solution analyses of siderite dissolution experiments in the presence of Pb under oxic and anoxic conditions.

Experiment	**Duration**	**Volume**	**Ionic strength**	**Siderite**	**pH**		**Pb** (10^{-3} mol kg^{-1})	
	(h)	(g)[e]	(10^{-3} mol kg^{-1})		*initial*	*final*	*initial*	*final*
Lead-bearing aqueous control solutions				(± 0.1-1.8)	(± 0.01)		*calculated*	*average*
C O ST[a]	240[c]	10.0	5.28	--	3.05	3.06	0.483	0.475
C O LT[a]	1008[d]	250.9	5.02	--	3.06	3.05	0.483	0.471
C A ST[a]	240[c]	10.0	4.89	--	3.02	3.11	0.482	0.462
C A LT[a]	1008[d]	100.0	5.17	--	3.02	--	0.482	0.477
Siderite dissolution in lead-bearing aqueous solutions							*measured (± 0.003-0.05)*	
Pb O ST[a]	240[c]	10.0	5.28	51.9	3.06	4.83	0.47	0.27
Pb O LT[a]	1008[d]	124.8	5.02	51.7	3.03	5.33	0.47	0.05
Pb A ST[a]	240[c]	10.0	5.17	52.0	3.08	6.39	0.46	0.0
Pb A LT[b]	1008[d]	100.0	5.17	53.2	3.02	6.89	0.48	0.0

C = aqueous Pb control solution; Pb = siderite dissolution in the presence of lead; **O = oxic**; **A = anoxic**; ST = short-term (240 h); LT = long-term (1008 h). O ST experiments were performed in PE-capped PP tubes; O LT in LDPE Nalgene™ narrow mouth bottles. A ST and LT experiments were performed in butyl rubber aluminum crimp seal glass vials and serum bottles, respectively. [a]Performed and measured at the University College London. [b]Performed in anaerobic chamber and measured at the German Research Centre for Geosciences. [c]Series of 15 batches in duplicate run for 0.5, 1, 2, 3, 6, 12, 20, 28, 36, 48, 60, 72, 96, 144, 240 h. [d]Series of 6 batches in duplicate run for 6, 12, 36, 72, 288, 1008 h. [e]Uncertainty ± 0.05-0.06; Pb O LT: ± 1.1; Pb A LT: ±2.5 g.

A.3.1. Solid reaction products, Pb speciation and type of bonding

Results from **XRD** analyses of the siderite samples collected after 1008 h of reaction with Pb under oxic and anoxic conditions are compiled in Table A4. Note that the given relative amounts of phases identified in the XRD patterns are approximate and by no means accurate, as no Rietveld refinement was applied.

Table A4. Relative quantities of identified phases in XRD measurements. '*Residue*' refers to coarser grained, '*fines*' refers to ultra-fine grained reacted solids and precipitates collected after 1008 h of reaction. Note that these are approximate values based on peak width and intensity, given in %.

Mineral	**Chemical Formula**	**Powder Diffraction File (PDF)** Reference	**OXIC[a]**		**ANOXIC[b]**
			Residue	*Fines*	*Residue*
Siderite	$FeCO_3$	PDF 01-083-1764 Effenberger et al. (1981)	86	59	95
Fluorite	CaF_2	PDF 01-077-2093 Batchelder & Simmons (1964)	12	19	2
Quartz	SiO_2	PDF 01-086-2237 Young et al. (1977)	2	7	–
Goethite	α-FeOOH	PDF 00-029-0713 Harrison et al. (1975)	0.2	16	–
Hematite	Fe_2O_3	PDF 01-089-0598 Sadykov et al. (1996)	0.1	–	–
Cerussite	$PbCO_3$	PDF 01-076-2056 Chevrier et al. (1992)	–	–	2
*Lead Oxide Hydroxide**	*$Pb_5O_3(OH)_4$*	*PDF 00-028-1326 Glemser (1971)*	–	–	*(< 2)*

[a]oxic = Pb O LT; [b]anoxic = Pb A LT (long-term experiments). *High uncertainty (only two peaks assigned).

Reacted siderite material collected from the oxic and anoxic experiments after 1008 h of reaction (Pb O/A LT) were further analysed by **XAFS spectroscopy** to determine the speciation and bonding characteristics of solid-associated Pb.

For the **EXAFS** analysis of the sample collected from the **oxic** experiment (Pb O LT), first shell of oxygens at 2.31 Å distance from the central Pb atom was fit to the 4-fold coordination of Pb–O in litharge (PbO; Boher, 1985) to describe the data. The third shell neighbouring Fe atom at 3.31 Å distance from the absorbing Pb atom was assumed in a bidentate inner-sphere surface complexation coordination. Based on previous fits of spectra of cerussite and trace metal–iron (oxyhydr)oxide studies obtained from the same beamline (ANKA-KIT SUL-X), the amplitude reduction factor S_0^2 was set to 0.9, and the Debye-Waller disorder term σ^2 was set to 0.01 $Å^2$. All other parameters were allowed to vary in this fit. With N_{ind} = 14, the goodness-of-fit is demonstrated by 4 degrees of freedom, a R-factor of 0.020 and a χ_ν^2 of 100.3.

Based on the complementary solid analysis results and previous XANES Pb L_3-edge analyses indicating cerussite as primary form of Pb in the reacted solids collected from the **anoxic** experiment (Pb A LT), the **EXAFS** spectrum obtained from this sample was directly

fitted to the theoretical structure of cerussite (Chevrier et al., 1992). That is, for the five shells used in this model, the coordination numbers were constrained to values predicted by FEFF6, and due to the high correlation to N, σ^2 values were also constrained while S_0^2 was set to 0.9. The numerical and statistical goodness-of-fit values of this physically reasonable model with N_{ind} = 18 are 4 degrees of freedom, a R-factor of 0.034, and a χ_ν^2 of 94.7.

A summary of the results of **XPS** performed on the siderite reaction products collected after 1008 h of reaction with Pb under anoxic conditions is given in Table A5.

Table A5. Summary of **XPS** of Fe 2p, O 1s, C 1s, and Pb 4f measured binding energy peak positions and literature values. Data shown are obtained from the unreacted siderite and siderite reacted with Pb under anoxic conditions.

Atomic shell	**Binding Energy (eV)**			**Speciation / Compound**	**Reference**
	Siderite	Pb A LT[a]	Literature		
Fe 2p$_{3/2}$	710.2	710.6	710.0	Fe^{2+}	Hochella, 1988
O 1s	529.4	529.8	530.0	O^{2-}	Junta & Hochella, 1994
	531.4	531.7	531.9	CO_3^{2-}	Stipp & Hochella, 1991
			532.3		Duckworth & Martin, 2004
	533.0	532.6	533.2	$H_2O_{surface}$	Stipp & Hochella, 1991
			532.3	(OH^-)	Duckworth & Martin, 2004
C 1s	284.9	284.8	284.4 - 285.0	‚adventitious carbon'	Stipp & Hochella, 1991;
			284.8 - 285.0	*hydrocarbons*	Miller et al., 2002; Feng et
			284.4	*amorphous C*	al., 2016
	286.0	286.1	286.2 - 286.6	Alcohol	Stipp & Hochella, 1991;
				(C-O bond)	Rouxhet & Genet, 2011
	289.2	289.6	290.0 - 290.4		Stipp & Hochella, 1991;
			289.3	CO_3^{2-}	Feng et al., 2016
			288.6		Miller et al., 2002
	290.9	290.2	290.7 - 291.5	HCO_3^-	Stipp & Hochella, 1991
Pb 4f$_{7/2}$	-	138.6	138.2	$2PbCO_3 \cdot Pb(OH)_2$	Pederson, 1982
			138.6	Pb-Calcite	Fulghum et al., 1988
			138.8	Pb-Aragonite	Godelitsas et al., 2003
			138.8	$PbCO_3$	Feng et al., 2016
Pb 4f$_{5/2}$	-	143.5	+4.9		Pederson, 1982

[a]Siderite reaction products collected after 1008 h of reaction with Pb under anoxic conditions.

A.3.2. Reaction kinetics and thermodynamic model calculations

Simplified **dissolution rates** of siderite dissolution under oxic conditions in the absence and presence of Pb were calculated according to

$$R_{\text{dissolution}} = \frac{\Delta[\text{Fe}_i]_{\text{SA}}}{\Delta t_i} \qquad \text{(eq. A1)},$$

where the dissolution rate R is described by the change in measured Fe^{total} concentrations normalised to the BET surface area (SA) of siderite for each consecutive sample i divided by the time change between each sampling time step t_i. Calculations were constrained to data collected within the first 2 h of reaction, i.e., prior to detectable ferric (oxyhydr)oxide precipitation. Note that the aqueous solutions were strongly undersaturated with respect to siderite and (re)precipitation of siderite is negligible at pH < 5. Hence, only the forward reaction of siderite dissolution was considered. The obtained dissolution rates agree well with rates reported in the literature for comparable study conditions (Figure A5; Table A6).

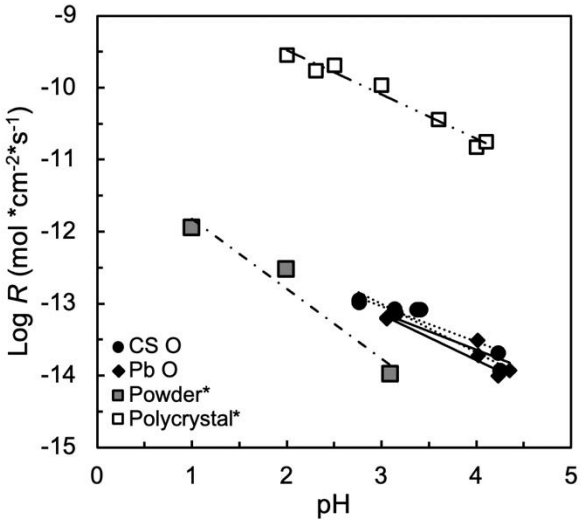

Figure A5. Siderite dissolution rates based on Fe^{total} concentrations in the reactive solution at room temperature shown as a function of solution pH. Black symbols represent rate data obtained from fine-grained siderite powder (<63 µm, BET surface area of 9.952 $m^2\ g^{-1}$) dissolved in the presence (Pb O) and absence (CS O) of Pb(II) (this study). Dissolution rate data obtained under similar conditions reported by Golubev et al. (2009) for powdered (BET surface area of 7.08 $m^2\ g^{-1}$) and polycrystalline material (rotary disc) are shown for comparison as open symbols (indicated by *).

To compliment and based on the results from aqueous solution and solid reaction product analyses, theoretical aqueous solution compositions and mineral saturation indices were calculated using the **PHREEQC** v3 code (Parkhurst & Appelo, 2013). Results for selected time steps from the siderite dissolution experiments in the absence and presence of Pb(II) under oxic and anoxic conditions are compiled in Tables A7 and A8. For the model calculations, the Lawrence Livermore National Library database (2017) was used and modified with thermodynamic data for siderite taken from the CarbFix database (Voigt et al., 2018).

Table A6. Siderite dissolution rates calculated for the Pb-free[a] (CS O) and Pb-containing[b] (Pb O) siderite dissolution experiments prior to oxidative ferric (oxyhydr)oxide precipitation. Siderite dissolution rates were calculated at a given pH according to $R = k_{+H+} \cdot a_{H+}^{n}$ using the kinetic rate constant $k_{+H+} = 1.79 \cdot 10^{-8}$ and n = 0.75 as reported for siderite dissolution at 25 °C (Golubev et al., 2009).

			This study[c]		*Calculated from Golubev et al., 2009*	
Experiment	**Time (h)**	**pH**	***R*** (mol cm^{-2} s^{-1})	**log *R***	***R*** (mol cm^{-2} s^{-1})	**log *R***
CS O[a]	0	2.8	1.09×10^{-13}	-12.965	3.11×10^{-13}	-12.507
	0.55	3.1	7.88×10^{-14}	-13.104	1.29×10^{-13}	-12.890
	1.07	3.4	8.29×10^{-14}	-13.087	7.32×10^{-14}	-13.136
	2.03	4.2	1.62×10^{-14}	-13.805	1.04×10^{-14}	-13.981
Pb O[b]	0	3.1	6.28×10^{-14}	-13.202	1.56×10^{-13}	-12.807
	0.51	4.0	2.53×10^{-14}	-13.609	1.73×10^{-14}	-13.762
	0.99	4.3	1.10×10^{-14}	-13.961	9.39×10^{-14}	-14.032

[c]Based on a siderite BET surface area of 9.952 m^2 g^{-1}.

Table A7. Solution chemistry and mineral saturation states for siderite dissolution in the absence of metals under oxic (CS O) and anoxic (CS A) conditions calculated in PHREEQC based on measured aqueous solution compositions[a] assuming stoichiometric dissolution of siderite and no CO_2(g) leakage from the experiment solution. Concentrations are given in $\times 10^{-3}$ mol kg^{-1}.

Measured				**Modelled**				**Saturation Indices**		
Experiment	Time (h)	pH	Fe^{2+a}	Fe^{3+b}	Alk.	CO_2	HCO_3^-	Sid	Goe	Hem
CS O	0	3.1	0.0	0.0	-1.05	0.0	0.0	-	-	-
	0.5	3.2	0.13	0.0016	0.26	1280.1	1.00	-3.63	-4.49	-7.98
	3	4.6	0.42	0.58	0.84	37.34	0.75	-1.83	0.26	1.51
	96	4.4	0.23	0.21	-0.04	0.23	0.0034	-4.50	-0.32	0.34
CS A	0	2.8	0.0	–	-1.95	0.0	0.0	–	–	–
	0.5	5.3	0.042	–	0.08	0.76	0.082	-3.00	–	–
	3	6.2	0.065	–	0.13	0.14	0.12	-1.77	–	–
	96	6.9	0.088	–	0.18	0.04	0.16	-0.83	–	–

[a]ICP-OES data determined at given time steps. [b]In $\times 10^{-9}$ mol kg^{-1}. Sid = siderite; Goe = goethite; Hem = hematite.

Table A8. Solution chemistry ($\times 10^{-3}$ mol kg^{-1}) and mineral saturation states for siderite dissolution in the presence of Pb(II) under oxic (Pb O) and anoxic (Pb A) conditions modelled in PHREEQC based on aqueous solution data[a]. Stoichiometric dissolution of siderite and no CO_2(g) leakage from the experiment solution were assumed.

	Measured				**Modelled**			**Saturation Indices**				
Experiment	Time (h)	pH	Fe^{2+a}	Pb^{2+a}	Alk.	CO_2	HCO_3^-	Sid	Goe	Hem	Cer	Hyc
Pb O	0	3.1	0.0	0.48	-0.96	0.0	0.0	–	–	–	–	–
	0.5	4.0	0.067	0.46	1.05	189.0	1.07	-3.05	-2.21	-3.44	0.18	-3.96
	96	4.5	0.033	0.34	0.75	40.0	0.72	-3.01	-1.00	-1.01	0.37	-2.70
	336	4.8	0.002	0.23	0.46	12.4	0.44	-4.23	-1.41	-1.83	0.29	-2.42
	504	5.0	0.002	0.18	0.36	6.08	0.34	-4.13	-0.80	-0.61	0.28	-2.16
	672	5.0	0.002	0.12	0.24	4.13	0.23	-4.29	-0.79	-0.60	-0.07	-3.02
	840	5.2	0.002	0.07	0.14	1.54	0.14	-4.31	-0.18	0.62	-0.33	-3.38
	1008	5.3	0.002	0.049	0.10	0.86	0.10	-4.36	0.12	1.23	-0.54	-3.76
Pb A	0	3.1	0.0	0.48	-0.96	0.0	0.0	–	–	–	–	–
	0.5	5.1	0.025	0.40	0.85	12.1	0.79	-2.53	–	–	1.04	-0.17
	3	5.5	0.038	0.34	0.76	4.32	0.69	-2.00	–	–	1.30	1.06
	96	6.5	0.28	0.0007	0.56	0.27	0.49	-0.22	–	–	-0.48	-3.09
	1008	6.9	0.30	0.0001	0.61	0.12	0.53	0.24	–	–	-1.01	-4.30

[a]ICP-OES data determined at given time steps. Alk. = alkalinity; Sid = siderite; Goe = goethite; Hem = hematite; Cer = cerussite; Hyc = hydrocerussite.

Under **oxic** conditions, siderite dissolution is not considerably affected by the formation of surface precipitation. Ferric (oxyhydr)oxide precipitation was observed within 2 h of reaction in both Pb-bearing and Pb-free experiments. Assuming stoichiometric dissolution of siderite, for each bicarbonate ion produced and Fe(II) released, three protons are produced upon oxidative precipitation of ferric (oxyhydr)oxides:

$$FeCO_3 + H^+ \rightarrow Fe^{2+} + HCO_3^- \qquad \text{(eq. A2)}$$

$$Fe^{2+} + 3H_2O \rightarrow Fe(OH)_3 + 3H^+ + e^- \qquad \text{(eq. A3).}$$

Because the solution pH initially continues to increase until plateauing throughout the remaining duration of the experiment, siderite dissolution rates must continue to outcompete oxidative precipitation rates of the ferric (oxyhydr)oxides. Notably, the structural difference between substrate (siderite, trigonal) and surface precipitates (goethite, orthorhombic) suggests heterogeneous precipitation, which may not considerably affect the dissolution rates of the dissolving substrate (e.g., Hudson, 2003). The apparent difference in the dissolution behaviour

of siderite in the absence and presence of Pb under otherwise identical (oxic) experimental conditions (c.f., Figures A3A and 4.1A) can be explained by the difference of 0.3 pH units of the aqueous starting solutions (c.f., Tables A2 and A3). Note that CO_2(g) leakage from the reactive solutions during sampling could not be entirely avoided and was therefore not considered in the dissolution rate calculations.

Siderite dissolution under **anoxic** conditions in contrast, is enhanced in the presence of Pb. That is, the precipitation of cerussite drives carbonate consumption and therewith promotes siderite dissolution following equation A2 and

$$HCO_3^- + H^+ \rightarrow H_2CO_3(aq) \qquad \text{(eq. A4)}$$

$$Pb^{2+} + H_2CO_3(aq) \rightarrow PbCO_3 + 2H^+ \qquad \text{(eq. A5).}$$

The overall reaction can be given as

$$FeCO_3 + Pb^{2+} \rightarrow Fe^{2+} + PbCO_3 \qquad \text{(eq. A6).}$$

Notably, this reaction buffers the reactive solution pH until all Pb is consumed. Upon complete Pb consumption, siderite continues to dissolve until a pH 6.9 is reached and the dissolution rate of siderite slows markedly (e.g., Duckworth & Martin, 2004a). Based on the measured reactive solution composition, PHREEQC model calculations further indicate that the system approximates saturation with respect to siderite at this point ($SI_{siderite}$ = 0.24 after 1008 h of reaction; Table A8).

A.4. Siderite dissolution in the presence of Cu (chapter 5)

Siderite dissolution in the presence of dissolved Cu(II) was studied under oxic and anoxic conditions in a series of short-term (ST) and long-term (LT) batch experiments as presented in detail in chapter 5.2. A summary of the initial and final **aqueous solution specifications** is given in Table A9.

Table A9. Experimental parameters and initial and final aqueous solution specifications for siderite dissolution experiments in the presence of Cu(II) under oxic and anoxic conditions.

Experiment	**Duration** (h)	**Volume** (g)[c]	**Ionic strength** (10^{-3} mol kg^{-1})	**Siderite**	**pH** *initial*	**pH** *final*	**Cu** (10^{-3} mol kg^{-1}) *initial*	**Cu** (10^{-3} mol kg^{-1}) *final*
Copper-bearing aqueous control solutions				(±0.1-1.9)	(±0.01)		*calculated*	*measured*
C O ST[a]	240*	9.91	5.68	--	3.02	3.05	1.55	1.55
C O LT[a]	1008	251.9	5.79	--	3.04	3.06	1.57	1.51
C A ST[b]	240*	10.0	5.70	--	3.04	3.08	1.54	1.53
C A LT[b]	1008	100.0	5.45	--	3.04	3.07	1.54	1.53
Siderite dissolution in copper-bearing aqueous solutions							*measured (±0.003-0.05)*	
Cu O ST[a]	240*	9.99	5.68	52.3	3.06[d]	4.4/5.4[e]	1.55	1.20/1.40[e]
Cu O LT[a]	1008**	125.30	5.79	51.7	3.04	4.79	1.51	0.27
Cu A ST[b]	240*	10.0	5.52	52.0	3.04	5.44	1.53	1.27
Cu A LT[b]	1008	100.0	5.45	53.1	3.04	5.77	1.53	bdl[f]

C = aqueous Cu control solution; Cu = siderite dissolution in the presence of copper; **O = oxic**; **A = anoxic**; ST = short-term (240 h); LT = long-term (1008 h). Oxic ST experiments were performed in PE-capped PP tubes; Oxic LT in LDPE Nalgene™ narrow mouth bottles. Anoxic ST and LT experiments were performed in butyl rubber aluminium crimp seal glass vials and serum bottles, respectively. *Series of 15 batches performed in duplicate run for 0.5, 1, 2, 3, 6, 12, 20, 28, 36, 48, 60, 72, 96, 144, 240 h. **Series of 4 batches performed in duplicate run for 6, 36, 286, 1008 h. [a]Performed and measured at the University College London. [b]Performed in anaerobic chamber and measured at the German Research Centre for Geosciences. [c]Uncertainty = 0.02-0.06 g; Cu O LT: ± 0.27 g; Cu A LT: ± 0.6 g. [d]Average taken form the control solution data. [e]Obtained from repeated ST experiments performed at the GFZ using a siderite size fraction of 38–64 µm (no ultrafine fraction). [f]bdl = below detection limit (< 0.46 x 10^{-6} mol kg^{-1}).

A.4.1. Solid reaction products, Cu speciation and type of bonding

Solid reaction products collected after 1008 h from the long-term experiments of reacting siderite with aqueous Cu(II) under oxic and anoxic conditions (Cu O/A LT) were characterised by **XRD** analyses. Note that the reported relative quantities (Table A10) of the phases identified in the XRD patterns are approximate.

Table A10. Relative amounts of phases identified by XRD analysis of solids collected from the oxic and anoxic experiments after 1008 h of reaction. '*Residue*' refers to coarser grained, '*fines*' refers to ultrafine grained reacted solids and precipitates. Note that these are approximate values based on peak width and intensity, given in %.

Mineral	**Chemical Formula**	**Powder Diffraction File (PDF)**	**OXIC[a]**		**ANOXIC[b]**
		Reference	*Residue*	*Fines*	*Residue*
Siderite	$FeCO_3$	PDF 01-083-1764 Effenberger et al. (1981)	77	11	91
Fluorite	CaF_2	PDF 01-077-2093 Batchelder & Simmons (1964)	16	–	< 1
Goethite	α-FeOOH	PDF 01-081-0462 Hazemann et al. (1991)	7	47	–
Hematite	Fe_2O_3	PDF 01-089-0598 Sadykov et al. (1996)	< 1	42	–
Lepidocrocite	γ-FeOOH	PDF 01-074-1877 Ewing (1935)	–	–	5
Copper metal	Cu(0)	PDF 01-085-1326 Swanson & Tatge (1953)	–	–	4

[a]oxic = Cu O LT; [b]anoxic = Cu A LT (long-term experiments).

The reacted solids were further morphologically and structurally characterised by **HRTEM** and FFT imaging. A list of measured *d*-spacings and reference values from structural data taken from the literature (Powder Diffraction Files; *references as in* Table A10) used for phase identification is provided in Table A11 on the following page.

Table A11. List of the most commonly observed characteristic lattice distances (*d*-spacings, Å) in HRTEM and corresponding FFT images of ultrafine-grained solid samples recovered from the oxic and anoxic experiments after 1008 h of reaction. Dominant *d*-spacings used for phase identification are highlighted in **bold**.

	Measured		**Reference**			Lattice plane		
	d_m (Å)	σ	d_R (Å)	±5%[c]	Δd (Å)[d]	*h*	*k*	*l*
OXIC *F*[a]								
Siderite	**3.667**	0.013	**3.592**	0.180	0.075	0	1	2
	2.853	0.029	**2.793**	0.140	0.060	1	0	4
	2.420	0.024	2.346	0.117	0.074	1	1	0
	2.176	0.007	2.133	0.107	0.043	1	1	3
	1.743	0.036	1.738	0.087	0.006	0	1	8
Goethite	**2.576**	0.007	**2.583**	0.129	-0.007	0	2	1
	2.264	0.013	**2.253**	0.113	0.011	1	2	1
Hematite	**3.778**	0.071	**3.686**	0.184	0.092	0	1	2
	2.727	0.021	**2.703**	0.135	0.024	1	0	4
ANOXIC *F*[b]								
Lepidocrocite	3.188	0.076	3.291	0.165	-0.104	1	2	0
	2.451	0.028	**2.467**	0.123	-0.016	0	3	1
	2.352	0.051	2.357	0.118	-0.005	1	1	1
	2.010	0.011	1.937	0.097	0.073	0	5	1
	1.741	0.012	**1.732**	0.087	0.009	1	5	1
	1.495	0.003	1.523	0.076	-0.027	2	3	1
Goethite	**2.700**	0.056	**2.693**	0.135	0.007	1	3	0
	2.582	0.024	**2.583**	0.129	-0.001	0	2	1
	2.268	0.014	2.253	0.113	0.015	1	2	1
Copper	**2.037**[e]	0.059	2.087	0.104	-0.050	1	1	1
	1.886	-	1.808	0.090	0.079	2	0	0
						Possible phase	*h*	*k*	*l*
Unknown	2.869[f]	0.055	*2.972*	*0.149*	*-0.103*	*Lepidocrocite*	*0*	*1*	*1*
			2.793	*0.140*	*0.076*	*Siderite*	*1*	*0*	*4*
			2.844	*0.142*	*0.026*	*Calcite*	*0*	*0*	*6*
			2.888	*0.144*	*-0.018*	*Cerussite*	*0*	*1*	*2*
			2.856	*0.143*	*0.014*	*Malachite*	*-2*	*0*	*1*
			2.840	*0.142*	*0.029*	*Rhodochrosite*	*1*	*0*	*4*
	2.126[g]	0.055	*2.190*	*0.110*	*-0.064*	*Goethite*	*1*	*4*	*0*
			2.087	*0.104*	*0.039*	*Copper*	*1*	*1*	*1*

[a]Cu O and [b]Cu A long-term experiments; ultrafine solids (*F*) dispersed on carbon film Cu TEM grid. d_m = average values of measured *d*-spacings in HRTEM and corresponding FFT images (σ = standard deviation); d_R = reference values from X-ray powder diffraction files; [c]5% uncertainty. [d]Deviation of measured from reference value ($\Delta d = d_m - d_R$). [e]Falls within the 5% uncertainty of lepidocrocite (051). [f]In laths; [g]in laths and in nanoparticle clusters.

XPS spectra were collected from the granular (residue, *R*) and ultrafine (*F*) reacted samples recovered 1008 h of reaction from the long-term experiments performed under oxic and anoxic conditions after. For brevity, the samples will be referred to as "oxic" and "anoxic" samples in the following paragraphs. The unreacted siderite material was analysed as reference, showing Fe $2p_{3/2}$ peaks at binding energies of 709.9 eV characteristic for ferrous iron (Hochella, 1988; Yamashita & Hayes, 2008), with no measurable degrees of surface oxidation (Figure A6 *top row*), and major O 1s peaks at 531.4 eV and C 1s lines at 289.3 eV representative for the carbonate species (Figure A6B–C *top row*; Stipp & Hochella, 1991; Junta & Hochella, 1994; Duckworth & Martin, 2004b; Feng et al., 2016).

The Fe $2p_{3/2}$ spectra obtained from the **oxic** samples demonstrate the near complete oxidation of surface Fe (98 to 100% Fe^{3+}), indicated by the shifts of the main Fe $2p_{3/2}$ peaks towards higher binding energies of 711.1 and 711.7 eV characteristic for ferric iron species (Figure A6A *second and third top rows*; Yamashita & Hayes, 2008; Radu et al., 2017). In tandem with the O 1s and C 1s spectra, the predominance of Fe^{3+} most likely represents the oxidised ferric (oxyhydr)oxide precipitates on the reacted siderite surface (*R*), which are the dominant form of Fe in the suspended ultrafine particle fraction (*F*) (Figure A6A–C *second and third top rows*, and Table A12). The predominance of oxidised Fe at the siderite surface and in the ultrafine fraction agrees well with the wide coverage of the reacted siderite surfaces with precipitates, while minor peak contributions of Fe^{2+} in the Fe $2p_{3/2}$ spectrum of the residue sample result from sporadic areas of less heavily covered siderite surfaces. The ultrafine fraction in contrast almost entirely consists of fully oxidised Fe precipitates. In the O 1s spectrum, peaks at 531.1 and 529.7 eV are indicative for structural OH^- and O^{2-} in FeOOH, respectively (Figure A6B *second and third top rows*; Junta & Hochella, 1994; Duckworth & Martin, 2004b; Yamashita & Hayes, 2008). Ideal FeOOH stoichiometry is characterised by an interpeak distance of ~1.3 eV and a 1:1 intensity ratio of the two peak contributions (Junta & Hochella, 1994; Duckworth & Martin, 2004b). The offsets from this ideal observed in the O 1s spectra likely represent the different contributions of the various amounts of Fe_2O_3 in the residue and ultrafine precipitates (c.f. Table A10). The predominance of ferric (oxyhydr)oxide precipitates at the reacted siderite surface and in suspension is further supported by the only minor CO_3^{2-} contributions in the C 1s spectra (Figure A6C *second and third top rows*).

The Fe $2p_{3/2}$ spectra obtained from the **anoxic** samples indicate considerable oxidation of surface Fe on the reacted siderite grains (64% Fe^{3+}; *R*) and in the filtered suspended particles (95% Fe^{3+}; *F*). In combination with simultaneously obtained O 1s and C 1s spectra of the same

samples, a more heterogeneous, less wide oxidation and coverage of the reacted siderite surface by oxidised ferric (oxyhydr)oxide precipitation supports previous microscopic observations. Remaining contributions of Fe^{2+} and carbonate in the Fe $2p_{3/2}$ and C 1s spectra, respectively, additionally confirm areas of unoxidised siderite surface (Figure A6A–C *fourth and fifth bottom rows*, and Table A12). Notably, the O 1s main peaks in both spectra collected from the residue and ultrafine sample fractions indicate lines at 530.8 and 530.9 eV. These binding energies are about –0.3 eV lower than the binding energy of structural OH^- groups (531.0–531.3 eV; Junta & Hochella, 1994; Poulston et al., 1996; Duckworth & Martin, 2004b), and –0.5 eV lower than the reference carbonate line at 531.4 eV (Stipp & Hochella, 1991; Duckworth & Martin, 2004b; Feng et al., 2016). This offset may suggest advanced hydration of the reacted siderite surface. In the ultrafine fractions of both the oxic and the anoxic samples, the broad and low intensity carbonate peaks in the C 1s spectra showed a shift by –0.6 and –0.4 eV towards lower binding energies respective to the 289.3 eV line in siderite (Table A12). This shift may further indicate a (structural) change in the reacted carbonate component. Possibly, this indicates surface structure relaxation upon dissolution (e.g., Hochella, 1988) or contraction resulting from structural surface Fe^{2+} oxidation (ionic radius of $^{[6]}Fe^{3+}$ = 0.645 Å, which is smaller than Fe^{2+} = 0.78 Å; Shannon, 1976). Incorporation of Cu(II) (0.73 Å; Shannon, 1976) is considered unlikely, as the Jahn-Teller distortion caused by its d-orbital configuration already prevents incorporation into the much larger Ca^{2+} site in calcite (1.0 Å; Shannon, 1976; Elzinga & Reeder, 2002; Elzinga et al., 2006).

See next page: **Figure A6.** XPS spectra of the Fe $2p_{3/2}$ (A), O 1s (B), and C 1s (C) photoelectron lines obtained from the unreacted siderite material (top row), the reacted solids collected after 1008 h of reaction under oxic conditions (second and third top rows; *R* = residue, *F* = ultrafine fraction), and under anoxic conditions (fourth and fifth bottom rows; *R* = residue, *F* = ultrafine fraction). Note the various peak shapes of the O 1s line, suggesting contributions from different oxyhydroxide species in the oxic samples, while siderite surface modification upon dissolution may contribute to the asymmetry of the peak in the anoxic *R* sample. Black solid lines represent the data, black dotted lines show the sum of fitted components indicated by grey lines and assigned species. Grey dotted lines in the Fe 2p spectra (A) indicate satellite structures ('shake-up lines'; sat.) resulting from excitation of a valence electron upon interaction with an outgoing photoelectron. $H_2O_{surface}$ = surface sorbed water; π–π* = refers to non-covalent interactions of the covalent (double) π-bonds (p-orbitals; such as the double bound in the carbonate Lewis structure) with another, e.g., metal π*-system; C-O = alcohol remnants from sample storage; adv. = adventitious carbon (used for charge reference), surface contamination from sample exposure to the aqueous solution, air and possibly also from CO or CO_2 species within the XPS vacuum chamber (Miller et al., 2002).

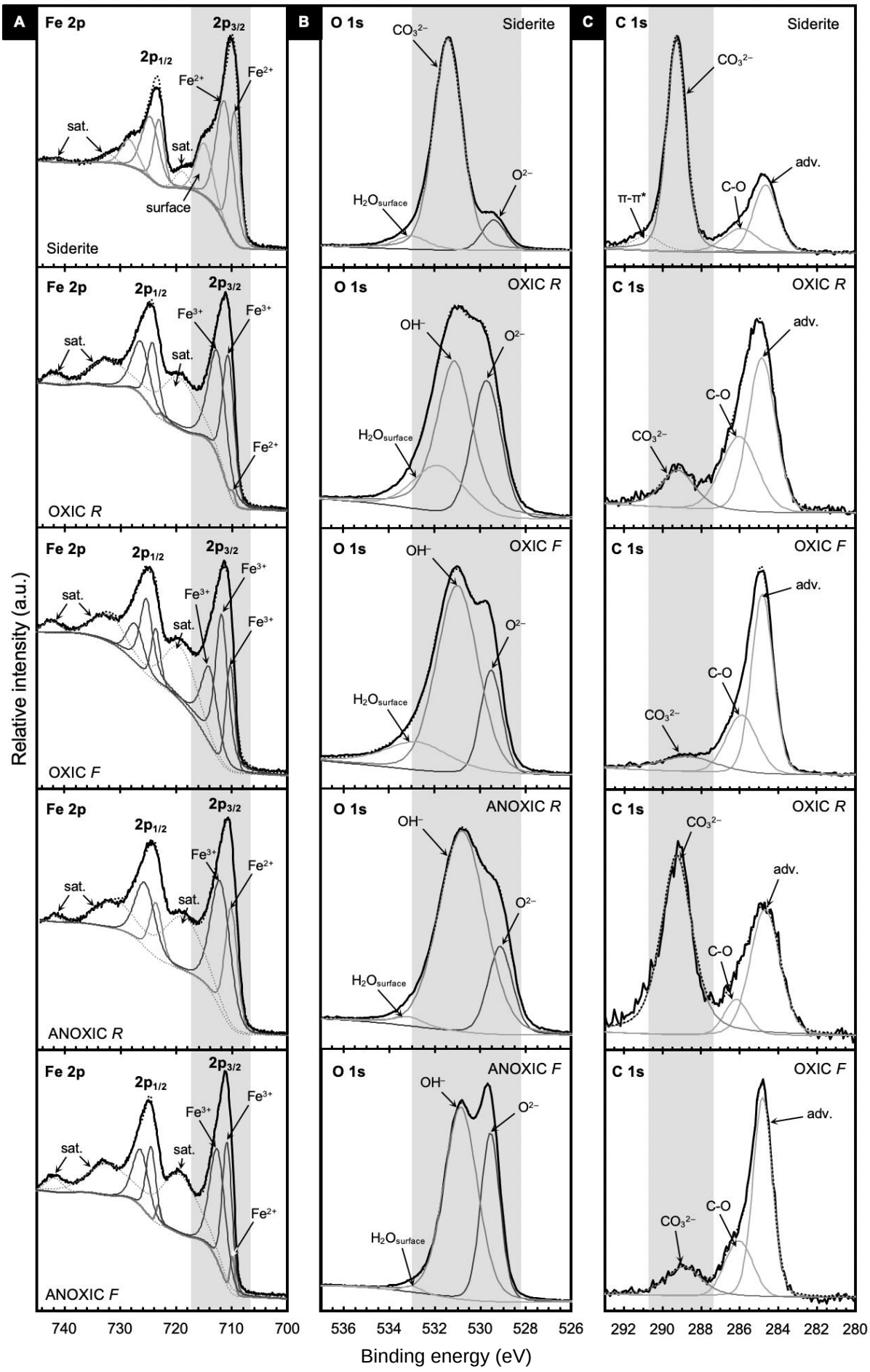
A
Fe 2p
2p1/2
2p3/2
Fe2+
Fe3+
sat.
surface
Siderite
OXIC R
OXIC F
ANOXIC R
ANOXIC F
B
O 1s
CO3 2−
H2Osurface
OH−
O2−
C
C 1s
π-π*
C-O
adv.
Relative intensity (a.u.)
740 730 720 710 700
536 534 532 530 528 526
292 290 288 286 284 282 280
Binding energy (eV)

Table A12. XPS binding energies of the Fe 2p, O 1s, C 1s, and Cu 2p lines obtained from solids collected from the oxic and anoxic experiments after 1008 h given in comparison to literature values and suggested speciation.

Atomic shell	Binding energy (eV)						Speciation/ Compound	Reference
	Siderite	OXIC[a]		ANOXIC[b]		Literature[c]		
		R	*F*	*R*	*F*			
Fe $2p_{3/2}$	**709.9**	**711.1**	**711.7**	**710.7**	**711.3**			
	709.5	709.8	–	710.2	709.9	709.0 – 710.0	Fe^{2+} / Fe_2SiO_4	(1, 2)
	711.2	710.6	710.3	–	710.9	710.4 – 710.6	Fe^{2+}, Fe^{3+} / Fe_3O_4	(2, 3)
	–	712.6	711.8	712.1	712.6	710.9 – 711.0	Fe^{3+} / Fe_2O_3	(2, 3)
O 1s	529.4	529.7	529.5	529.1	529.6	530.0 – 530.2	Lattice O^{2-}	(2, 4–7)
	–	531.1	531.0	530.8	530.9	531.0 –531.3(8)	Lattice/hyd. OH^-	(4, 5, 6)
	531.4	–	–	–	–	531.9 – 532.4	Structural CO_3^{2-}	(6, 8–9)
	533.0	531.8	532.8	533.1	533.0	532.9 – 533.2	$H_2O_{surface}$	(4, 9)
C 1s	284.7	284.9	284.8	284.7	284.8	284.4 – 285.2	Adv. C	(1, 5–10)
	286.0	286.0	285.9	286.2	286.1	286.3	Alcohol (C-O)	(8–9, 11)
	289.3	289.2	288.7	289.3	288.9	289.3	Structural CO_3^{2-}	(8–10)
Cu $2p_{3/2}$	–	**933.7**	**933.2**	–	**932.7**			
	–	–	–	–	932.7	932.6	Metal, Cu^0	(7, 12–13)
	–	932.4	932.8	–	–	932.2 – 932.4	Cu^+ oxides	(7, 12–14)
						932.8	Cu^+ spinel	(15)
	–	933.9	–	–	–	933.6 – 933.8	Cu^{2+} / CuO	(5, 7, 12–14)
	–	–	934.3	–	934.2	934.0 – 934.7	Cu^{2+} / $Cu(OH)_2$	(7, 15)
	–	–	–	–	–	934.6 – 935.0	Cu^{2+} / carbonate	(13)

[a]Cu O LT; [b]Cu A LT; R = residue; F = ultrafine precipitates. Binding energies (eV) of summed component peaks maxima are given in **bold**, otherwise values refer to individually fitted binding energies. [c]Average uncertainty of cited literature values is ± 0.18 eV. Fayalite: Fe_2SiO_4; magnetite: Fe_3O_4; hematite: Fe_2O_3. Cu(I)-oxides: cuprite (Cu_2O), delafossite ($FeCuO_2$) with 2 oxygen neighbours, tenorite (CuO) with Cu(II) in tetrahedral coordination, spinel ($CuFe_2O_4$) with Cu(I) in tetrahedral coordination. $Cu(OH)_2$: Cu(II) in a distorted octahedral coordination. Reference key: (1) Hochella, 1988, (2) Yamashita & Hayes, 2008, (3) Radu et al., 2017, (4) Junta & Hochella, 1994, (5) Poulston et al., 1996, (6) Duckworth & Martin, 2004b, (7) Biesinger et al., 2010, (8) Stipp & Hochella, 1991, (9) Feng et al., 2016, (10) Miller et al., 2002, (11) Rouxhet & Genet, 2011, (12) Tobin et al., 1983, (13) Wagner et al., 2012 (NIST database), (14) Brabers, 1983, (15) D'Huysser et al., 1981.

The assessment of the Cu speciation in **XPS** spectra collected from the Cu O/A LT samples is challenged by the overlap of Cu $2p_{3/2}$ binding energies of the various Cu oxidations states. While Cu^{2+} species can be identified by the characteristic presence of satellite structures (shake-up lines) at energies about +6 eV above the main Cu $2p_{3/2}$ peak, the peak positions of Cu^0 and Cu^+ are statistically too similar to be readily distinguished. Therefore, the apparent Cu $L_3M_{4,5}M_{4,5}$ Auger binding energies (E_B) were additionally measured using the same instrumental set-up and X-ray source (Al Kα, 1486.6 eV) as described in section A.1. (Figure A7). Note that the signal-to-noise ratio of the XPS spectra obtained from the samples collected from the anoxic experiments (Cu A LT) was insufficient to collect additional Auger spectra. The Cu $L_3M_{4,5}M_{4,5}$ (modified; short LMM) Auger parameter was determined for the Cu $2p_{3/2}$ photoelectron main peak at 933 eV and the peak contributions indicative for either Cu^0 or Cu^+ at 932 eV by following the procedure described in section 2.2.1. (equation 2.3; Table A13). Reduction of Cu species due to the ultra-high vacuum conditions is considered insignificant, as the Cu(II) satellite features remained well established in all samples. A detailed discussion of the peak assignment is provided in the main text (section 5.3.3.).

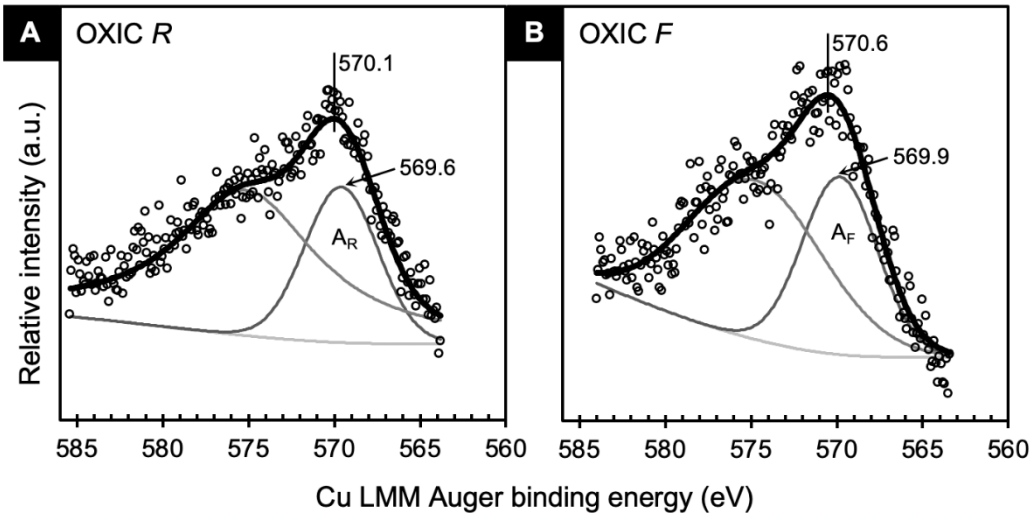

Figure A7. Complementary Cu LMM Auger spectra of the fine-granular (R = residue; A) and ultrafine (F = fines; B) solid samples collected from the long-term experiments after 1008 h of reaction under oxic conditions (Cu O LT). Maximum peak energies were used to determine the chemical state of the Cu species. (*the peak shape resembles most closely that of $Cu(OH)_2$, the positions agree well with peak maxima indicative for Cu_2O and $Cu(OH)_2$ Cu LMM Auger spectra; Biesinger, 2013, unpublished data*).

Table A13. Cu $2p_{3/2}$ and apparent Cu $L_3M_{4,5}M_{4,5}$ (LMM) Auger binding and kinetic energies of solids collected from the oxic experiments after 1008 h of reaction, and calculated Auger parameter values and compiled from literature. For the Cu LMM Auger peak assignment see Figure A7.

Compound	Cu $2p_{3/2}$ peak max. E_B (eV)	Cu LMM Auger E_B (eV)	Cu LMM Auger peak max. E_K (eV)	Modified Auger parameter (eV)	Reference
OXIC *R*[a] main peak	933.7	570.1	*916.5*	1850.2	*this study*
A_R	932.4	569.6	*917.0*	1849.4	
OXIC *F*[b] main peak	933.2	570.6	*916.0*	1849.2	*this study*
A_F	932.8	569.9	*916.7*	1849.5	
Cu(0)	932.6 (0.2)	*568.0*	918.6	1851.2	(1) n = 23
	932.6 (0.2)	*568.0*	918.6	1851.2	(2) n = 28
Cu_2O	932.4 (0.2)	*569.8*	916.8	1849.2	(1) n = 10
	932.4 (0.2)	*569.6*	917.0	1849.2	(2) n = 19
CuO	933.6 (0.4)	*568.7*	917.9	1851.5	(1) n = 10
	933.7 (0.4)	569.6	917.6	1851.4	(2) n = 19
$Cu(OH)_2$	934.8 (1.3)	*570.1*	916.5	1851.3	(1) n = 1
	934.7 (0.3)	*570.4*	916.3	1850.9	(2) n = 3

(a) Cu O LT *Residue* (*R*), (b) Cu O LT *ultrafine fraction* (*F*). Values given in *italics* were calculated based on an Al Kα source (1486.6 eV). Reference key: (1) Wagner et al., 2012 (NIST database), (2) Biesinger et al., 2010. n = number of averaged values.

In addition to the XPS analyses, the bonding environment of solid-associated Cu in the reacted solids collected from the long-term experiments (Cu O/A LT) were further assessed by **XAFS** analyses. The Fourier transform (FT) of the Cu K-edge **EXAFS** spectrum was fitted to theoretical structure data in ARTEMIS. Note that the shell-by-shell fitting approach is complicated by the high interrelations of fitting parameters in the EXAFS equation, hence results can be somewhat ambiguous and are influenced by what is about the sample characteristics. A list of reported Cu K-edge shell fit results in the literature is provided in Table A14, including data from Cu-adsorption studies, selected half path lengths calculated in FEFFIT6 (integrated in ARTEMIS), and reported values for hydrated aqueous Cu species. Corresponding references are given in Table A15.

Shell-fitting of the **EXAFS** data collected from the **oxic** reaction products (Cu O LT) reveals an adsorption complex geometry of Cu (Table 5.4). The first shell oxygens around the central

Cu atom could be well-described by the distorted polyhedral structure in copper hydroxide ($Cu(OH)_2$; Oswald et al., 1990), with four equatorial oxygens at 1.98 Å, and one axial oxygen at about 2.36 Å distance from the central Cu atom. Second and third shell neighbouring metal atoms at 2.99 Å and 3.19 Å distance produced physically reasonable fits with the theoretical path geometries of $Cu(OH)_2$. Note that including the second shell hydrogen scattering contributions at 2.69 Å significantly improved the fit statistics according to

$$\frac{\chi^2_{\nu\ initial}}{\chi^2_{\nu\ final}} - 1 \geq 2\sqrt{\frac{2}{\nu}} \qquad \text{(eq. A7)},$$

which indicates that the change in the goodness-of-fit parameter χ^2_ν between the initial and the final values is greater than two standard deviations represented by the degrees of freedom ν in the fit (Kelly, 2008). During the fitting procedure, the amplitude reduction factor S_0^2 was continuously very close to 0.9. Based on comparable fit results of Cu K-edge EXAFS reported in the literature (e.g., Peacock & Sherman, 2004; Gräfe et al., 2008; Gilbert et al., 2009; Moon & Peacock, 2012; Bowron et al., 2013; Dale et al., 2015; Stegemeier et al, 2015) and the fitting experience on this very spectrum, S_0^2 was set to 0.9, reducing the number of independent points in the fit. The Debye-Waller disorder term σ^2 was set for all shells according to previous best fit results and to values comparable to those reported in the literature. The energy shift parameter ΔE_0 was set to the best fit result (–1.0 eV) obtained during the fitting procedure. All other parameters were allowed to vary. With $N_{ind} = 14$, the goodness-of-fit is represented by 5 degrees of freedom, a R-factor of 0.0038, and a χ^2_ν of 19.9.

In the reacted solids collected from the **anoxic** experiment (Cu A LT), previous XANES Cu K-edge analyses indicated that Cu is predominantly present in its metallic form. The FT of the **EXAFS** spectrum obtained from this sample was hence directly fitted to the theoretical structure of Cu metal (Wyckoff, 1963) by constraining the coordination numbers to values predicted by FEFF6 (Table 5.4). Except for the disorder term σ^2 of the second multiscattering path, which was set to 0.01 $Å^2$, all other parameters were allowed to vary. The numerical and statistical goodness-of-fit of this model with $N_{ind} = 24$ is represented by 14 degrees of freedom, a R-factor of 0.0039, and a χ^2_ν of 22.3.

Table A14. Averaged values of reported shell-by-shell fit parameter of Cu K-edge EXAFS spectra and proposed geometries of the absorbing Cu atom. Set or crystallographic are values given in *italics.*

Material	Shell	N	R (Å)	σ^2 (Å^2)	Geometry
Cu adsorbed to					
Ferric (oxyhydr)oxides	Cu–O (n = 4)	5.1 (3)	1.96 (1)	0.005 (1)	*– distorted octahedral or*
pH 4.7 to 6.5	Cu–O_{eq} (n = 11)	4.0 (1)	1.96 (2)	0.006 (3)	*trigonal bi-pyramidal Cu*
	Cu–O_{ax} (n = 11)	1.3 (4)	2.31 (40)	0.105 (10)	*hydroxo-complex*
	Cu–Me1 (n = 11)	1.4 (7)	3.04 (7)	0.014 (6)	*– bidentate edge- or corner-*
	Cu–Me2 (n = 9)	1.3 (6)	3.34 (15)	0.013 (4)	*sharing with Fe(O,OH)$_6$*
Ferric (oxyhydr)oxide	Cu–O (n = 14)	3.3 (4)	1.95 (1)	0.004 (03)	*– bidentate edge- and/or*
nanoparticles	Cu–Me1 (n = 14)	1.8 (5)	2.96 (29)	*0.010*	*corner-sharing complexes*
pH 6 to 6.5	Cu–Me2 (n = 11)	1.8 (4)	3.27 (2)	*0.010*	*– intraparticulate dimers in*
	Cu–Me3 (n = 4)	1.1 (4)	3.88 (3)	*0.010*	*nanopores and/or substitution*
Calcite	Cu–O (n = 7)	4.3 (2)	1.95 (1)	0.006 (1)	*– distorted octahedral*
pH 8.3	Cu–C (n = 7)	2.3 (5)	2.94 (2)	*0.010*	*complex linked via CO_3-*
	Cu–O (n = 7)	1.5 (5)	3.32 (3)	*0.010*	*ligands to the metal site*
	Cu–Ca (n = 7)	1.6 (4)	3.87 (4)	*0.010*	
Cu(II) compounds					
$Cu_xCa_{1-x}CO_3$	Cu–O	4.1	2.01	0.006	*– Cu(II) incorporation into*
pH 7.7 to 7.9	Cu–C	*6.0*	2.99	0.007	*metal site*
	Cu–O	*6.0*	3.21	0.015	
	Cu–Ca	*6.0*	3.97	0.007	
$Cu(OH)_2$	Cu–O_{eq}	*4*	*1.960*		*– Jahn-Teller distorted*
(crystal data)	Cu–O_{ax1}	*1*	*2.356*		*Cu(II)O_6 octahedra*
	Cu–O_{ax2}	*1*	*2.915*		
	Cu–H	*2*	*2.758*		*– hydrogen linked to O_{eq}*
	Cu–Cu	*2*	*2.947*		
	Cu–Cu	*4*	*3.340*		
Malachite	Cu–O	*1*	*1.987*		*– strongly distorted Cu(II)O_6*
(crystal data)	Cu–O	*1*	*2.070*		*octahedra linked via CO_3-*
	Cu–O	*1*	*2.520*		*ligands in same lattice plane*
	Cu–O	*1*	*2.630*		
	Cu–C	*1*	*2.985*		
	Cu–Cu	*1*	*3.064*		
Hydrated Cu(II) (aq)	Cu–O_{eq}	*4*	1.96	0.005	*– hydration complex*
$Cu(NO_3)_2 \bullet 2.5H_2O$	Cu–O_{ax1}	*1*	2.18	0.008	
	Cu–O_{ax2}	*1*	2.39	0.008	
Hydrated Cu(II) (aq)	Cu–O (low)	4.1 (3)	1.95 (1)		*– higher Cu(II) molality*
$Cu(ClO_4)_2$ (aq)	Cu–O (high)	4.5 (6)			*associated with higher*
pH 1	Cu–H	8 to 10	2.63 (1)		*O-coordination*

References to the cited values are given in Table A15. O_{eq} = equatorial oxygen; O_{ax} = axial oxygen; Me1-3 = neighbouring (divalent) metal atoms in the 1st, 2nd, or 3rd shell (note that Fe and Cu cannot be distinguished); n = number of averaged literature values.

Table A15. References of reported EXAFS Cu K-edge model parameter and proposed geometries of the absorbing Cu atom compiled in Table A14.

Material	Specification	References
Cu adsorbed to		
Ferric (oxyhydr)oxides	hematite	Peacock & Sherman (2004)
	goethite	Bochatay et al. (1997) Parkman et al. (1999) Alcacio et al. (2001) Peacock & Sherman (2004) Gräfe et al. (2008) Yang et al. (2014)
	lepidocrocite	Parkman et al. (1999) Peacock & Sherman (2004)
	ferrihydrite	Scheinost et al. (2001) Moon & Peacock (2012)
	aggregated nanoparticles	Gilbert et al. (2009) Dale et al. (2015) Stegemeier et al. (2015)
Calcite		Elzinga & Reeder (2002) Elzinga et al. (2006)
Cu(II) compounds		
$Cu_xCa_{1-x}CO_3$	coprecipitated	Elzinga & Reeder (2002)
$Cu(OH)_2$	crystal data	Oswald et al. (1990)
Malachite	crystal data	Süsse (1967)
Hydrated Cu(II) in water	dissolved species	Persson et al. (2020) Bowron et al. (2013)

A.4.2. Thermodynamic (model) calculations

In support of analytical results, thermodynamic reaction and model calculations were performed to identify species and reactions leading to the observations made in the experiment. The standard state **Gibbs free energy** of formation (ΔG_f^o) for reactants and products was used to determine the standard state Gibbs free energy of reactions (ΔG_r^o; Table A18) according to

$$\Delta G_r^\circ = \sum \Delta G_f^\circ \text{(products)} - \sum \Delta G_f^\circ \text{(reactants)} \qquad \text{(eq. A8).}$$

The corresponding ΔG_f^o, half-reactions and references to the thermodynamic data used for the calculations are listed in Tables A16–A17. With particular focus on the redox reactions, the reduction potential Eh_r of the reactions were additionally calculated according to

$$Eh_r = E^0 - \frac{2.303 \cdot RT}{nF} \log(Q_r) \qquad \text{(eq. A9)}$$

whereby Q_r is the reaction quotient and n the number of electrons exchanged.

Table A16. Standard state Gibbs free energy of formation (ΔG_f^o) of phases used in reactions.

Reaction component	ΔG_f^o (kJ mol^{-1})	Reference
Mineral		
Siderite ($Fe^{II}CO_3$)	–681.0	Reffass et al. (2006)
2-line Ferrihydrite	–708.5	Majzlan et al. (2004)
6-line Ferrihydrite	–711.0	Majzlan et al. (2004)
$Fe(OH)_3$	–705.2 / –708.5	Majzlan et al. (2004)
Ferrihydrite ($Fe^{III}(OH)_3$ / $Fe^{III}OOH$)	–473.3	Hiemstra (2015)
Lepidocrocite (γ-$Fe^{III}OOH$)	–480.1	Majzlan et al. (2003)
Goethite (α-$Fe^{III}OOH$)	–489.8	Majzlan et al. (2003)
Hematite (α-$Fe^{III}_2O_3$)	–744.4	Robie & Hemingway (1995)
Cerussite ($PbCO_3$)	–625.5	Robie & Hemingway (1995)
Aqueous species		
Fe^{2+}	–91.5	Bard et al. (1985)
Cu^{+}	50.0	Robie & Hemingway (1995)
Cu^{2+}	65.1	Robie & Hemingway (1995)
Pb^{2+}	–24.2	Robie & Hemingway (1995)
H_2O	–237.1	Robie & Hemingway (1995)
$H_2CO_3^0$	–623.2	Robie & Hemingway (1995)

Table A17. Half-reactions and standard electrode potentials (E^0) used for standard state Gibbs free energy (ΔG_r^o) calculations describing the redox reactions in the oxic and anoxic study systems.

	Half reactions	E^0 **(V)**
1	$Cu^{2+} + e^- \longrightarrow Cu^+$	0.16[a]
2	$Cu^+ + e^- \longrightarrow Cu^0$	0.52[a]
3	$Cu^{2+} + 2e^- \longrightarrow Cu^0$	0.34[b]
4	$Fe^{3+} + e^- \longrightarrow Fe^{2+}$	0.77[a,b]
5	$O_2(g) + 4H^+ + 4e^- \longrightarrow 2H_2O(l)$	1.23[a]
6	$Fe(OH)_3 + 3H^+ + e^- \longrightarrow Fe^{2+} + 3H_2O$	0.94[c] / 0.98[a]
7	$FeOOH + 3H^+ + e^- \longrightarrow Fe^{2+} + 2H_2O$	0.846 (L)[c] / 0.768 (G)[c]
8	$Fe_2O_3 + 6H^+ + 2e^- \longrightarrow 2Fe^{2+} + 3H_2O$	0.769[c]
9	$FeOOH + H_2CO_3^0 + H^+ + e^- \longrightarrow FeCO_3 + 2H_2O$	
10	$Fe_2O_3 + 2H_2CO_3^0 + 2H^+ + 2e^- \longrightarrow 2FeCO_3 + 3H_2O$	

[a]Appelo & Postma, 2005. [b]Anderson, 2005. [c]Stewart et al., 2018.

Table A18. Standard state Gibbs free energy (ΔG_r^o) calculations of possible redox reactions in the study systems.

	Chemical reactions	ΔG_r^o **(kJ mol^{-1})[a]**
	Oxic reactions	
1	$Fe^{2+} + Cu^{2+} + 3H_2O \rightleftharpoons Fe^{III}(OH)_3 + Cu^+ + 3H^+$	79.2
2	$Fe^{2+} + Cu^{2+} + 2H_2O \rightleftharpoons \alpha\text{-}Fe^{III}OOH + Cu^+ + 3H^+$	60.8
3	$2Fe^{2+} + 2Cu^{2+} + 3H_2O \rightleftharpoons \alpha\text{-}Fe^{III}_2O_3 + 2Cu^+ + 6H^+$	119.7
4	$Fe^{II}CO_3 + Cu^{2+} + 3H_2O \rightleftharpoons Fe^{III}(OH)_3 + Cu^+ + H_2CO_3^0 + H^+$	45.5
5	$Fe^{II}CO_3 + Cu^{2+} + 2H_2O \rightleftharpoons \alpha\text{-}Fe^{III}OOH + Cu^+ + H_2CO_3^0 + H^+$	27.1
6	$2Fe^{II}CO_3 + 2Cu^{2+} + 3H_2O \rightleftharpoons \alpha\text{-}Fe^{III}_2O_3 + 2Cu^+ + 2H_2CO_3^0 + 2H^+$	52.3
	Anoxic reactions	
7	$2Fe^{2+} + Cu^{2+} + 6H_2O \rightleftharpoons 2Fe^{III}(OH)_3 + Cu^0 + 6H^+$	123.5
8	$2Fe^{2+} + Cu^{2+} + 4H_2O \rightleftharpoons 2\gamma\text{-}Fe^{III}OOH + Cu^0 + 6H^+$	106.1
9	$2Fe^{2+} + Cu^{2+} + 4H_2O \rightleftharpoons 2\alpha\text{-}Fe^{III}OOH + Cu^0 + 6H^+$	86.7
10	$2Fe^{2+} + Cu^{2+} + 3H_2O \rightleftharpoons \alpha\text{-}Fe^{III}_2O_3 + Cu^0 + 6H^+$	84.8
11	$2Fe^{II}CO_3 + Cu^{2+} + 6H_2O \rightleftharpoons 2Fe^{III}(OH)_3 + Cu^0 + 2H_2CO_3^0 + 2H^+$	56.1
12	$2Fe^{II}CO_3 + Cu^{2+} + 4H_2O \rightleftharpoons 2\gamma\text{-}Fe^{III}OOH + Cu^0 + 2H_2CO_3^0 + 2H^+$	38.7
13	$2Fe^{II}CO_3 + Cu^{2+} + 4H_2O \rightleftharpoons 2\alpha\text{-}Fe^{III}OOH + Cu^0 + 2H_2CO_3^0 + 2H^+$	19.3
14	$2Fe^{II}CO_3 + Cu^{2+} + 3H_2O \rightleftharpoons \alpha\text{-}Fe^{III}_2O_3 + Cu^0 + 2H_2CO_3^0 + 2H^+$	17.4

[a]Thermodynamic values used for the calculations and respective references are given in Table A16.

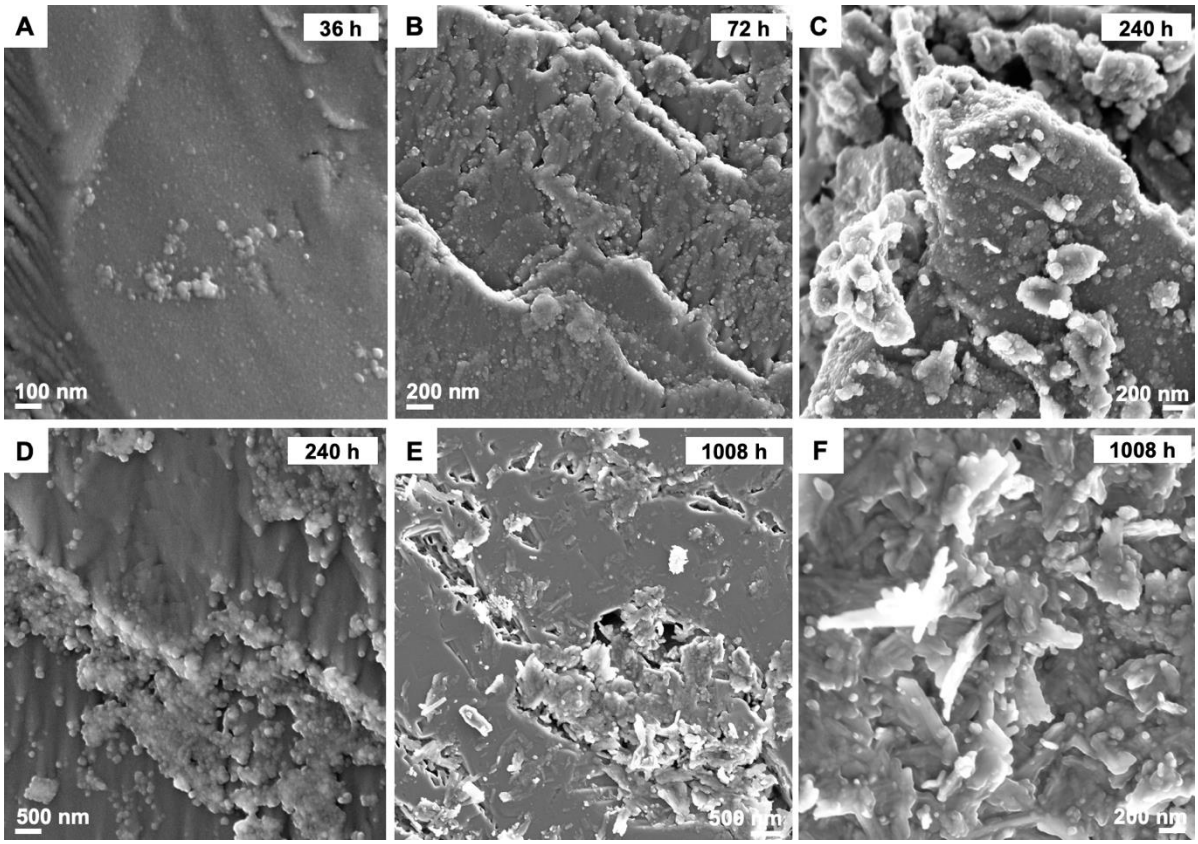

Figure A8. Scanning electron micrographs of solids collected after (A) 36 h, (B) 72 h, (C–D) 240 h, and (E–F) 1008 h of siderite reaction with dissolved Cu(II) under anoxic conditions. Solids shown in (A–D) were recovered from the short-term experiment (Cu A ST), solids shown in (E–F) were recovered from the long-term experiment (Cu A LT). *R* = residue (granular reacted solids, mostly siderite with surface precipitates); *F* = ultrafine grained reacted solids (predominantly secondary phases). In the earlier stages of the overall experiment (up to 240 h), precipitates are predominantly nanoscale-spheres that aggregate to clusters (A, D) and eventually to crusts (B–C) of poor crystallinity. Reduced copper species are assumed to be entrapped within these nanoprecipitate aggregates. By the end of the experiment (1008 h), the particles are largely replaced by lath-shaped lepidocrocite crystallites intercalated with nanoparticulate clusters of ca. 50 nm in diameter (E–F; *see also* Figure 5.4 *in the main text*).

Additional supporting model calculations of the solution chemistry and mineral saturation indices at selected time steps of the oxic and anoxic experiments using PHREEQC with the database LLNL including data from the CarbFix and MINTEQ.v4 data bases are presented in Tables A19–A20 and Figures A9–A10.

Table A19. Solution chemistry and mineral saturation states calculated for siderite dissolution in the presence of Cu(II) under oxic (Cu O) conditions using PHREEQC based on aqueous solution data. Stoichiometric dissolution of siderite and equilibrium with air and the H_2/N_2-atmosphere in the anaerobic chamber were assumed.

Solution specifications Cu O							**Model calculations**		
Solution	**Time (h)**	**pH$_m$**	**pe$_c$**	***I***	**Cu$^{total}{}_m$**	**Fe$^{total}{}_m$**	**C(4)**	**HCO_3^-**	**CO_2**
mol L^{-1}				*10^{-3}*	*10^{-3}*	*10^{-3}*	*10^{-3}*	*10^{-6}*	*10^{-3}*
O0	0	3.05	17.6	3.53	1.53	0	0.014	0.007	0.014
O1	1	5.17	15.4	3.11	1.54	0.081	0.096	6.07	0.089
O2	1	4.65	15.96	3.08	1.50	0.12	0.134	2.69	0.131
O3	2	5.35	15.3	3.02	1.50	0.075	0.091	8.38	0.082
O4	240	5.39	15.2	2.78	1.40	0.006	0.022	2.20	0.020
O5	240	4.47	16.1	2.45	1.20	0.045	0.059	0.78	0.058
O6	1008	4.79	15.8	0.55	0.27	0.009	0.024	0.64	0.023

Model calculations for Fe speciation and saturation indices of Fe phases

Solution	**Fe(2)**	**Fe(3)**	**$Fe(OH)_3$**	**$FeOH_2^+$**	**Mag**	**Fhy**	**Goe**	**Lep**	**Hem**
mol L^{-1}	*10^{-12}*	*10^{-5}*	*10^{-6}*	*10^{-6}*					
O0	–	–	–	–	–	_	–	–	–
O1	7.89	8.10	4.84	1.82	2.08	3.49	6.15	5.31	13.3
O2	34.8	12.0	2.14	8.83	0.98	3.14	5.80	4.96	12.6
O3	3.92	7.50	6.63	1.09	2.42	3.63	6.29	5.45	13.6
O4	0.32	0.60	0.58	0.08	-0.70	2.57	5.23	4.39	11.5
O5	20.7	4.50	0.52	4.78	-0.83	2.52	5.18	4.34	11.4
O6	1.83	0.90	0.23	0.44	-1.88	2.18	4.84	4.00	10.7

Model calculations for Cu speciation and saturation indices of Cu phases

Solution	**Cu(1)**	**Cu(2)**	**$CuCO_3$**	**$CuOH^+$**	**Mlc**	**Tnr**	**Cpr**	**Del**	**Cu^0**
mol L^{-1}	*10^{-16}*	*10^{-3}*	*10^{-8}*	*10^{-6}*					
O0	0.0	1.53	0.0004	0.07	-10.77	-4.47	-	-	-26.4
O1	2.8	1.54	43.2	9.79	-1.47	-0.23	-18.9	2.71	-22.0
O2	0.8	1.50	5.66	2.90	-3.40	-1.27	-21.1	1.27	-23.1
O3	3.4	1.50	87.9	14.4	-0.81	0.12	-18.4	3.12	-21.8
O4	4.0	1.40	23.8	14.8	-1.33	0.18	-18.1	2.17	-21.6
O5	0.4	1.20	0.90	1.56	-4.65	-1.72	-21.9	0.25	-23.5
O6	0.2	0.27	0.39	0.79	-4.97	-1.68	-21.9	-0.08	-23.5

I = ionic strength; pe = electrical potential; *m* = measured; *c* = calculated; Mag = magnetite; Fhy = ferrihydrite; Goe = goethite; Lep = lepidocrocite; Hem = hematite; Mlc = malachite; Tnr = tenorite (CuO); Cpr = cuprite (Cu_2O); Del= delafossite ($CuFeO_2$); Cu^0 = metal. *Only most dominant species are listed.*

Table A20. Solution chemistry and mineral saturation states calculated for siderite dissolution in the presence of Cu(II) under anoxic (Cu A) conditions using PHREEQC based on aqueous solution data. Stoichiometric dissolution of siderite and equilibrium with air and the H_2/N_2-atmosphere in the anaerobic chamber were assumed.

Solution specifications of Cu A							**Model calculations**		
Solution *mol L^{-1}*	**Time (h)**	**pH$_m$**	**pe$_c$**	***I*** *10^{-3}*	**Cu$^{total}_m$** *10^{-3}*	**Fe$^{total}_m$** *10^{-3}*	**C(4)** *10^{-3}*	**HCO$_3^-$** *10^{-6}*	**CO$_2$** *10^{-6}*
A0	0	3.04	4.21	1.65	1.530	-	-	-	-
A1	0.5	5.12	2.11	2.04	1.494	0.030	0.002	0.14	2.27
A2	6	5.53	0.89	1.99	1.452	0.038	0.031	3.93	25.6
A3	168	5.13	2.17	1.63	1.212	0.125	0.103	5.78	94.9
A4	240	5.44	1.21	1.73	1.270	0.059	0.049	5.15	41.4
A5	338	5.04	2.79	0.69	0.513	0.690	0.057	2.62	53.7
A6	505	5.41	4.03	0.52	0.001	1.196	0.983	100	881
A7	1008	5.77	0.73	0.61	0.000	1.110	0.913	184	706

Model calculations of Fe speciation					**Model calculations of Fe mineral saturation indices**				
Solution *mol L^{-1}*	**Fe(2)** *10^{-3}*	**Fe(3)** *10^{-10}*	**FeOH$^+$** *10^{-8}*	**FeCO$_3$** *10^{-10}*	**Mag**	**Fhy**	**Goe**	**Lep*** *10^{-3}*	**Hem**
A0	–	–	–	–	–	–	–	–	–
A1	1.02	4.35	3.67	0.36	-0.51	-1.82	0.84	-1.24	2.67
A2	0.99	1.81	9.20	26.1	0.30	-1.82	0.84	-1.17	2.67
A3	0.82	4.23	3.04	12.8	-0.58	-1.82	0.84	-0.87	2.67
A4	0.87	2.17	6.57	24.6	0.06	-1.82	0.84	-0.99	2.67
A5	0.34	5.10	1.08	2.11	-1.12	-1.82	0.84	-0.34	2.67
A6	0.002	2.27	0.01	0.86	-2.72	-1.82	0.84	1.19	2.67
A7	0.27	1.12	4.33	601	0.22	-1.82	0.84	0.78	2.67

Model calculations of Cu speciation					**Model calculations of mineral saturation indices**				
Solution *mol L^{-1}*	**Cu(1)** *10^{-6}*	**Cu(2)** *10^{-6}*	**CuCO$_3$** *10^{-13}*	**CuOH$^+$** *10^{-10}*	**Mlc**	**Tnr**	**Cpr**	**Del**	**Cu0*** *10^{-3}*
A0	17.0	581	-	288	–	–	-1.59	-	0.80
A1	0.13	0.04	2.13	2.12	-12.5	-4.94	-1.64	6.03	1.49
A2	0.01	0.00	0.58	0.02	-14.7	-6.55	-3.26	5.22	1.45
A3	0.15	0.05	123	2.84	-10.6	-4.80	-1.51	6.10	1.21
A4	0.02	0.00	2.76	0.07	-13.5	-6.08	-2.79	5.46	1.27
A5	0.63	0.78	815	40.3	-8.69	-3.73	-0.44	6.64	0.51
A6	10.9	234	2.20	2.82*	-1.05	-0.51	2.78	8.24	-0.30
A7	0.01	0.00	22.9	0.02	-12.9	-6.40	-3.11	5.30	0.00

*Forced to precipitate. *I* = ionic strength; pe = electrical potential; *m* = measured; *c* = calculated; Mag = magnetite; Fhy = ferrihydrite; Goe = goethite; Lep = lepidocrocite; Hem = hematite; Mlc = malachite; Tnr = tenorite (CuO); Cpr = cuprite (Cu_2O); Del = delafossite ($CuFeO_2$); Cu^0 = metal. *Only most dominant species are listed.*

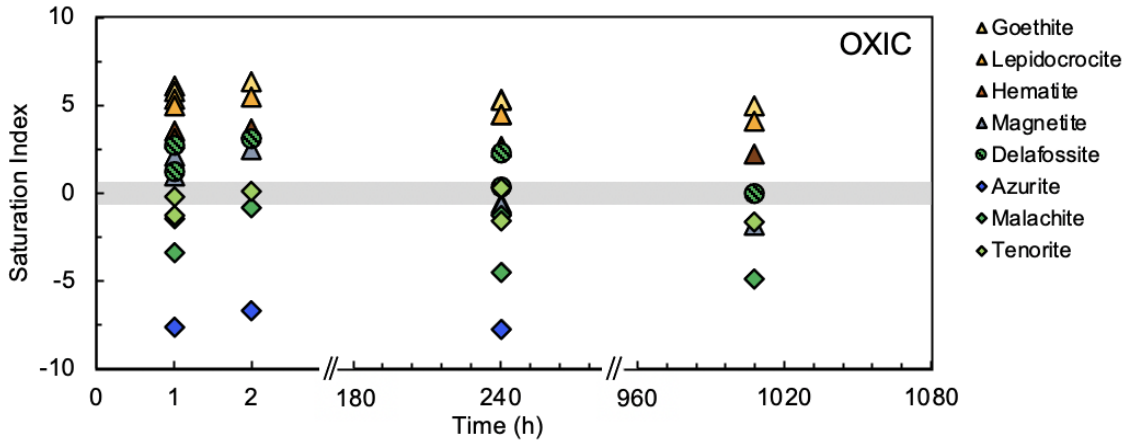

Figure A9. Saturation indices shown as a function of time of minerals potentially present in the experimental Cu O system of siderite dissolution in the presence of Cu(II) under oxic conditions. Data generated in PHREEQC, given in Table A19. Although indicated as supersaturated, no traces of magnetite, delafossite or tenorite were found in the final reaction products. Despite a large stability field over a wide range of pH–Eh conditions (Aquino et al., 2020), the formation of delafossite is unlikely, as – *to my knowledge* – 70º C is the lowest reported temperature for a successful precipitation from an aqueous solution (John et al., 2016).

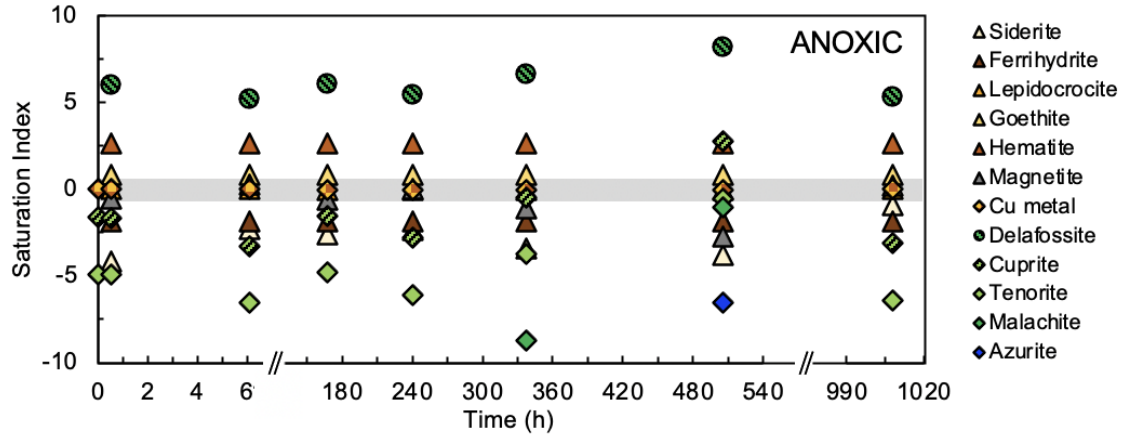

Figure A10. Saturation indices shown as a function of time of minerals potentially present in the experimental Cu A system of siderite dissolution in the presence of Cu(II) under anoxic conditions. Data generated in PHREEQC (Table A20). Formation of delafossite is unlikely under the applied study conditions, and no indications for its presence were found in the final reaction products.

References

Acharyya, S. K.; Lahiri, S.; Raymahashay, B. C.; Bhowmik, A. Arsenic toxicity of groundwater in parts of the Bengal basin in India and Bangladesh: the role of Quaternary stratigraphy and Holocene sea-level fluctuation. *Environ. Geol.* ***2000****, 39,* 1127–1137.

Adamcová, D.; Radziemska, M.; Ridošková, A.; Bartoň, S.; Pelcová, P.; Ebl, J.; Kynický, J.; Brtnický, M.; Vaverková, M. D. Environmental assessment of the effects of a municipal landfill on the content and distribution of heavy metals in *Tanacetum vulgare* L. *Chemosphere* ***2017****, 185*, 1011–1018.

Alcacio, T.E.; Hesterberg, D.; Chou, J. W.; Martin, J. D.; Beauchemin, S.; Sayers, D. E. Molecular scale characteristics of Cu(II) bonding in goethite–humate complexes. *Geochim. Cosmochim. Acta* ***2001****, 65* (9), 1355–1366.

Alexandratos, V. G.; Elzinga, E. J.; Reeder, R. J. Arsenate uptake by calcite: Macroscopic and spectroscopic characterisation of adsorption and incorporation mechanisms. *Geochim. Cosmochim. Acta* ***2007****, 71,* 4172–4187.

Alvarez, M.; Sileo, E. E.; Rueda, E. H. Structure and reactivity of synthetic co-substituted goethites. *Am. Mineral.* ***2008****, 93,* 584–590.

Anderson, G. M. Thermodynamics of Natural Systems. *Cambridge University Press,* ***2005****,* pp. 498. Online ISBN 9780511840258.

Antoniadis, V.; Shaheen, S. M.; Boersch, J.; Frohne, T.; Laing, G. D.; Rinklebe, J. Bioavailability and risk assessment of potentially toxic elements in garden edible vegetables and soils around a highly contaminated former mining area in Germany. *J. Environ. Manag.* ***2017****, 186*, 192–200.

Appelo, C. A. J.; Postma, D. Geochemistry, groundwater and pollution. 2nd ed. *A. A. Balkema Publisher, Amsterdam,* ***2005****,* pp. 634. ISBN 04-1536-421-3.

Appelo, C. A. J.; Van der Weiden, M. J. J.; Tournassat, C.; Charlet, L. Surface complexation of ferrous iron and carbonate on ferrihydrite and the mobilisation of arsenic. *Environ. Sci. Technol.* ***2002****, 36,* 3096–3103.

Aquino, A.; Lezzerini, M.; Giaccherini, A.; Montegrossi, G.; Di Benedetto, F. Thermodynamic stability of delafossite and other relevant ternary phases in the Cu–Fe–S–O–H system. *Appl. Geochem.* ***2020****, 123,* 104795.

Arthur, S. E.; Brady, P. V.; Cygan, R. T.; Anderson, H. L.; Westrich, H. R.; Nagy, K. L. Irreversible sorption of contaminants during ferrihydrite transformation. *Proceed. Waste Manag. Conference, WM,* ***1999****,* 1–14.

Atafar, Z.; Mesdaghinia, A.; Nouri, J.; Homaee, M.; Yunesian, M.; Ahmadimoghaddam, M.; Mahvi, A. H. Effect of fertilizer application on soil heavy metal concentrations. *Environ. Monitor. Assess.* ***2010****, 160,* 83–89.

Ayres, D. E. Genesis of iron-bearing minerals in banded iron formation mesobands in the Dales Gorge Member, Hamersley group, Western Australia. *Econ. Geol.* ***1972****, 67,* 1214–1233.

Bachan, A.; Kump, L. R. The rise of oxygen and siderite oxidation during the Lomagundi Event. *Proc. Natl. Acad. Sci.* ***2015****, 112* (21), 6562–6567.

Bajt, S.; Sutton, S. R.; Delaney, J. S. X-ray microprobe analysis of iron oxidation states in silicates and oxides using X-ray absorption near edge structure (XANES). *Geochim. Cosmochim. Acta* ***1994****, 58* (23), 5200–5214.

Baker, M. J.; Blowes, D. W.; Ptacek, C. J. Laboratory development if permeable reactive mixtures for the removal of phosphorous from onsite wastewater disposal systems. *Environ. Sci. Technol.* ***1998****, 32,* 2308–2316.

Banfield, J. F.; Welch, S. A.; Zhang, H.; Ebert, T. T.; Penn, R. L. Aggregation-based crystal growth and microstructure development in natural iron oxyhydroxide biomineralization products. *Science* ***2000****, 289,* 751–754.

Barceloux, D. Copper. *Clinical Toxicol.* ***1999****, 47* (2), 217–230.

Bard, A. J.; Parsons, R.; Jordan, J. Standard Potentials in Aqueous Solution. *Taylor & Francis,* ***1985***.

Bargar, J. R.; Towle, S. N.; Brown, Jr., G. E.; Parks, G. A. Outer-sphere Pb(II) adsorbed at specific sites on single crystal α-alumina. *Geochim. Cosmochim. Acta* ***1996****, 60* (18), 3541–3547.

Bargar, J. R.; Brown, G. E. Jr.; Parks, G. A. Surface complexation of Pb(II) as oxide–water interfaces: I. XAFS and bond-valence determination of mononuclear and polynuclear Pb(II) sorption products on aluminum oxides. *Geochim. Cosmochim. Acta* ***1997a****, 61* (13), 2617–2637.

Bargar, J. R.; Brown, Jr., G. E.; Parks, G. A. Surface complexation of Pb(II) at oxide–water interfaces: II. XAFS and bond-valence determination of mononuclear Pb(II) sorption products and surface functional groups on iron oxides. *Geochim. Cosmochim. Acta* ***1997b****, 61* (13), 2639–2652.

Bargar, J. R.; Towle, S. N.; Brown, Jr., G. E.; Parks, G. A. XAFS and bond-valence determination of the structures and compositions of surface functional groups and Pb(II) and Co(II) sorption products on single crystal α-Al_2O_3. *J. Colloid Interface Sci.* ***1997c****, 1185,* 473–792.

Bargar, J. R.; Brown, Jr., G. E.; Parks, G. A. Surface complexation of Pb(II) at oxide-water interfaces: III. XAFS determination of Pb(II) and Pb(II)-chloro adsorption complexes on goethite and alumina. *Geochim. Cosmochim. Acta* ***1998****, 62* (2), 193–207.

Bargar, J. R.; Reitmeyer, R.; Lenhart, J.; Davis, J. A. Characterisation of U(VI)-carbonato ternary complexes on hematite: EXAFS and electrophoretic mobility measurements. *Geochim. Cosmochim. Acta* ***2000****, 64* (16), 2737–2749.

Barrón, V.; Torrent, J. Surface hydroxyl configuration of various crystal faces of hematite and goethite. *J. Colloid Interface Sci.* ***1996****, 177,* 407–410.

Bassettt, W. A.; Brown, G. E. Jr. Synchrotron radiation: Applications in the Earth sciences. *Annu. Rev. Earth Planet. Sci.* ***1990****, 18,* 387–447.

Batchelder, D. N.; Simmons, B. O. Lattice constants and thermal expansivities of silicon and of calcium fluoride between 6° and 322°K. *J. Chem. Phys.* ***1964****, 41,* 2324–2329.

Bekker, A.; Slack, J. F.; Planavsky, N.; Krapež, B.; Hofman, A.; Konhauser, K. O.; Rouxel, O. J. Iron formation: The sedimentary product of a complex interplay among mantle, tectonic, oceanic, and biospheric processes. *Econ. Geol.* ***2010****, 105,* 467–508.

Bénézeth, P.; Dandurand, J. L.; Harrichoury, J. L. Solubility product of siderite ($FeCO_3$) as a function of temperature (25–250 °C). *Chem. Geol.* ***2009***, *265*, 3–12.

Benjamin, M. M.; Leckie, J. O. Conceptual model for metal–ligand–surface interactions during adsorption. *Environ. Sci. Technol.* ***1981***, *15* (9), 1050–1057.

Beveridge, T. J.; Murray, R. G. E. Uptake and retention of metals by cell wall of *Bacillus subtilis*. *J. Bacteriol.* ***1976***, *127* (3), 1502–1518.

Beveridge, T. J.; Murray, R. G. E. Sites of metal deposition in the cell wall of *Bacillus subtilis*. *J. Bacteriol.* ***1980***, *141* (2), 876–887.

Berner, R. A.; Lasaga, A. C.; Garrels, R. M. The carbonate–silicate geochemical cycle and its effect on atmospheric carbon dioxide over the past 100 million years. *Am. J. Sci.* ***1983***, *283*, 641–683.

Bibi, I.; Niazi, N. K.; Choppala, G.; Burton, E. D. Chromium(VI) removal by siderite ($FeCO_3$) in anoxic aqueous solutions: An X-ray absorption spectroscopy investigation. *Sci. Total Environ.* ***2018***, *640–641*, 1424–1431.

Biesinger, M. C.; Hart, B. R.; Polack, R.; Kobe, B.; Smart, R. St.C. Analysis of mineral surface chemistry in flotation separation using imaging XPS. *Minerals Engin.* ***2007***, *20*, 152–162.

Biesinger, M. C.; Lau, L. W. M.; Gerson, A. R.; Smart, R. S. C. Resolving surface chemical states in XPS analysis of first row transition metals, oxides and hydroxides: Sc, Ti, V, Cu and Zn. *Appl. Surface Sci.* ***2010***, *257*, 887–898.

Biesinger, M. C.; Lao, L. W. M.; Gerson, A. R.; Smart, R. St. C. The role of the Auger parameter in XPS studies of nickel metal, halides and oxides. *Phys. Chem. Chem. Phys.* ***2012***, *14*, 2434–2442.

Biesinger, M. C. Advanced analysis of copper X-ray photoelectron spectra. *Surf. Interface Anal.* ***2017***, *49*, 1325–1334.

Bilinski, H.; Schindler, P. Solubility and equilibrium constants of lead in carbonate solutions (25 ºC, I = 0.3 mol dm^{-3}). *Geochim. Cosmochim. Acta* ***1982***, *46*, 921–928.

Bischoff, J. L.; Fyee, W. S. Catalysis, inhibition, and the calcite–aragonite problem. *Am. J. Sci.* ***1968***, *266*, 65–79.

Bloundi, M. K.; Duplay, J.; Quaranta, G. Heavy metal contamination of coastal lagoon sediments by anthropogenic activities: the case of Nador (East Morocco). *Environ. Geol.* ***2009***, *56*, 833–843.

Blowes, D. W.; Ptacek, C. J.; Jambor, J. L. *In-situ* remediation of Cr(VI)-contaminated groundwater using permeable reactive walls: Laboratory studies. *Environ. Sci. Technol.* ***1997***, *31* (12), 3348–3357.

Bochatay, L.; Persson, P.; Lövgren, L.; Brown Jr., G. E. XAFS study of Cu(II) at the water-goethite (α-FeOOH) interface. *J. Phys. IV France* ***1997***, *7*, 819–820.

Boher, P.; Garnier, P.; Gavarri, J. R.; Hewat, A. W. Monoxyde quadratique PbOa(II): description de la transition structurale ferroélastique. *J. Solid State Chem.* ***1985***, *58*, 343–350.

Bolan, N.; Kunhikrishnan, A.; Thangarajan, R.; Kumpiene, J.; Park, J.; Makino, T.; Kirkham, M. B.; Scheckel, K. Remediation of heavy metal(loid)s contaminated soils – to mobilize or to immobilize? *J. Hazard. Mater.* ***2014***, *266*, 141–166.

Boland, D. D.; Collins, R. N.; Miller, C. J.; Glover, C. J.; Waite, T. D. Effect of solution and solid-phase conditions on the Fe(II)-accelerated transformation of ferrihydrite to lepidocrocite and goethite. *Environ. Sci. Technol.* ***2014***, *48*, 5477–5485.

Bouzenoune, A.; Lécolle, P. Petrographic and geochemical arguments for the hydrothermal formation of the Ouenza siderite deposit (NE Algeria). *Mineral. Deposita* ***1997***, *32*, 189–196.

Bowron, D. T.; Amboage, M.; Boada, R.; Freeman, A.; Hayama, S.; Díaz-Moreno, S. The hydration structure of Cu^{2+}: more tetrahedral then octahedral? *RSC Advances* ***2013***, *3*, 17803–17812.

Brabers, V. A. M. Cation valences and surface segregation in copper ferrites. *Mat. Res. Bull.* ***1983***, *18*, 861–868.

Braun, R. D. Solubility of iron(II) carbonate at temperatures between 30 and 80 ºC. *Talanta* ***1991***, *38* (2), 205–211.

Brinkel, J.; Khan, Md. M. H.; Krämer, A. A systematic review of arsenic exposure and its social and mental health effects with special reference to Bangladesh. *Int. J. Environ. Res. Public Health* ***2009***, *6*, 1609–1619.

Brown, G. E. Jr. Spectroscopic studies of chemisorption reaction mechanisms at oxide–water interfaces. *Rev. Mineral.* ***1990***, *23*, 309–364.

Brown, G. E. Jr.; Parks, G. A. Synchrotron-based X-ray absorption studies of cation environments in earth materials. *Rev. Geophys.* ***1989***, *27* (4), 519–533.

Brown, G. E. Jr.; Parks, G. A. Sorption of trace elements on mineral surfaces: Modern perspectives from spectroscopic studies, and comments on sorption in the marine environment. *Inter. Geol. Rev.* ***2001***, *43*, 963–1073.

Brown, G. E. Jr.; Henrich, V. E.; Casey, W. H.; Clark, D. L.; Eggleston, C.; Felmy, A.; Goodman, D. W.; Grätzel, M.; Maciel, G.; McCarthy, M. I.; Nealson, K. H.; Sverjenski, D. A.; Toney, M. F.; Zachara, J. M. Metal oxide surfaces and their interactions with aqueous solutions and microbial organisms. *Chem. Rev.* ***1999***, *99*, 77–174.

Brunauer, S.; Emmett, P.H.; Teller, E. Adsorption of Gases in multimolecular layers. *J. Am. Chem. Soc.* ***1938***, *60* (2), 309–319.

Bruno, J.; Wersin, P.; Stumm, W. On the influence of carbonate in mineral dissolution: II. The solubility of $FeCO_3$(s) at 25 ºC and 1 atm total pressure. *Geochim. Cosmochim. Acta* ***1992***, *56*, 1149–1155.

Buerge, I. J.; Hug, S. J. Kinetics and pH dependence of chromium(VI) reduction by iron(II). *Environ. Sci. Technol.* ***1997***, *31*, 1426–1432.

Buerge, I. J.; Hug, S. J. Influence of mineral surfaces on chromium(VI) reduction by iron(II). *Environ. Sci. Technol.* ***1999***, *33*, 4285–4291.

Burleson, D. J.; Penn, R. L. Two-step growth of goethite from ferrihydrite. *Langmuir* ***2006***, *22*, 402–409.

Burt, D. M. Mineralogy and petrology of skarn deposits. *Soc. Italiana Mineral. Petrol.* ***1977***, *33* (2), 859–873.

Buseck, P. R. Principles of transmission electron microscopy. *Rev. Mineral.* ***1992***, *27*, 1–36.

Callagon, E. B. R.; Lee, S. S.; Eng, P. J.; Laanait, N.; Sturchio, N. C.; Nagy, K. L.; Fenter, P. Heteroepitaxial growth of cadmium carbonate at dolomite and calcite surfaces: Mechanisms and rates. *Geochim. Cosmochim. Acta* ***2017***, *205*, 360–380.

Calmano, W.; Hong, J.; Förstner, U. Binding and mobilisation of heavy metals in contaminated sediments affected by pH and redox potential. *Wat. Sci. Technol.* ***1993***, *28* (8-9), 223–235.

Cang, L.; Wang, Y.; Zhou, D.; Dong, Y. Heavy metals pollution in poultry and livestock feeds and manures under intensive farming in Jiangsu Province, China. *J. Environ. Sci.* ***2004****, 16,* 371–374.

Carlson, L.; Schwertmann, U. The effect of CO_2 and oxidation rate on the formation of goethite versus lepidocrocite from an Fe(II) system at pH 6 and 7. *Clay Miner.* ***1990****, 25,* 65–71.

Carroll, S. A.; O'Day, P. A.; Piechowski, M. Rock–water interactions controlling zinc, cadmium, and lead concentrations in surface waters and sediments, U.S. Tri-State Mining District. 2. Geochemical interpretation. *Environ. Sci. Technol.* ***1998****, 32,* 956–965.

Celis, R.; Hermosín, M. C.; Cornejo, J. Heavy metal adsorption by functionalized clays. *Environ. Sci. Technol.* ***2000****, 34,* 4593–4599.

Chada, V. G. R.; Hausner, D. B.; Strongin, D. R.; Rouff, A. A.; Reeder, R. J. Divalent Cd and Pb uptake on calcite $\{10\bar{1}4\}$ cleavage faces: An XPS and AFM study. *J. Colloid Interface Sci.* ***2005****, 288,* 350–360.

Chakraborty, M.; Mukherjee, A.; Ahmed, K. M. A Review of groundwater arsenic in the Bengal Basin and India: from source to sink. *Curr. Pollution Rep.* ***2015****, 1,* 220–247.

Charlet, L.; Wersin, P.; Stumm, W. Surface charge of $MnCO_3$ and $FeCO_3$. *Geochim. Cosmochim. Acta Lett.* ***1990****, 54,* 2329–2336.

Charlet, L.; Scheinost, A. C.; Tournasaat, C.; Greneche, J. M.; Géhin, A.; Fernández-Martínez, A.; Coudert, S.; Tisserand, D.; Brendle, J. Electron transfer at the mineral/water interface: Selenium reduction by ferrous iron sorbed on clay. *Geochim. Cosmochim. Acta* ***2007****, 71,* 5731–5749.

Chen, Y.; Liu, Y.; Liu, Y.; Lin, A.; Kong, X.; Liu, D.; Li, X.; Zhang, Y.; Gao, Y.; Wang, D. Mapping of Cu and Pb contaminations in soil using combined geochemistry, topography, and remote sensing: A case study in the Le'an River floodplain, China. *Int. J. Environ. Res. Public Health* ***2012****, 9,* 1874–1886.

Cheng, S. Heavy Metal Pollution in China: Origin, pattern and control. *Environ. Sci. Pollution Res.* ***2003****, 10,* 192–198.

Cheng, Y.; Holman, H.-Y.; Lin, Z. Remediation of chromium and uranium contamination by microbial activity. *Elements* ***2012****, 8* (2), 107–112.

Chevrier, G.; Giester, G.; Heger, G.; Jarosch, D.; Wildner, M.; Zemann, J. Neutron single-crystal refinement of cerussite, $PbCO_3$, and comparison with other aragonite-type carbonates. *Zeit. Krist.* ***1992****, 199,* 67–74.

Chi Fru, E.; Rodriguez, N. P.; Partin, C. A.; Lalonde, S. V.; Andersson, P.; Weiss, D. J.; El Albani, A.; Rodushkin, I.; Konhauser, K. O. Cu isotopes in marine black shales record the Great Oxidation Event. *Proc. Natl. Acad. Sci.* ***2016****, 113* (18), 4941–4946.

Chisholm-Brause, C. J.; Roe, A. L.; Hayes, K. F.; Brown Jr., G. E.; Parks, G. A.; Leckie, J. O. XANES and EXAFS study of aqueous Pb(II) adsorbed on oxide surfaces. *Physica* ***1989****, B159,* 647–675.

Chisholm-Brause, C. J.; Hayes, K. F.; Roe, A. L.; Brown Jr., G. E.; Parks, G. A.; Leckie, J. O. Spectroscopic investigation of Pb(II) complexes at the γ-Al_2O_3/water interface. *Geochim. Cosmochim. Acta* ***1990a****, 54,* 1897–1909.

Chisholm-Brause, C. J.; O'Day, P. A.; Brown, G. E. Jr.; Parks, G. A. Evidence for multinuclear metal-ion complexes at solid/water interfaces from X-ray absorption spectroscopy. *Nature* ***1990b****, 348,* 528–531.

Chrysochoou, M.; Dermatas, D.; Grubb, D. G. Phosphate application to firing range soils for Pb immobilisation: The unclear role of phosphate. *J. Hazard. Mater.* ***2007****, 144,* 1–14.

Chuan, M. C.; Shu, G. Y.; Liu, J. C. Solubility of heavy metals in a contaminated soil: Effects of redox potential and pH. *Water, Air, Soil Pollution* ***1996,*** *90,* 543–556.

Ciscato, E. R.; Bontognali, T. R. R.; Poulton, S. W.; Vance, D. Copper and its isotopes in organic-rich sediments: From the modern Peru Margin to Archean Shales. *Geosciences* ***2019****, 9,* 325–351.

Claessens, J.; Van Cappellen, P. Competitive binding of Cu^{2+} and Zn^{2+} to live cells of *Shewanella putrefaciens*. *Environ. Sci. Technol.* ***2007****, 41,* 909–914.

Cornell, R. M. The influence of some divalent cations on the transformation of ferrihydrite to more crystalline products. *Clay Minerals* ***1988****, 23,* 329–332.

Cornell, R. M.; Giovanoli, R. The influence of copper on the transformation of ferrihydrite ($5Fe_2O_3•9H_2O$) into crystalline products in alkaline media. *Polyhedron* ***1988****, 7* (5), 385–391.

Cornell, R. M.; Schneider, W. Formation of goethite from ferrihydrite at physiological pH under the influence of cysteine. *Polyhedron* ***1989****, 8* (2), 149–155.

Cornell, R. M; Schwertmann, U. The iron oxides. Structure, properties, reactions, occurrences and uses. 2nd Ed. *Wiley-VCH Verlag, Weinheim,* ***2003****,* pp. 664. ISBN 3-537-30274-3.

Cornwall, H. R. A summary of ideas on the origin of native copper deposits. *Econ. Geol. Bull. Soc. Econ. Geol.* ***1956****, 51* (7), 1–8.

Cortecci, G.; Frizzo, P. Prigin of siderite deposits from the Lombardy Valleys, northern Italy: a carbon, oxygen and strontium isotope study. *Chem. Geol.* ***1993****, 105,* 293–303.

Coughlin, B. R.; Stone, A. T. Nonreversible adsorption of divalent metal ions (Mn(II), Co(II), Ni(II), Cu(II), and Pb(II)) onto goethite: Effects of acidification, Fe(II) addition, and picolinic acid addition. *Environ. Sci. Technol.* ***1995****, 29,* 2445–2455.

Couture, R.-M.; Gobeil, C.; Tessier, A. Arsenic, iron and sulfur co-diagenesis in lake sediments. *Geochim. Cosmochi. Acta* ***2010****, 74,* 1238–1255.

Crawford, R. J.; Harding, I. H.; Mainwaring, D. E. Adsorption and coprecipitation of single heavy metal ions onto the hydrated oxides of iron and chromium. *Langmuir* ***1993****, 9,* 3050–3056.

Cubillas, P.; Köhler, S.; Prieto, M.; Chaïrat, C.; Oelkers, E. H. Experimental determination of the dissolution rates of calcite, aragonite, and bivalves. *Chem. Geol.* ***2005a****, 216,* 59–77.

Cubillas, P.; Köhler, S.; Prieto, M.; Causserand, C.; Oelkers, E. H. How do mineral coatings affect dissolution rates? An experimental study of coupled $CaCO_3$ dissolution–$CdCO_3$ precipitation. *Geochim. Cosmochim. Acta* ***2005b****, 69* (23), 5459–5476.

Dale, J. G.; Stegemeier, J. P.; Kim, C. S. Aggregation of nanoscale ion oxyhydroxides and corresponding effects on metal uptake, retention, and speciation: I. Ionic-strength and pH. *Geochim. Cosmochim. Acta* ***2015****, 148,* 100–112.

Danková, Z.; Bekényiová, A.; Štyriaková, I.; Federová, E. Study of Cu(II)Adsorption by siderite and kaolin. *Procedia Earth Planet Sci.* ***2015****, 15,* 821–826.

Davis, J. A.; Leckie, J. O. Surface ionisation and complexation at the oxide/water interface. II. Surface properties of amorphous iron oxyhydroxide and adsorption of metal ions. *J. Colloid Interface Sci.* ***1978****, 67* (1), 90–107.

Davis, J. A.; James, R. O.; Leckie, J. O. Surface Ionisation and complexation at the oxide/water interface. I. Computation of electrical double layer properties in simple electrolytes. *J. Colloid Interface Sci.* ***1978****, 63* (3), 480–499.

Davis, J. A.; Fuller, C. C.; Cook, A. D. A model for trace metal sorption processes at the calcite surface: Adsorption of Cd^{2+} and subsequent solid solution formation. *Geochim. Cosmochim. Acta* ***1987****,*

Davis, J. A.; Kent, D. B. Surface complexation modelling in aqueous geochemistry. *Rev. Mineral.* ***1990****, 23,* 177–260.

Davranche, M.; Bollinger, J.-C. Heavy metals desorption from synthesized and natural iron and manganese oxyhydroxides: Effect of reductive conditions. *J. Colloid Interface Sci.* ***2000****, 227,* 531–539.

Defarge, N.; Spiroux de Vendômois, J.; Séralini, G. E. Toxicity of formulants and heavy metals in glyphosate-based herbicides and other pesticides. *Toxicol. Rep.* ***2018****, 5,* 156–163.

Dekov, V. M.; Rouxel, O.; Asael, D.; Hålenius, U.; Munnik, F. Native Cu from the oceanic crust: Isotopic insights into native metal origin. *Chem. Geol.* ***2013****, 359,* 136–149.

De Yoreo, J. J.; Gilbert, P. U. P.; Sommerdijk, N. A. J. M.; Penn, R. L.; Whitelam, S.; Joester, D.; Zhang, H.; Rimer, J. D.; Navrotsky, A.; Banfield, J. F.; Wallace, A. F.; Michel, F. M.; Meldrum, F. C.; Cölfen, H.; Dove, P. M. Crystallization by particle attachment in synthetic, biogenic, and geologic environments. *Science* ***2015****, 349,* aaa6760.

D'Hyusser, A.; Lereboure-Hannoyer, B.; Lenglet, M.; Bonnelle, J. P. La spectroscopie de photoélectrons induits par rayons X et la repartition des ions cuivre Cu^{+} et Cu^{2+} dans les ferrites de cuivre. *J. Solid State Chem.* ***1981****, 39,* 246–256.

Di Lorenzo, F.; Cametti, G.; Vanhecke, D.; Churakov, S. V. The role of interfaces in controlling Pb^{2+} removal by calcium carbonate minerals. *Cryst. Growth Des.* ***2020****, 20,* 6157–6169.

Dixit, S.; Hering, J. G. Comparison of arsenic(V) and arsenic(III) sorption onto iron oxide minerals: Implications for arsenic mobility. *Environ. Sci. Technol.* ***2003****, 37,* 4182–4189.

Dold, B. Acid rock drainage prediction: A critical review. *J. Geochem. Exploration* ***2016****, 172,* 120–132.

Dold, B.; Blowes, D. W.; Dickhout, R.; Spangenber, J. E.; Pfeifer, H.-R. Low molecular weight carboxylic acids in oxidising porphyry copper tailings. *Environ. Sci. Technol.* ***2005****, 39,* 2515–2521.

Dong, H.; Lu, A. Mineral–microbe interactions and implications for remediation. *Elements* ***2012****, 8* (2), 95–100.

Dragović, S.; Mihailović, N. Analysis of mosses and topsoils for detecting sources of heavy metal pollution: multivariate and enrichment factor analysis. *Environ. Monitor. Assess.* ***2009****, 157,* 383–390.

Du, H.; Huang, Q.; Peacock, C. L.; Tie, B.; Lei, M.; Liu, X.; Wei, X. Competitive binding of Cd, Ni, and Cu on goethite organo–mineral composites made with soil bacteria. *Environ. Pollut.* ***2018****, 243,* 444–452.

Dublet, G.; Juillot, F.; Morin, G.; Fritsch, E.; Noel, V.; Brest, J.; Brown, G. E. Jr. XAS evidence for Ni sequestration by siderite in a laterite Ni-deposit from New Caledonia. *Am. Mineral.* ***2014****, 99,* 225–234.

Duckworth, O. W.; Martin, S. T. Dissolution rates and pit morphology of rhombohedral carbonate minerals. *Am. Mineral.* ***2004a****, 89,* 554–563.

Duckworth, O. W.; Martin, S. T. Role of molecular oxygen in the dissolution of siderite and rhodochrosite. *Geochim. Cosmochim. Acta* ***2004b****, 68* (3), 607–621.

Duckworth, O. W.; Cygan, R. Y.; Martin, S. T. Linear free relationship between dissolution rates and molecular modelling energies of rhombohedral carbonates. *Langmuir* ***2004****, 20,* 2938–2946.

Eary, L. E.; Rai, D. Chromate removal from aqueous wastes by reduction with ferrous ion. *Environ. Sci. Technol.* ***1988****, 22,* 972–977.

Edwards, D. P.; Lim, F.; James, R. H.; Pearce, C. R.; Scholes, J.; Freckleton, R. P.; Beerling, D. J. Climate change mitigation: potential benefits and pitfalls of enhanced rock weathering on tropical agriculture. *Biol. Lett.* ***2017****, 13,* 20160715, 1–7.

Effenberger, H.; Mereiter, K.; Zemann, J. Crystal structure refinements of magnesite, calcite, rhodochrosite, siderite, smithsonite, and dolomite, with discussion of some aspects of the stereochemistry of calcite type carbonates. *Zeit. Krist.* ***1981****, 156,* 233–243.

Ellis, A. S.; Johnson, T. M.; Bullen, T. D. Chromium isotopes and the fate of hexavalent chromium in the environment. *Science* ***2002****, 295,* 2060–2062.

Elzinga, E. J.; Reeder, R. J. X-ray absorption spectroscopy study of Cu^{2+} and Zn^{2+} adsorption complexes at the calcite surface: Implications for the site-specific metal incorporation preferences during calcite crystal. *Geochim. Cosmochim. Acta.* ***2002****, 66* (22), 3943–3954.

Elzinga, E. J.; Rouff, A. A.; Reeder, R. J. The long-term fate of Cu^{2+}, Zn^{2+}, and Pb^{2+} adsorption complexes at the calcite surface: An X-ray absorption spectroscopy study. *Geochim. Cosmochim. Acta* ***2006****, 70,* 2715–2725.

Erdem, M.; Gür, F.; Tümen, F. Cr(VI) reduction in aqueous solutions by siderite. *J. Hazard. Mater.* ***2004****, B113,* 217–222.

Erdem, M.; Özverdi, A. Lead adsorption from aqueous solution onto siderite. *Sep. Purification Technol.* ***2005****, 42,* 259–264.

European Union Council Directive 98/83/EC. On the quality of water intended for human consumption OJ L 330. 1998L0083-EN-07.10.2015; Commission Directive (EU) 2015/1787; The Council of the European Union: Brussels, **2015**. *Accessible via:*

https://eur-lex.europa.eu/legal-content/EN/TXT/PDF/?uri=CELEX:01998L0083-20151027&from=EN

Ewing, F. J. The crystal structure of lepidocrocite. *J. Chem. Phys.* ***1935****, 3,* 420–424.

Farley, K. J.; Dzombak, D. A.; Morel, F. M. M. A surface precipitation model for the sorption of cations on metal oxides. *J. Colloid Interface Sci.* ***1985****, 106* (1), 226–242.

Fein, F. B.; Daughney, C. J.; Yee, N., Davis; T. A. A chemical equilibrium model for metal adsorption onto bacterial surfaces. *Geochim. Cosmochim. Acta* ***1997****, 61* (16), 3319–3328.

Feng, H. X.; Zhai, L. M.; Tan, W. F.; Liu, F.; He, J. Z. Adsorption and redox reactions of heavy metals on synthesized Mn oxide minerals. *Environ. Pollut.* ***2007****, 147,* 366–373.

Feng, Q.; Wen, S.; Zhao, W.; Deng, J.; Xian, Y. Adsorption of sulfide ions on the cerussite surfaces and implications for floatation. *Appl. Surf. Sci.* ***2016****, 360,* 365–372.

Ferris, F. G.; Schultze, S.; Witten, T. C.; Fyfe, W. S.; Beveridge, T. J. Metal interactions with microbial biofilms in acidic and neutral pH environments. *Appl. Environ, Microbiol.* ***1989****, 55* (5), 1249–1257.

Finlay, N. C.; Peacock, C. L.; Hudson-Edwards, K. A.; Johnson, K. L. Characterisation and mechanisms of Pb(II) sorption onto Fe-rich waste water treatment residue (WTR): A potential sustainable immobilisation technology for soils. *J. Hazard. Mater.* ***2020****, 402,* 123433.

Fischer, L.; Brümmer, G. W.; Barrow, N. J. Observation and modelling of the reactions of 10 metals with goethite: adsorption and diffusion processes. *Eu. J. Soil Sci.* ***2007****, 58,*1304–1315.

Flaathen, T. K.; Gíslason, S. R.; Oelkers, E. H.; Sveinbjörnsdóttir, Á. Chemical evolution of the Mt. Hekla, Iceland, groundwaters: A natural analogue for CO_2 sequestration in basaltic rocks. *Appl. Geochem.* ***2009****, 24,* 463–474.

Flemming, C. A.; Trevors, J. T. Copper toxicity and chemistry in the environment. *Water Air Soil Pollut.* ***1989****, 44,* 143–158.

Forsey, T. Toxic metal release in mafic and ultramafic rocks from mineral carbonation efforts. *MSci. Thesis* ***2020****,* UCL, Dept. Earth Sci., London, pp.59.

Freundlich, H. Kapillarchemie: eine Darstellung der Chemie der Kolloide und verwandter Gebiete. *Akadem. Verlagsgesell.* ***1909****, Leipzig.*

Frierdich, A. J.; Luo, Y.; Catalano, J. G. Trace element cycling through iron oxide minerals during redox-driven dynamic recrystallisation. *Geology* ***2011****, 39* (11), 1083–1086.

Frierdich, A. J.; Catalano, J. G. Controls on Fe(II)-activated trace element release from goethite and hematite. *Environ. Sci. Technol.* ***2012a****, 46,* 1519–1526.

Frierdich, A. J.; Catalano, J. G. Fe(II)-mediated reduction and repartitioning of structurally incorporated Cu, Co, and Mn in iron oxides. *Environ. Sci. Technol.* ***2012b****, 46,* 11070–11077.

Fulghum, J. E.; Bryan, S. R.; Linton, R. W. Discrimination between adsorption and coprecipitation in aquatic particle standards by surface analysis techniques: Lead distributions in calcium carbonates. *Environ. Sci. Technol.* ***1988****, 22,* 463–467.

Füllenbach, L. C. Mineral identification with focus on HFSE-bearing minerals in ore samples from the Strange Lake deposit (Canada): Application of XRD and electron micro-beam techniques. *MSc Thesis (Brombacher, L. C.), TU Bergakademie Freiberg* ***2015****,* pp. 136.

Füllenbach, L. C.; Perez, J. P. H.; Freeman, H. M.; Thomas, A. N.; Mayanna, S.; Parker, J. E.; Göttlicher, J.; Steininger, R.; Radnik, J.; Benning, L. G.; Oelkers, E. H. Nanoanalytical identification of siderite dissolution-coupled Pb removal mechanisms from oxic and anoxic aqueous solutions. *ACS Earth Space Chem.* ***2020****, 4,* 1966–1977.

Fuller, C. C.; Davis, J. A.; Waychunas, G. A. Surface chemistry of ferrihydrite: Part 2. Kinetics of arsenate adsorption and coprecipitation. *Geochim. Cosmochim. Acta* ***1993****, 57,* 2271–2282.

Furrer, G.; Stumm, W. The coordination chemistry of weathering: I. Dissolution kinetics of δ-Al_2O_3 and BeO. *Geochim. Cosmochim. Acta* ***1986****, 50,* 1847–1860.

Gaarenstroom, S. W.; Winograd, N. Initial and final state effects in the ESCA spectra of cadmium and silver oxides. *J. Chem. Phys.* ***1977****, 67* (8), 3500–3506.

Gäbler, H.-E.; Schneider, J. Assessment of heavy-metal contamination of floodplain soils due to mining and mineral processing in the Harz Mountains, Germany. *Environ. Geol.* ***2000****, 39* (7), 774–782.

Gadde, R. R.; Laitinen, H. A. Studies of heavy metal adsorption by hydrous iron and manganese oxides. *Anal. Chem.* ***1974****, 46* (13), 2022–2026.

Gankhurel, B.; Fukushi, K.; Akehi, A.; Takahashi, Y.; Zhao, X.; Kawasaki, K. Comparison of chemical speciation of lead, arsenic, and cadmium in contaminated soils from a historical mining site: Implications for different mobilities of heavy metals. *ACS Earth Space Chem.* ***2020****, 4* (7), 1064–1077.

Garrels, R. M. Mineral species as functions of pH and oxidation–reduction potentials, with special reference to the zone of oxidation and secondary enrichment of sulphide ore deposits. *Geochim. Cosmochim. Acta* ***1954****, 5,* 153–168.

Garrels, R. M.; Thompson, M. E. Oxidation of pyrite by iron sulfate solutions. *Am. J. Sci.* ***1960****, 258,* 57–67.

Gilbert, B.; Ono, R. K.; Ching, K. A.; Kim, C. S. The effects of nanoparticle aggregation processes on aggregate structure and metal uptake. *J. Colloid Interface Sci.* ***2009****, 339,* 285–295.

Gimeno-García, E.; Andreu, V.; Boluda, R. Heavy metals in the application of inorganic fertilizers and pesticides to rice farming soils. *Environ. Pollution* ***1996****, 92,* 19–25.

Gíslason, S. R.; Oelkers, E. H. Carbon storage in basalt. *Science* ***2014****, 344,* 373–374.

Glemser, O.; Lin, T.-P. Über Blei(II)-oxidhydroxid $Pb_5O_3(OH)_4$. *Zeit. Anorg. Allg. Chem.* ***1971****, 382,* 244–248.

Godelitsas, A.; Astilleros, J. M.; Hallam, K.; Harissopoulos, S.; Putnis, A. Interaction of calcium carbonates with lead in aqueous solutions. *Environ. Sci. Technol.* ***2003****, 37,* 3351–3360.

Goh, S. W.; Buckley, A. N.; Lamb, R. N.; Rosenberg, R. A.; Moran, D. The oxidation states of copper and iron in mineral sulfides, and the oxides formed on initial exposure of chalcopyrite and bornite to air. *Geochim. Cosmochim. Acta* ***2006****, 70,* 2210–2228.

Goldberg, S. Chemical modelling of anion competition on goethite using the constant capacitance model. *Soil Sci. Soc. Am. J.* ***1985****, 49,* 851–856.

Golubev, S. V.; Bénézeth, P.; Schott, J.; Dandurand, J. L.; Castillo, A. Siderite dissolution kinetics in acidic aqueous solutions from 25 to 100 °C and 0 to 50 atm pCO_2. *Chem. Geol.* ***2009****, 265,* 13–19.

Goring–Harford, H. J.; Klar, J. K.; Donald, H. K.; Pearce, C. R.; Connelly, D. P.; James, R. H. Behaviour of chromium and chromium isotopes during estuarine mixing in the Beaulieu Estuary, UK. *Earth Planet. Sci. Lett.* ***2020****, 536,* 116166, 1–10.

Gorski, C. A.; Edwards, R.; Sander, M.; Hofstetter, T. B.; Stewart, S. M. Thermodynamic characterisation of iron oxide–aqueous Fe^{2+} redox couples. *Environ. Sci. Technol.* ***2016****, 50,* 8538–8547.

Graf, D. L. Crystallographic tables for the rhombohedral carbonates. *Am. Mineral.* ***1961****, 46,* 1283–1316.

Gräfe, M.; Beattie, D. A.; Smith, E.; Skinner, W. M.; Singh, B. Copper and arsenate co-sorption at the mineral–water interfaces of goethite and jarosite. *J. Colloid Interface Sci.* ***2008****, 322,* 399–413.

Grauer, R. Solubility products of M(II)-carbonates. *PSI report 99-04,* ***1999****,* ed. Berner, U.; ISSN 1019-0643.

Greenberg, J.; Tomson, M. Precipitation and dissolution kinetics and equilibria of aqueous ferrous carbonate vs temperature. *Appl. Geochem.* ***1992****, 7,* 185–190.

Gunneriusson, L.; Lövgren, L.; Sjöberg, S. Complexation of Pb(II) at the goethite (α-FeOOH)/water interface: The influence of chloride. *Geochim. Cosmochim. Acta* ***1994***, *58* (22), 4973–4983.

Guo, H.; Stüben, D.; Berner, Z. Removal of arsenic from aqueous solution by natural siderite and hematite. *Appl. Geochim.* ***2007a***, *22*, 1039–1051.

Guo, H.; Stüben, D.; Berner, Z. Arsenic removal from water using natural iron mineral–quartz sand columns. *Sci. Total Environ.* ***2007b***, *377*, 142–151.

Guo, H.; Stüben, D.; Berner, Z. Adsorption of arsenic(III) and arsenic(V) from groundwater using natural siderite as the adsorbent. *J. Colloid Interface Sci.* ***2007c***, *315*, 47–53.

Guo, H.; Stüben, D.; Berner, Z.; Qingchun, Y. Characteristic of arsenic adsorption from aqueous solution: Effect of arsenic species and natural adsorbents. *Appl. Geochim.* ***2009***, *24*, 657–663.

Guo, H.; Li, Y.; Zhao, Kao. Arsenate removal from aqueous solutions using synthetic siderite. *J. Hazard. Mater*. ***2010***, *176*, 174–180.

Guo, H.; Li, Y.; Zhao, K.; Ren, Y.; Wei, C. Removal of arsenite from water by synthetic siderite: Behaviors and mechanisms. *J. Hazard. Mater*. ***2011***, *186*, 1847–1854.

Gutjahr, A.; Dabringhaus, H.; Lacmann, R. Studies of the growth and dissolution kinetics of the $CaCO_3$ polymorphs calcite and aragonite II. The influence of divalent cation additives on the growth and dissolution rates. *J. Cryst. Growth* ***1996a***, *158*, 310–315.

Gutjahr, A.; Dabringhaus, H.; Lacmann, R. Studies of the growth and dissolution kinetics of the $CaCO_3$ polymorphs calcite and aragonite I. Growth and dissolution rates in water. *J. Cryst. Growth* ***1996b***, *158*, 296–309.

Ha, J.; Trainor, T. P., Farges, F.; Brown, G. E. Jr. Interaction of aqueous Zn(II) with hematite nanoparticles and microparticles. Part 1. EXAFS study of Zn(II) adsorption and precipitation. *Langmuir* ***2009***, *25* (10), 5574–5585.

Ha, J.; Zhao, X.; Yu, R.; Barkay, T.; Yee, N. Hg(II) reduction by siderite ($FeCO_3$). *Appl. Geochem.* ***2017***, *78*, 211–218.

Hajji, S.; Montes-Hernandez, G.; Sarret, G.; Tordo, A.; Morin, G.; Ona-Nguema, G.; Bureau, S.; Turki, T.; Mzoughi, N. Arsenite and chromate sequestration onto ferrihydrite, siderite and goethite nanostructured minerals: Isotherms from flow-through reaction experiments and XAS measurements. *J. Hazard. Mater*. ***2019***, *362*, 358–367.

Halevy, I.; Alesker, M.; Schuster, E. M.; Popovitz-Biro, R.; Feldman, Y. A key role for green rust in the Precambrian oceans and the genesis of iron formations. *Nat. Geosci.* ***2017***, *10* (2), 135–139.

Han, F. X.; Banin, A.; Su, Y.; Monts, D. L.; Plodinec, M. J.; Kingery, W. L.; Triplett, G. E. Industrial age anthropogenic inputs of heavy metals into the pedosphere. *Naturwiss.* ***2002***, *89*, 497–504.

Handler, R. M.; Beard, B. L.; Johnson, C. M.; Scherer, M. M. Atom exchange between aqueous Fe(II) and goethite: An Fe isotope tracer study. *Environ. Sci. Technol.* ***2009***, *43*, 1102–1107.

Handler, R. M.; Frierdich, A. J.; Johnson, C. M.; Rosso, K. M.; Bear, B. L.; Wang, C.; Latta, D. E.; Neumann, A.; Pasakarnis, T.; Premaratne, W. A. P. J.; Scherer, M. M. Fe(II)-catalyzed recrystallisation of goethite revisited. *Environ. Sci. Technol.* ***2014***, *48*, 11302–11311.

Hansel, C. M.; Benner, S. G.; Fendorf, S. Competing Fe(II)-induced mineralisation pathways of ferrihydrite. *Environ. Sci. Technol.* ***2005***, *39*, 7147–7153.

Harrison, R. K.; Aitkenhead, N.; Young, B. R.; Dagger, P. F. Goethite form Hindlow, Derbyshire. *Bull. Geol. Surv. G.B.* ***1975***, *52*, 51–54.

Hartmann, J.; West, A.J.; Renforth, P.; Köhler, P.; De La Rocha, C.; Wolf-Gladrow, D. A.; Dürr, H. H.; Scheffran, J. Enhanced chemical weathering as a geoengineering strategy to reduce atmospheric carbon dioxide, supply nutrients, and mitigate ocean acidification. *Rev. Geophys.* ***2013***, *51*, 113–149.

Hayes, K. F.; Leckie, J. O. Modelling ionic strength effects on cation adsorption at hydrous oxide/solution interfaces. *J. Colloid Interface Sci.* ***1987***, *115* (2), 564–572

Hayes, K. F.; Roe, A. L.; Brown, G. E. Jr.; Hodgson, K. O.; Leckie, J. O., Parks, G. A. In situ X-ray absorption study of surface complexes: Selenium oxyanions on α-FeOOH. *Science* ***1987***, *238*, 783–786.

Haynes, E. Potential for heavy metal release during terrestrial enhanced silicate weathering regimes. *MSci. Thesis* ***2021***, UCL, Dept. Earth Sci., London, pp.79.

Hazemann, J.-L.; Bérar, J.-F.; Manceau, A. Rietveld studies of the aluminium-iron substitution in synthetic goethite. *Mater. Sci. Forum* ***1991***, *79-82*, 821–826.

Hering, J. G.; Stumm, W. Oxidation and reductive dissolution of minerals. *Rev. Mineral.* ***1990***, *23*, 427–466.

Hesse, R.; Denecke, R. Improved Tougaard background calculation by introduction of fittable parameters for the inelastic electron scattering cross-section in the peak fit of photoelectron spectra with UNIFIT 2011. *Surf. Interface Anal.* ***2011***, *43*, 1514–1526.

Hesse, R.; Streubel, P.; Szargan, R. Product or sum: comparative tests of Voigt, and product or sum of Gaussian and Lorentzian functions in the fitting of synthetic Voigt-based X-ray photoelectron spectra. *Surf. Interface Anal.* ***2007***, *39*, 381–391.

Hiemstra, T.; Van Riemsdijk, W. H.; Bolt, G. H. Multisite proton adsorption modelling at the solid/solution interface of (hydr)oxides: A new approach. I. Model description and evaluation of intrinsic reaction constants. *J. Colloid Interface Sci.* ***1989a***, *133* (1), 91–104.

Hiemstra, T.; De Wit, J. C. M.; Van Riemsdijk, W. H. Multisite proton adsorption modelling at the solid/solution interface of (hydr)oxides: A new approach. II. Application to various important (hydr)oxides. *J. Colloid Interface Sci.* ***1989b***, *133* (1), 105–117.

Hiemstra, T.; Van Riemsdijk, W. H. A surface structural approach to ion adsorption: The charge distribution (CD) model. *J. Colloid Interface Sci.* ***1996***, *179*, 488–508.

Hiemstra, T.; Venema, P.; Van Riemsdijk, W. H. Intrinsic proton affinity of reactive surface groups of metal (hydr)oxides: The bond valence principle. *J. Colloid Interface Sci.* ***1996***, *184*, 680–692.

Hiemstra, T. Surface and mineral structure of ferrihydrite. *Geochim. Cosmochim. Acta* ***2013***, *105*, 316–325.

Hiemstra, T. Formation, stability, and solubility of metal oxide nanoparticles: Surface entropy, enthalpy, and free energy of ferrihydrite. *Geochim. Cosmochim. Acta* ***2015***, *158*, 179–198.

Hochella, Jr., M. F. Auger electron and X-ray photoelectron spectroscopies. *Rev. Min. Geochem.* ***1988***, 573–637.

Hochella, M. F. Jr. Atomic structure, microtopography, composition, and reactivity of mineral surfaces. *Rev. Mineral.* ***1990***, *23*, 87–132.

Hochella, M. F. Jr.; White, A. F. Mineral–water interface geochemistry: An overview. *Rev. Mineral.* ***1990***, *23*, 1–16.

Holm, N. G. The $^{13}C/^{12}C$ ratios of siderite and organic matter of a modern metalliferous hydrothermal sediment and their implications for banded iron formations. *Chem. Geol.* ***1989****, 77,* 41–45.

Hseu, Z.-Y.; Su, Y.-C.; Zehetner, F.; Hsi, H.-C. Leaching potential of geogenic nickel in serpentine soils from Taiwan and Austria. *J. Environ. Manage.* ***2017****, 186,* 151–157.

Hsu, P. H.; Marion, G. The solubility product of goethite. *Soil Sci.* ***1985****, 140* (5), 344–351.

Hu, W.; Zhang, Z.; Li, M.; Liu, H.; Zhang, C.; Chen, T.; Zhou, Y. Enhanced uptake capacity for uranium(VI) in aqueous solutions by activated natural siderite: Performance and mechanism. *Appl. Geochem.* ***2019****, 100,* 96–103.

Hua, M.; Zhang, S.; Pan, B.; Zhang, W.; Lv, L.; Zhang, Q. Heavy metal removal from water/wastewater by nanosized metal oxides: A review. *J. Hazard. Mater.* ***2012****, 211–212,* 317–331.

Hudson, M. E. The influence of Fe-rich coatings on the dissolution of anorthite at pH 2.6. *Geochim. Cosmochim. Acta* ***2003****, 67 (18),* 3355–3363.

Hunter, K. S.; Wang, Y.; Van Cappellen, P. Kinetic modelling of microbially-driven redox chemistry o subsurface environments: coupling transport, microbial metabolism and geochemistry. *J. Hydrol.* ***1998****, 209,* 53–80.

Irwin, R. J. Copper. *In:* Environmental Contaminants Encyclopedia. *National Park Services* ***1997****,* 99 p.

Islam, Md. R.; Lahermo, P.; Salminen, R.; Rojstaczer, S.; Peuraniemi, V. Lake and reservoir water quality affected by metals leaching from tropical soils, Bangladesh. *Environ. Geol.* ***2000****, 39,* 1083–1089.

ISO 15472:2010, Surface chemical analysis – X-ray photoelectron spectrometers – Calibration of energy scales; https://www.iso.org/standard/55796.html

Ithurbide, A., Peulon, S.; Miserque, F.; Beaucaire, C.; Chaussé, A. Interaction between uranium(VI) and sierite ($FeCO_3$) surfaces in carbonate solution. R*adiochim. Acta* ***2009****, 97,* 177–180.

Ithurbide, A., Peulon, S.; Miserque, F.; Beaucaire, C.; Chaussé, A. Retention and redox behaviour of uranium(VI) by siderite ($FeCO_3$). *Radiochim. Acta* ***2010****, 98,* 563–568.

Jaisi, D. P.; Dong, H.; Plymale, A. E.; Frederickson, J. K.; Zachara, J. M. Heald, S.; Liu, C. Reduction and long-term immobilization of technetium by Fe(II) associated with clay mineral nontronite. *Chem. Geol.* ***2009****, 264,* 127–138.

Janney, D. E.; Cowley, J. M.; Buseck, P. R. Transmission electron microscopy of synthetic 2- and 6-line ferrihydrite. *Clays Clay Minerals* ***2000****, 48* (1), 111–119.

Jamieson, H. E. Geochemistry and mineralogy of solid mine waste: Essential knowledge for predicting environmental impact. *Elements* ***2011****, 7* (6), 381–386.

Järup, L. Hazards of heavy metal contamination. *Brit. Med. Bulletin* ***2003****, 68,* 167–182.

Jensen, D. L.; Boddum, J. K.; Tjell, J. C.; Christensen, T. H. The solubility of rhodochrosite ($MnCO_3$) and siderite ($FeCO_3$) in anaerobic aquatic environments. *Appl. Geochem.* ***2002****, 17,* 503–511.

Jeon, B.-H.; Dempsey, B. A.; Burgos, W. D.; Royer, R. A. Reaction of ferrous iron with hematite. *Colloids Surfaces A* ***2001****, 191,* 41–55.

Jeon, B.-H.; Dempsey, B. A.; Burgos, W. D.; Royer, R. Sorption kinetics of Fe(II), Zn(II), Co(II), Ni(II), Cd(II), and Fe(II)/Me(II) onto hematite. *Water Res.* ***2003****, 37,* 4135–4142.

Jeppu, G. P.; Clement, T. P. A modified Langmuir–Freundlich isotherm model for simulating pH-dependent adsorption effects. *J. Contam. Hydrol.* ***2012****, 129–130,* 46–53.

Jiang, C. Z.; Tosca, N. J. Fe(II)-carbonate precipitation kinetics and the chemistry of anoxic ferruginous seawater. *Earth Planet. Sci. Lett.* ***2019****, 506,* 231–242.

Jiang, C. Z.; Tosca, N. J. Growth kinetics of siderite at 298.15 K and 1 bar. *Geochim. Cosmochim. Acta* ***2020****, 274,* 97–117.

Jiang, C. Z.; Halevy, I.; Tosca, N. J. Kinetic isotope effect in siderite growth: Implications for the origin of banded iron formations. *Geochim. Cosmochim. Acta* ***2022****, in press*.

Joe-Wong, C.; Brown, G. E.; Maher, K. Kinetics and products of chromium(VI) reduction by iron(II/III)-bearing clay minerals. *Environ. Sci. Technol.* ***2017****, 51,* 9817–9825.

John, M. Heuss-Aßbichler, S.; Park, S.-H.; Ullrich, A.; Benka, G.; Petersen, N.; Rettenwander, D.; Horn, S. R. Low-temperature synthesis of $CuFeO_2$ (delafossite) at 70 ºC: A new process solely by precipitation and ageing. *J. Solid State Chem.* ***2016****, 233,* 390–396.

Johnson, D. B.; Hallberg, K. B. Acid mine drainage remediation options: A review. *Sci. Total Environ.* ***2005****, 338,* 3–14.

Jönsson, J.; Sherman, D. M. Sorption of As(III) and As(V) to siderite, green rust (fougerite) and magnetite: Implications for arsenic release in anoxic groundwaters. *Chem. Geol.* ***2008****, 255,* 173–181.

Jung, H. B.; Xu, H.; Konishi, H.; Roden, E. E. Role of nano-goethite in controlling U(VI) sorption-desorption in subsurface soil. *J. Geochem. Explor.* ***2016****, 169,* 80–88.

Junta, J. I.; Hochella, Jr., M. F. Manganese(II) oxidation at mineral surfaces: A microscopic and spectroscopic study. *Geochim. Cosmochim. Acta* ***1994****, 58* (22), 4985–4999.

Kamrimian, N.; Johnston, S. G.; Burton, E. D. Iron and sulfur cycling in acid sulfate soil wetlands under dynamic redox conditions: A review. *Chemosphere* ***2018****, 197,* 803–816.

Karlsson, T.; Persson, P.; Skyllberg, U. Complexation of copper(II) in organic soils and in dissolved organic matter – EXAFS evidence for chelating ring structures. *Environ. Sci. Technol.* ***2006****, 40,* 2623–2628.

Kasassi, A.; Ramkimbei, P.; Karagiannidis, A.; Zabaniotou, A.; Tsiouvaras, K.; Nastis, A.; Tzafeiropoulou, K. Soil contamination by heavy metals: Measurements from a closed unlined landfill. *Biores. Technol.* ***2008****, 99,* 8578–8584.

Kelly, S. D.; Hesterberg, D.; Ravel, B. Analysis of soils and minerals using X-ray absorption spectroscopy. In: Methods of Soil Analysis. Part 5. Mineralogical Methods. *SSSA Book Series* ***2008****, 5,* 387–463.

Kelly, S. D.; Kemner, K. M.; Fein, J. B.; Fowle, D. A.; Boyanov, M. I.; Bunker, B. A.; Yee, N. X-ray absorption fine structure determination of pH-dependent U-bacterial cell wall interactions. *Geochim. Cosmochim. Acta* ***2002****, 66* (22), 3855–3871.

Khalid, S.; Shahid, M.; Niazi, N. K.; Murtaza, B.; Bibi, I.; Dumat, C. A comparison of technologies for remediation of heavy metal contaminated soils. *J. Geochem. Explor.* ***2017****, 182,* 247–268.

Kim, C. S.; Lentini, C. J.; Waychunas, G. A. Associations between iron oxyhydroxide nanoparticle growth and metal adsorption/structural incorporation. *In:* Chapter 6, Barnett, M. O.; Kent, D. B. Developments in Earth & Environmental Sciences. *Elsevier* ***2008****, 7,* 154–185.

Kimura, Y.; Miller, V. L. The degradation of organomercury fungicides in soil. *Agric. Food Chem.* ***1964****, 12* (3), 253–257.

Kiseleva, I. A.; Orgodova, L. P.; Melchakova, L. V.; Bisengalieva, M. R.; Becturganov, N. S. Thermodynamic properties of copper carbonates – malachite $Cu_2(OH)_2CO_3$ and azurite $Cu_3(OH)_2(CO_3)_2$. *Phys. Chem. Minerals* ***1992****, 19,* 322–333.

Kleber, W.; Bautsch, H.-J.; Bohm, J. Einführung in die Kristallographie, 19th ed. *Oldenbourg Verlag: München,* ***2010****,* 468 p.

Klementiev, K. V. *XAFSmass*; freeware: www.cells.es/Beamlines/CLAESS/software/xafsmass.html

Köhler, P.; Hartmann, J.; Wolf-Gladrow, D. A. Geoengineering potential of **artificially** enhanced silicate weathering of olivine. *Proc. Natl. Acad. Sci.* ***2010****, 107* (47), 20228–20233.

Köhler, P.; Abrams, J. F.; Völker, C.; Hauck, J.; Wolf-Gladrow, D. A. Geoengineering impact of open dissolution of olivine on atmospheric CO_2, surface ocean pH and marine biology. *Environ. Res. Lett.* ***2013****, 8,* 1–9.

Köhler, S. J.; Cubillas, P.; Rodríguez–Blanco, J. D.; Bauer, C.; Prieto, M. Removal of cadmium from wastewaters by aragonite shells and the influence of other divalent cations. *Environ. Sci. Technol.* ***2007****, 41,* 112–118.

Konhauser, K. O.; Kappler, A.; Roden, E. E. Iron in microbial metabolism. *Elements* ***2011****, 7* (2), 89–93.

Konhauser, K. O.; Planavsky, N. J.; Fardisty, D. S.; Robbins, L. J.; Warchola, T. J.; Haugaard, R.; Lalonde, S. V.; Partin, C. A.; Oonk, P. B. H.; Tsikos, H.; Lyons, T. W.; Bekker, A.; Johnson, C. M. Iron formations: A global record of Neoarchaean to Palaeoproterozoic environmental history. *Earth-Sci. Rev.* ***2017****, 172,* 140–177.

Koretsky, C. The significance of surface complexation reactions in hydrologic systems: a geochemist's perspective. *J. Hydrol.* ***2000****, 230,* 127–171.

Kornicker, W. A.; Morse, J. W.; Damasceno, R. N. The chemistry of Co^{2+} interaction with calcite and aragonite surfaces. *Chem. Geol.* ***1985****, 53,* 229–236.

Kumpiene, J.; Lagerkvist, A.; Maurice, C. Stabilisation of As, Cr, Cu, Pb, and Zn in soil using amendments – a review. *Waste Manag.* ***2008****, 28,* 215–225.

Lackner, K. S.; Wendt, C. H.; Butt, D. P.; Joyce, E. L. Jr.; Sharp, D. H. Carbon dioxide disposal in carbonate minerals. *Energy* ***1995****, 20* (11), 1153–1170.

Lammers, K.; Murphy, R.; Riendeau, A.; Smirnov, A., Schoonen, M. A. A.; Strongin, D. R. CO_2 sequestration through mineral carbonation of iron oxyhydroxides. *Environ. Sci. Technol.* ***2011****, 45,* 10422–10428.

Langmuir, D. Aqueous environmental geochemistry. *Prentice Hall, Upper Saddle River, New Jersey,* ***1997****,* pp. 600. ISBN 0-02-367412-1.

Langmuir, I. The Adsorption of gases on plane surfaces of glass, mica and platinum. *J. Am. Chem. Soc.* ***1918,*** *40* (9), 1361-1403.

Larese-Casanova, P.; Kappler, A.; Haderlein, S. B. Heterogeneous oxidation of Fe(II) on iron oxides in aqueous systems: Identification and controls of Fe(III) product formation. *Geochim. Cosmochim. Acta* ***2012****, 91,* 171–186.

Larsen, O.; Postma, D. Kinetics of reductive bulk dissolution of lepidocrocite, ferrihydrite, and goethite. *Geochim. Cosmochim. Acta* ***2001****, 65* (9), 1367–1379.

Lasaga, A. C. Transition state theory. *Rev. Mineral.* ***1981****, 8,* 135–170.

Lasaga, A. C. Chemical kinetics of water–rock interactions. *J. Geophys. Res.* ***1984****, 89* (B6), 4009–4025.

Lasaga, A. C. Atomic treatment of mineral–water surface reactions. *Rev. Mineral.* ***1990****, 23,* 17–86.

Laube, N.; Frimmel, H. E.; Hoernes, S. Oxygen and carbon isotopic study on the genesis of the Steierischer Erzberg siderite deposit (Austria). *Mineral. Deposita* ***1995****, 285–293,* 285–293.

Lecce, S. A.; Pavlowsky, R. T. Floodplain storage of sediment contamination by mercury and copper from historic gold mining at Gold Hill, North Carolina, USA. *Geomorphology* ***2014****, 206,* 122–132.

Li, P, Wang, X., Allison, G., Li, X., Xiong, X. (2009) Risk assessment in soil previously irrigated with industrial wastewater in Shenyang, China. *J. Hazard. Mater*. ***2009****, 161,* 516–521.

Liger, E.; Charlet, L.; Van Cappellen, P. Surface catalysis of uranium(VI) reduction by iron(II). *Geochim. Cosmochim. Acta* ***1999****, 63* (19-20), 2939–2955.

Lindsay, W. L. Chemical equilibria in soils. *Wiley Interscience, New York* ***1979****,* 449 p.

Lindsay, W. L., Sadiq, M. Use of pe + pH to predict and interpret metal solubility relationships in soils. *Sci. total Environ.* ***1983****, 28,* 169–178.

Linke, T.; Gíslason, S. R. Stability of iron mineral sin Icelandic peat areas and transport of heavy metals and nutrients across oxidation and salinity gradients – a modelling approach. *Energy Proceedia* ***2018****, 146,* 30–37.

Lim, H.-S.; Lee; J.-S.; Chon, H.-T.; Sage, M. Heavy metal contamination and health risk assessment in the vicinity of the abandoned Songcheon Au–Ag mine in Korea. *J. Geochem. Explor*. ***2008****, 96,* 223–230.

Liu, F.; De Cristofaro, A.; Violante, A. Effect of pH, phosphate and oxalate on the adsorption/desorption of arsenate on/from goethite. *Soil Sci.* ***2001****, 166* (3), 197–208.

Liu, H.; Li, P.; Zhu, M.; Wei, Y.; Sun, Y. Fe(II)-induced transformation from ferrihydrite to lepidocrocite and goethite. *J. Solid State Chem.* ***2007****, 180,* 2121–2128.

Liu, H.; Lu, X.; Li, M.; Zhang, L.; Pan, C.; Li, J.; Xiang, W. Structural incorporation of manganese into goethite and its enhancement of Pb(II) adsorption. *Environ. Sci. Technol.* ***2018****, 52,* 4719–4727.

Lofts, S.; Spurgeon, D. J.; Svendsen, C.; Tipping, E. Deriving soil critical limits for Cu, Zn, Cd, and Pb: A method based on free ion concentrations. *Environ. Sci. Technol.* ***2004****, 38,* 3623–3631.

Loyaux-Lawniczak, S.; Refait, P.; Ehrhardt, J.-J.; Lecomte, P.; Génin, J.-M. R. Trapping of Cr by formation of ferrihydrite during the reduction of chromate ions by Fe(II)-Fe(III) hydroxysalt green rust. *Environ. Sci. Technol.* ***2000****, 34,* 438–443.

Lu, X.; Wang, H. Microbial oxidation of tailings and the environmental consequences. *Elements* ***2012****, 8* (2), 119–124.

Lu, Y.; Hu, S.; Liang, Z.; Wang, Z.; Wang, X.; Liang, Y.; Dang, Z.; Shi, Z. Incorporation of Pb(II) into hematite during ferrihydrite transformation. *Environ. Sci. Nano* ***2020****, 7,* 829–841.

Ma, Q. Y.; Logan, T. J.; Traina, S. J. Lead immobilisation from aqueous solutions and contaminated soils using phosphate rocks. *Environ. Sci. Technol.* ***1995****, 29,* 1118–1126.

Macías, F.; Caraballo, M. A.; Nieto, J. M.; Rötting, T. S.; Ayora, C. Natural pre-treatment and passive remediation of highly polluted acid mine drainage. *J. Environ. Manag.* ***2012****, 104,* 93–100.

MacInnis, I. N.; Brantley, S. L. The role of dislocations and surface morphology in calcite dissolution. *Geochim. Cosmochim. Acta* ***1992****, 56,* 1113–1126.

Majzlan, J.; Grevel, K.-D.; Navrotsky, A. Thermodynamics of Fe oxides: Part II. Enthalpies of formation and relative stability of goethite (α-FeOOH), lepidocrocite (γ-FeOOH), and maghemite (γ-Fe_2O_3). *Am. Mineral.* ***2003***, *88*, 855–859.

Majzlan, J.; Navrotsky, A.; Schwertmann, U. Thermodynamics of iron oxides: Part III. Enthalpies of formation and stability of ferrihydrite (~$Fe(OH)_3$), schwertmannite (~$Fe(OH)_{3/4}(SO_4)_{1/8}$), and ε-Fe_2O_3. *Geochim. Cosmochim. Acta* ***2004***, *68* (5), 1049–1059.

Manceau, A.; Charlet, L.; Boisset, M. C.; Didier, B.; Spadini, L. Sorption and speciation of heavy metals in hydrous Fe and Mn oxides. From microscopic to macroscopic. *Appl. Clay Sci.* ***1992***, *7*, 201–233.

Manceau, A.; Boisset, M.-C.; Sarret, G.; Hazemann, J.-L.; Mench, M.; Cambier, P.; Prost, R. Direct determination of lead speciation in contaminated soils by EXAFS spectroscopy. *Environ. Sci. Technol.* ***1996***, *30*, 1540–1552.

Manceau, A.; Schlegel, M. L.; Musso, M.; Sole, V. A.; Gauthier, C.; Petit, P. E.; Trolard, F. Crystal chemistry of trace elements in natural and synthetic goethite. *Geochim. Cosmochim. Acta* ***2000***, *64* (21), 3643–3661.

Manceau, A.; Marcus, M. A.; Tamura, N. Quantitative speciation of heavy metals in soils and sediments by synchrotron X-ray techniques. *Rev. Mineral. Geochem.* ***2002***, *49*, 341–428.

Manceau, A.; Matynia, A. The nature of Cu bonding to natural organic matter. *Geochim. Cosmochim. Acta* ***2010***, *74*, 2556–280.

Marron, D. C. The transport of mine tailings as suspended sediment in the Belle Fourche River, west-central South Dakota, USA. *Sed. Environ.* ***1989***, *184*, 19–26.

Marshall, T. A.; Morris, K.; Law, G. T. W.; Livens, F. R.; Mosselmans, J. F. W.; Bots, P.; Shaw, S. Incorporation of uranium into hematite during crystallisation from ferrihydrite. *Environ. Sci. Technol.* ***2014***, *48*, 3724–3732.

Martin, S.; Toffolo, L.; Moroni, M.; Montorfano, C.; Secco, L.; Agnini, C.; Nimis, P.; Tumiati, S. Siderite deposits in northern Italy: Early Permian to Early Triassic hydrothermalism in the Southern Alps. *Lithos* ***2017***, *284–285*, 276–295.

Martínez, C. E.; McBride, M. B. Coprecipitaiton of Cd, Cu, Pb and Zn in iron oxides: solid phase transformation and metal solubility after aging and thermal treatment. *Clays Clay Minerals* ***1998***, *46* (5), 537–545.

Matocha, C. J.; Karathanasis, A. D.; Rakshit, S.; Wagner, K. M. Reduction of Cu(II) by iron(II). *J. Environ. Qual.* ***2005***, *34*, 1539–1546.

McArthur, J. M.; Banerjee, D. M.; Hudson-Edwards, K. A.; Mishra, R.; Purohit, R.; Ravenscroft, P.; Cronin, A.; Howarth, R. J.; Chatterjee, A.; Talukder, T.; Lowry, D.; Houghton, S.; Chadha, D.K. Natural organic matter in sedimentary basins and its relation to arsenic in anoxic groundwater: the example of West Bengal and its worldwide implications. *Appl. Geochem.* ***2004***, *19*, 1255–1293.

McBride, M.; Sauvé, S.; Hendershot, W. Solubility control of Cu, Zn, Cd and Pb in contaminated soils. *European J. Soil Sci.* ***1997***, *48*, 337–446.

McLaren, A. C. Transmission electron microscopy of minerals and rocks. Cambridge University Press, *New York*, ***1991***, pp. 387.

McLean, L. C. W.; Beauchenim, S.; Rasmussen, P. E. Lead speciation in house dust from Canadian urban homes using EXAFS, micro-XRF, and micro-XRD. *Environ. Sci. Technol.* ***2011***, *45,* 5491–5497.

Merten, D.; Kothe, E.; Büchel, G. Studies on microbial retention from uranium mine drainage water with special emphasis on rare earth elements. *Mine Water Environ.* ***2004***, *23,* 34–43.

Miller, D. J.; Biesinger, M. C.; McIntyre, N. S. Interactions of CO_2 and CO at fractional atmosphere pressures with iron and iron oxide surfaces: one possible mechanism for surface contamination? *Surf. Interface Anal.* ***2002***, *33,* 299–305.

Monsterrat, F.; Renforth, P.; Hartmann, J.; Leermakers, M.; Knops, P.; Meysman, F. J. R. Olivine dissolution in seawater: Implications for CO_2 sequestration through enhanced weathering in coastal environments. *Environ. Sci. Technol.* ***2017***, *51,* 3960–3972.

Moon, E. M.; Peacock, C. L. Adsorption of Cu(II) to *Bacillus subtilis*: A pH-dependent EXAFS and thermodynamic modelling study. *Geochim. Cosmochim. Acta* ***2011***, *75,* 6705–6719.

Moon, E. M.; Peacock, C. L. Adsorption of Cu(II) to ferrihydrite and ferrihydrite–bacteria composites: Importance of the carboxyl group for Cu mobility in natural environments. *Geochim. Cosmochim. Acta* ***2012***, *92,* 203–219.

Moon, H. D.; Kim, K.-W.; Yoon, I.-H.; Grubb, D. G.; Shin, D.-Y.; Cheong, K. H.; Choi, H.-I.; Ok, Y. S.; Park, J.-H. Stabilisation of arsenic contaminated mine tailings using natural and calcined oyster shells. *Environ. Earth. Sci.* ***2011***, *64,* 597–605.

Moosdorf, N.; Renforth, P.; Hartmann, J. Carbon dioxide efficiency of terrestrial enhanced weathering. *Environ. Sci. Technol.* ***2014***, *48,* 4809–4816.

Morgan, B.; Lahav, O. The effect of pH on the kinetics of spontaneous Fe(II) oxidation by O_2 in aqueous solution – basic principles and a simple heuristic description. *Chemosphere* ***2007***, *68,* 2080–2084.

Morse, J. W. The surface chemistry of calcium carbonate minerals in natural waters: An overview. *Marine Chem.* ***1986***, *20,* 91–112.

Morton, R. L.; Nebel, M. L. Hydrothermal alteration of felsic volcanic rocks at the Helen siderite deposit, Wawa, Ontario. *Econ. Geol.* ***1984***, *79,* 1319–1333.

Mozley, P. S. Relation between depositional environment and the elemental composition of early diagenetic siderite. *Geology* ***1989***, *17,* 704–706.

Mozley, P. S.; Wersin, P. Isotopic composition of siderite as an indicator of depositional environment. *Geology* ***1992***, *20,* 817–820.

Mulders, J. J. P. A.; Tobler, D. J.; Oelkers, E. H. Siderite nucleation pathways as a function of aqueous solution saturation state at 25 ºC. *Chem. Geol.* ***2021***, *559,* 119947, 1–10.

Mulders, J. J. P. A. Experimental studies of mineral dissolution, nucleation and growth in aqueous solutions. *PhD Thesis, University College London* ***2021***, p. 145–164.

Newville, M. EXAFS analysis using FEFF and FEFFIT. *J. Synchrotron Rad.* ***2001***, *8,* 96– 100.

Newville, M. Fundamentals of XAFS. *Rev. Min. Geochem.* ***2014***, *78,* 33–74.

Nicholson, F. A.; Chambers, B. J.; Williams, J. R.; Unwin, R. J. Heavy metal contents in livestock feeds and animal manures in England and Wales. *Bioresource Technol.* ***1999***, *70,* 23–31.

Nordstrom, D. K. Aqueous pyrite oxidation and the consequent formation of secondary iron minerals. *In:* Kittrick, J.A., Fanning, D.S., Hossner, L.R. *ed.*, **1982**. Acid Sulfate Weathering. SSSA Special Publication 10, Madison, WI.

Nordstrom, D. K. Mine waters: Acidic to circumneutral. *Elements* ***2011a****, 7* (6), 393–398.

Nordstrom, D. K. Hydrogeochemical processes governing the origin, transport and fate of major and trace elements from mine wastes and mineralized rock to surface waters. *Appl. Geochem.* ***2011b****, 26,* 1777–1791.

Obiri-Nyarko, F.; Grajales-Mesa, S. J.; Malina, G. An overview of permeable reactive barriers for *in situ* sustainable groundwater remediation. *Chemosphere* ***2014****, 11,* 243–259.

O'Day, P. Molecular environmental geochemistry. *Rev. Geophysics* ***1999****, 37* (2), 249–274.

O'Day, P. A.; Carroll, S. A.; Waychunas, G. A. Rock–water interactions controlling zinc, cadmium, and lead concentrations in surface waters and sediments, U.S. Tri-State Mining District. 1. Molecular identification using X-ray Absorption spectroscopy. *Environ. Sci. Technol.* ***1998****, 38,* 943–955.

O'Day, P. A.; Vlassopoulos, D.; Root, R.; Rivera, N. The influence of sulfur and iron on dissolved arsenic concentrations in the shallow subsurface under changing redox conditions. *Proc. Natl. Acad. Sci.* ***2004****, 101* (38), 13703–13708.

O'Loughlin, E. J.; Kelly, S. D.; Cook, R. E.; Csencsits, R.; Kemner, K. M. Reduction of uranium(VI) by mixed iron(II)/iron(III) hydroxide (green rust): Formation of UO_2 nanoparticles. *Environ. Sci. Technol.* ***2003a****, 37,* 721–727.

O'Loughlin, E. J.; Kelly, S. D.; Kemner, K. M.; Csencsits, R.; Cook, R. E. Reduction of Ag^{I}, Au^{III}, Cu^{II}, and Hg^{II} by Fe^{II}/Fe^{III} hydroxysulphate green rust. *Chemosphere* ***2003b****, 53,* 437–446.

O'Loughlin, E. J.; Kelly, S. D.; Kemner, K. K. XAFS investigation of the interactions of U^{VI} with secondary mineralisation products from the bioreduction of Fe^{III} oxides. *Environ. Sci. Technol.* ***2010****, 44* (5), 1656–1661.

Oelkers, E. H. An experimental study of forsterite dissolution rates as a function of temperature and aqueous Mg and Si concentrations. *Chem. Geol.* ***2001****, 175,* 485–494.

Oelkers, E. H.; Gíslason, S. R. The mechanism, rates and consequences of basaltic glass dissolution: I. An experimental study of dissolution rates of basaltic glass as a function of aqueous Al, Si and oxalic acid concentration at 25 ºC and pH = 3 to 11. *Geochim. Cosmochim. Acta* ***2011****, 65* (21), 3671–3681.

Olsson, J.; Stipp, S. L. S.; Gíslason, S. R. Metal scavenging by calcium carbonate at the Eyjafjallajökull volcano: A carbon capture and storage analogue. *Chem. Geol.* ***2014****, 384,* 135–148.

Ona-Nguema, G.; Abdelmoula, M.; Jorand, F.; Benali, O.; Géhin, A.; Block, J.-C.; Génin, J.-M. R. Iron(II,III) hydroxycarbonate green rust formation and stabilisation from lepidocrocite bioreduction. *Environ. Sci. Technol.* ***2002****, 36,* 16–20.

Ona-Nguema, G.; Morin, G.; Wang, Y.; Menguy, N.; Juillot, F.; Olivi, L.; Aquilanti, G.; Abdelmoula, M.; Ruby, C.; Bargar, J. R.; Guyot, F.; Calas, G.; Brown, G. E. Jr. Arsenite sequestration at the surface of nano-$Fe(OH)_2$, ferrous-carbonate hydroxide, and green-rust after bioreduction of arsenic-sorbed lepidocrocite by *Shewanella putrefaciens*. *Geochim. Cosmochim. Acta* ***2009****, 73,* 1359–1381.

Ostergren, J. D.; Bargar, J. R.; Brown, Jr., G. E.; Parks, G. A. Combined EXAFS and FTIR investigation of sulfate and carbonate effects on Pb(II) sorption to goethite (α-FeOOH). *J. Synchrotron Rad.* ***1999***, *6*, 645–647.

Ostergren, J. D.; Trainor, T. P.; Bargar, J. R.; Brown, Jr., G. E.; Parks, G. A. Inorganic ligand effects on Pb(II) sorption to goethite (α-FeOOH). I. Carbonate. *J. Colloid Interface Sci.* ***2000a***, *225*, 466-482.

Ostergren, J. D.; Brown, G. E. Jr.; Parks, G. A.; Persson, Per. Inorganic ligand effects on Pb(II) sorption to goethite (α-FeOOH). II. Sulfate. *J. Colloid Interface Sci.* ***2000b***, *225*, 483–493.

Oswald, H. R.; Reller, A.; Schmalle, H. W.; Dubler, E. Structure of copper(II) hydroxide, $Cu(OH)_2$. *Acta Cryst.* ***1990***, *C46*, 2279–2284.

Otero Fariña, A.; Peacock, C. L.; Fiol, S.; Antelo, J.; Carvin, B. A universal adsorption behaviour for Cu uptake by iron (hydr)oxide organo–mineral composites. *Chem. Geol.* ***2018***, *479*, 22–35.

Pan, Y.; Li, H. Investigating heavy metal pollution in mining brownfield and its policy implications: A case study of the Bayan Obo Rare Earth Min, Inner Mongolia, China. *Environ. Manage.* ***2016***, 57, 879–893.

Paquette, J.; Reeder, R. J. Relationship between surface structure, growth mechanism, and trace element incorporation in calcite. *Geochim. Cosmochim. Acta* ***1995***, *59* (4), 735–349.

Pareja-Carrera, J.; Mateo, R.; Rodríguez-Estival, J. Lead (Pb) in sheep exposed to mining pollution: Implications for animal and human health. *Ecotoxicol. Environ. Safety* ***2014***, *108*, 210-216.

Parkhurst, D. L.; Appelo, C. A. J. Description of input and examples for PHREEQC version 3 – A computer program for speciation, batch-reaction, one-dimensional transport, and inverse geochemical calculations. In *U.S. Geological Survey Techniques and methods, book 6*; U.S. Geological Survey: Denver, Colorado **2013**; p. 1–497.

Parkman, R. H.; Charnock, J. M.; Bryan, N. D.; Livens, F. R.; Vaughan, D. J. Reactions of copper and cadmium ions in aqueous solution with goethite, lepidocrocite, mackinawite, and pyrite. *Am. Mineral.* ***1999***, *84*, 407–419.

Parks, G. A. Surface energy and adsorption as mineral/water interfaces: An introduction. *Rev. Mineral.* ***1990***, *23*, 133–176.

Payne, J. F.; Malins, D. C.; Gunselman, S.; Rahimtula, A.; Yeats, P. A. DNA oxidative damage and vitamin A reduction in fish from a large lake system in Labrador, Newfoundland, contaminated with iron-ore mine tailings. *Marine Environ. Res.* ***1998***, *46*, 289–294.

Peacock, C. L.; Sherman, D. M. Copper(II) sorption onto goethite, hematite and lepidocrocite: A surface complexation model based on ab initio molecular geometries and EXAFS spectroscopy. *Geochim. Cosmochim. Acta* ***2004***, *68* (12), 2623–2637.

Peacor, D. R. Analytical electron microscopy: X-ray analysis. *Rev. Mineral.* ***1992***, *27*, 113–140.

Penn, R. L.; Banfield, J. F. Imperfect oriented attachment: Dislocation generation in defect-free nanocrystals. *Science* ***1998***, *281*, 969–971.

Pedersen, H. D.; Postma, D.; Jakobsen, R.; Larsen, O. Fast transformation of iron oxyhydroxides by the catalytic action of aqueous Fe(II). *Geochim. Cosmochim. Acta* ***2005***, *69* (16), 3967–3977.

Pedersen, H. D.; Postma, D.; Jakobsen, R. Release of arsenic associated with the reduction and transformation of iron oxides. *Geochim. Cosmochim. Acta* ***2006***, *70*, 4116–4129.

Pederson, L. R. Two-dimensional chemical state plot for lead using XPS. *J. Electron Spectr. Rel. Phen.* ***1982****, 28,* 203–209.

Pérez-Garrido, C.; Fernández-Díaz, L.; Pina, C. M.; Prieto, M. In situ AFM observations of the interaction between calcite ($10\bar{1}4$) surfaces and Cd-bearing aqueous solutions. *Surface Sci.* ***2007****, 601,* 5499–5509.

Perez, J. P. H.; Tobler, D. J.; Thomas, A. N.; Freeman, H. M.; Dideriksen, K.; Radnik, J.; Benning, L. G. Adsorption and reduction of arsenate during Fe^{2+}-induced transformation of ferrihydrite. *ACS Earth Space Chem.* ***2019****, 3,* 884–894.

Perez, J. P. H.; Freeman, H. M.; Brown, A. P.; van Genuchten, C. M.; Dideriksen, K.; S'ari, M.; Tobler, D. J.; Benning, L. G. Direct Visualisation of arsenic binding on green rust sulfate. *Environ. Sci. Technol.* ***2020****, 54,* 3297–3305.

Persson, I.; Lundberg, D.; Bajnóczi, É. G.; Klementiev, K.; Just, J.; Sigfridsson Clauss, K. G. V. EXAFS study on the coordination chemistry of the Solvated copper(II) ion in a series of oxygen donor solvents. *Inorg. Chem.* ***2020****, 59,* 9538–9550.

Petit, P.-E.; Farges, F.; Wilke, M.; Solé, A. Determination of the iron oxidation state in Earth materials using XANES pre-edge information. *J. Synchrotron Rad.* ***2001****, 8,* 952–954.

Pikett, G. Modification of the Brunauer–Emmett–Teller theory of multimolecular adsorption. *J. Am. Chem. Soc.* ***1945****, 67* (11), 1958–1962.

Plumlee, G. S., and Morman, S. A. Mine wastes and human health. *Elements* ***2011****, 7* (6), 399–404.

Plummer, L. N.; Busenberg, E. The solubilities of calcite, aragonite and vaterite in CO_2–H_2O solutions between 0 and 90 ºC, and an evaluation of the aqueous model for the system $CaCO_3$–CO_2–H_2O. *Geochim. Cosmochim. Acta,* ***1982****, 46,* 1011–1040.

Plummer, L. N.; Wigley, T. M. L.; Parkhurst, D. L. The kinetics of calcite dissolution in CO_2-water systems at 5 ºC to 60 ºC and 0.0 to 1.0 atm CO_2. *Am. J. Sci.* ***1978****, 278,* 179–216.

Pokrovsky, O. S.; Schott, J.; Thomas, F. Dolomite surface speciation and reactivity in aquatic systems. *Geochim. Cosmochim. Acta* ***1999****, 63* (19/20), 3133–3143.

Pokrovsky, O. S.; Schott, J. Forsterite surface composition in aqueous solutions: A combined potentiometric, electrokinetic, and spectroscopic approach. *Geochim. Cosmochim. Acta* ***2000a****, 64* (19), 3299–3312.

Pokrovsky, O. S.; Schott, J. Kinetics and mechanism of forsterite dissolution at 25 ºC and pH from 1 to 12. *Geochim. Cosmochim. Acta* ***2000b****, 64* (19), 3313–3325.

Pokrovsky, O. S.; Schott, J. Surface chemistry and dissolution kinetics of divalent metal carbonates. *Environ. Sci. Technol.* ***2002****, 36,* 426–432.

Pokrovsky, O. S.; Golubev, S. V.; Schott, J.; Castillo, A. Calcite, dolomite and magnesite dissolution kinetics in aqueous solutions at acid to circumneutral pH, 25 to 150 ºC and 1 to 55 atm pCO_2: New constraints on CO_2 sequestration in sedimentary basins. *Chem. Geol.* ***2009****, 265,* 20–32.

Ponthieu, M.; Juillot, F.; Hiemstra, T.; Van Riemsdijk, W. H., Benedetti, M. F. Metal ion binding to iron oxides. *Geochim. Cosmochim. Acta* ***2006****, 70,* 2679–2698.

Postma, D. Formation of siderite and vivianite and the pore-water composition of a recent bog sediment in Denmark. *Chem. Geol.* ***1981****, 31,* 225–244.

Postma, D. Pyrite and siderite oxidation in swamp sediments. *J. Soil Sci.* ***1983****, 34,* 163–182.

Postma, D. The reactivity of iron oxides in sediments: A kinetic approach. *Geochim. Cosmochim. Acta* ***1993****, 57,* 5027–5034.

Postma, D.; Jakobsen, R. Redox zonation: Equilibrium constraints on the Fe(III)/SO_4-reduction interface. *Geochim. Cosmochim. Acta* ***1996****, 60* (17), 3169–3175.

Poulston, S.; Parlett, P. M.; Stone, P.; Bowker, M. Surface oxidation and reduction of CuO and Cu_2O studied using XPS and XAES. *Surf. Interface Anal.* ***1996****, 2*, 811–820.

Pourrut, B.; Jean, S.; Silvetsre, J.; Pinelli, E. Lead-induced DNA damage in *Vicia faba* root cells: Potential involvement of oxidative stress. *Mutation Res.* ***2011****, 726,* 123–128.

Prieto, M.; Cubillas, P.; Fernández-Gonzalez, Á. Uptake of dissolved Cd by biogenic and abiogenic aragonite: A comparison with sorption onto calcite. *Geochim. Cosmochim. Acta* ***2003****, 67* (20), 3859–3869.

Puigdomenech, I.; Taxén, C. Thermodynamic data for copper. Implications for the corrosion of copper under repository conditions. *Technical Report* ***2000****, SKB*, TR-00-13, pp. 96.

Rasmussen, B.; Muhling, J. R. Making magnetite late again: Evidence for widespread magnetite growth by thermal decomposition of siderite in Hamersley banded iron formations. *Precambrian Res.* ***2018****, 306,* 64–93.

Rasmussen, B.; Muhling, J. R.; Krapež, B. Greenalite and its role in the genesis of early Precambrian iron formations – A review. *Earth-Sci. Rev.* ***2021****, 217*, 103613, 1–29.

Ravel, B.; Newville, M. ATHENA, ARTEMIS, HEPHAESTUS: data analysis for X-ray absorption spectroscopy using IFEFFIT. *J. Synchrotron Rad.* ***2005****, 12,* 537–541.

Raven, K. P.; Jain, A.; Loeppert, R. H. Arsenite and arsenate adsorption to ferrihydrite: Kinetics, equilibrium, and adsorption envelopes. *Environ. Sci. Technol.* ***1998****, 32,* 344–349.

Reeder, R. J. Crystal chemistry of the rhombohedral carbonates. *Rev. Mineral. Chem.* ***1983****, 11,* 1–48.

Reeder, R. J. Interaction of divalent cobalt, zinc, cadmium, and barium with the calcite surface during layer growth. *Geochim. Cosmochim. Acta* ***1996****, 60* (9), 1543–1552.

Reeder, R. J.; Lamble, G. M.; Northrup, P.A. XAFS study of the coordination and local relaxation around Co^{2+}, Zn^{2+}, Pb^{2+}, and Ba^{2+} trace elements in calcite. *Am. Mineral.* ***1999****, 84*, 1048–1060.

Reeder, R. J.; Nugent, M.; Tait, C. D.; Morris, D. E.; Heald, S. M.; Beck, K. M.; Hess, W. P.; Lanzirotti, A. Coprecipitation of Uranium(VI) with calcite: XAFS, micro-XAS, and luminescence characterisation. *Geochim. Cosmochim. Acta* ***2001****, 65* (20), 3491–3503.

Reffass, M.; Sabot, R.; Savall, C.; Jeannin, M.; Creus, J.; Refait, P. Localised corrosion of carbon steel in $NaHCO_3$/NaCl electrolytes: role of Fe(II)-containing compounds. *Corr. Sci.* ***2006****,48*, 709–726.

Reischer, M.; Sun, W.; Perez, J. P. H.; Mangayayam, M. C.; Füllenbach, L. C.; Nilabh, S.; Digiacomo, F.; Mulders, J. J. P. A.; Alonso de Linaje, V.; Schiefler, A. A.; Linke, T.; Christensen, A. G.; Weber, K.; Tobler, D. J.; Dideriksen, K. Injection and transport of sulfidized nanoparticulate zero valent iron (S-nZVI) in clastic sediments: a tank experiment. *J. Contam. Hydrol.* ***2022****, in review.*

Reiterer, F. Löslichkeitskonstanten und freie Bildungsenthalpien neutraler Übergansmetallcarbonate. *Thesis, Montanuniversität Leoben* ***1980***.

Renard, F.; Putnis, C. V.; Montes-Hernandez, G.; Ruiz-Agudo, E.; Hovelmann, J.; Sarret, G. Interaction of arsenic with calcite surfaces revealed by in situ nanoscale imaging. *Geochim. Cosmochim. Acta* ***2015****, 159,* 61–79.

Renard, F.; Putnis, C. V.; Montes–Hernandez, G.; King, H. E. Siderite dissolution coupled to iron oxyhydroxide precipitation in the presence of arsenic revealed by nanoscale imaging. *Chem. Geol.* ***2017****, 449,* 123–134.

Renard, F.; Røyne, A.; Putnis, C. V. Timescale of interface-coupled dissolution-precipitation reactions on carbonates. *Geosci. Front.* ***2019****, 10,* 17–27.

Reza, A. H. M.; Jean, J.-S.; Yang, H.-J.; Lee, M.-K.; Woodall, B.; Liu, C.-C.; Lee, J.-F.; Luo, S.-D. Occurrence of arsenic in core sediments and groundwaters in the Chapai-Nawabganj District, northwestern Bangladesh. *Water Res.* ***2010****, 44,* 2021–2037.

Rietra, R. P. J. J.; Hiemstra, T.; Van Riemsdijk, W. H. The relationship between molecular structure and ion adsorption on variable charge minerals. *Geochim. Cosmochim. Acta* ***1999****, 63* (19/20), 3009–3015.

Rinklebe, J.; Shaheen, S. M. Redox chemistry of nickel in soils and sediments: A review. *Chemosphere* ***2017****, 179,* 256–278.

Robie, R. A.; Hemingway, B. S. Thermodynamic properties of minerals and related substances at 298.15 K and 1 bar (10^5 pascals) pressure and at higher temperatures. *USGS* ***1995****, Bulletin 2131,* 470 p.

Roh, Y.; Zhang, C.-L.; Vali, H.; Lauf, R. J.; Zhou, J.; Phleps, T. J. Biogeochemical and environmental factors on Fe biomineralisation: Magnetite and siderite formation. *Clays Clay Minerals* ***2003****, 51* (1), 83–95.

Rosso, K. M.; Yanina, S. V.; Gorski, C. A.; Larese-Casanova, P.; Scherer, M. M. Connecting observations of hematite (α-Fe_2O_3) growth catalyzed by Fe(II). *Environ. Sci. Technol.* ***2010****, 44,* 61–67.

Rouff, A. A.; Reeder, R. J.; Fisher, N. S. Pb(II) sorption with calcite: A radio tracer study. *Aquat. Geochem.* ***2002****, 8,* 203–228.

Rouff, A. A.; Elzinga, E. J.; Reeder, R. J. X-ray absorption spectroscopic evidence for the formation of Pb(II) inner-sphere adsorption complexes and precipitates at the calcite–water interface. *Environ. Sci. Technol.* ***2004****, 38,* 1700–1707.

Rouff, A. A.; Elzinga, E. J.; Reeder, R. J.; Fisher, N. S. The influence of pH on the kinetics, reversibility and mechanisms of Pb(II) sorption at the calcite–water interface. *Geochim. Cosmochim. Acta* ***2005****, 69* (22), 5173–5186.

Rouff, A. A.; Elzinga, E. J.; Reeder, R. J.; Fisher, N. S. The effect of aging and pH on Pb(II) sorption processes at the calcite–water interface. *Environ. Sci. Technol.* ***2006****, 40,* 1792–1798.

Rouxhet, P. G.; Genet, M. J. XPS analysis of bio-organic systems. *Surf. Interface Anal.* ***2011****, 43,* 1453–1470.

Rustad, J. R.; Felmy, A. R. The influence of edge sites on the development of surface charge on goethite nanoparticles: A molecular dynamics investigation. *Geochim. Cosmochim. Acta* ***2005****, 69* (6), 1405–1411.

Sadykov, V.A.; Isupova, L.A.; Tsybulya, S.V.; Cherepanova, S.V.; Litvak, G.S.; Burgina, E.B.; Kustova, G.N.; Kolomiichuk, V.N.; Ivanov, V.P.; Paukshtis, E.A.; Golovin, A.V.; Avvakumov,

E.G. Effect of mechanical activation on the real structure and reactivity of iron(III) oxide with corundum-type structure. *J. Solid State Chem.* ***1996****, 123*, 191–202.

Saha, J. G.; Lee, Y. W.; Tinline, R. D.; Chinn, S. H. F.; Austenson, H. M. Mercury residues in cereal grains from seeds or soil treated with organomercury compounds. Canadian *J. Plant Sci.* ***1970****, 50*, 597–599.

Sahai, N.; Sverjenski, D. A. Evaluation of internally consistent parameters for the triple-layer model by the systematic analysis of oxide surface titration data. *Geochim. Cosmochim. Acta* ***1997a****, 61* (4), 2801–2826.

Sahai, N.; Sverjenski, D. A. Solvation and electrostatic model for specific electrolyte adsorption. *Geochim. Cosmochim. Acta* ***1997b****, 61* (4), 2827–2848.

Sahai, N.; Lee, Y. J.; Xu, H.; Ciardelli, M.; Gaillard, J.-F. Role of Fe(II) and phosphate in arsenic uptake by coprecipitation. *Geochim. Cosmochim. Acta* ***2007****, 71*, 3193–3210.

Salem, M. R.; Mangood, A. H.; Hamdona, S. K.; Dissolution of calcite crystals in the presence of some metal ions. *J. Mater. Sci.* ***1994****, 29*, 6463–6467.

Scheffer, F.; Schachtschabel, P. Lehrbuch der Bodenkunde. 16th ed. *Eds.* Blume, H.-P.; Brümmer, G. W.; Horn, R.; Kandeler, E.; Kögel-Knabner, I.; Kretzschmar, R.; Stahr, K.; Wilke, B.-M. *Spektrum Akademischer Verlag, Heidelberg,* ***2010****,* pp.569. ISBN 978-3-8274-1444-1.

Scheinost, A. C.; Abend, S.; Pandya, K. I.; Sparks, D. L. Kinetic controls on Cu and Pb sorption by ferrihydrite. *Environ. Sci. Technol.* ***2001****, 35*, 1090–1096.

Scheinost, A. C.; Charlet, L. Selenite reduction by mackinawite, magnetite and siderite: XAS characterisation of nanosized redox products. *Environ. Sci. Technol.* ***2008****, 42*, 1984–1989.

Scheinost, A. C.; Steudtner, R.; Hübner, R.; Weiss, S.; Bok, F. Neptunium(V) retention by siderite under anoxic conditions: Precipitation of NpO_2-like nanoparticles and of Np(IV) pentacarbonate. *Environ. Sci. Technol.* ***2016****, 50*, 10413–10420.

Schindler, P. W. Co-adsorption of metal ions and organic ligands: formation of ternary surface complexes. *Rev. Mineral.* ***1990****, 23*, 281–308.

Schindler, P.; Reinert, M.; Gamsjäger, H. Zur Thermodynamik der Metallcarbonate 3. Löslichkeitskonstanten und freie Bildungsenthalpien von $ZnCO_3$ und $Zn_5(OH)_6(CO_3)_2$ bei 25ºC. *Helv. Chim. Acta* ***1969****, 52*, p. 2327.

Schott, J.; Pokrovsky, O. S.; Oelkers, E. H. The link between mineral dissolution/precipitation kinetics and solution chemistry. *Rev. Mineral. Geochem.* ***2009****, 70*, 207–258.

Schuiling, R. D.; Krijgsman, P. Enhanced weathering: an effective and cheap tool to sequester CO_2. *Climate Change* ***2006****, 74*, 349–354.

Schultz, M. F.; Benjamin, M. M.; Ferguson, J. F. Adsorption and desorption of metals on ferrihydrite: Reversibility of the reaction and sorption properties of the regenerated solid. *Environ. Sci. Technol.* ***1987****, 21* (9), 963–869.

Schwertmann, U.; Murad, E. Effect of pH on the formation of goethite and hematite from ferrihydrite. *Clays Clay Miner.* ***1983****, 31* (4), 277–284.

Schwertmann, U.; Fechter, H. The formation of green rust and its transformation to lepidocrocite. *Clay Minerals* ***1994****, 29*, 87–92.

Schwertmann, U.; Fried, J.; Stanjek, H. From Fe(III) ions to ferrihydrite and then to hematite. *J. Colloid. Interface Sci.* ***1999****, 209*, 215–223.

Sdiri, A.; Higashi, T.; Jamussi, F.; Bouaziz, S. Effects of impurities on the removal of heavy metals by natural limestones in aqueous systems. *J. Environ. Manage.* ***2012****, 93,* 245–253.

Seifritz, W. CO_2 disposal by means of silicates. *Nature* ***1990****, 345,* 486.

Senaki, A. L.; Dixon, J. B.; Hossner, L. R. Todorokite, goethite, and hematite: Alteration products of siderite in east Texas lignite overburden. *Soil. Sci.* ***1986****, 142* (1), 36–42.

Sengupta, R.; Tosca, N. J.; Robinson, S. A. Geochemical controls on the elemental composition of siderite: Implications for palaeo-environmental reconstructions. *Geochim. Cosmochim. Acta* ***2020****, 271,* 1–15.

Shaheen, S.; Rinklebe, J. Sugar beet factory lime affects the mobilisation of Cd, Co, Cr, Cu, Mo, Ni, Pb and Zn, under dynamic redox conditions in a contaminated floodplain soil. *J. Environ. Manage.* ***2017****, 186,* 253–260.

Shaheen, S. M.; Kwon, E. E.; Biswas, J. K.; Tack, F. M. G.; Ok, Y. S.; Rinklebe, J. Arsenic, chromium, molybdenum, and selenium: Geochemical fractions and potential mobilisation in riverine soil profiles originating from Germany and Egypt. *Chemosphere* ***2017****, 180,* 553–563.

Shannon, R. D. Revised effective ionic radii and systematic studies of interatomic distances in halides and chalcogenides. *Acta Cryst.* ***1976****, A 32,* 751–767.

Sherman, D.M. Molecular orbital (SCF-Xα-SW) theory of metal-metal charge transfer processes in minerals. I. Application to $Fe^{2+} \longrightarrow Fe^{3+}$ charge transfer and "electron delocalisation" in mixed-valence iron oxides and silicate. *Phys. Chem. Minerals* ***1987****, 14,* 355–363.

Sherman, D. M. Equilibrium isotopic fractionation of copper during oxidation/reduction, aqueous complexation and ore-forming processes: Predictions from hybrid density functional theory. *Geochim. Cosmochim. Acta* ***2013****, 118,* 85–97.

Sherman, D. M.; Randall, S. R. Surface complexation of arsenic(V) to iron(III) (hydr)oxides: Structural mechanism from ab initio molecular geometries and EXAFS spectroscopy. *Geochim. Cosmochim. Acta* ***2003****, 67* (22), 4223–4230.

Sherman, D. M.; Little, S. H. Isotopic disequilibrium of Cu in marine ferromanganese crusts: Evidence from *ab initio* predictions of Cu isotope fractionation on sorption to birnessite. *Earth Planet. Sci. Lett.* ***2020****, 549,* 116540, 1–7.

Silva, C. A. R.;Liu, X.; Millero, F. J. Solubility of siderite ($FeCO_3$) in NaCl solutions. *J. Soln. Chem.* ***2002****, 31* (2), 97–108.

Singer, P. C.; Stumm, W. Acid mine drainage: The rate determining step. *Science* ***1970****, 167,* 1121–1123.

Skousen, J. G.; Ziemkiewcz, P. F.; McDonald, L. M. Acid mine drainage formation, control and treatment: Approaches and strategies. *Extractive Ind. Soc.* ***2019****, 6,* 241-249.

Southam, G. Minerals as substrates for life: The procaryotic view. *Elements* ***2012****, 8* (2), 101–106.

Spadini, L.; Manceau, A.; Schindler, P. W.; Charlet, L. Structure and stability of Cd^{2+} surface complexes on ferric oxides. 1. Results from EXAFS spectroscopy. *J. Colloid Interface Sci.* ***1994****, 168,* 73–86.

Speer, J. A. Crystal chemistry and phase relations of orthorhombic carbonates. *Rev. Mineral. Chem.* ***1983****, 11,* 145–190.

Sposito, G. Molecular models of ion adsorption on mineral surfaces. *Rev. Mineral.* ***1990****, 23,* 261–280.

Stegemeier, J. P.; Reinsch, B. C.; Lentini, C. J.; Dale, J. G.; Kim, C. S. Aggregation of nanoscale iron oxyhydroxides and corresponding effects on metal uptake, retention, and speciation: II. Temperature and time. *Geochim. Cosmochim. Acta* ***2015****, 148,* 113–129.

Steinnes, E.; Allen, R. O.; Petersen, H. M.; Rambæk, J. P.; Varskog, P. Evidence of large scale heavy-metal contamination of natural surface soils in Norway from long-range atmospheric transport. *Sci. Total Environ.* ***1997****, 205,* 255–266.

Stel, H. Diagenetic crystallisation and oxidation of siderite in red bed (Bundsandstein) sediments from the Central Iberian Chain, Spain. *Sediment. Geol.* ***2009****, 213,* 89–96.

Stewart S. M.; Hofstetter, T. B; Joshi, P.; Gorski, C. A. Linking thermodynamics to pollutant reduction kinetics by Fe^{2+} bound to iron oxides. *Environ. Sci. Technol.* ***2018****, 52,* 5600–5609.

Stipp, S. L.; Hochella, Jr., M. F. Structure and binding environments at the surface as observed with X-ray photoelectron spectroscopy (XPS) and low energy electron diffraction (LEED). *Geochim. Cosmochim. Acta* ***1991****, 55,* 1723–1736.

Stipp, S. L.; Hochella, Jr., M. F.; Parks, G. A.; Leckie, J. O. Cd^{2+} uptake by calcite, solid-state diffusion, and the formation of solid-solution: Interface processes observed with near-surface sensitive techniques (XPS, LEED, and AES). *Geochim. Cosmochim. Acta* ***1992****, 56,* 1941–1954.

Stipp, S. L.; Parks, G. A.; Nordstrom, D. K.; Leckie, J. O. Solubility-product constant and thermodynamic properties for synthetic otavite, $CdCO_{3(s)}$, and aqueous association constants for the Cd(II)–CO_2–H_2O system. *Geochim. Cosmochim. Acta* ***1993****, 57,* 2699–2713.

Stookey, L. L. Ferrozine – A new spectrophotometric reagent for iron. *Anal. Chem.* ***1970****, 42* (7), 779–781.

Strawn, D. G.; Scheidegger, A. M.; Sparks, D. L. Kinetics and mechanisms of Pb(II) sorption and desorption at the aluminum oxide–water interface. *Environ. Sci. Technol.* ***1998****, 32,* 2596–2601.

Strawn, D. G.; Sparks, D. L. The use of XAFS to distinguish between inner- and outer-sphere lead adsorption complexes on montmorillonite. *J. Colloid Interface Sci.* ***1999****, 216,* 257–269.

Strawn, D. G.; Baker, L. L. Molecular characterization of copper in soils using X-ray absorption spectroscopy. *Environ. Pollut.* ***2009****, 157,* 2813–2821.

Stumm, W.; Lee, G. F. Oxygenation of ferrous iron. *Ind. Eng. Chem.* ***1961****, 53* (2), 143–146.

Stumm, W.; Huang, C.P.; Jenkins, S. R. Specific chemical interaction affecting the stability of dispersed systems. *Croatia Chem. Acta* ***1970****, 42,* 223–245.

Stumm, W.; Hohl, H.; Dalang, F. Interaction of metal ions with hydrous oxide surfaces. *Croatia Chem. Acta* ***1976****, 48* (4), 491–504.

Stumm, W.; Kummert, R.; Sigg, L. A ligand exchange model for the adsorption of inorganic and organic ligands at hydrous oxide interfaces. *Croatia Chem. Acta* ***1980****, 53* (2), 291–312.

Stumm, W.; Wollast, R. Coordination chemistry of weathering: Kinetics of the surface-controlled dissolution of oxide minerals. *Rev. Geophys.* ***1990****, 28* (1), 53–69.

Stumm, W.; Sulzberger, B. The cycling of iron in natural environments: Considerations based on laboratory studies of heterogeneous redox processes. *Geochim. Cosmochim. Acta* ***1992****, 56,* 3233–3257.

Stumm, W. Catalysis of redox processes by hydrous oxide surfaces. *Croatia Chem. Acta* ***1997****, 70* (1), 71–93.

Sulzberger, B.; Suter, D.; Siffert, C.; Banwart, S.; Stumm, W. Dissolution of Fe(III)(hydr)oxides in natural waters; laboratory assessment on the kinetics controlled by surface coordination. *Marine Chem.* ***1989****, 28,* 127–144.

Sun, C.; Liu, J.; Wang, Y.; Sun, L.; Yu, H. Multivariate and geostatistical analyses of the spatial distribution and sources of heavy metals in agricultural soil in Dehui, Northeast China. *Chemosphere* ***2013****, 92,* 517–523.

Sutton, S. R.; Bertsch, P. M.; Newville, M.; Rivers, M.; Lanzirotti, A.; Eng, P. Microfluorescence and microtomography analyses of heterogeneous earth and environmental materials. *Rev. Mineral. Geochem.* ***2002****, 49,*

Süsse, P. Verfeinerung der Kristallstruktur des Malachits, $Cu_2(OH)_2CO_3$. *Acta Cryst.* ***1967****, 22,* 146–151.

Swallow, K. C.; Hume, D. N.; Morel, F. M. M. Sorption of copper and Pb by hydrous ferric oxide. *Environ. Sci. Technol.* ***1980****, 14* (11), 1326–1331.

Swanson, H. E.; Tatge, E. Standard X-ray diffraction powder patterns, Vol. I. *Natl. Bur. Stand., Washington, DC,* ***1953****, 539,* pp. 359.

Tang, D.; Shi, X.; Jiang, G.; Wu, T.; Ma, J.; Zhou, X. Stratiform siderites from the Mesoproterozoic Xiamaling Formation in North China: Genesis and environmental implications. *Gondwana Res.* ***2018****, 58,* 1–15.

Tang, Y.; Elzinga, E. J.; Lee, Y. J.; Reeder, R. J. Coprecipitation of chromate with calcite: Batch experiments and X-ray absorption spectroscopy. *Geochim. Cosmochim. Acta* ***2007****, 71,* 1480–1493.

Tang, Y.; Martin, S. T. Siderite dissolution in the presence of chromate. *Geochim. Cosmochim. Acta* ***2011****, 75,* 4951–4962.

Taylor, L. L.; Quirk, J.; Thorley, R. M. S.; Kharecha, P. A.; Hansen, J.; Ridgwell, A.; Lomas, M. R.; Banwart, S. A.; Beerling, D. J. Enhanced weathering strategies for stabilizing climate and adverting ocean acidification. *Nature Climate Lett.* ***2015****, 6,* 402–408.

Taylor, S. D.; Becker, U.; Rosso, K. M. Electron transfer pathways facilitating U(VI) reduction by Fe(II) on Al- vs. Fe-oxides. *J. Phys. Chem. C* ***2017****, 121,* 19887–19903.

Terjesen, S. G.; Erga, O.; Thorsen, G.; Ve, A. I1. Phase boundary processes as rate determining steps in reactions between solids and liquids: The inhibitory action of metal ions on the formation of calcium bicarbonate by the reaction of calcite with aqueous carbon dioxide. *Chem. Eng. Sci.* ***1961****, 14* (1), 277–288.

Thomas, A. N.; Eiche, E.; Göttlicher, J.; Steininger, R.; Benning, L. G.; Freeman, H. M.; Dideriksen, K.; Neumann, T. Products of hexavalent chromium reduction by green rust sodium sulfate and associated reaction mechanisms. *Soil Syst.* ***2018****, 58* (2), 1–19.

Tipping, E.; Cooke, D. The effects of adsorbed humic substances on the surface charge of goethite (a-FeOOH) in freshwaters. *Geochim. Cosmochim. Acta* ***1982****, 46,* 75–80.

Tipping, E.; Griffith, J. R.; Hilton, J. The effect of adsorbed humic substances on the uptake of copper(II) by goethite. *Croatia Chem. Acta* ***1983****, 56* (4), 613–621.

Tipping, E.; Rieuwerts, J.; Pan, G.; Ashmore, M. R.; Lofts, S.; Hill, M. T. R.; Farago, M. E.; Thornton, I. The solid–solution partitioning of heavy metals (Cu, Zn, Cd, Pb) in upland soils of England and Wales. *Environ. Pollut.* ***2003*** *125,* 231–225.

Tobin, J. P.; Hirschwald, W.; Cunningham, J. XPS and XAES studies of transient enhancement of Cu^{I} at CuO surfaces during vacuum outgassing. *Appl. Surf. Sci.* ***1983***, *16*, 441–452.

Toner, B.; Manceau, A.; Marcus, M. A.; Millet, D. B.; Sposito, G. Zinc sorption by a bacterial biofilm. *Environ. Sci. Technol.* ***2005***, *39*, 8288–8294.

Toner, B.; Manceau, A.; Webb, S.; Sposito, G. Zinc sorption to biogenic hexagonal birnessite particles within a hydrated bacterial biofilm. *Geochim. Cosmochim. Acta* ***2006***, *70*, 27–43.

Tosca, N. J.; Jiang, C. Z.; Rasmussen, B.; Muhling, J. Products of the iron cycle on the early Earth. *Free Radic. Biol. Med.* ***2019***, *140*, 138–153.

Trivedi, P.; Axe, L.; Tyson, T. A. An analysis of Zn sorption to amorphous versus crystalline iron oxides using XAS. *J. Colloid Interface Sci.* ***2001***, *244*, 230–238.

Trivedi, P.; Dyer, J. A.; Sparks, D. L. Lead sorption onto ferrihydrite. 1. A Macroscopic and spectroscopic assessment. *Environ. Sci. Technol.* ***2003***, *37* (5), 908–914.

Tronc, E.; Belleville, P.; Jolivet, J.-P.; Livage, J. Transformation of ferric hydroxide into spinel by Fe(II) adsorption. *Langmuir* ***1992***, *8*, 313–319.

Uddin, M. K. A review on the adsorption of heavy metals by clay minerals, with special focus on the past decade. *Chem. Eng. J.* ***2017***, *308*, 438–462.

Usman, M.; Hanna, K.; Abdelmoula, M.; Zegeye, A.; Faure, P.; Ruby, C. Formation of green rust *via* mineralogical transformation of ferric oxides (ferrihydrite, goethite, hematite). *Appl. Clay Sci.* ***2012***, *64*, 38–43.

Van Cappellen, P.; Charlet, L.; Stumm, W.; Wersin, P. A surface complexation model of the carbonate mineral-aqueous solution interface. *Geochim. Cosmochim. Acta* ***1993***, *57*, 3505–3518.

Van Geen, A.; Robertson, A. P.; Leckie, J. O. Complexation of carbonate species at the goethite surface: Implications for adsorption of metal ions in natural waters. *Geochim. Cosmochim. Acta* ***1994***, *58* (9), 2073–2086.

Veli, S.; Alyüz, B. Adsorption of copper and zinc from aqueous solutions by using natural clay. *J. Hazard. Mater.* ***2007***, *149*, 226–233.

Venema, P.; Hiemstra, T.; Van Riemsdijk, W. H. Multisite adsorption of cadmium on goethite. *J. Colloid Interface Sci.* ***1996***, *183*, 515–527.

Villalobos, M.; Leckie, J. O. Carbonate adsorption on goethite under closed and open CO_2 conditions. *Geochim. Cosmochim. Acta* ***2000***, *64* (22), 3787–3802.

Villalobos, M.; Trotz, M. A.; Leckie, J. O. Surface complexation modelling of carbonate effects on the adsorption of Cr(VI), Pb(II), and U(VI) on goethite. *Environ. Sci. Technol.* ***2001***, *35*, 3849–3856.

Villalobos, M.; Cheney, M. A.; Alcaraz-Cienfuegos, J. Goethite surface reactivity: II. A microscopic site-density model that describes its surface area-normalized variability. *J. Colloid Interface Sci.* ***2009***, *336*, 412–422.

Voigt, M.; Marieni, C.; Clark, D. E.; Gíslason, S. R.; Oelkers, E. H. Evaluation and refinement of thermodynamic databases for mineral carbonation. *Energy Procedia* ***2018***, *146*, 81-91.

Vouk, V. B.; Piver, W. T. Metallic elements in fossil fuel combustion product: Amounts and form of emissions and evaluation of carcinogenicity and mutagenicity. *Environ. Health Perspectives,* ***1983***, *47*, 201–225.

Vu, H. P.; Shaw, S.; Brinza, L.; Benning, L. G. Partitioning of Pb(II) during goethite and hematite crystallisation: Implications for Pb transport in natural systems. *Appl. Geochem.* ***2013****, 39,* 119–128.

Vulkan, R.; Zhao, F.-J.; Barbosa-Jefferson, V.; Preston, S.; Paton, G. I.; Tipping, E.; McGrath, S. P. Copper speciation and impacts on bacterial biosensors in pore water of copper-contaminated soils. *Environ. Sci. Technol.* ***2000****, 34,* 5115–5121.

Wagner, C. D. Auger lines in X-ray photoelectron spectroscopy. *Anal. Chem.* ***1972****, 44* (6), 967–973.

Wagner, C. D., Naumkin, A. V.; Kraut-Vass, A.; Gaarenstroom, S. W.; Powell, C. J. NIST X-ray Photoelectron Spectroscopy Database. *NIST Standard Reference Database 20, Version 4.1 (web version)* ***2012***: https://srdata.nist.gov/xps/Default.aspx.

Waite, T. D.; Davis, J. A.; Payne, T. E.; Waychunas, G. A.; Xu, N. Uranium(VI) adsorption to ferrihydrite: Application of a surface complexation model. *Geochim. Cosmochim. Acta* ***1994****, 58* (24), 5465–5478.

Walker, S. R.; Jamieson, H. E.; Lanzirotti, A.; Andrande, C. F.; Hall, G. E. M. The speciation of arsenic in iron oxides in mine wastes from the giant gold mine, N.W.T.: Application of synchrotron micro-XRD and micro-XANES at the grain scale. *Can. Mineral.* ***2005****, 43,* 1205–1224.

Wang, H.; Dong, Y.; Wang, H. Hazardous metals in animal manure and their changes from 1990 to 2010 in China. *Toxicol. Environ. Chem.* ***2014****, 96,* 1346–1355.

Wang, Y.; Reardon, E. J. A siderite/limestone reactor to remove arsenic and cadmium from wastewaters. *Appl. Geochem.* ***2001****, 16,* 1241–1249.

Wang, Z.; Ma, T.; Zhu, Y.; Abass, O. K.; Liu, L.; Su, C.; Shan, H. Application of siderite tailings in water-supply well for As removal: Experiments and field tests. *Inter. Bioredeterior. Bioredegrad.* ***2018****, 128,* 85–93.

Waychunas, G. A.; Kim, C. S.; Banfield, J. F. Nanoparticulate iron oxide minerals in soils and sediments: unique properties and contaminant scavenging mechanisms. *J. Nanoparticle Res.* ***2005****, 7,* 409–433.

Waychunas, G. A; Zhang, H. Structure, chemistry, and properties of mineral nanoparticles. *Elements* ***2008****, 4* (6), 381–387.

Wehrli, B.; Sulzberger, B.; Stumm, W. Redox processes catalyzed by hydrous oxide surfaces. *Chem. Geol.* ***1989****, 78,* 167–179.

Weinman, B.; Goodbred, S. L. Jr.; Zheng, Y.; Aziz, Z.; Steckler, M.; van Geen, A.; Singhvi, A. K.; Nagar, Y. C. Contributions of floodplain stratigraphy and evolution to the spatial patterns of groundwater arsenic in Araihazaar, Bangladesh. *Geol. Soc. Am. Bulletin 2008, 120* (11-12), 1567–1580.

Weng, L.; Temminghoff, E. J. M.; Lofts, S.; Tipping, E.; Van Riemsdijk, W. H. Complexation with dissolved organic matter and solubility control of heavy metals in a sandy soil. *Environ. Sci. Technol.* ***2002****, 36,* 4804–4810.

White, A. F.; Peterson, M. L. Reduction of aqueous transition metal species on the surfaces of Fe(II)-containing oxides. *Geochim. Cosmochim. Acta* ***1996****, 60* (20), 3799–3814.

Wilke, M.; Farges, F.; Petit, P.-E.; Brown, G. E. Jr.; Martin, F. Oxidation state and coordination of Fe in minerals: An Fe *K*-XANES spectroscopic study. *Am. Mineral.* ***2001****, 86,* 714–730.

Williams, A. G. B.; Scherer, M. M. Kinetics of Cr(VI) reduction by carbonate green rust. *Environ. Sci. Technol.* ***2001****, 35,* 3488–3494.

Williams, A. G. B.; Scherer, M. M. Spectroscopic evidence for Fe(II)–Fe(III) electron transfer at the iron oxide–water interface. *Environ. Sci. Technol.* ***2004****, 38,* 4782–4790.

Wolthers, M.; Charlet, L.; Van Cappellen, P. The surface chemistry of divalent carbonate minerals; a critical assessment of surface charge and potential data using the charge distribution multi-site ion complexation model. *Am. J. Sci.* ***2008****, 308,* 905–941.

Wong, K. K.; Lee, C. K.; Low, K. S.; Haron, M. J. Removal of Cu and Pb from electroplating wastewater using tartaric acid modified rice husk. *Proc. Biochem.* ***2003****, 39,* 437–445.

Wu, S.; Lu, J.; Ding, Z.; Li, N.; Fu, F.; Tang, B. Cr(VI) removal by mesoporous FeOOH polymorphs: performance and mechanism. *RSC Adv.* ***2016****, 6,* 82118–82130.

Wuana, R. A.; Okieimen, F. E. Heavy metals in contaminated soils: A review of sources, chemistry, risks and best available strategies for remediation. International Scholarly Research network ISRN, *Ecology* ***2011****, 402647*, 1–20.

Wyckoff, R. W. G. Cubic closest packed, ccp, structure. *Cryst. Structures* ***1963****, 1*, 7-83.

Xia, K.; Bleam, W.; Helmke, P. A. Studies of the nature of Cu^{2+} and Pb^{2+} binding sites in soil humic substances using X-ray absorption spectroscopy. *Geochim. Cosmochim. Acta* ***1997****, 61* (11), 2211–2221.

Xie, X.; Wang, Y.; Ellis, A.; Su, C.; Li, J.; Li, M. The sources of geogenic arsenic in aquifers at Datong basin, northern China: Constraints from isotopic and geochemical data. *J. Geochem. Exploration* ***2011****, 110,* 155–166.

Xu, M.; Kovarik, L.; Arey, B. W.; Felmy, A. R.; Rosso, K. M.; Kerisit, S. Kinetics and mechanisms of cadmium carbonate heteroepitaxial growth at the calcite ($10\bar{1}4$) surface. *Geochim. Cosmochim. Acta* ***2014****, 134,* 221–233.

Xu, M; Ilton, E. S.; Engelhard, M. H.; Qafoku, O.; Felmy, A. R.; Rosso, K. M.; Kerisit, S. Heterogeneous growth of cadmium and cobalt carbonate phases at the ($10\bar{1}4$) calcite surface. *Chem. Geol.* ***2015****, 397,* 24–36.

Xu, M.; Riechers, S. L.; Ilton, E. S.; Du, Y.; Kovarik, L.; Varga, T.; Arey, B. W.; Qafoku, O.; Kerisit, S. Manganese-calcium intermixing facilitates heteroepitaxial growth at the ($10\bar{1}4$) calcite-water interface. *Chem. Geol.* ***2017****, 470,* 152–163.

Xu, X.; Zhao, Y.; Zhao, X.; Wang, Y.; Deng, W. Sources of heavy metal pollution in agricultural soils of a rapidly industrializing area in the Yangtze Delta of China. *Ecotoxicol. Environ. Safety* ***2014****, 108,* 161–167.

Yang, J.; Liu, J.; Dynes, J. J.; Peak, D.; Regier, T.; Wang, J.; Zhu, S.; Shi, J.; Tse, J. S. Speciation and distribution of copper in a mining soil using multiple synchrotron-based bulk and microscopic techniques. *Environ. Sci. Pollut. Res.* ***2014****, 21,* 2943–2954.

Yang, L.; Steefel, C. I.; Marcus, M. A.; Bargar, J. R. Kinetics of Fe(II)-catalyzed transformation of 6-line ferrihydrite under anaerobic flow conditions. *Environ. Sci. Technol.* ***2010****, 44,* 5469–5475.

Yanina, S. V.; Rosso, K. M. Linked reactivity at mineral–water interfaces through bulk crystal conduction. *Science* ***2008****, 320* (5873), 218–222.

Young, R. A.; Mackie, P. E.; von Dreele, R. B. Application of the pattern-fitting structure refinement method to X-ray powder diffraction patterns. *J. Appl. Cryst.* ***1977****, 10,* 262–269.

Yuan, K., Lee, S. S., De Andrade, V.; Sturchio, N. C.; Fenter, P. Replacement of calcite ($CaCO_3$) by cerussite ($PbCO_3$). *Environ. Sci. Technol.* ***2016***, *50*, 12984–12991.

Yunus, F. Md.; Khan, S.; Chowdhury, P.; Milton, A. H.; Hussain, S.; Rahman, M. A review of groundwater arsenic contamination in Bangladesh: The millennium development goal era and beyond. *Inter. J. Environ. Res. Public Health* ***2016***, *13*, 1–18.

Zachara, J. M.; Kittrick, J. A.; Harsh, J. B. The mechanism of Zn^{2+} adsorption on calcite. *Geochim. Cosmochim. Acta* ***1988***, *52*, 2281–2291.

Zachara, J. M.; Cowan, C. E.; Resch, C. T. Sorption of divalent metals on calcite. *Geochim. Cosmochim. Acta* ***1991***, *55*, 1549–1562.

Zhao, K.; Guo, H.; Zhou, X. Adsorption and heterogeneous oxidation of arsenite on modified granular natural siderite: Characterisation and behaviors. *Appl. Geochem.* ***2014***, *48*, 184–192.

Zinder, B.; Furrer, G.; Stumm, W. The coordination chemistry of weathering: II. Dissolution of Fe(III) oxides. *Geochim. Cosmochim. Acta* ***1986***, *50*, 1861–1869.